Development of a Polarizable Transferable Force Field for Vapor-Liquid Equilibria Calculations

Von der Fakultät Energie-, Verfahrens- und Biotechnik der Universität Stuttgart und dem Stuttgart Research Centre for Simulation Technology zur Erlangung der Würde eines Doktors der Ingenieurwissenschaft (Dr.-Ing.) genehmigte Abhandlung

Vorgelegt von

Christian Waibel

aus Schwäbisch Gmünd

Hauptberichter: Prof. Dr.-Ing. Joachim Groß
Mitberichter: Prof. Dr.-Ing. habil. Jadran Vrabec

Tag der mündlichen Prüfung: 28.01.2019

Institut für Technische Thermodynamik und Thermische Verfahrenstechnik der Universität Stuttgart

2019

Erklärung zu meiner Dissertation mit dem Titel:

Development of a Polarizable Transferable Force Field for Vapor-Liquid Equilibria Calculations

Hiermit erkläre ich, dass ich die beigefügte Dissertation selbstständig verfasst und keine anderen als die angegebenen Hilfsmittel genutzt habe. Alle wörtlich oder inhaltlich übernommenen Stellen habe ich als solche gekennzeichnet.

Ich versichere außerdem, dass ich die beigefügte Dissertation nur in diesem und keinem anderen Promotionsverfahren eingereicht habe und dass diesem Promotionsverfahren keine endgültig gescheiterten Promotionsverfahren vorausgegangen sind.

Ort, Datum	Unterschrift

Contents

List of symbols

Latin letters

AAD	absolute average deviation
C	collection matrix
$c_{ij},\ c_{\alpha\beta},\ c_{ab}$	prefactor of Mie potential
CORR	correlation coefficient
D	self diffusion coefficient
E	system energy
E_i	electric field
E_i^0	static electric field
ERR	relative deviation
F	force
f_{obj}	objective function
H	histogram / probability distribution
$\Delta^{LV}h$	enthalpy of evaporation
$\hat{I}_{ij}\ I_{\alpha\beta}$	correlation integrals
J^0	atomic "hardness"
k	force constant
k	reciprocal space vector
k_B	Boltzmann constant
k_{ij}	binary interaction parameter of PC-SAFT
L	box length
M	net dipole moment
m_{ij}	attractive exponent of Mie potential
$\hat{m}$	segment number of PC-SAFT
n	new state of Monte Carlo move
n	iteration step
N	number of molecules
$n_{ij},\ n_{\alpha\beta},\ n_{ab}$	repulsive exponent of Mie potential
o	old state of Monte Carlo move
$\mathcal{O}$	scaling of simulation effort
p	pressure
P	transition probability
P	molecular number probability
P_{xy}	pressure tensor
q	partial charge
Q	partition function

$\Delta q_i(R_c)$	net-charge within cutoff sphere
r	distance
R_c	cutoff radius
s	reduced coordinate
SD	standard deviation
T	temperature
T_{ij}	dipole-dipole interaction tensor
u	potential
U^0	constant of fluctuating charge model
v	velocity
V	volume
x	mole fraction

Greek letters

α	damping parameter of Wolf summation
α	polarizability
β	inverse temperature scaled with the Boltzmann constant
β	scaling parameter of mDSF method
δ_n	phase shift of torsional potential
ϵ_0	vacuum permittivity
ϵ_r	relative dielectric constant
$\epsilon_{ij},\ \epsilon_{\alpha\beta},\ \epsilon_{ab}$	energy parameter of Mie potential
$\hat{\epsilon}_{ii}$	energy parameter PC-SAFT
η	shear viscosity
θ	bending angle
κ	Ewald splitting (damping) parameter
$\kappa_{ij},\ \kappa_{\alpha\beta},\ \kappa_{ab}$	binary interaction parameter between interaction sites
Λ	de Broglie wavelength
μ	chemical potential
μ	dipole moment
ξ_{ij}	binary interaction parameter between species
π^{acc}	acceptance probability
ρ	charge density
ρ	molecule density
$\sigma_{ij},\ \sigma_{\alpha\beta}$	size parameter of Mie potential
$\hat{\sigma_{ii}}$	segment diameter PC-SAFT
τ	time step
ϕ	torsional angle

ϕ	electrostatic potential
ϕ_{ij}	adjustable parameter for $k_{\alpha\beta}$ estimation
χ^0	electro-negativity
$\psi_{i,ab}$	intramolecular interaction operator
ω	weighting function for bias
Ω	observable

Subscripts

a, b	indices for interaction sites
bend	bending angle
c	value at critical point
c	core
CBMC	configurational bias Monte Carlo
D	charge-on-spring / shell / Drude model
eq	equilibrium
i, j	indices for interaction site / molecule / species / segment
i	index for sate condition
inter	intermolecular
intra	intramolecular
k	index for molecule number windows
l	bond
max	maximum
min	minimum
n	periodicity
n	new state of Monte Carlo move
o	old state of Monte Carlo move
vdW	van der Waals
I,II	indices of boxes in Gibbs ensemble
α, β	indices for interaction site
θ	angle
ϕ	torsion

Superscripts

bias	quantity obtained with bias
Coulomb	Coulombic energy
Ewald	Ewald summation
exp	experimental
Gibbs	Gibbs ensemble

l, L	liquid phase
long	long-ranged
mod	modified
opt	optimal
pol	polarizable
sat	saturation
self	self interaction
set	training set
short	short-ranged
sim	simulation
tot	total
v, V	vapor phase
Wolf	Wolf summation
*	reduced variable

Abbreviations

COS	charge-on-spring
DSF	damped shifted force
DSP	damped shifted potential
MC	Monte Carlo
MD	molecular dynamics
mDSF	modified damped shifted force
mSF	modified shifted force
NpT	isobaric-isothermal ensemble
NVT	canonical ensemble
PC-SAFT	Perturbed-Chain Statistical Associating Fluid Theory
ref	reference
SF	shifted force
SP	shifted potential
UA	united atom
VLE	vapor-liquid phase equilibrium
μVT	grand canonical ensemble

Zusammenfassung

Die Vorhersage thermodynamischer Eigenschaften für Stoffe mit nicht ausreichenden oder fehlenden experimentellen Daten ist eine Grundvoraussetzung für die Auslegung vieler Prozesse, insbesondere in der chemischen Industrie. Molekulare Simulationen in Kombination mit übertragbaren Kraftfeldern ermöglichen solche Vorhersagen. In dieser Arbeit werden hierfür Monte Carlo Simulationen im großkanonischen Ensemble verwendet um Dampf-Flüssig Phasengleichgewichte zu berechnen. Die Qualität der Vorhersagen ist dabei stark von der Güte des verwendeten Kraftfeldes abhängig. Elektrostatische Wechselwirkungen sind Teil der meisten Kraftfelder und erfordern rechenaufwändige Algorithmen zur Auswertung. Deshalb wird eine effiziente sphärische Abschneidemethode entwickelt, die auf der Wolf Summe basiert, und die Energie als auch die Kräfte präzise wiedergibt. Um binäre Mischungen besser beschreiben zu können wird außerdem die Anwendung und Übertragbarkeit von kreuzweisen van der Waals Energie Parametern untersucht. Die Simulationsergebnisse zeigen dabei eine ausgezeichnete Übereinstimmung mit experimentellen Daten. Des Weiteren wird ein polarisierbares Kraftfeld für Alkane, Ether und Stickstoff entwickelt, welches die elektronische Polarisation explizit berücksichtigt. Die Genauigkeit des Kraftfeldes wird durch Vergleich experimenteller Daten von Dampf-Flüssig Gleichgewichten mit Simulationsergebnissen validiert. Dabei wird eine sehr gute Übereinstimmung mit experimentellen Daten erreicht.

Summary

The possibility of predicting thermodynamic properties for substances with scarce or absent experimental data is crucial for the design of processes in the chemical industry. Molecular simulations in combination with transferable force fields allow such predictions. In this thesis, Monte Carlo simulations in the grand canonical ensemble are applied to calculation of vapor-liquid phase equilibria. The quality of these predictions depends strongly on the quality of the applied force fields. Electrostatic interactions, which need computationally demanding algorithms for evaluation, are part of most force fields. Therefore, an efficient spherical truncation method, based on the Wolf summation, is introduced, which reproduces energy and forces accurately. To improve the description of binary mixtures the application and transferability of cross-wise van der Waals energy parameters is studied. Simulation results show excellent agreement with experimental data. Furthermore, a polarizable force field, including explicit description of electronic polarization, is developed for alkanes, ethers, and nitrogen. To verify the accuracy of the force field, vapor-liquid equilibria of pure substances as well as binary mixtures are calculated, and very good agreement with experimental data is achieved.

Journal publications

This thesis led to the following publications:

- Chapter 2: C. Waibel and J. Gross: Modification of the Wolf Method and Evaluation for Molecular Simulation of Vapor–Liquid Equilibria, Journal of Chemical Theory and Computation, 14 (4), 2018, 2198-2206

- Chapter 3: C. Waibel, F. M. Feinler and J. Gross: A Modified Shifted Force Approach to the Wolf Summation, Journal of Chemical Theory and Computation, 2018, submitted [in the meantime it was published with minor modifications in Journal of Chemical Theory and Computation, 15 (1), 2019, 572-583]

- Chapter 4: C. Waibel, R. Stierle, and J. Gross: Transferability of cross-interaction pair potentials: Vapor-liquid phase equilibria of n-alkane/nitrogen mixtures using the TAMie force field, Fluid Phase Equilibria, 456, 2018, 124-130

- Chapter 5: C. Waibel and J. Gross: Polarizable Transferable Anisotropic United-Atom Force Field Based on the Mie Potential for Phase Equilibria: n-Alkanes, Ethers, and Nitrogen, Journal of Chemical Theory and Computation, 2018, submitted [in the meantime it was published with minor modifications in Journal of Chemical Theory and Computation, 15 (4), 2019, 2561-2573]

The chapters 2 to 5 present literal quotes of the published work. Any addition with respect to the published work is marked. Any deletion is indicated with square brackets as ‚[...]'. Cross-references between chapters of this thesis, which are added to the published version of the text to increase readability, are marked by square brackets. The Supporting Informations to the single chapters are presented in the Appendix of this thesis.

Acknowledgements

First and foremost, I would like to express my gratitude to my supervisor Joachim Groß, for giving me the opportunity to work on this interesting topic. I really appreciate your encouragement, motivation, and guidance during my work on this thesis. In many instructive discussions I learned a lot and you gave me a deeper understanding of scientific working.
I would also like to thank all my colleagues of the ITT team for the friendly and creative atmosphere – it was very joyful.
Finally, I express my gratitude to my friends and family, especially to Anne, for their support during the last five years.

Chapter 1

Introduction

Correlating and predicting vapor-liquid phase equilibria (VLE) is essential for an efficient design of separation processes in chemical industry. Especially for substances, where experiments are expensive, predictive models are requested. In these cases it is desirable to predict physical properties based only on fundamental molecular models of the considered substances, including structure and interactions. A powerful tool for achieving predictions of physical properties are molecular simulations, where the underlying molecular model is described through classical force fields. The quality of results obtained from molecular simulation is entirely determined by the quality of the considered force fields (apart from algorithmic and numerical settings to sample the considered quantities). Classical force fields consist of different types of interaction sites, describing the energy landscape within molecules and between molecules. Some of these interaction types need special methods for evaluation.
This thesis aims to enhance efficiency of methods for the calculation of long-ranged electrostatic interactions in molecular simulation, which are, by nature computationally demanding. Furthermore, polarizable force fields for the determination of vapor-liquid equilibria are developed. The so-obtained efficiency and predictive power of molecular simulation methods shall help process optimization.

1.1 Vapor-Liquid Equilibria in Molecular Simulation

Molecular simulation is a suitable tool to predict vapor-liquid equilibria (VLE). Several methods for molecular dynamics (configurations from solving Newton's equations of motion) as well as Monte Carlo simulations (configurations from probability distribution) have been proposed. Two common methods to determine VLEs directly are the Gibbs ensemble Monte Carlo method[1–3] and the histogram-reweighting method[4,5], utilizing a grand canonical ensemble simulation.
In the Gibbs ensemble method the coexisting phases are calculated in two coupled sim-

ulations connected via volume change and particle transfer moves. It is a conceptually simple method, however, for each equilibrium point of the phase envelope a new simulation is needed. With the histogram-reweighting method the complete phase envelope of pure substances or mixtures at given temperature can be obtained from one or only a few simulations. The VLE is calculated from the sampled probability distribution using histogram-reweighting. A more efficient histogram reweighting method is obtained by combination with a Transition Matrix approach[6–9]. The Gibbs ensemble method and the Transition Matrix histogram-reweigthing approach are presented in more detail in the following two subsections 1.1.1 and 1.1.2.
VLEs can further be determined with the NpT + test particle method[10–13], where multiple simulations at different state points are carried out for the liquid and vapor phase. The equilibrium point is then obtained by calculating the chemical potential of each state point with the Widom test particle method[14] or any other appropriate method[15], and searching for a match of the liquid and vapor value. In the Grand Equilibrium method[16] a NpT + test particle simulation is conducted for the liquid phase and combined with a grand canonical ensemble simulation for the vapor phase. Another alternative is the Gibbs-Duhem integration method[17,18], which calculates the phase envelope by integrating along the saturation line coupled with NpT simulations, starting from a known coexisting point. The intuitive way to calculate a VLE is to simulate the two coexisting bulk phases with its diffuse interface directly in one simulation box[19]. But such simulations need a large number of particles, a long equilibration time, and special methods for long-range corrections. Therefore, they are currently only reasonable if the diffuse interface itself is of interest.

1.1.1 Gibbs Ensemble Monte Carlo

The Gibbs ensemble Monte Carlo method[1–3] allows the direct calculation of VLEs using two separated simulation boxes, denoted with I and II, each with periodic boundary conditions. The boxes are connected by the phase equilibrium conditions of thermal ($T_\mathrm{I} = T_\mathrm{II}$), mechanical ($p_\mathrm{I} = p_\mathrm{II}$), and chemical equilibrium ($\mu_{i,\mathrm{I}}^\mathrm{tot} = \mu_{i,\mathrm{II}}^\mathrm{tot}$). Each box represents one phase of the VLE and is in internal equilibrium. The total number of molecules $N = N_\mathrm{I} + N_\mathrm{II}$ is constant and the simulations can be carried out either in a NVT ensemble with constant total volume $V = V_\mathrm{I} + V_\mathrm{II}$ or a NpT ensemble. For pure components the NVT ensemble is eligible, because in VLEs only one independent intensive variable (T or p) exists, whereas for mixtures the NpT ensemble is used, specifying one further intensive variable (T and p). Thermal equilibration is achieved by displacement, rotation, and (partial-) molecular reconfiguration ('regrow') moves within each box. Pressure equilibrium between the two boxes is reached with volume moves. The volume change of the boxes is correlated in the NVT ensemble (with constant total volume $V = V_\mathrm{I} + V_\mathrm{II}$)

and in the NpT ensemble the volume of each box can be changed independently. For equilibration of the chemical potential a particle transfer between the two boxes is used. The NVT Gibbs ensemble partition function of a pure substance is given by[20]

$$Q_{NVT}^{Gibbs} = \sum_{N_\mathrm{I}=0}^{N} \frac{1}{\Lambda^{3N} N_\mathrm{I}!(N-N_\mathrm{I})!} \int_0^V V_\mathrm{I}^{N_\mathrm{I}} (V-V_\mathrm{I})^{N-N_\mathrm{I}} \mathrm{d}V_\mathrm{I} \\ \times \int e^{-\beta E(\mathbf{s}_\mathrm{I}^{N_\mathrm{I}})} \mathrm{d}\mathbf{s}_\mathrm{I}^{N_\mathrm{I}} \int e^{-\beta E(\mathbf{s}_\mathrm{II}^{N-N_\mathrm{I}})} \mathrm{d}\mathbf{s}_\mathrm{II}^{N-N_\mathrm{I}} \tag{1.1}$$

with reduced coordinates $\mathbf{s} = \mathbf{r}/L$, made dimensionless with box length L, the de Broglie wavelength Λ, the potential energy E, and the inverse temperature $\beta = 1/k_B T$, scaled with the Boltzmann constant k_B. Hence, the acceptance probability π^{acc} for the box-internal displacement, rotation and regrow moves from an old state o to a new state n, which is the same for both simulation boxes, yields exemplarily for box I

$$\pi_{o\to n}^{\mathrm{acc}} = \min\left[1,\ e^{-\beta\left[E(\mathbf{s}_n^{N_\mathrm{I}}) - E(\mathbf{s}_o^{N_\mathrm{I}})\right]}\right] \tag{1.2}$$

which is the same as for a move in the conventional NVT ensemble. For the coupled volume move the acceptance probability is given by

$$\pi_{o\to n}^{\mathrm{acc}} = \min\left[1,\ \left(\frac{V_{\mathrm{I},n}}{V_{\mathrm{I},o}}\right)^{N_\mathrm{I}} \left(\frac{V-V_{\mathrm{I},n}}{V-V_{\mathrm{I},o}}\right)^{N-N_\mathrm{I}} e^{-\beta\left[E(\mathbf{s}_n^{N}) - E(\mathbf{s}_o^{N})\right]}\right] \tag{1.3}$$

A particle transfer move, where a particle is removed in box I and inserted in box II, leads to

$$\pi_{o\to n}^{\mathrm{acc}} = \min\left[1,\ \frac{N_{\mathrm{I},o}(V-V_\mathrm{I})}{(N-N_{\mathrm{I},o}+1)V_\mathrm{I}} e^{-\beta\left[E(\mathbf{s}_n^{N}) - E(\mathbf{s}_o^{N})\right]}\right] \tag{1.4}$$

For mixtures the NpT Gibbs ensemble is used, specifying the two independent variables T and p. Instead of a coupled volume move, each box volume can be changed independently and the acceptance probability changes to (here exemplarily for box I and for simplicity for a pure component system)

$$\pi_{o\to n}^{\mathrm{acc}} = \min\left[1,\ \left(\frac{V_{\mathrm{I},n}}{V_{\mathrm{I},o}}\right)^{N_\mathrm{I}} e^{-\beta p(V_{\mathrm{I},n} - V_{\mathrm{I},o})} e^{-\beta\left[E(\mathbf{s}_n^{N_\mathrm{I}}) - E(\mathbf{s}_o^{N_\mathrm{I}})\right]}\right] \tag{1.5}$$

All other acceptance rules remain the same, considering the independent volume of each box.

1.1.2 Grand Canonical Transition Matrix Monte Carlo

In the grand canonical ensemble the chemical potential μ^{tot}, the volume V, and the temperature T are specified, whereas the number of molecules N and the energy E are fluctuating quantities. The partition function of the grand canonical ensemble is defined as[20]

$$Q_{\mu VT} = \sum_{N=0}^{\infty} \frac{e^{\beta\mu^{\text{tot}}N} V^N}{\Lambda^{3N} N!} \int e^{-\beta E(\mathbf{s}^N)} \mathrm{d}\mathbf{s}^N \tag{1.6}$$

In most practical calculations, the chemical potential μ^{tot} is replaced by the excess chemical potential $\mu = \mu^{\text{tot}} - k_B T \ln(\Lambda^3)$. The acceptance probability, satisfying detailed balance, for a molecule insertion move then is

$$\pi^{\text{acc}}_{o\to n} = \pi^{\text{acc}}_{N\to N+1} = \min\left[1,\ \frac{V}{N+1} e^{\beta\mu} e^{-\beta\left[E(\mathbf{s}_n^{N+1}) - E(\mathbf{s}_o^N)\right]}\right] \tag{1.7}$$

and for a molecule deletion move

$$\pi^{\text{acc}}_{o\to n} = \pi^{\text{acc}}_{N\to N-1} = \min\left[1,\ \frac{N}{V} e^{-\beta\mu} e^{-\beta\left[E(\mathbf{s}_n^{N-1}) - E(\mathbf{s}_o^N)\right]}\right] \tag{1.8}$$

These two moves equilibrate the number of molecules in the system for a given (excess) chemical potential. For thermal equilibration displacement, rotation, and (partial-) regrow moves are performed with the acceptance probability identical to acceptance criterion of the conventional NVT ensemble (see eq. 1.2).

In the grand canonical ensemble the sampling of a visited state histogram over the molecule number allows the calculation of vapor-liquid equilibria by utilizing histogram-reweighting techniques[4,5]. Due to the large energy barrier between the vapor and liquid phase, a uniform sampling of molecule numbers is not feasible. An alternative is offered by Transition Matrix sampling[21–26], which uses not only information from visited states but also from discarded moves by utilizing the acceptance probability of each move. Moreover, the Transition Matrix can be used for biasing insertion and deletion moves leading to a more uniform sampling of the N-space allowing to sample through energy barriers. In the following the VLE calculation method used in this thesis is presented briefly. This method is based on the Transition Matrix Monte Carlo method of Errington[6–8] which was extended by Hemmen et al.[9] using an analytic equation of state to determine suitable conditions of the chemical potential, temperature, and intervals of molecule numbers to trace the entire phase envelope.

Transition Matrix Sampling

In the Transition Matrix method of Fitzgerald et al.[24,25], the molecule number probability distribution is determined using attempted transitions between different states of (here) molecule numbers. Therefore, a collection matrix C with an entry for each stepwise transition ($C_{N\to N+1}$, $C_{N\to N}$, $C_{N\to N-1}$) of each molecule number N is updated in each Monte Carlo step with the unbiased acceptance probability from eq. 1.7 and eq. 1.8. For an insertion move, two elements of the collection matrix are updated

$$C_{N\to N+1} \doteq C_{N\to N+1} + \pi^{\text{acc}}_{N\to N+1} \tag{1.9}$$

$$C_{N\to N} \doteq C_{N\to N} + \left(1 - \pi^{\text{acc}}_{N\to N+1}\right) \tag{1.10}$$

These equations are algorithmic equations, for updating a quantity, which is indicated by the dot above the equal sign. For a deletion move a updating scheme according to the same pattern is used. All other moves lead to an update of $C_{N\to N} \doteq C_{N\to N} + 1$, because the molecule number remains constant. The macroscopic transition probability for each state-change can be determined from the collection matrix C according to

$$P_{N\to N+\delta} = \frac{C_{N\to N+\delta}}{C_{N\to N+1} + C_{N\to N} + C_{N\to N-1}} \tag{1.11}$$

with $\delta \in \{+1,\ 0,\ -1\}$ indicating the state-change. The non-normalized molecule number probability can then be calculated recursively from the detailed balance expression as

$$P(N+1) = P(N)\frac{P_{N\to N+1}}{P_{N+1\to N}} \tag{1.12}$$

The so-obtained probability distribution is used to bias the insertion and deletion moves, to sample each molecule number with equal probability. As weighting function $w(N) = -\ln P(N)$ is used, which leads to a scaling of the right-hand side of the minimum condition in eq. 1.7 and eq. 1.8 with $e^{\Delta w}$. During the simulation the collection matrix becomes more precise, which is used to adapt the biasing function. However, in a simulation with Transition Matrix bias, the collection matrix is still updated with the unbiased acceptance probabilities.

The probability distribution can then be used to calculate VLEs in a post processing step. The VLE condition requires equal pressures in each phase. In the probability distribution, which is bimodal at coexistence, this is ensured if the area under the vapor and liquid peak is equal. The obtained probability distribution at the temperature T and chemical potential μ of the simulation can iteratively be shifted to the chemical potential at coexistence using histogram reweighting[4]

$$P(N;\beta,\mu) = P(N;\beta,\mu_o)\cdot e^{N\beta(\mu-\mu_o)} \tag{1.13}$$

where o indicates the old state, from which the shift starts.
With a normalized probability distribution at coexistence the associated thermodynamic properties can be calculated. The pressure is determined in the ideal gas limit ($N = 0$) according to

$$p^{\mathrm{sat}} = -\frac{k_B T}{V} \ln[2P(N = 0;\ \mu^{\mathrm{sat}},\ T)] \tag{1.14}$$

and other static properties can be calculated for each phase by determining the ensemble averages using the probability distribution.

Pure Components

To determine an entire phase envelope for pure components from one simulation, an additional reweighting in temperature is possible. For reweighting the chemical potential and the temperature, a probability distribution $P(N, E)$, that additionally includes energy, has to be sampled. This is achieved using a combination of Transition Matrix sampling, allowing uniform sampling of each molecule number, and additionally collecting a visited state histogram $H^{\mathrm{bias}}(N, E)$ of the energies. The energy is thereby discretized in bins. Due to the use of the Transition Matrix method the obtained histogram $H^{\mathrm{bias}}(N, E)$ is sampled evenly for each N, but it is biased. An unbiased probability distribution $H(N, E)$ is obtained by scaling with the unbiased probability distribution $P(N)$ from the Transition Matrix scheme[6]

$$H(N, E) = \frac{H^{\mathrm{bias}}(N, E)}{\sum_E H^{\mathrm{bias}}(N, E)} P(N) \tag{1.15}$$

where $\sum_E H^{\mathrm{bias}}(N, E)$ indicates a summation over all entries of the energy distribution for a given N. A probability distribution $H(N, E)$ at other conditions of chemical potential and temperature, can again be obtained using histogram reweighting[4]

$$H(N, E; \beta, \mu) = H(N, E; \beta_o, \mu_o) \cdot e^{-(\beta-\beta_o)E + N(\beta\mu - \beta_o\mu_o)} \tag{1.16}$$

The results from histogram reweighting are only reasonable in the vicinity of the simulation condition, where sufficient overlap in the corresponding phase spaces exists. To cover the entire phase envelope, statistics of the probability distributions can be improved by performing multiple simulations at different conditions $\{\mu_i,\ T_i\}$ and using histogram reweighting to obtain a unified distribution function. Hence, Hemmen et al.[9] divided the N-space in intervals with different conditions $\{\mu_i,\ T_i\}$, respectively, and an overlap of one molecule at each boundary. A schematic description of this division is shown in Fig. 1.1. Suitable conditions are estimated using the Perturbed-Chain Statistical Associating Fluid Theory (PC-SAFT)[27] equation of state. Furthermore, the intervals in the N-space are

subdivided in windows of usually $\Delta N = 5$ to $\Delta N = 10$ molecules. All windows can run in parallel to improve simulation time. For a sufficient number of sample steps, the window width does thereby not affect the statistical uncertainties[28].

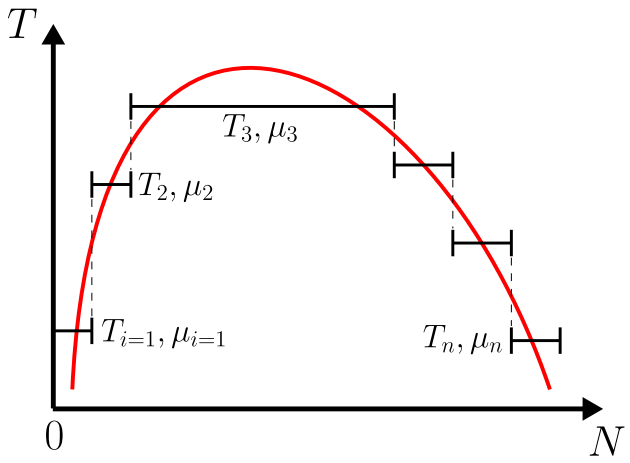

Figure 1.1: Schematic division of the N space in different simulation conditions $\{\mu_i,\ T_i\}$ to trace the entire phase envelope (red line) for a pure component system.

In each window k a histogram $H_k^{\text{bias}}(N, E)$ and the collection matrix of the Transition Matrix method is sampled. For all windows of the same condition $\{\mu_i,\ T_i\}$ the histograms can be combined to $H_i^{\text{bias}}(N, E)$ and the probability distribution $P_i(N)$ can be determined recursively by eq. 1.12 within the interval of condition $\{\mu_i,\ T_i\}$. Afterwards the unbiased probability distribution $H_i(N, E)$ can be obtained with eq. 1.15. A unified probability distribution $H(N, E)$ is obtained using histogram reweighting. Based on the uniform sampling of all molecule numbers, including the overlapping between two conditions, the histograms are combined using the requirement that the probability of two neighboring conditions i are equal for an average inverse temperature $\overline{\beta} = (\beta_i + \beta_{i+1})/2$ and an average chemical potential $\overline{\beta\mu} = (\beta_i\mu + \beta_{i+1}\mu_{i+1})/2$. This leads to an algorithmic equation which updates each histogram $H_{i+1} = H(N, E; \beta_{i+1}, \mu_{i+1})$ of a certain condition[9]

$$H_{i+1} \doteq H_{i+1} \frac{\sum_E H_i e^{-(\overline{\beta}-\beta_i)E+N(\overline{\beta\mu}-\beta_i\mu_i)}}{\sum_E H_{i+1} e^{-(\overline{\beta}-\beta_{i+1})E+N(\overline{\beta\mu}-\beta_{i+1}\mu_{i+1})}} \tag{1.17}$$

With the histogram reweighting scheme of eq. 1.16, the unified histogram can be transformed to other conditions $\{T, \mu\}$ and then the probability distribution $P(N; T, \mu)$ can be obtained to calculate a VLE. The probability distribution $P(N; T, \mu)$ at a condition $\{T, \mu\}$ can be calculated from the unified histogram $H(N, E; \beta_j, \mu_j)$ according to

$$P(N; T, \mu) = \frac{\sum_E H(N, E; \beta_j, \mu_j) e^{-(\beta-\beta_j)E+N(\beta\mu-\beta_j\mu_j)}}{\sum_N \sum_E H(N, E; \beta_j, \mu_j) e^{-(\beta-\beta_j)E+N(\beta\mu-\beta_j\mu_j)}} \tag{1.18}$$

with a generic index j specifying the condition in which a given N falls. The phase

equilibrium condition is again the equality of the areas under the vapor and liquid peak of the probability distribution $P(N;T,\mu)$ and the VLE for a specified temperature is determined by iterating the chemical potential.

Binary Mixtures

For the determination of VLE for binary mixtures at given temperature T the Transition Matrix approach with histogram reweigthing[8,9] can also be applied. The simulation is carried out at temperature T and chemical potential $\boldsymbol{\mu} = (\mu_1, \mu_2)$. To simplify the sampling, the now two-dimensional $\boldsymbol{N} = (N_1, N_2)$-space is divided into windows of $\Delta N_1 \times \Delta N_2$, usually rectangular with ΔN up to 10. Suitable estimates for $\boldsymbol{\mu}$ and $\boldsymbol{N}$ are calculated with the PC-SAFT equation of state. A division of the $\boldsymbol{N}$-space can be seen in Fig. 1.2. To obtain a better sampling, the molecule number within a window can not freely fluctuate, instead all points (N_1, N_2) are visited stepwise for a given number of Monte Carlo steps. During the successive screening a collection matrix is sampled. The probability distribution of a state (N_1, N_2) can then be determined in two steps. First the probabilities at two edges of the $\boldsymbol{N}$-space are calculated up to the maximum particle number $N_{i,\max}$ of each species i using eq. 1.12

$$P(N_1+1, N_2) = P(N_1, N_2)\frac{P_{N_1,N_2\to N_1+1,N_2}}{P_{N_1+1,N_2\to N_1,N_2}} \tag{1.19}$$

with $N_1 = 0...N_{1,\max}$, $N_2 = 0$ and

$$P(N_1, N_2+1) = P(N_1, N_2)\frac{P_{N_1,N_2\to N_1,N_2+1}}{P_{N_1,N_2+1\to N_1,N_2}} \tag{1.20}$$

with $N_1 = 0$, $N_2 = ...N_{2,\max}$.

Afterwards the probabilities of all remaining compositions are calculated according to

$$P(N_1, N_2) = \frac{1}{2}\left(P(N_1-1, N_2)\frac{P_{N_1-1,N_2\to N_1,N_2}}{P_{N_1,N_2\to N_1-1,N_2}} + P(N_1, N_2-1)\frac{P_{N_1,N_2-1\to N_1,N_2}}{P_{N_1,N_2\to N_1,N_2-1}}\right) \tag{1.21}$$

As in the pure component case, phase equilibrium is obtained if the area under the vapor and liquid peak of the probability distribution $P(N_1, N_2)$, which is now stretched over two dimensions (N_1, N_2), is equal. The probability distribution at phase equilibrium conditions can again be obtained using histogram reweighting (eq. 1.13) for the two dimensional case.

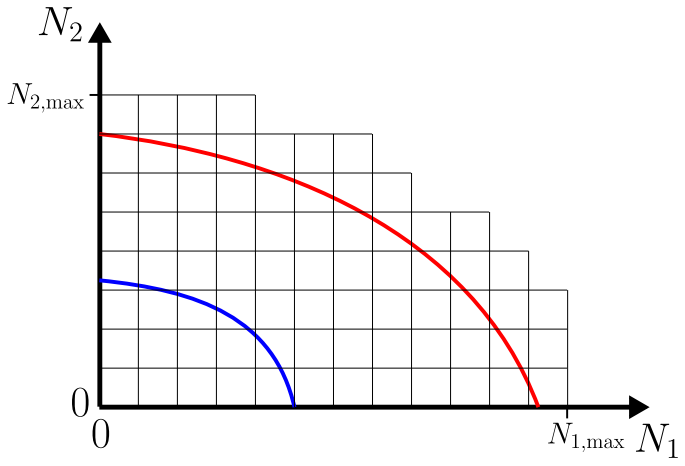

Figure 1.2: Schematic division of the $\boldsymbol{N}$-space in single windows to trace the entire phase envelope for a binary mixture at specified temperature. Red line is the bubble point curve and blue line is the dew point curve.

1.2 Molecular Model

A molecular description of molecules, containing information on the structure and interactions, is required in molecular simulations. Molecules are thereby, according to the Born-Oppenheimer approximation, separated in slowly moving nuclei and instantly moving averaged electron densities. Different types of empirical potentials are applied to describe the interactions between the nuclei, trying to roughly mimic the real energy surface. To achieve a certain level of precision various approaches are available. Choosing a model to describe the interactions accurately while maintaining computationally efficiency is challenging in force field development. In this section, the underlying functional forms of classical and of polarizable force fields are summarized. The structure of the molecules can be described in an all-atom manner, where each atom has its own interaction site, or a coarse-grained manner, where hydrogen atoms are combined with neighboring larger atoms of a molecule to single effective interaction site, thus decreasing the computational effort.

1.2.1 Classical Force Fields

Nowadays, in molecular simulations pairwise additive force fields are most commonly used. The energy landscape between two molecules is composed of relatively simple pairwise potential functions, whereby three-body or higher-body interactions are included effectively in the parameterization of the pairwise potentials. Three-body and four-body potentials then only prevail as bond-angle and as torsional potentials intramolecularly, i.e. within all molecules. That decreases the computational effort significantly. The functional

form of these potentials commonly has the form

$$E = \sum_{\text{bonds}} \frac{k_l}{2} \left(l - l_{\text{eq}}\right)^2 + \sum_{\text{angles}} \frac{k_\theta}{2} \left(\theta - \theta_{\text{eq}}\right)^2 + \sum_{\text{torsions}} \sum_{n} k_{\phi,n} \left[1 + \cos(n\phi - \delta_n)\right]$$
$$+ \sum_{\substack{\text{nonbonded} \\ \text{vdW pairs}}} c_{ij}\epsilon_{ij} \left[\left(\frac{\sigma_{ij}}{r_{ij}}\right)^{n_{ij}} - \left(\frac{\sigma_{ij}}{r_{ij}}\right)^{m_{ij}}\right] + \sum_{\substack{\text{nonbonded} \\ \text{charge pairs}}} \frac{q_i q_j}{4\pi\epsilon_0 r_{ij}} \tag{1.22}$$

The potentials can be separated in two main parts, the intramolecular (covalent) interactions (first line of eq. 1.22), and second, the intermolecular (non-covalent) interactions (second line of eq. 1.22). The summations of the intramolecular interactions run over all bonds (1–2 interactions), bending angles (1–3 interactions), and torsional angles (1–4 interactions). For bond lengths l and angles θ a harmonic potential with equilibrium values l_{eq} and θ_{eq}, and force constants k_l and k_θ are used. Because bond lengths only deviate slightly from zero-Kelvin lengths, fixed bond lengths are often used. The functional form of the torsional term is characterized through a cosine expansion determined by periodicity n, force constant $k_{\phi,n}$, and phase shift δ_n.

The intermolecular interactions are described by repulsive and attractive van der Waals interactions and by electrostatic interactions. The summations run over all non-bonded pairs of interaction sites separated by distance r_{ij}. Here, a Mie potential[29] is used for the van der Waals interactions, with energy parameter ϵ_{ij}, size parameter σ_{ij}, prefactor c_{ij} (chosen to ensure the minimum of the potential reaches $-\epsilon_{ij}$), repulsive exponent n_{ij}, and attractive exponent m_{ij}. Instead of the Mie potential other functional forms can be used, i.e. an Exp-6 potential[30]. Usually, the parameters for van der Waals interactions are determined for single interaction sites and not for every possible cross-wise interaction between different interaction sites. Rather, simple combining rules are used for cross-wise potentials, like the Lorentz-Berthelot[31,32] rules

$$\sigma_{ij} = \left(\sigma_{ii} + \sigma_{jj}\right)/2 \tag{1.23}$$
$$\epsilon_{ij} = \sqrt{\epsilon_{ii}\epsilon_{jj}} \tag{1.24}$$

A simple arithmetic average is used as a combining rule for the repulsive exponents[33] n_{ij}. In mixtures, as a consequence, the unlike interactions between different molecules are also determined using these simple combining rules. To improve the accuracy of mixture properties, it is possible to adjust the cross-energy parameter, which is done by rescaling the Berthelot cross-energy parameter

$$\epsilon_{ij} = \left(\epsilon_{ii}\epsilon_{jj}\right)^{1/2} \left(1 - \kappa_{ij}\right) \tag{1.25}$$

Parameter κ_{ij} is defined as a single constant for each pair of interaction sites between two

species. For like pairs $i = j$, parameter κ_{ij} is zero, and for unlike pairs, both of the same species, κ_{ij} is also zero. A detailed discussion of the combining rules for mixtures and a study on the transferability of the parameter $\kappa_{\alpha\beta}$ is presented in Chapter 4. Electrostatic interactions are described with the Coulomb law and are commonly modelled as point charges q_i, or, alternatively, as Gaussian charges[34], which spread the electron density. The partial charges are determined to approximately reproduce the electric field of the molecule and all higher order multipole effects. In order to do so, the charges can be rescaled, to effectively capture polarizable effects that appear in dense phases.
In eq. 1.22 only relatively simple functional forms are used to describe the energy landscapes of molecules. After diligent parameterization, however, these models capture the true molecular interactions sufficiently well to reproduce to good approximation many properties of real substances and mixtures in a wide range of fluid conditions. Therefore, these kinds of force fields are most commonly used force fields today.

1.2.2 Polarizable Force Fields

In the majority of force fields the electrostatic interactions are only described as pairwise interactions. This treatment does not consider the many-body effect caused by the static polarizability of molecules, i.e. the redistribution of the electron density due to the environment. In classical force fields the effect of static polarizability is approximately captured in a mean-field manner, by rescaled static partial charges. The electrostatic contribution due to polarizability, however is a strong function of species densities and a function of temperature. Fixed point charges can thus not adequate description of properties of fluids with varying mixture conditions.
In transferable force fields molecules are build from single interaction site types, where the same type is used in different molecules. In this case, the applicability of effective partial charges, which are optimized for only one molecule type, is particularly questionable. To capture the redistribution of the electron density in molecules, classical force fields can be extended with a polarizable model. This leads to a many-body character of the interactions, which makes the simulation more time consuming. Electronic polarization is commonly included using one of three basic methods: the fluctuating charge model[35,36], the induced point dipole model[37], and the charge-on-spring model (also referred to as Drude oscillator model or as shell model)[38–40].
In the fluctuating charge model the values of the partial charges are treated dynamically. According to the electronegativity of each atom the charges are redistributed as response to the outer electric field, while maintaining the total charge of the molecule. All orders of charge moments in polarizability are recovered, but only within the plane of the defined partial charges. The distribution of the charges in a molecule is determined in each step of a simulation by minimizing the total electrostatic energy of the system[41]

$$E = \sum_i \left(U_i^0 + \chi_i^0 q_i + \frac{1}{2} J_i^0 q_i^2 \right) + \sum_i \sum_{j>i} \frac{1}{4\pi\epsilon_0} \frac{q_i q_j}{r_{ij}} \tag{1.26}$$

The first summation is the energy required to create the charge q_i on each atom i and the right side is the Coulombic interaction between the charges. Here U_i^0 is a constant, χ_i^0 the electro-negativity defined by Mulliken[42], and J_i^0 the atomic "hardness"[43]. As boundary condition in the optimization step the total charge of a molecule has to be preserved.
In the inducible point dipole model, inducible point dipoles $\boldsymbol{\mu}_i$ with polarizability $\boldsymbol{\alpha}_i$ are added to different sites of a molecule. The point dipole $\boldsymbol{\mu}_i$ of a site i responds to the local electric field $\boldsymbol{E}_i$ assuming linear proportionality to the polarizability $\boldsymbol{\alpha}_i$[41]

$$\boldsymbol{\mu}_i = \boldsymbol{\alpha}_i \boldsymbol{E}_i = \boldsymbol{\alpha}_i \left[\boldsymbol{E}_i^0 - \sum_{j \neq i} \boldsymbol{T}_{ij} \boldsymbol{\mu}_j \right] \tag{1.27}$$

The local electric field $\boldsymbol{E}_i$ consists of two parts: the static electric field $\boldsymbol{E}_i^0$ and a part resulting from dipole-dipole interactions with other inducible dipoles connected via the dipole-dipole interaction tensor $\boldsymbol{T}_{ij}$. The electrostatic energy of the system consists of charge-charge, charge-dipole, and dipole-dipole interactions and requires a self-consistent solution of the inducible dipoles (orientation and strength) in each simulation step.
In the charge-on-spring model the inducible point dipoles are replaced by finite ones, which are represented by two charges of opposite sign connected with a harmonic spring. The spring is connected to the polarizability $\boldsymbol{\alpha}_i$ and only charge-charge interactions have to be calculated. A detailed description of the charge-on-spring model is presented in Chapter 5. There, this model is used to develop a polarizable force field for n-alkanes, ethers, and nitrogen.

1.3 Methods for Electrostatic Energy Calculation

Most force fields used in molecular simulations for real substances contain partial charges. Because the electrostatic potential is long-ranged (only decaying with r^{-1}), even interactions reaching outside of the simulation box have to be considered, if periodic boundary conditions are applied. The Coulombic energy can then be written as

$$E^{\text{Coulomb}} = \frac{1}{2} \sum_{i=1}^{N} \sum_{j \neq i}^{\infty} \frac{1}{4\pi\epsilon_0} \frac{q_i q_j}{|\mathbf{r}_{ij}|} \tag{1.28}$$

where q_i is a partial charge (dimensionless, as a factor of electron charge), $\mathbf{r}_{ij}$ denotes the distance vector between partial charge i and j, ϵ_0 is the dielectric constant, and N the number of partial charges in the simulation box. Index j points at every charge within the simulation box (except to $j = i$) and to all charges of periodic images (including $i = j$).

The summation is conditionally convergent and hence special methods have to be used to handle these interactions properly. In the following two methods are briefly reviewed: the Ewald summation[44], which is accepted as the standard method, and the Wolf method[45], which is a spherically truncated pairwise summation that can serve as a computationally efficient alternative.

1.3.1 Ewald Summation

In a system with periodic boundary conditions, the (for simplicity) cubic simulation box with a boxlength of L is repeated infinitely in all dimensions. The electrostatic energy can then be expressed by

$$E^{\text{Coulomb}} = \frac{1}{2} \sum_{\mathbf{n} \in \mathbb{Z}^3}{}' \sum_{i=1}^{N} \sum_{j=1}^{N} \frac{1}{4\pi\epsilon_0} \frac{q_i q_j}{|\mathbf{r}_{ij} + \mathbf{n} \cdot L|} \tag{1.29}$$

with a sum over all periodic images $\mathbf{n}$ of the simulation box. The prime thereby indicates, that for the unit cell ($\mathbf{n} = 0$) the interaction $i = j$ have to be omitted. The main idea of the Ewald summation approach is to divide the slowly decaying Coulomb potential into two parts. A, for small distances r, rapidly vanishing potential and a slowly varying potential. The selection is done using the error function with a splitting parameter κ

$$\frac{1}{|\mathbf{r}_{ij}|} = \frac{1 - \text{erf}(\kappa|\mathbf{r}_{ij}|)}{|\mathbf{r}_{ij}|} + \frac{\text{erf}(\kappa|\mathbf{r}_{ij}|)}{|\mathbf{r}_{ij}|} \tag{1.30}$$

with $\text{erfc}(\kappa r) = 1 - \text{erf}(\kappa r)$ as the complementary error function. The short-ranged part $\frac{\text{erfc}(\kappa|\mathbf{r}_{ij}|)}{|\mathbf{r}_{ij}|}$ can be treated in a direct summation within a cutoff radius R_c. The long-ranged part is a periodic and slowly varying function, which can be represented in a rapidly converging Fourier series and evaluated in the reciprocal space. Thereby, the Ewald parameter κ can be used to weight the contribution of the long- to the short-ranged part. To get a periodic Fourier series of the long-ranged part along the $\mathbf{n}$ lattice, the long-ranged potential $\phi(\mathbf{r})$ has to be transformed into a charge density $\rho(\mathbf{r})$ using the Poisson's equation

$$\nabla^2 \phi(\mathbf{r}) = -\frac{1}{\epsilon_0} \rho(\mathbf{r}) \tag{1.31}$$

The so obtained charge density corresponds to a Gaussian distribution, which can be seen as a screening of the partial charges. With this charge density a Fourier transformation can be performed and the Poission's equation can be applied again in Fourier space. An inverse Fourier transformation results in an expression of the potential with a summation over the reciprocal space vectors $\mathbf{k} = 2\pi\mathbf{n}/L$. The electrostatic potential due to the charge distribution in the simulation cell with periodic images at point $\mathbf{r}$ is

$$\phi(\mathbf{r}) = \sum_{\mathbf{k}\neq 0} \sum_{j=1}^{N} \frac{q_j}{V\epsilon_0 \mathbf{k}^2} \exp\left(\frac{-\mathbf{k}^2}{4\kappa^2}\right) \exp\left(i\mathbf{k}(\mathbf{r}-\mathbf{r}_j)\right) \tag{1.32}$$

Note that for $\mathbf{k} = 0$ the potential is diverging, but for a charge-neutral simulation box this term can be neglected. Hence, the Coulombic energy can be written as[46]

$$\begin{aligned} E^{\text{Ewald}} =& \frac{1}{2} \sum_{\mathbf{n}\in\mathbb{Z}^3}{}' \sum_{i=1}^{N} \sum_{j=1}^{N} \frac{1}{4\pi\epsilon_0} \frac{q_i q_j \operatorname{erfc}(\kappa|\mathbf{r}_{ij}+\mathbf{n}\cdot L|)}{|\mathbf{r}_{ij}+\mathbf{n}\cdot L|} \\ &+ \frac{1}{2} \sum_{\mathbf{k}\neq 0} \sum_{i=1}^{N} \sum_{j=1}^{N} \frac{q_i q_j}{V\epsilon_0 \mathbf{k}^2} \exp\left(\frac{-\mathbf{k}^2}{4\kappa^2}\right) \exp\left(i\mathbf{k}(\mathbf{r}_i-\mathbf{r}_j)\right) \\ &- \frac{1}{2} \sum_{i}^{\text{intra}} \sum_{j} \frac{q_i q_j \operatorname{erf}(\kappa|\mathbf{r}_{ij}|)}{|\mathbf{r}_{ij}|} - \frac{\kappa}{\sqrt{\pi}} \sum_{i=1}^{N} q_i^2 \end{aligned} \tag{1.33}$$

The first line of eq. 1.33 is the short-ranged part evaluated in the real space. The splitting parameter κ has to be chosen in such a way that the short-ranged potential will be negligible beyond a cutoff radius R_c. The cutoff radius has to be chosen as $R_c < L/2$, with L as the length of the simulation box. Using the minimum image convention the periodicity can be omitted and only interactions in the unit cell are evaluated. The second line is the periodic long-ranged part evaluated in the Fourier space, allowing an efficient calculation of these interactions. For infinite Fourier space evaluations the Ewald summations reaches the exact Coulombic energy, but for an efficient and still precise simulation the $\mathbf{k}$-vectors can be restricted to lie within a sphere with $|\mathbf{k}| < k_{\max}$. For further improvement of the Fourier part (the double sum can be rewritten in two single sums) and due to the periodicity the summation runs over all i and j, including all interactions. Hence, the self interaction and the intramolecular interactions within a molecule, which are already included in the bonded interactions, have to be omitted. This correction is done in the third line of eq. 1.33. To get a computationally efficient calculation, with relatively small cutoff radii in the real and reciprocal space, and without loosing too much accuracy, the parameters κ, k_{max} and R_c can be determined using expressions for error tolerances[47,48].

The Ewald summation has a simulation effort of $\mathcal{O}(N^2)$ in a simple implementation, but can be scaled down to $\mathcal{O}(N^{3/2})$ by using a smart algorithm and cutoff radii optimized to the splitting parameter κ[49]. A further improvement down to $\mathcal{O}(N\log(N))$ can be achieved by utilizing the fast Fourier transform. This transformation needs an interpolating grid and leads to the particle-particle particle mesh Ewald[50], particle mesh Ewald[51] and smooth particle mesh Ewald[52].

1.3.2 Wolf Summation

It would be beneficial to use only an efficient pairwise summation within a cutoff radius instead of additionally evaluating periodic images in Fourier space. But that is prevented by the long-ranged and conditionally convergent behavior of the Coulombic potential, which does not allow for naive spherically truncation methods[53–57]. With the observation, that the *effective* electrostatic potential is rather short ranged, Wolf et al.[45] developed a charge-neutralizing scheme, to mimic the screening effect of the surrounding medium with compensatory charges on a cutoff radius. A detailed discussion about the suitability of this approach to calculate energies and forces, as well as modifications of this method are one of the main objectives of this thesis and are presented in Chapters 2 and 3.

1.4 Outline of this thesis

In Chapter 2, the calculation of electrostatic interactions using the Wolf method is discussed and applied to the calculation of VLEs in grand canonical Monte Carlo simulations. This is an ensemble with fluctuating particle number, where the correct absolute electrostatic energy is important to describe properties accurately. To achieve better results for the energy and VLE properties, the original Wolf method is modified and compared to results from Ewald summation and the original Wolf summation.
The charge-neutralizing scheme of the Wolf summation describes energies well, whereas forces have discontinuities. To overcome this problem the method can be extended with a shifted force approach leading to a more reliable and continuous representation of the forces, which improves molecular dynamic simulations. However, the description of potential energy deteriorates. In Chapter 3 a modified shifted force approach is developed, improving the description of force and energy. The method is evaluated for VLE properties as well as dynamic properties and the results are compared to Ewald summation results and results obtained with the original shifted force extension.
The effect of cross-wise van der Waals energy parameters on binary n-alkane/nitrogen mixtures is studied in Chapter 4. These cross-energy parameters are defined for individual pairs of (united-)atom groups and adjusted to a training set using an analytic equation of state. In particular the transferability of the so-obtained force field is investigated by calculating VLEs for varying temperatures and mixtures not included in the training set.
In Chapter 5 a transferable force field, which explicitly includes electronic polarization effects, is developed for n-alkanes, ethers, and nitrogen. The non-polarizable Transferable Anisotropic Mie force field (TAMie)[9,58,59] is thereby extended by a charge-on-spring approach. VLE results obtained with this new force field for pure substances and mixtures are evaluated and compared to experimental data.

Bibliography

[1] Panagiotopoulos, A. Z. (1987) Direct determination of phase coexistence properties of fluids by Monte Carlo simulation in a new ensemble. *Mol. Phys. 61*, 813–826.

[2] Panagiotopoulos, A., Quirke, N., Stapleton, M., and Tildesley, D. (1988) Phase equilibria by simulation in the Gibbs ensemble. *Mol. Phys. 63*, 527–545.

[3] Smit, B., Smedt, P. D., and Frenkel, D. (1989) Computer simulations in the Gibbs ensemble. *Mol. Phys. 68*, 931–950.

[4] Ferrenberg, A. M., and Swendsen, R. H. (1988) New Monte Carlo technique for studying phase transitions. *Phys. Rev. Lett. 61*, 2635.

[5] Ferrenberg, A. M., and Swendsen, R. H. (1989) Optimized monte carlo data analysis. *Comput. Phys. 3*, 101–104.

[6] Errington, J. R. (2003) Direct calculation of liquid–vapor phase equilibria from transition matrix Monte Carlo simulation. *J. Chem. Phys. 118*, 9915–9925.

[7] Shen, V. K., and Errington, J. R. (2005) Determination of fluid-phase behavior using transition-matrix Monte Carlo: binary Lennard-Jones mixtures. *J. Chem. Phys. 122*, 064508.

[8] Errington, J. R., and Shen, V. K. (2005) Direct evaluation of multicomponent phase equilibria using flat-histogram methods. *J. Chem. Phys. 123*, 164103.

[9] Hemmen, A., Panagiotopoulos, A. Z., and Gross, J. (2015) Grand Canonical Monte Carlo Simulations Guided by an Analytic Equation of State - Transferable Anisotropic Mie Potentials for Ethers. *J. Phys. Chem. B 119*, 7087–7099.

[10] Möller, D., and Fischer, J. (1990) Vapour liquid equilibrium of a pure fluid from test particle method in combination with NpT molecular dynamics simulations. *Mol. Phys. 69*, 463–473.

[11] Lotfi, A., Vrabec, J., and Fischer, J. (1992) Vapour liquid equilibria of the Lennard-Jones fluid from the NpT plus test particle method. *Mol. Phys. 76*, 1319–1333.

[12] Vrabec, J., and Fischer, J. (1995) Vapour liquid equilibria of mixtures from the NpT plus test particle method. *Mol. Phys. 85*, 781–792.

[13] Vrabec, J., Lotfi, A., and Fischer, J. (1995) Vapour liquid equilibria of Lennard-Jones model mixtures from the NpT plus test particle method. *Fluid Phase Equilibr. 112*, 173–197.

[14] Widom, B. (1963) Some topics in the theory of fluids. *J. Chem. Phys. 39*, 2808–2812.

[15] Kofke, D. A., and Cummings, P. T. (1997) Quantitative comparison and optimization of methods for evaluating the chemical potential by molecular simulation. *Mol. Phys. 92*, 973–996.

[16] Vrabec, J., and Hasse, H. (2002) Grand Equilibrium: vapour-liquid equilibria by a new molecular simulation method. *Mol. Phys. 100*, 3375–3383.

[17] Kofke, D. A. (1993) Gibbs-Duhem integration: a new method for direct evaluation of phase coexistence by molecular simulation. *Mol. Phys. 78*, 1331–1336.

[18] Kofke, D. A. (1993) Direct evaluation of phase coexistence by molecular simulation via integration along the saturation line. *J. Chem. Phys. 98*, 4149–4162.

[19] Gubbins, K. E. (1989) The role of computer simulation in studying fluid phase equilibria. *Mol. Simulat. 2*, 223–252.

[20] Smit, B., and Frenkel, D. (1989) Calculation of the chemical potential in the Gibbs ensemble. *Mol. Phys. 68*, 951–958.

[21] Smith, G., and Bruce, A. (1995) A study of the multi-canonical Monte Carlo method. *J. Phys. A-Math. Gen. 28*, 6623.

[22] Wang, J.-S. (1999) Transition matrix Monte Carlo method. *Comput. Phys. Commun. 121-122*, 22 – 25.

[23] Wang, J.-S., Tay, T. K., and Swendsen, R. H. (1999) Transition matrix Monte Carlo reweighting and dynamics. *Phys. Rev. Lett. 82*, 476.

[24] Fitzgerald, M., Picard, R., and Silver, R. (1999) Canonical transition probabilities for adaptive Metropolis simulation. *EPL (Europhys. Lett.) 46*, 282.

[25] Fitzgerald, M., Picard, R., and Silver, R. (2000) Monte Carlo transition dynamics and variance reduction. *J. Stat. Phys. 98*, 321–345.

[26] Wang, J.-S., and Swendsen, R. H. (2002) Transition matrix monte carlo method. *J. Stat. Phys. 106*, 245–285.

[27] Gross, J., and Sadowski, G. (2001) Perturbed-chain SAFT: An equation of state based on a perturbation theory for chain molecules. *Ind. Eng. Chem. Res. 40*, 1244–1260.

[28] Virnau, P., and Müller, M. (2004) Calculation of free energy through successive umbrella sampling. *J. Chem. Phys. 120*, 10925–10930.

[29] Mie, G. (1903) Zur kinetischen Theorie der einatomigen Körper. *Ann. Phys. 316*, 657–697.

[30] Mason, E. A. (1954) Transport Properties of Gases Obeying a Modified Buckingham (Exp-Six) Potential. *J. Chem. Phys. 22*, 169–186.

[31] Lorentz, H. (1881) Ueber die Anwendung des Satzes vom Virial in der kinetischen Theorie der Gase. *Ann. Phys. 248*, 127–136.

[32] Berthelot, D. (1898) Sur le mélange des gaz. *Compt. Rendus 126*, 1703–1706.

[33] Potoff, J. J., and Bernard-Brunel, D. A. (2009) Mie potentials for phase equilibria calculations: Application to alkanes and perfluoroalkanes. *J. Phys. Chem. B 113*, 14725–14731.

[34] Chialvo, A. A., and Cummings, P. T. (1998) Simple transferable intermolecular potential for the molecular simulation of water over wide ranges of state conditions. *Fluid Phase Equilibr. 150*, 73–81.

[35] Rappe, A. K., and Goddard III, W. A. (1991) Charge equilibration for molecular dynamics simulations. *J. Phys. Chem. 95*, 3358–3363.

[36] Rick, S. W., Stuart, S. J., and Berne, B. J. (1994) Dynamical fluctuating charge force fields: Application to liquid water. *J. Chem. Phys. 101*, 6141–6156.

[37] Vesely, F. J. (1977) N-particle dynamics of polarizable Stockmayer-type molecules. *J. Comput. Phys. 24*, 361–371.

[38] Drude, P. *Lehrbuch der Optik*; S. Hirzel: Leipzig, 1900.

[39] Born, M., and Huang, K. *Dynamical theory of crystal lattices*; Clarendon press: London, 1954.

[40] Straatsma, T., and McCammon, J. (1990) Molecular dynamics simulations with interaction potentials including polarization development of a noniterative method and application to water. *Mol. Simulat. 5*, 181–192.

[41] Yu, H., and Van Gunsteren, W. F. (2005) Accounting for polarization in molecular simulation. *Comput. Phys. Commun. 172*, 69–85.

[42] Mulliken, R. S. (1934) A new electroaffinity scale; together with data on valence states and on valence ionization potentials and electron affinities. *J. Chem. Phys. 2*, 782–793.

[43] Parr, R. G., and Pearson, R. G. (1983) Absolute hardness: companion parameter to absolute electronegativity. *J. Am. Chem. Soc. 105*, 7512–7516.

[44] Ewald, P. P. (1921) Die Berechnung optischer und elektrostatischer Gitterpotentiale. *Ann. Phys. 369*, 253–287.

[45] Wolf, D., Keblinski, P., Phillpot, S., and Eggebrecht, J. (1999) Exact method for the simulation of Coulombic systems by spherically truncated, pairwise r^{-1} summation. *J. Chem. Phys. 110*, 8254–8282.

[46] Tuckerman, M. *Statistical mechanics: theory and molecular simulation*; Oxford University Press: New York, 2010.

[47] Kolafa, J., and Perram, J. W. (1992) Cutoff errors in the Ewald summation formulae for point charge systems. *Mol. Simulat. 9*, 351–368.

[48] Petersen, H. G. (1995) Accuracy and efficiency of the particle mesh Ewald method. *J. Chem. Phys. 103*, 3668–3679.

[49] Perram, J. W., Petersen, H. G., and De Leeuw, S. W. (1988) An algorithm for the simulation of condensed matter which grows as the 3/2 power of the number of particles. *Mol. Phys. 65*, 875–893.

[50] Hockney, R. W., and Eastwood, J. W. *Computer simulation using particles*; Taylor & Francis Group: New York, 1988.

[51] Darden, T., York, D., and Pedersen, L. (1993) Particle mesh Ewald: An N log(N) method for Ewald sums in large systems. *J. Chem. Phys. 98*, 10089–10092.

[52] Essmann, U., Perera, L., Berkowitz, M. L., Darden, T., Lee, H., and Pedersen, L. G. (1995) A smooth particle mesh Ewald method. *J. Chem. Phys. 103*, 8577–8593.

[53] Brooks III, C. L. (1987) The influence of long-range force truncation on the thermodynamics of aqueous ionic solutions. *J. Chem. Phys. 86*, 5156–5162.

[54] Schreiber, H., and Steinhauser, O. (1992) Cutoff size does strongly influence molecular dynamics results on solvated polypeptides. *Biochemistry 31*, 5856–5860.

[55] Feller, S. E., Pastor, R. W., Rojnuckarin, A., Bogusz, S., and Brooks, B. R. (1996) Effect of electrostatic force truncation on interfacial and transport properties of water. *J. Phys. Chem. 100*, 17011–17020.

[56] Spohr, E. (1997) Effect of electrostatic boundary conditions and system size on the interfacial properties of water and aqueous solutions. *J. Chem. Phys. 107*, 6342–6348.

[57] Cisneros, G. A., Karttunen, M., Ren, P., and Sagui, C. (2014) Classical electrostatics for biomolecular simulations. *Chem. Rev. 114*, 779–814.

[58] Hemmen, A., and Gross, J. (2015) Transferable Anisotropic United-Atom Force Field Based on the Mie Potential for Phase Equilibrium Calculations: n-Alkanes and n-Olefins. *J. Phys. Chem. B 119*, 11695–11707.

[59] Weidler, D., and Gross, J. (2016) Transferable Anisotropic United-Atom Force Field Based on the Mie Potential for Phase Equilibria: Aldehydes, Ketones, and Small Cyclic Alkanes. *Ind. Eng. Chem. Res. 55*, 12123–12132.

Chapter 2

Modification of the Wolf Method and Evaluation for Molecular Simulation of Vapor-Liquid Equilibria

The content of this chapter is a literal quote of the publication

> *Waibel, Gross, Journal of Chemical Theory and Computation, 14 (4), 2018, 2198-2206 (reproduced with permission from ACS, copyright 2019).*

In comparison to the published work, the abstract is here omitted. Additions or deletions compared to the published work are marked with angular brackets.

Determining the potential energy from Coulombic charges is a computationally most demanding task in molecular simulations with classical force fields. To treat the slow decaying r^{-1} electrostatic potential, various methods have been developed.
The Ewald summation[1] is accepted as the standard method, in which the simulation box is repeated infinitely. This allows splitting the electrostatic interactions in a truncated and short-ranged, quickly decaying pairwise real-space summation and a long-range summation in the reciprocal-space. The simulation effort in a simple implementation is $\mathcal{O}(N^2)$. There are some derivatives of the Ewald summation, e.g. particle–particle particle mesh Ewald[2], particle mesh Ewald[3], and smooth particle mesh Ewald[4], which can decrease the scaling of the simulation effort down to $\mathcal{O}(N \log(N))$. The Ewald method is an exact method in the limit of infinite reciprocal-space evaluations. Simpler methods to handle long-range Coulomb interactions are spherically truncation methods. These short-range methods evaluate only pairwise interactions within a cutoff radius and have the advantage of linear scaling $\mathcal{O}(N)$. However, truncation of long-range Coulomb interactions introduces severe truncation artifacts[5–8]. In some cases, these errors can be reduced by using a shifted potential or shifted force potential[9–12].

Knowing that the effective electrostatic potential is rather short ranged, Wolf et al. detected that the errors in truncation methods are high for configurations where the charge is non-neutral in the cut-off sphere. They developed a pairwise truncated summation method which ensures charge neutrality within the cutoff sphere[13] (Wolf method). This leads to good agreement with results from the Ewald summation. There are various modified versions[14–24] based on the Wolf method principles including better energy conservation or reduced potential discontinuities at the cutoff. The reliability and accuracy of the Wolf method was investigated for different condensed-phase molecular dynamic and Monte Carlo (MC) simulations of molecules[25–34]. For MC simulations the original Wolf method[13] provided best results calculating the energy of electrostatic interactions[15,19].
To our knowledge only Kolafa et al.[35] used the Wolf method with a shifted force approach for evaluating the electrostatic potential for simulations in an ensemble with fluctuating particle number. They calculated vapor-liquid phase equilibria with Gibbs ensemble MC simulations, but the obtained vapor densities have a high relative deviation compared to reference simulations using the Ewald method. In such simulations with fluctuating particle number the self-energy terms in the treatment of electrostatic interactions of molecules become important because the potential energy will change with inserting or deleting a molecule.
In this work we propose a modification of the self-term of the Wolf summation which significantly improves the description of the potential energy in a ensemble with fluctuating particle numbers. This modification is assessed for calculating phase equilibrium properties using simulations in the grand canonical ensemble.

2.1 Wolf Summation

The electrostatic energy between partial charges of a system with N charges, where the system is embedded with periodic images of the system, is given by the Coulomb sum

$$E^{Coulomb} = \frac{1}{2}\sum_{i=1}^{N}\sum_{j\neq i}^{\infty}\frac{1}{4\pi\epsilon_0}\frac{q_i q_j}{r_{ij}} \tag{2.1}$$

where q_i is the partial charge, r_{ij} denotes the distance between partial charge i and j, and ϵ_0 is the dielectric constant. To simplify the notation, we henceforth redefine the unit of the partial charge q_i to include the Coulomb constant $(4\pi\epsilon_0)^{-0.5}$, so that the prefactor $(4\pi\epsilon_0)^{-1}$ in the expression for the Coulomb potential disappears. Electrostatic interactions are long-range interactions. For practical applications, however, a finite summation is needed. The standard technique to account for an infinite number of interactions (of a periodic system) with a finite summation, is to introduce periodicity as a Fourier series. This method is known as Ewald summation[1] in which the electrostatic potential is split

into a short-ranged part and a long-ranged contribution. The summation over electrostatic potentials is then split into a real contribution capturing short-ranged interactions and a summation in reciprocal (Fourier) space term, as well as a self-term.

As a computationally more efficient approach, Wolf et al.[13] proposed a finite pairwise summation by introducing a spherical cutoff radius R_c. Applying such a truncation naively will not describe the electrostatic energy accurate in a converging summation, even for large cutoff radii, because the summation is a conditionally convergent sum. Knowing that the effective electrostatic potential has to be rather short ranged due to screening of charges with surrounding charges of opposite sign, Wolf et al. identified the reason for the weakly converging behavior of potential truncation schemes in the lack of charge neutrality within the cutoff sphere[13]. They showed, that the result of simply truncated intermolecular potentials was satisfying if the system within the cutoff radius of a selected charge is (by coincidence) electroneutral. They proposed to determine the net-charge $\Delta q_i(R_c)$ within the cutoff sphere (of radius R_c) around a considered charge i. To enforce charge-neutrality they placed the negative of this net-charge $\Delta q_i(R_c)$ as a hypothetical charge onto the cutoff surface to interact with the center charge i, as to approximately screen the surrounding medium.

$$E^{\text{Wolf, 1}} = E^{\text{cutoff, 1}} - E^{\text{neutral, 1}} = \frac{1}{2}\sum_{\substack{i=1 \\ (r_{ij}<R_c)}}^{N}\sum_{j\neq i}^{N}\frac{q_i q_j}{r_{ij}} - \frac{1}{2}\sum_{i=1}^{N}\frac{q_i \Delta q_i(R_c)}{R_c} \tag{2.2}$$

This equation reveals the concept of the Wolf-summation. It is possible to consider the Coulombic charges only up to cutoff length R_c. Beyond the cutoff length the charges are sufficiently screened so that they lead to a negligible potential contribution for the central charge. The hypothetical neutralizing net-charge $-\Delta q_i(R_c)$ is considered distributed at the cutoff distance, with

$$\Delta q_i(R_c) = \sum_{\substack{j=1 \\ (r_{ij}<R_c)}}^{N} q_j \tag{2.3}$$

Despite the neutralizing charge, large cutoff values of R_c would have to be used to justify the truncation of electrostatic interactions beyond distance R_c. To reach a more practical expression, i.e. an expression that does not demand an overly high value of R_c, Wolf et al. introduce successive approximations. We use an index, e.g. index '1' in eq. 2.2, to discriminate between the various approximations.

Eq. 2.2 can, after rearranging with eq. 2.3, be viewed as a shifted pair potential with a self-correction term located at the cutoff surface.

$$E^{\text{Wolf, 1}} = \frac{1}{2}\sum_{\substack{i=1 \\ (r_{ij}<R_c)}}^{N}\sum_{j\neq i}^{N} q_i q_j \left(\frac{1}{r_{ij}} - \frac{1}{R_c}\right) - \frac{1}{2R_c}\sum_{i=1}^{N} q_i^2 \tag{2.4}$$

In analyzing ionic solids and liquids, Wolf et al realized that the results of this equation oscillate around the actual Coulombic energy and have a rather slow oscillatory decay with increasing cutoff radius R_c. A more robust behavior for lower values of the cutoff radius R_c was obtained by introducing a complementary error function as a damping function. We retrace the development by decomposing the function $\frac{1}{r_{ij}} = \frac{\operatorname{erfc}(\alpha r_{ij})}{r_{ij}} + \frac{\operatorname{erf}(\alpha r_{ij})}{r_{ij}}$ (i.e. short-ranged contribution plus long-ranged part) where α denotes the damping parameter.

We return to eq. (2.2) and consider only the first term, i.e. the Coulombic energy within the cutoff. With the decomposition of $\frac{1}{r_{ij}}$ this term can be rewritten into a short-ranged and long-ranged contribution

$$E^{\text{cutoff, 1}} = \frac{1}{2}\sum_{\substack{i=1 \\ (r_{ij}<R_c)}}^{N}\sum_{j\neq i}^{N} \frac{q_i q_j \operatorname{erfc}(\alpha r_{ij})}{r_{ij}} + \frac{1}{2}\sum_{\substack{i=1 \\ (r_{ij}<R_c)}}^{N}\sum_{j\neq i}^{N} \frac{q_i q_j \operatorname{erf}(\alpha r_{ij})}{r_{ij}} \tag{2.5}$$

The long-ranged (erf)-term excludes the self-contribution, by requiring $j \neq i$. The self-contribution $i = j$, however, has finite values

$$\lim_{r_{ij}\to 0}\left\{\frac{1}{2}\sum_{i=1}^{N} \frac{q_i^2 \operatorname{erf}(\alpha r_{ij})}{r_{ij}})\right\} = \frac{\alpha}{\pi^{\frac{1}{2}}}\sum_{i=1}^{N} q_i^2 \tag{2.6}$$

We can add and subtract the left- and right-hand side of eq. 2.6, respectively, to the long-ranged (erf)-term of eq. 2.5, leading to

$$E^{\text{cutoff, 1}} = \frac{1}{2}\sum_{\substack{i=1 \\ (r_{ij}<R_c)}}^{N}\sum_{j\neq i}^{N} \frac{q_i q_j \operatorname{erfc}(\alpha r_{ij})}{r_{ij}} + \frac{1}{2}\sum_{\substack{i=1 \\ (r_{ij}<R_c)}}^{N}\sum_{j=1}^{N} \frac{q_i q_j \operatorname{erf}(\alpha r_{ij})}{r_{ij}} - \frac{\alpha}{\pi^{\frac{1}{2}}}\sum_{i=1}^{N} q_i^2 \tag{2.7}$$

For ionic solids or liquids and moderate values of the cutoff length R_c, the long-ranged (erf)-contribution in this form oscillates around zero as Wolf et al. showed. Omitting this contribution improves convergence of the energy, for reasonable cutoff values.

The charge neutralizing term, second term of eq. (2.2), can analogously be decomposed, $\frac{1}{R_c} = \frac{\operatorname{erfc}(\alpha R_c)}{R_c} + \frac{\operatorname{erf}(\alpha R_c)}{R_c}$. If the long-ranged (erf)-contribution is also neglected, one obtains

the original Wolf summation

$$E^{\text{Wolf, 2}} = \frac{1}{2}\sum_{i=1}^{N}\sum_{\substack{j\neq i\\(r_{ij}<R_c)}}^{N} q_i q_j \left(\frac{\operatorname{erfc}(\alpha r_{ij})}{r_{ij}} - \frac{\operatorname{erfc}(\alpha R_c)}{R_c}\right) - \left(\frac{\operatorname{erfc}(\alpha R_c)}{2R_c} + \frac{\alpha}{\pi^{1/2}}\right)\sum_{i=1}^{N} q_i^2 \tag{2.8}$$

It is a simple and computationally efficient expression for the electrostatic energy, based only on pair-interactions within a cutoff radius. The two adjustable parameters α and R_c have to be defined carefully to ensure optimal results.

We now consider molecules, composed of several interaction sites with intramolecular bonding potentials. Intramolecular electrostatic interactions of two charges that are close to one another (usually up to 3 or 4 interaction sites apart, depending on the considered force field) need to be excluded from the electrostatic energy calculation. These intramolecular charge–charge interactions are already effectively captured in the intramolecular bond-angle and torsional potentials. One then excludes these intramolecular Coulomb–Coulomb potentials, and eq. (2.8) needs to be adjusted accordingly, because the sum indices, that run over all partial charges, do so far not exclude intramolecular interactions (of interaction sites up to 3 or 4 interaction sites apart). We therefore extend the notation with index i and j counting molecules and a and b counting the partial charges in these molecules, respectively. We subtract the intramolecular charge–charge interactions that should be ignored by introducing an operator $\psi_{i,ab}$ so that

$$\begin{aligned} E^{\text{Wolf, 2 molecular}} = &\frac{1}{2}\sum_{i=1}^{N}\sum_{a=1}^{N_a}\sum_{\substack{j\neq i\\(r_{iajb}<R_c)\\\text{inter}}}^{N}\sum_{b=1}^{N_b} q_{ia} q_{jb} \left(\frac{\operatorname{erfc}(\alpha r_{iajb})}{r_{iajb}} - \frac{\operatorname{erfc}(\alpha R_c)}{R_c}\right) \\ &+ \frac{1}{2}\sum_{i=1}^{N}\sum_{a=1}^{N_a}\sum_{\substack{b\neq a\\(r_{iab}<R_c)\\\text{intra}}}^{N_b} q_{ia} q_{ib} \left(\frac{\operatorname{erfc}(\alpha r_{iaib})}{r_{iaib}} - \frac{\operatorname{erfc}(\alpha R_c)}{R_c} - \frac{\psi_{i,ab}}{r_{iaib}}\right) \\ &- \left(\frac{\operatorname{erfc}(\alpha R_c)}{2R_c} + \frac{\alpha}{\pi^{1/2}}\right)\sum_{\substack{i=1\\\text{self}}}^{N}\sum_{a=1}^{N_a} q_{ia}^2 \end{aligned} \tag{2.9}$$

The first and last lines of eq. (2.9) are immediately obtained from eq. (2.8) in segment notation, whereas the second line is for the intramolecular interactions. The intramolecular charge–charge interactions that need to be ignored in the calculation of the electrostatic energy are subtracted. We thereby introduce the operator $\psi_{i,ab}$, with $\psi_{i,ab} = 1$ for all intramolecular electrostatic potentials to be ignored (usually for interaction sites a and

b separated by up to 3 or 4 interaction sites, depending on the considered force field), whereas $\psi_{i,ab} = 0$ for all interaction sites sufficiently far apart (like for distant functional groups of a molecule). The spherical truncation at the cutoff radius is used strictly, even when a partial charge of a molecule is considered within the cutoff radius while another partial charge of the same molecule is outside of the cutoff, i.e. we do not enforce charge-neutral conditions within the cutoff. Through the image charges the charge neutrality in the cutoff sphere is ensured. We note, that our tests showed no advantage for working with electroneutral charge groups (i.e., with entire molecules) that are either considered entirely or not at all, depending on their location toward the cutoff radius.
For subtracting the bonded interactions in line two of eq. (2.9) we use the damping scheme again. The reciprocal distance is replaced by $\frac{\psi_{i,ab}}{r_{iaib}} = \frac{\psi_{i,ab}\,\mathrm{erfc}(\alpha r_{iaib})}{r_{iaib}} + \frac{\psi_{i,ab}\,\mathrm{erf}(\alpha r_{iaib})}{r_{iaib}}$. Like Wolf et al. in their original derivation (eq. (2.7)), the intramolecular summation of the resulting long-range (erf)-part can be extended to a summation including the self-contribution $\frac{\alpha}{\pi^{1/2}}$ (eq. (2.6)). After rearrangement of the sums we get

$$
\begin{aligned}
E^{\text{Wolf, 2 molecular}} =& \frac{1}{2}\sum_{i=1}^{N}\sum_{a=1}^{N_a}\sum_{\substack{j=1\\ j\neq i}}^{N}\sum_{b=1}^{N_b}{}^{\prime}\, q_{ia}q_{jb}\left(\frac{\mathrm{erfc}(\alpha r_{iajb})}{r_{iajb}} - \frac{\mathrm{erfc}(\alpha R_c)}{R_c}\right) \\
&\qquad \underset{\substack{(r_{iajb}<R_c)\\ \text{inter}}}{} \\
&- \frac{1}{2}\sum_{i=1}^{N}\sum_{a=1}^{N_a}\sum_{b=1}^{N_b}{}^{\prime}\, \frac{q_{ia}q_{ib}\,\mathrm{erf}(\alpha r_{iaib})}{r_{iaib}}\cdot\psi_{i,ab} \\
&\qquad \underset{\substack{(r_{iab}<R_c)\\ \text{intra + self}}}{} \\
&+ \frac{1}{2}\sum_{i=1}^{N}\sum_{a=1}^{N_a}\sum_{b\neq a}^{N_b}{}^{\prime}\, \frac{q_{ia}q_{ib}\,\mathrm{erfc}(\alpha r_{iaib})}{r_{iaib}}\cdot(1-\psi_{i,ab}) \\
&\qquad \underset{\substack{(r_{iab}<R_c)\\ \text{intra}}}{} \\
&- \frac{\mathrm{erfc}(\alpha R_c)}{2R_c}\sum_{i=1}^{N}\sum_{a=1}^{N_a}\sum_{b=1}^{N_b}{}^{\prime}\, q_{ia}q_{ib} \\
&\qquad \underset{\substack{(r_{iab}<R_c)\\ \text{intra + self}}}{}
\end{aligned}
\tag{2.10}
$$

Thus the received summation of the long-range (erf)-part can be neglected again, for the same reasons as in the original derivation (eq. (2.7) to (2.8)). With this modification we get a modified Wolf summation for molecules

$$
\begin{aligned}
E^{\text{Wolf, mod}} =& \frac{1}{2}\sum_{i=1}^{N}\sum_{a=1}^{N_a}\sum_{\substack{j\neq i\\(r_{iajb}<R_c)\\\text{inter}}}^{N}\sum_{b=1}^{N_b} q_{ia}q_{jb}\left(\frac{\operatorname{erfc}(\alpha r_{iajb})}{r_{iajb}} - \frac{\operatorname{erfc}(\alpha R_c)}{R_c}\right) \\
&+ \frac{1}{2}\sum_{i=1}^{N}\sum_{\substack{a=1\\(r_{iab}<R_c)\\\text{intra}}}^{N_a}\sum_{b\neq a}^{N_b} \frac{q_{ia}q_{ib}\operatorname{erfc}(\alpha r_{iaib})}{r_{iaib}}\cdot(1-\psi_{i,ab}) \\
&- \frac{\operatorname{erfc}(\alpha R_c)}{2R_c}\sum_{\substack{i=1\\(r_{iab}<R_c)\\\text{intra + self}}}^{N}\sum_{a=1}^{N_a}\sum_{b=1}^{N_b} q_{ia}q_{ib}
\end{aligned}
\tag{2.11}
$$

The Wolf summation introduces two model parameters, the damping factor α and the cutoff radius R_c. These parameters need to be carefully defined in order to obtain good results, as we will show in the results section. We note that there exists no systematic scheme to determine these model parameters based on a defined error tolerance, as available for the Ewald summation[36]. The reason lies in the fact that the Wolf summation is exact only for infinite cutoff radii, so that convergence criteria are not available.

2.2 Molecular Simulation Technique

2.2.1 Simulation Method

We conduct MC simulations in the grand canonical ensemble $\{\mu, V, T\}$ to determine vapor–liquid phase coexistence properties for pure components and binary mixtures. In this ensemble the excess chemical potential μ, volume V, and temperature T are defined variables, whereas the molecule number N and the energy E are fluctuating quantities. For pure components we divide the N-space into windows of $\Delta N = 10$ molecules for moderate densities and $\Delta N = 5$ molecules for high densities[37,38]. Trial moves for inserting or deleting a molecule to molecule numbers outside the defined N-window are trivially rejected. To cover the entire vapor–liquid phase envelope different $\{\mu_i, T_i\}$ conditions for different N-windows are chosen. Suitable $\{\mu_i, T_i\}$ conditions sufficiently close to the conditions at the phase envelope are determined prior to the simulations from the PC-SAFT[39] equation of state. For each window a separate simulation is performed, and the probability distribution $P(N; \mu_i, V, T_i)$ is sampled using a Transition Matrix scheme[40,41]. To sample the N-space more evenly a bias function is applied, determined on the fly from the Transition Matrix method. Histograms $H_i(N, E)$ for molecule number and energy are collected during the simulation. In a post processing step histogram reweighting is used

to obtain the probability distribution $P(N)$ at other conditions (μ, T). The phase equilibrium properties are determined using the histogram $H_i(N, E)$ and histogram reweighting, by iterating $\mu(T)$ until equal pressure is found for the vapor and for the liquid phase.[42–45] For binary mixtures at given temperature T we divide the $\boldsymbol{N} = (N_1, N_2)$-space into windows of $\Delta N_1 \times \Delta N_2 = 10 \times 10$ molecules and use also the Transition Matrix scheme to sample the probability distribution $P(\boldsymbol{N}; \boldsymbol{\mu}, V, T)$. Suitable $\{\boldsymbol{\mu} = (\mu_1, \mu_2), \boldsymbol{N} = (N_1, N_2)\}$ conditions are estimated with the PC-SAFT equation of state for a representative equilibrium point. In a postprocessing step histogram reweighting is used to determine phase equilibrium.
For a more detailed description of the simulation technique, we refer to Hemmen et al[46].

2.2.2 Molecular Model

The transferable anisotropic Mie (TAMie) force field[46–49] [Chapter 4] is used for several substances considered in this study (ethers, ketones, alkanes, and nitrogen). For methanol we use the force field proposed by Schnabel et al.[50], and for water we apply the SPC/E water model[51].
The intermolecular potential of all species considered in this study is described with a united-atom Mie potential, i.e. a generalized Lennard-Jones potential, and with an electrostatic potential, according to

$$u(r_{ab}) = c_{ab}\epsilon_{ab}\left[\left(\frac{\sigma_{ab}}{r_{ab}}\right)^{n_{ab}} - \left(\frac{\sigma_{ab}}{r_{ab}}\right)^{6}\right] + \frac{q_a q_b}{r_{ab}} \tag{2.12}$$

where r_{ab} denotes the distance between two interaction sites a and b, ϵ_{ab} and σ_{ab} are the well depth and diameter parameter, respectively, q_a is the partial charge, and n_{ab} is the repulsive exponent. A fixed attractive exponent of $m = 6$ is used for all substances. In the previous section we used a notation to indicate site a is located on molecule i. Here, we use index a instead of ia, because all force field parameters are specific to an interaction site (or site-pairs ab) and do not require mentioning on what molecule each interaction site is located. The prefactor c_{ab} is defined as

$$c_{ab} = \left(\frac{n_{ab}}{n_{ab} - 6}\right)\left(\frac{n_{ab}}{6}\right)^{6/(n_{ab}-6)} \tag{2.13}$$

Intramolecular interactions of the Mie or electrostatic potential up to 4 interaction sites apart are not considered explicitly. These interactions are already captured in the intramolecular bonding potentials.
The ϵ_{ab} and σ_{ab} parameters between different interactions sites are determined using Lorentz–Berthelot combining rules[52,53], and the repulsive exponents of the Mie potentials n_{ab} are combined as an arithmetic average[54]. For mixtures a correction for the ϵ-parameter

can be introduced

$$\epsilon_{ab} = (\epsilon_{aa}\epsilon_{bb})^{1/2}(1-\kappa_{ab}) \tag{2.14}$$

For the interaction between alkyl- and nitrogen groups for the mixture of n-pentane with nitrogen we use the mixture parameters $\kappa_{\mathrm{CH_3,N}} = 0.0087$ and $\kappa_{\mathrm{CH_2,N}} = 0.0509$ from our previous work[49] [Chapter 4].

2.2.3 Simulation Details

In the simulations we used five different MC moves, namely molecule insertion 15%, molecule deletion 15%, translational displacement 30%, rotation 30%, and partial molecule reconfiguration (regrow) 10%. To improve the statistics of insertion, deletion, and reconfiguration of molecules, a configurational bias scheme was applied with increasing trial numbers (up to 8) for higher densities. The Mie potential is evaluated for all interactions up to a spherical cutoff radius of $R_c = 14\,\text{Å}$. Beyond the cutoff distance analytical tail-corrections[55,56] are used. For reference simulations the Ewald summation is applied for calculating the electrostatic potential with a maximum index of $k_{max} = 9$ in the Fourier series expansion and a damping factor of $\kappa = 7.59/L$ for a cubic box length of L[55]. This parametrization was found reliable for our MC simulations, so that more conservative parameter sets gave nondistinguishable results within our statistical uncertainties. The simulations were conducted in cubic boxes with a volume of $V = 33000\,\text{Å}^3$ or $V = 64000\,\text{Å}^3$ for pure components and $V = 30000\,\text{Å}^3$ or $V = 44000\,\text{Å}^3$ for mixtures. For mixtures and pure components with a window of $\Delta N = 10$ we used 10 million MC steps for equilibration and 50 million MC steps for production. For higher densities and windows with $\Delta N = 5$ we used 15 million MC steps for equilibration and 25 million MC steps for production.

2.3 Results and Discussion

2.3.1 Wolf Parameter Estimation

The two model parameters α and R_c of the Wolf summation have to be determined to get close agreement to the average electrostatic energy obtained from the Ewald summation. In our simulations we use the grand canonical ensemble with fluctuating particle numbers N, but we divide the N-space into several smaller windows of $\Delta N = 10$ or $\Delta N = 5$. It is therefore possible to optimize the Wolf model parameters for a variety of density ranges. For assessing combinations of model parameters we conduct a series of simulations for fixed Wolf-parameters, namely for damping parameters from $\alpha = 0.06\,\text{Å}^{-1}$ to $0.14\,\text{Å}^{-1}$ in intervals of $0.005\,\text{Å}^{-1}$ and for cutoff lengths of $R_c = 14\,\text{Å}$ and $16\,\text{Å}$. For lower values of

R_c we have not found acceptable agreement of the Wolf method to results of the Ewald summation. The results are compared to results from simulations with the Ewald sum. We speak of the Ewald-simulations as the "reference" and regard relative deviations of results from the Wolf summation toward this reference, with

$$ERR = \frac{\langle E^{Wolf} \rangle - \langle E^{Ewald} \rangle}{\langle E^{Ewald} \rangle} \tag{2.15}$$

Figure 2.1 shows the absolute value of the relative deviations of the potential energy for varying damping parameters α for the case of pure dimethyl ether. The first diagram regards the system with a cutoff radius of $R_c = 14\,\text{Å}$, whereas the second diagram considers $R_c = 16\,\text{Å}$. Four ranges of molecule-numbers are shown in both diagrams, ranging from vapor-like values to liquid-like values. Generally the deviations show a minimum for a certain value of α. The minimum, however, depends on molecule number. Results at lower densities have higher uncertainties and are thus more scattered than results at higher densities. The optimum for α (i.e. the minimum in deviations of Fig. 2.1) shifts to higher α-values with increasing density. Furthermore, the optimal α-value decreases with increasing cutoff radius.

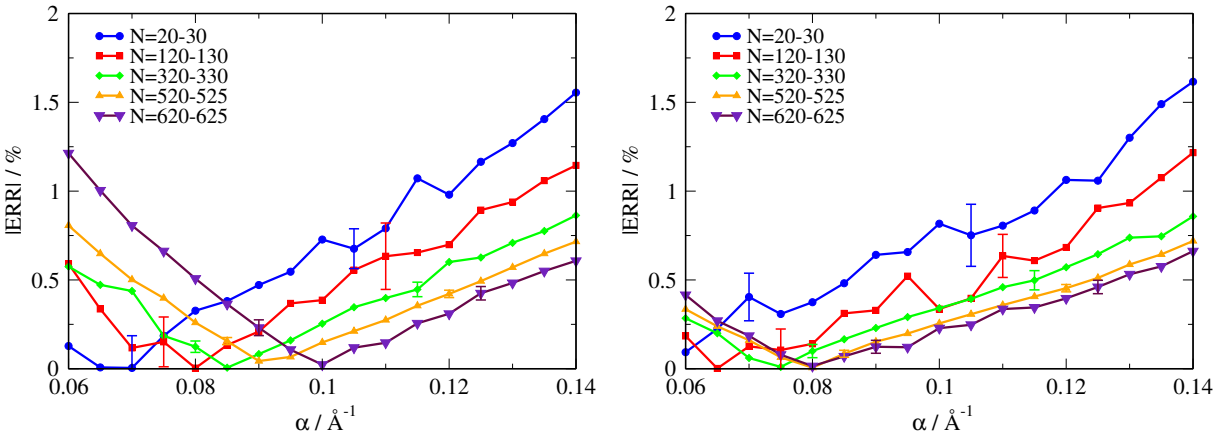

Figure 2.1: Relative deviation of total energy of modified Wolf summation from Ewald summation over damping parameter α for different particle number windows ΔN in a dimethyl ether system with a volume of $64000\,\text{Å}^3$ for cutoff radii $R_c = 14\,\text{Å}$ (left) and $R_c = 16\,\text{Å}$ (right).

It is unfortunate that the minimum in deviations, observed in Fig. 2.1, varies with density of the system. The diagram suggests that a single constant value of α cannot be sufficient for phase equilibrium properties in close agreement with results obtained using the Ewald sum. In the results section, however, we show that a constant value α can lead to very satisfying results. Choosing an appropriate value is thereby delicate. We here proceed differently, by introducing an iterative approach to determine the optimal value of α (for a window of defined ΔN) at the beginning of each simulation. In this iterative scheme a low number of MC trial moves (200,000) are carried out with an initial α-value. As

initial value we use $\alpha = 0.1\,\text{Å}^{-1}$ for $R_c = 14\,\text{Å}$ and $\alpha = 0.075\,\text{Å}^{-1}$ for $R_c = 16\,\text{Å}$. The energy of the system is calculated for varying α-values (ranging from $0.04\,\text{Å}^{-1}$ to $0.16\,\text{Å}^{-1}$ in intervals of $0.005\,\text{Å}^{-1}$) and for the Ewald summation. Then the relative deviation from Wolf to Ewald summation (eq. (2.15)) is calculated, and the α-value with the lowest deviation is chosen. This is repeated until two successive steps achieve the same value of α. The optimal α after each iteration step may fluctuate between two neighboring values, which is why we defined the maximum number of iteration as 10, and we proceed with the α-value of the last iteration step. Fig. 2.2 illustrates the running average of relative deviations of the Wolf method for varying α-values to the Ewald summation for two iteration steps. It can be seen that 200,000 MC trial moves are sufficient for assessing the various deviations. In the considered case two iteration steps are needed to arrive at the optimal damping parameter $\alpha = 0.075\,\text{Å}^{-1}$.

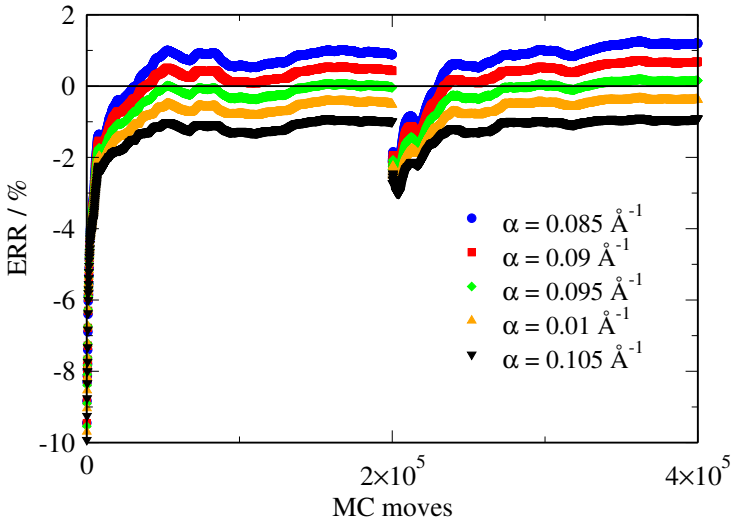

Figure 2.2: Relative deviation of total energy of modified Wolf summation from Ewald summation over MC steps in the iterative procedure (2 iteration steps) for varying $\alpha's$ in a dimethyl ether system ($R_c = 14\,\text{Å}$, $V = 33000\,\text{Å}^3$, N = 250-260).

We note that the iterative approach uses the Wolf method with a current value of α in the acceptance criterion of the MC simulation. Using the Ewald method in the acceptance criterion did not lead to values of α which gave convincing results. The reason for this subtlety has to be rooted in the probability distribution of calculated energy differences. The probability distributions of electrostatic energies in a simulation with constant molecule number for the Wolf and Ewald method in the acceptance criterion are shown in Fig. 2.3. The diagram shows two probability distributions, in red color, for the case where the Ewald summation is used in the acceptance rule of the MC algorithm: one line gives the energy distribution calculated according to the Ewald sum, and the other line shows the distribution calculated from the Wolf method. Two additional lines in blue color present the analogous energy distributions as obtained when the Wolf method

is used for accepting or rejecting MC trial moves. An optimized value for the damping parameter α is chosen in the Wolf approach. When the Wolf method is used in the acceptance criterion, the two (blue) distributions are in good agreement with each other, whereas the two (red) distributions are shifted from one another when the Ewald method is applied in the acceptance criterion.

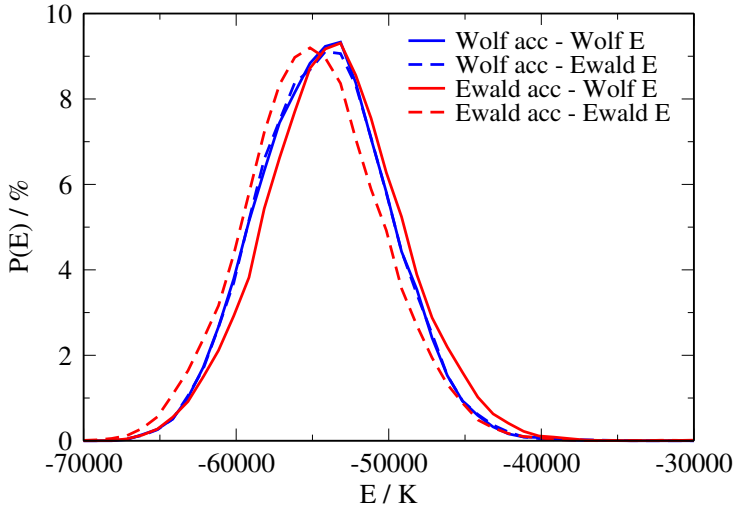

Figure 2.3: Probability distributions of reached electrostatic energies in an acetone system ($R_c = 14\,\text{Å}$, $V = 33000\,\text{Å}^3$, $N = 130$) for the Wolf (blue) and Ewald (red) method in the acceptance criterion. For each method in the acceptance criterion the energy is calculated with the Wolf (solid lines) and Ewald (dashed lines) summation. For the Wolf method the optimal damping parameter $\alpha = 0.085\,\text{Å}^{-1}$ is used.

Figure 2.4 shows the optimized values of α for various N and for a cutoff radius of $R_c = 14\,\text{Å}$ and $R_c = 16\,\text{Å}$, respectively. The damping parameter α increases with increasing density N/V (in agreement with Fig. 2.1). Furthermore, α decreases with a higher cutoff radius. Many systems build a plateau for high densities.

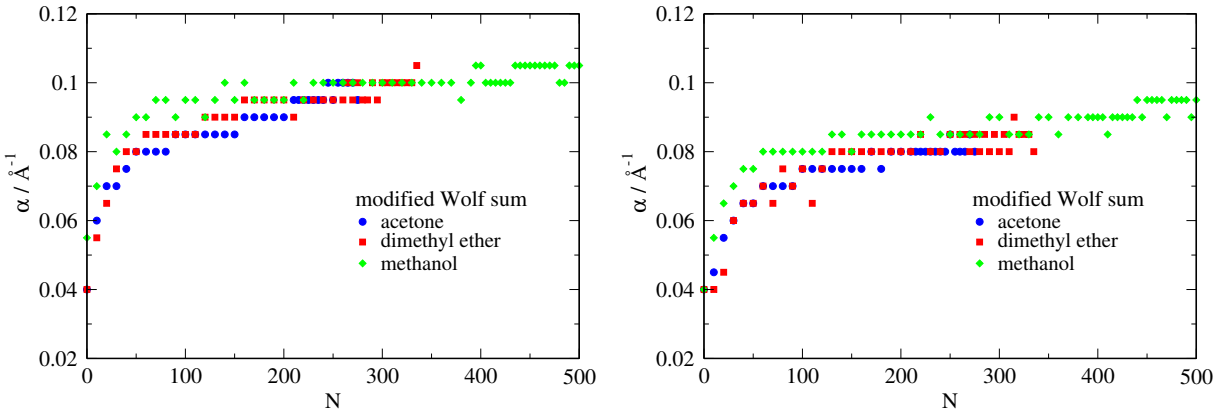

Figure 2.4: Estimated α values after iteration procedure over starting particle number of the particle number windows ΔN for different systems and cutoff radii of $R_c = 14\,\text{Å}$ (left) and $R_c = 16\,\text{Å}$ (right) at a volume of $V = 33000\,\text{Å}^3$.

The effect of the finite size simulation box is analyzed in Fig. 2.5. The results are for a methanol system at volumes $V = 33000\,\text{Å}^3$ and $V = 64000\,\text{Å}^3$. For high densities the optimal damping parameter α remains constant for different box volumes. For lower densities the α parameter differs slightly. We conclude that the optimal damping parameter α is correlated with the choice for cutoff radius R_c and depends on density N/V but is only mildly dependent on system size V.

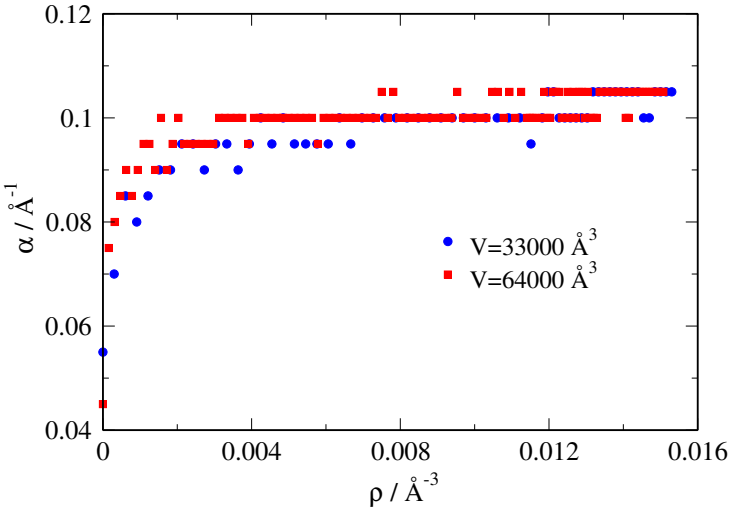

Figure 2.5: Estimated α values after iteration procedure over starting particle density of the particle number windows ΔN for different box volumes V in a methanol system with a cutoff radius of $R_c = 14\,\text{Å}$.

2.3.2 VLE Calculations

We have calculated the vapor–liquid equilibrium properties of pure dimethyl ether, methanol, acetone, and water using three approaches for the electrostatic potential: the Ewald summation, the original Wolf summation, and the modified Wolf summation. The results for the vapor pressure and the vapor–liquid coexistence densities are shown in Fig. 2.6. These diagrams present the relative deviation of the properties calculated with the Wolf summation from the Ewald summation. The lines represent relative deviations of vapor–liquid coexistence properties calculated analogous to eq. (2.15). The deviations reported in Fig. 2.6 are the mean average of three separate simulations. The calculation of the standard deviations is detailed in the Appendix. It can be seen that the modified Wolf summation gives better results, i.e. lower deviations, compared to the original Wolf summation. Only for methanol the deviations are in the same order. The lowest deviations are in the dimethyl ether system, where all deviations are below 1%. In the methanol system the same behavior is observed; only the deviation of the vapor density increases up to 3% with increasing temperature. In the acetone system the deviations in vapor pressure and vapor density reach up to 2% for low temperatures. For the SPC/E water system

the same behavior as for the methanol system can be seen. Thus, the modified Wolf summation shows good overall agreement with the Ewald summation for pure components. Results for a larger volume and cutoff radius are shown in the Supporting Information [Appendix A].

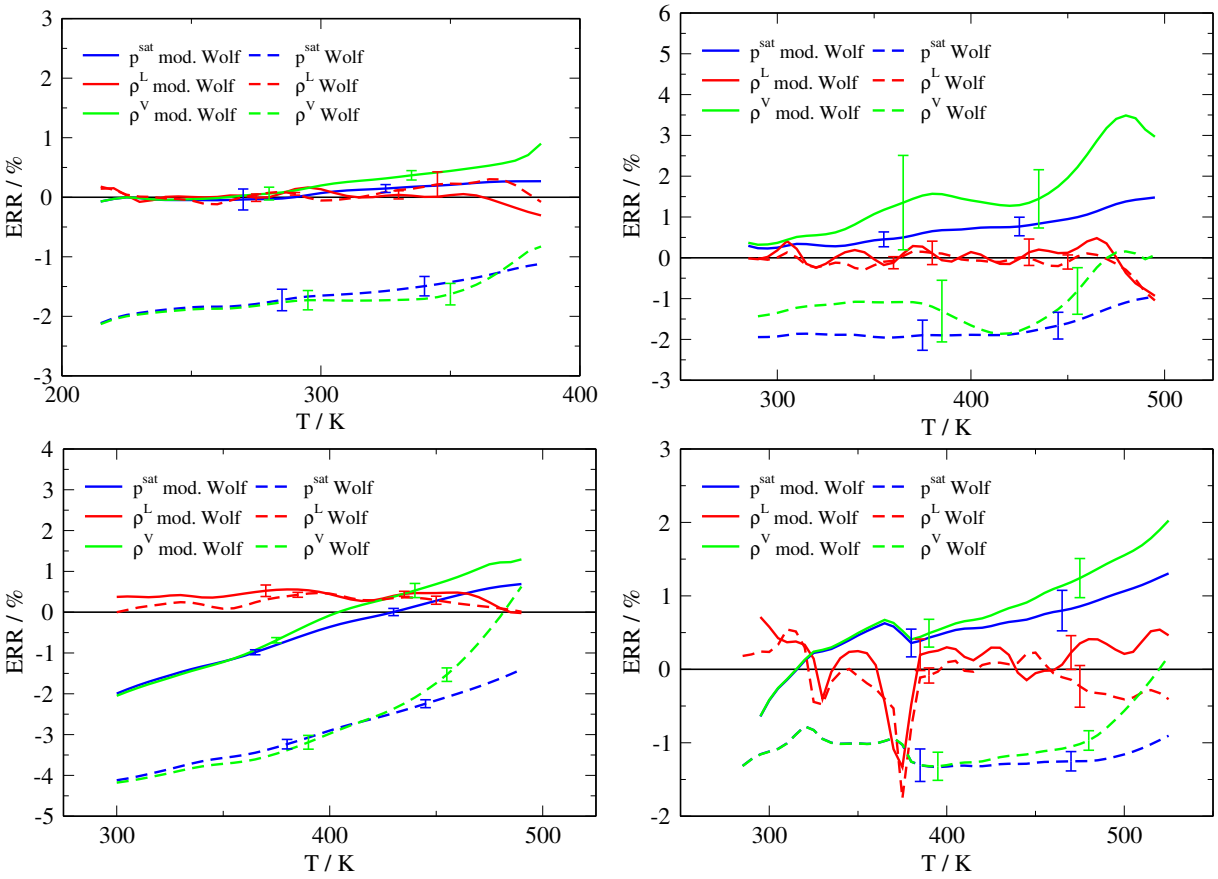

Figure 2.6: Relative deviation of vapor liquid equilibrium properties (vapor pressure p^{sat}, coexisting liquid and vapor density ρ^L, ρ^V) over temperature T for a dimethyl ether system (top left), methanol system (top right), acetone system (bottom left), and SPC/E water system (bottom right) with a volume of 33000 Å^3 and a cutoff radius of $R_c = 14\,\text{Å}$. The continuous lines represent the modified Wolf summation, and the dashed lines represent the original Wolf summation.

In section 2.3.1 it was shown that the optimal damping parameter α varies for different densities. Therefore, an iterative scheme was introduced at the beginning of each simulation. Vapor pressure calculations with different constant damping parameters are shown in Fig. 2.7 for acetone and SPC/E water. In both systems there is one specific α-value where the deviations are in the same range as for the simulations with varying damping parameter ($\alpha = 0.095\,\text{Å}^{-1}$ for acetone and $\alpha = 0.11\,\text{Å}^{-1}$ for SPC/E water). These α-values can be obtained in simulations with the same iterative scheme described above. A relevant liquid-like density then has to be considered. Identifying a suitable constant value for α is ambiguous in two ways. First, it is unclear, what the relevant

density for determining α (iteratively) should be. Second, the results for phase equilibria are so sensitive to α (see Fig. 2.7), that within the uncertainty of an iterative procedure, we find rather varying results for phase equilibria.

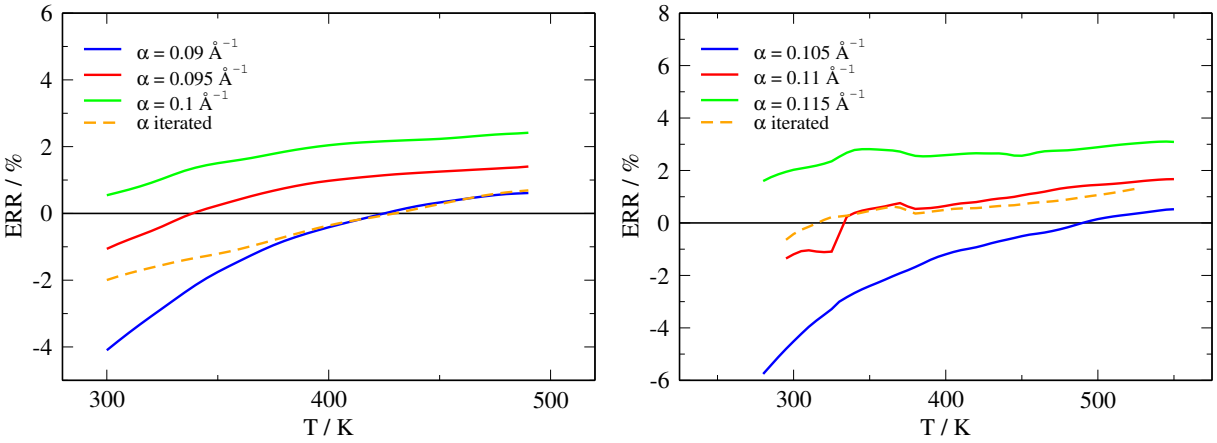

Figure 2.7: Relative deviation of vapor pressure p^{sat} over temperature T for simulations with different constant damping parameters α and a simulation with varying α-values obtained from the iterative scheme. The simulations are carried out for an acetone system (left) and SPC/E water system (right) with a volume of 33000 Å^3, a cutoff radius of $R_c = 14$ Å, and the modified Wolf summation.

In order to assess the modified Wolf approach for phase equilibria of mixtures, we regard vapor–liquid equilibria of two mixtures: a mixture of acetone with nitrogen at a temperature of 480 K and a mixture of n-pentane with nitrogen at 422.7 K. Both phase equilibria of these mixtures are shown in Fig. 2.8 (left). The results of the Wolf and Ewald method are in good agreement. Only for the acetone/nitrogen mixture there is a small deviation for high pressures at the vapor side. On the right of Fig. 2.8 the relative deviation of the phase coexistence densities is shown. For both densities a deviation lower than 1% is achieved.

2.4 Conclusion

In this study we propose a new self-energy term for the Wolf method. The modification improves the description of the electrostatic energy for open ensembles, i.e. for systems with fluctuating molecule number. We investigated the dependence of electrostatic cutoff radius and Wolf-damping parameter α and propose an iterative approach to determine the Wolf-damping parameter α. We applied the modified Wolf method within MC simulations in a grand canonical ensemble to calculate phase equilibrium properties of molecular fluids. For dimethyl ether, methanol, acetone, and for SPC/E water, as well as for two mixtures, we obtained good agreement with phase equilibrium results from the Ewald summation.

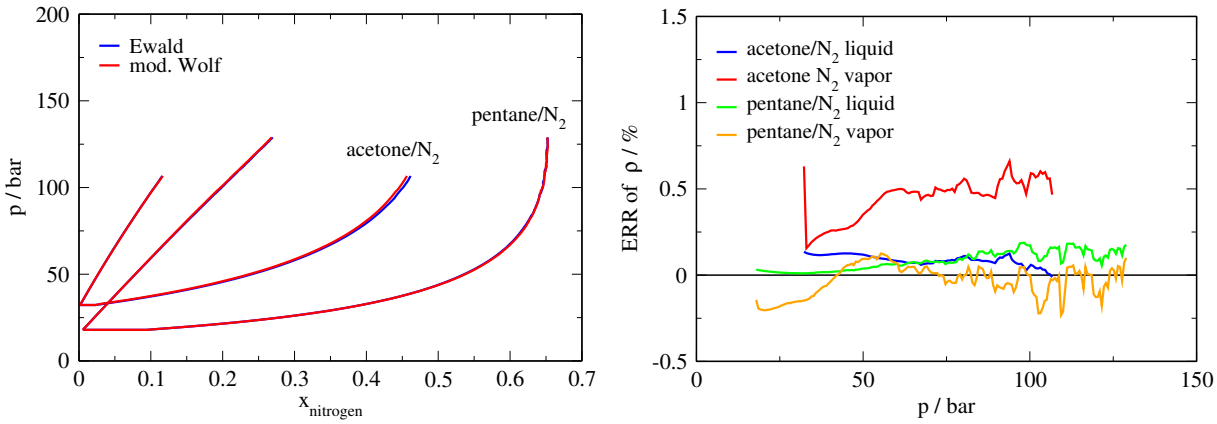

Figure 2.8: Vapor–liquid equilibrium (left) and relative deviations of coexisting densities (right) for binary mixtures of acetone/nitrogen at 480 K (44000 Å^3, $R_c = 14$ Å) and for n-pentane/nitrogen at 422.7 K (30000 Å^3, $R_c = 14$ Å).

Appendix

The standard deviation (SD) for the relative deviation is calculated from N^{Sim} simulations of the Wolf and Ewald method, respectively, as

$$SD = \sqrt{\frac{\sum_{i=1}^{N^{\mathrm{Sim}}} \sum_{j=1}^{N^{\mathrm{Sim}}} \left(\frac{x_i^{\mathrm{Wolf}} - x_j^{\mathrm{Ewald}}}{\overline{x}^{Ewald}} - \frac{\overline{x}^{\mathrm{Wolf}} - \overline{x}^{\mathrm{Ewald}}}{\overline{x}^{\mathrm{Ewald}}} \right)^2}{(N^{\mathrm{Sim}})^2 - 1}} \tag{2.16}$$

where i and j denote the index of a simulation, x the particular property and $\overline{x}$ the mean of the property of all simulations of the Ewald or Wolf method. $\overline{x}^{\mathrm{Ewald}}$ is used as factor for the first term of the summation in eq. 2.16 because the Ewald method is seen as the reference method with a correct result in the mean.

Bibliography

[1] Ewald, P. P. (1921) Die Berechnung optischer und elektrostatischer Gitterpotentiale. *Ann. Phys. 369*, 253–287.

[2] Hockney, R. W., and Eastwood, J. W. *Computer simulation using particles*; Taylor & Francis Group: New York, 1988.

[3] Darden, T., York, D., and Pedersen, L. (1993) Particle mesh Ewald: An N log(N) method for Ewald sums in large systems. *J. Chem. Phys. 98*, 10089–10092.

[4] Essmann, U., Perera, L., Berkowitz, M. L., Darden, T., Lee, H., and Pedersen, L. G. (1995) A smooth particle mesh Ewald method. *J. Chem. Phys. 103*, 8577–8593.

[5] Brooks III, C. L. (1987) The influence of long-range force truncation on the thermodynamics of aqueous ionic solutions. *J. Chem. Phys. 86*, 5156–5162.

[6] Schreiber, H., and Steinhauser, O. (1992) Cutoff size does strongly influence molecular dynamics results on solvated polypeptides. *Biochemistry 31*, 5856–5860.

[7] Spohr, E. (1997) Effect of electrostatic boundary conditions and system size on the interfacial properties of water and aqueous solutions. *J. Chem. Phys. 107*, 6342–6348.

[8] Cisneros, G. A., Karttunen, M., Ren, P., and Sagui, C. (2013) Classical electrostatics for biomolecular simulations. *Chem. Rev. 114*, 779–814.

[9] Schrimpf, G., Schlenkrich, M., Brickmann, J., and Bopp, P. (1992) Molecular dynamics simulation of zeolite NaY: a study of structure, dynamics, and thermalization of sorbates. *J. Phys. Chem. 96*, 7404–7410.

[10] Brooks III, C. L., Pettitt, B. M., and Karplus, M. (1985) Structural and energetic effects of truncating long ranged interactions in ionic and polar fluids. *J. Chem. Phys. 83*, 5897–5908.

[11] Steinbach, P. J., and Brooks, B. R. (1994) New spherical-cutoff methods for long-range forces in macromolecular simulation. *J. Comput. Chem. 15*, 667–683.

[12] Levitt, M., Hirshberg, M., Sharon, R., and Daggett, V. (1995) Potential energy function and parameters for simulations of the molecular dynamics of proteins and nucleic acids in solution. *Comput. Phys. Commun. 91*, 215–231.

[13] Wolf, D., Keblinski, P., Phillpot, S., and Eggebrecht, J. (1999) Exact method for the simulation of Coulombic systems by spherically truncated, pairwise r^{-1} summation. *J. Chem. Phys. 110*, 8254–8282.

[14] Zahn, D., Schilling, B., and Kast, S. M. (2002) Enhancement of the Wolf damped Coulomb potential: Static, dynamic, and dielectric properties of liquid water from molecular simulation. *J. Phys. Chem. B 106*, 10725–10732.

[15] Fennell, C. J., and Gezelter, J. D. (2006) Is the Ewald summation still necessary? Pairwise alternatives to the accepted standard for long-range electrostatics. *J. Chem. Phys. 124*, 234104.

[16] Kale, S., and Herzfeld, J. (2011) Pairwise long-range compensation for strongly ionic systems. *J. Chem. Theory Comput. 7*, 3620–3624.

[17] Fukuda, I., Yonezawa, Y., and Nakamura, H. (2011) Molecular dynamics scheme for precise estimation of electrostatic interaction via zero-dipole summation principle. *J. Chem. Phys. 134*, 164107.

[18] Yonezawa, Y. (2012) A long-range electrostatic potential based on the Wolf method charge-neutral condition. *J. Chem. Phys. 136*, 244103.

[19] McCann, B. W., and Acevedo, O. (2013) Pairwise alternatives to Ewald summation for calculating long-range electrostatics in ionic liquids. *J. Chem. Theory Comput. 9*, 944–950.

[20] Fukuda, I. (2013) Zero-multipole summation method for efficiently estimating electrostatic interactions in molecular system. *J. Chem. Phys. 139*, 174107.

[21] McLaughlin, K., Cioce, C. R., Pham, T., Belof, J. L., and Space, B. (2013) Efficient calculation of many-body induced electrostatics in molecular systems. *J. Chem. Phys. 139*, 184112.

[22] Lamichhane, M., Gezelter, J. D., and Newman, K. E. (2014) Real space electrostatics for multipoles. I. Development of methods. *J. Chem. Phys. 141*, 134109.

[23] Fanourgakis, G. S. (2015) An extension of Wolf's method for the treatment of electrostatic interactions: application to liquid water and aqueous solutions. *J. Phys. Chem. B 119*, 1974–1985.

[24] Stenqvist, B., Trulsson, M., Abrikosov, A. I., and Lund, M. (2015) Direct summation of dipole-dipole interactions using the Wolf formalism. *J. Chem. Phys. 143*, 014109.

[25] Demontis, P., Spanu, S., and Suffritti, G. B. (2001) Application of the Wolf method for the evaluation of Coulombic interactions to complex condensed matter systems: aluminosilicates and water. *J. Chem. Phys. 114*, 7980–7988.

[26] Mahadevan, T., and Garofalini, S. (2007) Dissociative water potential for molecular dynamics simulations. *J. Phys. Chem. B 111*, 8919–8927.

[27] Mendoza, F. N., López-Lemus, J., Chapela, G. A., and Alejandre, J. (2008) The wolf method applied to the liquid-vapor interface of water. *J. Chem. Phys. 129*, 024706.

[28] Avendaño, C., Gil-Villegas, A., and González-Tovar, E. (2008) Computer simulation of charged hard spherocylinders. *J. Chem. Phys. 128*, 044506.

[29] Kikugawa, G., Apostolov, R., Kamiya, N., Taiji, M., Himeno, R., Nakamura, H., and Yonezawa, Y. (2009) Application of MDGRAPE-3, a special purpose board for molecular dynamics simulations, to periodic biomolecular systems. *J. Comput. Chem. 30*, 110–118.

[30] Muscatello, J., and Bresme, F. (2011) A comparison of Coulombic interaction methods in non-equilibrium studies of heat transfer in water. *J. Chem. Phys. 135*, 234111.

[31] Jiménez-Serratos, G., Avendano, C., Gil-Villegas, A., and González-Tovar, E. (2011) Computer simulation of charged hard spherocylinders at low temperatures. *Mol. Phys. 109*, 27–36.

[32] Hansen, J. S., Schrøder, T. B., and Dyre, J. C. (2012) Simplistic Coulomb forces in molecular dynamics: Comparing the Wolf and shifted-force approximations. *J. Phys. Chem. B 116*, 5738–5743.

[33] Viveros-Méndez, P., and Gil-Villegas, A. (2012) Computer simulation of sedimentation of ionic systems using the Wolf method. *J. Chem. Phys. 136*, 154507.

[34] Wirnsberger, P., Fijan, D., Šarić, A., Neumann, M., Dellago, C., and Frenkel, D. (2016) Non-equilibrium simulations of thermally induced electric fields in water. *J. Chem. Phys. 144*, 224102.

[35] Kolafa, J., Moučka, F., and Nezbeda, I. (2008) Handling electrostatic interactions in molecular simulations: A systematic study. *Collect. Czech. Chem. C. 73*, 481–506.

[36] Kolafa, J., and Perram, J. W. (1992) Cutoff errors in the Ewald summation formulae for point charge systems. *Mol. Simulat. 9*, 351–368.

[37] Virnau, P., and Müller, M. (2004) Calculation of free energy through successive umbrella sampling. *J. Chem. Phys. 120*, 10925–10930.

[38] Shen, V. K., and Errington, J. R. (2004) Metastability and instability in the Lennard-Jones fluid investigated by transition-matrix Monte Carlo. *J. Phys. Chem. B 108*, 19595–19606.

[39] Gross, J., and Sadowski, G. (2001) Perturbed-chain SAFT: An equation of state based on a perturbation theory for chain molecules. *Ind. Eng. Chem. Res. 40*, 1244–1260.

[40] Errington, J. R. (2003) Direct calculation of liquid–vapor phase equilibria from transition matrix Monte Carlo simulation. *J. Chem. Phys. 118*, 9915–9925.

[41] Paluch, A. S., Shen, V. K., and Errington, J. R. (2008) Comparing the use of Gibbs ensemble and grand-canonical transition-matrix Monte Carlo methods to determine phase equilibria. *Ind. Eng. Chem. Res. 47*, 4533–4541.

[42] Ferrenberg, A. M., and Swendsen, R. H. (1989) Optimized monte carlo data analysis. *Phys. Rev. Lett. 63*, 1195.

[43] Wilding, N. B. (1995) Critical-point and coexistence-curve properties of the Lennard-Jones fluid: a finite-size scaling study. *Phys. Rev. E 52*, 602.

[44] Panagiotopoulos, A. Z., Wong, V., and Floriano, M. A. (1998) Phase equilibria of lattice polymers from histogram reweighting Monte Carlo simulations. *Macromolecules 31*, 912–918.

[45] Potoff, J. J., and Panagiotopoulos, A. Z. (1998) Critical point and phase behavior of the pure fluid and a Lennard-Jones mixture. *J. Chem. Phys. 109*, 10914–10920.

[46] Hemmen, A., Panagiotopoulos, A. Z., and Gross, J. (2015) Grand Canonical Monte Carlo Simulations Guided by an Analytic Equation of State - Transferable Anisotropic Mie Potentials for Ethers. *J. Phys. Chem. B 119*, 7087–7099.

[47] Hemmen, A., and Gross, J. (2015) Transferable Anisotropic United-Atom Force Field Based on the Mie Potential for Phase Equilibrium Calculations: n-Alkanes and n-Olefins. *J. Phys. Chem. B 119*, 11695–11707.

[48] Weidler, D., and Gross, J. (2016) Transferable Anisotropic United-Atom Force Field Based on the Mie Potential for Phase Equilibria: Aldehydes, Ketones, and Small Cyclic Alkanes. *Ind. Eng. Chem. Res. 55*, 12123–12132.

[49] Waibel, C., Stierle, R., and Gross, J. (2018) Transferability of cross-interaction pair potentials: Vapor-liquid phase equilibria of n-alkane/nitrogen mixtures using the TAMie force field. *Fluid Phase Equilibr. 456*, 124–130.

[50] Schnabel, T., Srivastava, A., Vrabec, J., and Hasse, H. (2007) Hydrogen bonding of methanol in supercritical CO2: comparison between 1H NMR spectroscopic data and molecular simulation results. *J. Phys. Chem. B 111*, 9871–9878.

[51] Berendsen, H. J. C., Grigera, J. R., and Straatsma, T. P. (1987) The missing term in effective pair potentials. *J. Phys. Chem. 91*, 6269–6271.

[52] Lorentz, H. (1881) Ueber die Anwendung des Satzes vom Virial in der kinetischen Theorie der Gase. *Ann. Phys. 248*, 127–136.

[53] Berthelot, D. (1898) Sur le mélange des gaz. *Compt. Rendus 126*, 1703–1706.

[54] Potoff, J. J., and Bernard-Brunel, D. A. (2009) Mie potentials for phase equilibria calculations: Application to alkanes and perfluoroalkanes. *J. Phys. Chem. B 113*, 14725–14731.

[55] Allen, M. P., and Tildesley, D. J. *Computer simulation of liquids*; Oxford University Press: New York, 1987.

[56] Smit, B. (1992) Phase diagrams of Lennard-Jones fluids. *J. Chem. Phys. 96*, 8639–8640.

Chapter 3

A Modified Shifted Force Approach to the Wolf Summation

The content of this chapter is a literal quote of the publication

> *Waibel, Feinler, Gross, Journal of Chemical Theory and Computation, 2018, submitted (reproduced with permission from ACS, unpublished work copyright 2018) [in the meantime it was published with minor modifications in Journal of Chemical Theory and Computation, 15 (1), 2019, 572-583].*

In comparison to the published work, the abstract is here omitted. Additions or deletions compared to the published work are marked with angular brackets.

The standard method for calculation of the electrostatic energy is the Ewald summation[1], which splits the potential in a short-ranged part handled in the real space and a long-ranged part treated in the Fourier space. This method is exact in the limit of infinite reciprocal-space evaluations. It can in practice be applied with a finite number of reciprocal-space evaluations, but it remains a computationally demanding approach that, in a simple implementation, scales as $\mathcal{O}(N^2)$ with the particle number N of the system. The simulation effort can be scaled down to $\mathcal{O}(N \log(N))$ using derivatives of the Ewald summation, which utilizing fast Fourier transform, such as particle-particle particle mesh Ewald[2], particle mesh Ewald[3] and smooth particle mesh Ewald[4]. Other methods are the reaction field approach[5] and the Fast Multipole Method[6] with a scaling of $\mathcal{O}(N)$. Thereby, the reaction-field method is an implicit method, needing the knowledge about the dielectric constant of the surrounding medium. In the Fast Multipole Method the treatment of periodicity is modified by clustering the system in groups of increasing size. Another approach are spherically truncation methods, evaluating only the pairwise interactions within a cutoff radius and a scaling of $\mathcal{O}(N)$. A naive truncation scheme, however, is not satisfactory for handling the slowly decaying electrostatic potential[7–11].

To get improved results Wolf et al.[12] suggested a charge-neutralization approach within the cutoff sphere by placing balancing charges on the cutoff radius, thereby mimicking the screening effect of the surrounding medium. The original Wolf summation takes form of a shifted electrostatic potential with a self interaction term. In Monte Carlo (MC) simulations of fluids with classical force fields only require a reliable description of the potential energy, but for molecular dynamics (MD) simulations also the forces have to be described appropriately. In the original Wolf summation the forces show discontinuous at the cutoff radius, which leads to several artifacts[13]. Several modifications were proposed to address this problem. Wolf et al.[12] redefined the derived force, however, leading to an inconsistency between the force and the potential. To overcome this inconsistency Zahn et al.[14,15] modified the potential based on the non-redefined forces of the original Wolf summation by extension with a force shifting term. Fukuda et al.[16] applied a force switching scheme and Fennell et al.[17] applied a shifted force approach. There are other variants addressing not only charge neutralization but also higher order multipole (moment) neutralization within the cutoff sphere[18–20] or higher order multipole shifts[21–23]. Furthermore, the neutralization scheme is extended to higher order point multipoles[24–26]. These modifications have a continuous and more reliable description of the force, which mainly improve MD simulations, as shown in several studies[27–35].

A drawback of all these modifications, however, is the higher deviation in potential energy of these methods as compared with the original Wolf summation, which is caused by a rather strongly altered intermolecular potential introduced in modifying the Wolf summation. In MC simulations with insertions or deletions of molecules the correct energy plays an important role. There are only a few studies in literature using the Wolf summation in an ensemble with fluctuating molecule number. The enthalpy of adsorption[36] or vapor-liquid phase equilibria[37] can only be calculated inaccurately with a shifted force approach, whereas the vapor-liquid equilibria determined without a shifted force approach leads to accurate results[38,39] [Chapter 2].

In this study we propose a modification of a shifted force approach to describe the energy as well as the force in good agreement to reference simulations using the Ewald sum. For an ensemble with fluctuating particle number the proposed method leads to much improved results for phase equilibria (and to good results for dynamic properties) compared to the original Wolf summation[12] or the original shifted force Wolf summation[17]. We regard molecular fluids with static partial charges and mixtures thereof as well as a fluid with a polarizable force field.

3.1 Wolf Summation

This section briefly reviews the classical Wolf summation and its shifted force extension, which removes discontinuities of the force. Subsequently we propose a modified shifted force approach that reproduces the electrostatic energy and force more accurately as the original shifted force approach[17].

3.1.1 Shifted Potential

The Coulomb interactions between partial charges q_i are long-ranged. Wolf et al.[12] introduced a computationally effective method for calculating the electrostatic energy through a simple finite pairwise summation. The electrostatic energy calculated from the Coulomb potential truncated at a spherical cutoff radius R_c around a selected charge i, as

$$E^{\text{cutoff}} = \frac{1}{2}\sum_{i=1}^{N}\sum_{\substack{j\neq 1 \\ (r_{ij}<R_c)}}^{N} \frac{1}{4\pi\epsilon_0}\frac{q_i q_j}{r_{ij}} \tag{3.1}$$

does not lead to the correct energy. Here N is the number of partial charges in the system, r_{ij} is the distance between partial charge i and j and ϵ_0 is the vacuum permittivity. To simplify the notation, we henceforth redefine the unit of the Coulomb charge q_i by absorbing the Coulomb constant $(4\pi\epsilon_0)^{-0.5}$. To get an approximately correct energy Wolf et al. enforced charge neutrality within the cutoff sphere. The negative of the net-charge $-\Delta q_i(R_c)$ within this sphere is placed on the cutoff surface. The net-charge mimics the electrostatic screening effect of the surrounding medium. The neutralizing net-charge can be expressed as a summation over all charges within the cutoff radius

$$\Delta q_i(R_c) = \sum_{\substack{j=1 \\ (r_{ij}<R_c)}}^{N} q_j \tag{3.2}$$

leading, thus, to a shifted pair potential (SP) with a self-correction term

$$E^{\text{SP}} = \frac{1}{2}\sum_{\substack{i=1 \\ (r_{ij}<R_c)}}^{N}\sum_{j\neq i}^{N} q_i q_j \left(\frac{1}{r_{ij}} - \frac{1}{R_c}\right) - \frac{1}{2R_c}\sum_{i=1}^{N} q_i^2 \tag{3.3}$$

Wolf et al.[12] realized that the average Coulombic energy as calculated from this equation, shows slowly decaying oscillations around the correct Coulombic energy with increasing cutoff length. They therefore introduced a damping function. By using the error function as damping function, the Coulombic potential $\phi(r) = 1/r$ can be decomposed into a short- and a long-ranged part, as

$$\phi(r) = \frac{1}{r} = \phi^{\text{short}} + \phi^{\text{long}} = \frac{\text{erfc}(\alpha r)}{r} + \frac{\text{erf}(\alpha r)}{r} \tag{3.4}$$

Eq. 3.3 excludes the self-contribution for $1/r_{ij}$, by requiring $j \neq i$. After introducing the decomposition, eq. 3.4, however, within the long-ranged erf-term, the self-contribution can be added and subtracted. The long-ranged self-contribution is analytically known, with a value of $\pi^{-1/2}\alpha$. The so-obtained long-ranged contribution can be omitted to get an expression for the Coulombic energy with well-behaved characteristics. That is so, because for short cutoff distances, the average of the long-ranged contribution shows systematic offset from zero, that depends on the cutoff distance. With increasing cutoff distance the averaged long-ranged part oscillates and slowly decays to zero. Omitting the long-ranged contribution leads to more well-behaved energies in good agreement to the actual Coulombic energies even for moderate cutoff distances R_c, providing that an appropriate value of damping parameter α is chosen. This leads to the original Wolf summation, a damped shifted potential, DSP. By introducing eq. 3.4 for $1/r_{ij}$ in eq. 3.3 one gets a double sum over an erfc-function and over an erf-function, excluding the self interaction by the requirement of $j \neq i$. Wolf et al. considered the double sum over the long-ranged erf-function and added as well as subtracted the self-contribution. The long-ranged self-contribution is analytically known, with a value of $\pi^{-1/2}\alpha$. The so-obtained double sum over the long-ranged contribution (including $j = i$) can be omitted to get an expression for the Coulombic energy with well-behaved characteristics. That is so, because for short cutoff distances, the average of the long-ranged contribution shows systematic offset from zero, that depends on the cutoff distance. With increasing cutoff distance the averaged long-ranged part oscillates and slowly decays to zero. Omitting the long-ranged contribution leads to more well-behaved energies in good agreement to the actual Coulombic energies even for moderate cutoff distances R_c, providing that an appropriate value of damping parameter α is chosen. This leads to the original Wolf summation, a damped shifted potential, DSP

$$\begin{aligned} E^{\text{DSP}} =& \frac{1}{2} \sum_{\substack{i=1 \\ (r_{ij}<R_c)}}^{N} \sum_{j \neq i}^{N} q_i q_j \left(\frac{\text{erfc}(\alpha r_{ij})}{r_{ij}} - \frac{\text{erfc}(\alpha R_c)}{R_c} \right) \\ & - \left(\frac{\text{erfc}(\alpha R_c)}{2R_c} + \frac{\alpha}{\pi^{1/2}} \right) \sum_{i=1}^{N} q_i^2 \end{aligned} \tag{3.5}$$

where the damping parameter α has to be chosen carefully to ensure accurate results. A detailed discussion of this derivation can be found in literature[12,38] [Chapter 2]. The

concept of the damped Wolf summation can be described in a general form as

$$E^{\mathrm{DSP}} = \frac{1}{2}\sum_{\substack{i=1\\(r_{ij}<R_c)}}^{N}\sum_{j\neq i}^{N} q_i q_j \Big[\phi^{\mathrm{short}}(r_{ij}) - \phi^{\mathrm{short}}(R_c)\Big] - \frac{1}{2}\left[\phi^{\mathrm{short}}(R_c) + \lim_{r\to 0}\left\{\phi^{\mathrm{long}}(r)\right\}\right]\sum_{i=1}^{N} q_i^2 \tag{3.6}$$

where the parts with $\phi^{\mathrm{short}}(R_c)$ result from charge neutralization and the limit of ϕ^{long} for $r \to 0$ comes from damping.

3.1.2 Shifted Force Potential

The original Wolf summation[12] can be regarded as a shifted pair potential with a self interaction term. The shift in the potential leads to a continuous course of the potential energy across the cutoff radius. To calculate intra- and intermolecular forces $\boldsymbol{F} = -{}^{\partial E}/_{\partial r}$ in MD simulations, the negative gradient of the potential has to be taken. Eq. 3.5 shows a discontinuity of the force at the cutoff radius R_c. The force between two interaction sites i and j is non-zero for all distances r_{ij} lower to R_c and jumps to zero beyond the cutoff distance. That leads to several artifacts, like poor energy conservation in molecular dynamic simulations.

To eliminate the discontinuity, a shifted force (SF) approach can be applied, ensuring a vanishing force at the cutoff radius. In this approach the initial potential $\phi(r) = {}^1/_r$ from eq. 3.4 is extended with the negative gradient of the initial potential (force) at the cutoff radius R_c scaled with the distance r

$$\phi^{\mathrm{SF}}(r) = \phi(r) - \left(\frac{\mathrm{d}\phi(r)}{\mathrm{d}r}\right)_{r=R_c} \cdot r \tag{3.7}$$

This potential $\phi^{\mathrm{SF}}(r)$ should not be confused with a shifted force potential itself. Only after introducing the charge neutralizing scheme of eq. 3.6 to eq. 3.7 for both, $\phi(r)$ and $\phi(R_c)$, one gets a (sum over) shifted force potentials. Decomposing the potential $\phi^{\mathrm{SF}}(r)$ in a short- and a long-ranged part with the error function and using the general form of the Wolf summation (eq. 3.6) leads to the damped shifted force method (DSF)

$$E^{\mathrm{DSF}} = \frac{1}{2}\sum_{\substack{i=1\\(r_{ij}<R_c)}}^{N}\sum_{j\neq i}^{N} q_i q_j \left[\frac{\mathrm{erfc}(\alpha r_{ij})}{r_{ij}} - \frac{\mathrm{erfc}(\alpha R_c)}{R_c} - \left(\frac{\partial\phi^{\mathrm{short}}(r)}{\partial r}\right)_{r=R_c} \cdot (r_{ij} - R_c)\right] - \left[\frac{\mathrm{erfc}(\alpha R_c)}{2R_c} - \left(\frac{\partial\phi^{\mathrm{short}}(r)}{\partial r}\right)_{r=R_c} \cdot \frac{R_c}{2} + \frac{\alpha}{\pi^{1/2}}\right]\sum_{i=1}^{N} q_i^2 \tag{3.8}$$

where $\pi^{-1/2}\alpha$ results from damping. The derivative of the short-ranged part of the potential can be expressed as

$$\left(\frac{\partial\phi^{\text{short}}(r)}{\partial r}\right)_{r=R_c} = -\frac{2\alpha}{\pi^{1/2}}\frac{\exp(-\alpha^2 R_c^2)}{R_c} - \frac{\text{erfc}(\alpha R_c)}{R_c^2} \tag{3.9}$$

The first line of eq. 3.8 is the classical form of a shifted force approach[40] (using a damped potential) that corresponds to a potential, where the Taylor expansion of the primary potential $\phi(r)$ around position $r_{ij} = R_c$, truncated after the first order, is subtracted from the primary potential. In literature there are several assumptions to handle the self term (second line of eq. 3.8), which is necessary to get the correct electrostatic energy, as Wolf et al.[12] have shown. A self term resulting from the general form of the Wolf summation (second line of eq. 3.8) is used by Fanourgakis[23]. If the shifted force approach is perceived as a small correction of the pair interaction potential in the Wolf summation, the self term of the original Wolf summation (second line of eq. 3.5) can be used[25], corresponding to $\left(\frac{\partial\phi^{\text{short}}(r)}{\partial r}\right)_{r=R_c} \cdot \frac{R_c}{2} = 0$ in eq. 3.8. That approach is taken, for example, in the Cassandra simulation package[41]. Furthermore, the self term is often neglected altogether[17,21,22,37]. The difference between these assumptions can be seen in the Supporting Information [Appendix B], where we report phase equilibrium calculations in the grand canonical ensemble. There are no appreciable differences between the two assumptions not neglecting the self term. But if the self term is neglected altogether, no results can be obtained in the grand canonical ensemble. In our further simulations of the original damped shifted force method we used the formulation of the Cassandra simulation package[41] with the self term of the original Wolf summation.

3.1.3 A Modified Shifted Force Approach

In this subsection, we propose a modified shifted force approach that provides improved agreement to reference results for static and dynamic properties of molecular fluids with partial charges. Fig. 3.1 shows the course of different pair potentials before and after the charge neutralization procedure. There is a substantial difference between the shifted potential and the shifted force potential. That clarifies that the calculated potential energy of both approaches will be different. To get closer to the shifted potential, while satisfying the constraint for a continuous force at the cutoff radius, we modify the switching function of the shifted force potential. Instead of scaling the negative gradient linearly with the radius r, as in eq. 3.7, we propose to scale it with $\beta^{-1}\exp(\beta(r - R_c))$, according to

$$\phi^{\text{mSF}}(r) = \phi(r) - \left(\frac{\partial\phi(r)}{\partial r}\right)_{r=R_c}\frac{\exp(\beta(r - R_c))}{\beta} \tag{3.10}$$

Like in eq. 3.7, only the combination of potential $\phi^{\mathrm{mSF}}(r)$ and the charge neutralizing scheme of eq. 3.6 leads to a shifted force potential. The new switching function increases exponentially with increasing distance. Through a strong scaling close to the cutoff the force is falling continuously to zero at the cutoff radius. The weaker scaling at small separations between two interaction sites (away from the cutoff radius) leads to better agreement to the simply shifted potential. Using this switching function allows us to calculate a potential with less differences and no discontinuities. Parameter β adjusts how sharply the switching function acts only in the vicinity of $r \to R_c$. We have seen that parameter β can be set to a constant value, as detailed at the end of this chapter.

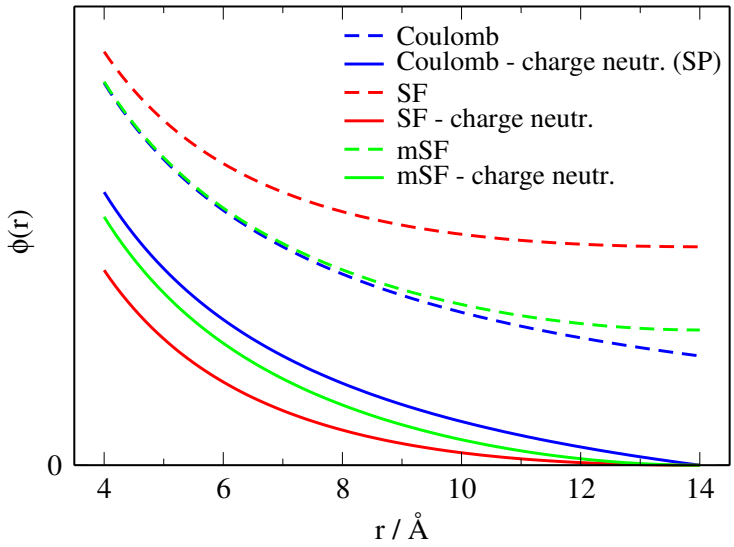

Figure 3.1: Representation of different types of pair potentials: Coulomb potential (eq. 3.4), shifted force potential (SF, eq. 3.7), and modified shifted force potential (mSF, eq. 3.10, $\beta = 0.3$) before (dashed lines) and after (solid lines) the charge neutralizing procedure using a cutoff radius of $R_c = 14\,\text{Å}$.

Dividing the potential into a short- and a long-ranged part using the error function and incorporating the approach into the general form of the Wolf summation (eq. 3.6) leads to

$$\begin{aligned} E^{\mathrm{mDSF}} =& \frac{1}{2}\sum_{\substack{i=1 \\ (r_{ij}<R_c)}}^{N}\sum_{j\neq i}^{N} q_i q_j \left[\frac{\operatorname{erfc}(\alpha r_{ij})}{r_{ij}} - \frac{\operatorname{erfc}(\alpha R_c)}{R_c} - \left(\frac{\partial\phi^{\mathrm{short}}(r)}{\partial r}\right)_{r=R_c} \cdot \frac{\exp(\beta(r_{ij}-R_c))-1}{\beta}\right] \\ & - \frac{1}{2}\left[\frac{\operatorname{erfc}(\alpha R_c)}{R_c} - \frac{1}{\beta}\left(\frac{\partial\phi^{\mathrm{short}}(r)}{\partial r}\right)_{r=R_c}\right. \\ & \left. + \lim_{r\to 0}\left\{\frac{\operatorname{erf}(\alpha r)}{r} - \left(\frac{\partial\phi^{\mathrm{long}}(r)}{\partial r}\right)_{r=R_c} \cdot \frac{\exp(\beta(r-R_c))}{\beta}\right\}\right] \sum_{i=1}^{N} q_i^2 \end{aligned} \tag{3.11}$$

where the limit-term ($r \to 0$) results from damping. The derivative of the long-ranged

part of the potential can be expressed as

$$\left(\frac{\partial\phi^{\text{long}}(r)}{\partial r}\right)_{r=R_c} = \frac{2\alpha}{\pi^{1/2}}\frac{\exp(-\alpha^2 R_c^2)}{R_c} - \frac{\text{erf}(\alpha R_c)}{R_c^2} \tag{3.12}$$

In molecules consisting of several interaction sites the intramolecular electrostatic interactions are already captured in the intramolecular bonding potentials (usually up to 3 or 4 interaction sites apart), connecting the interactions sites of the molecule. The charge-neutralization procedure (eq. 3.11) does not exclude intramolecular interactions captured in the bonding potential. Therefore we rewrite this equation counting molecules with index i and j and partial charges in these molecules with index a and b, respectively. With this extension for molecules we obtain

$$\begin{aligned}
E^{\text{mDSF}} =& \frac{1}{2}\sum_{i=1}^{N}\sum_{a=1}^{N_a}\sum_{\substack{j\neq i\\(r_{iajb}<R_c)\\\text{inter}}}^{N}\sum_{b=1}^{N_b} q_{ia}q_{jb}\left[\frac{\text{erfc}(\alpha r_{iajb})}{r_{iajb}} - \frac{\text{erfc}(\alpha R_c)}{R_c} - \left(\frac{\partial\phi^{\text{short}}(r)}{\partial r}\right)_{r=R_c}\cdot\frac{\exp(\beta(r_{iajb}-R_c))-1}{\beta}\right] \\
&+ \frac{1}{2}\sum_{\substack{i=1\\\text{intra}}}^{N}\sum_{a=1}^{N_a}\sum_{b\neq a}^{N_b} q_{ia}q_{ib}\left[\frac{\text{erfc}(\alpha r_{iaib})}{r_{iaib}} - \frac{\text{erfc}(\alpha R_c)}{R_c}\right. \\
&\left. - \left(\frac{\partial\phi^{\text{short}}(r)}{\partial r}\right)_{r=R_c}\cdot\frac{\exp(\beta(r_{iaib}-R_c))-1}{\beta} - \frac{\psi_{i,ab}}{r_{iaib}}\right] \\
&- \frac{1}{2}\left[\frac{\text{erfc}(\alpha R_c)}{R_c} - \frac{1}{\beta}\left(\frac{\partial\phi^{\text{short}}(r)}{\partial r}\right)_{r=R_c}\right. \\
&\left. + \lim_{r\to 0}\left\{\frac{\text{erf}(\alpha r)}{r} - \left(\frac{\partial\phi^{\text{long}}(r)}{\partial r}\right)_{r=R_c}\cdot\frac{\exp(\beta(r-R_c))}{\beta}\right\}\right]\sum_{\substack{i=1\\\text{self}}}^{N}\sum_{a=1}^{N_a} q_{ia}^2
\end{aligned} \tag{3.13}$$

where in the intramolecular part we subtract the interactions already captured in the bonded interactions, usually up to 3 or 4 interaction sites apart. Because the potential used in this derivation is the modified damped shifted force potential from eq. 3.10 we subtract the interaction with this potential. To decide whether an intramolecular interaction needs to be evaluated, we introduce the operator $\psi_{i,ab}$. This operator is 1 for intramolecular interactions captured in the bonding potential (angle and torsional potential) an 0 for intramolecular interactions sufficiently far apart.

The terms resulting from the long-ranged part of the subtracted potential can be combined with the long-ranged part of the self-interaction term (last line in eq. 3.13). Further reorganisation and reformulation of the equation leads to

$$
\begin{aligned}
E^{\mathrm{mDSF}} =& \frac{1}{2}\sum_{\substack{i=1\\(r_{iajb}<R_c)\\\text{inter}}}^{N}\sum_{a=1}^{N_a}\sum_{j\neq i}^{N}\sum_{b=1}^{N_b} q_{ia}q_{jb}\left[\frac{\operatorname{erfc}(\alpha r_{iajb})}{r_{iajb}} - \frac{\operatorname{erfc}(\alpha R_c)}{R_c} - \left(\frac{\partial\phi^{\mathrm{short}}(r)}{\partial r}\right)_{r=R_c}\cdot\frac{\exp(\beta(r_{iajb}-R_c))-1}{\beta}\right] \\
&+ \frac{1}{2}\sum_{\substack{i=1\\\text{intra}}}^{N}\sum_{a=1}^{N_a}\sum_{b\neq a}^{N_b} q_{ia}q_{ib}\left[-\frac{\operatorname{erfc}(\alpha R_c)}{R_c} + \left(\frac{\partial\phi^{\mathrm{short}}(r)}{\partial r}\right)_{r=R_c}\cdot\frac{1}{\beta}\right] \\
&+ \frac{1}{2}\sum_{\substack{i=1\\\text{intra}}}^{N}\sum_{a=1}^{N_a}\sum_{b=1}^{N_b} q_{ia}q_{ib}\left[-\frac{\operatorname{erf}(\alpha r_{iaib})}{r_{iaib}} + \left(\frac{\partial\phi^{\mathrm{long}}(r)}{\partial r}\right)_{r=R_c}\cdot\frac{\exp(\beta(r_{iaib}-R_c))}{\beta}\right]\cdot\psi_{i,ab} \\
&+ \frac{1}{2}\sum_{\substack{i=1\\\text{intra}}}^{N}\sum_{a=1}^{N_a}\sum_{b\neq a}^{N_b} q_{ia}q_{ib}\left[\frac{\operatorname{erfc}(\alpha r_{iaib})}{r_{iaib}} - \left(\frac{\partial\phi^{\mathrm{short}}(r)}{\partial r}\right)_{r=R_c}\cdot\frac{\exp(\beta(r_{iaib}-R_c))}{\beta}\right]\cdot(1-\psi_{i,ab}) \\
&- \frac{1}{2}\left[\frac{\operatorname{erfc}(\alpha R_c)}{R_c} - \frac{1}{\beta}\left(\frac{\partial\phi^{\mathrm{short}}(r)}{\partial r}\right)_{r=R_c}\right]\sum_{\substack{i=1\\\text{self}}}^{N}\sum_{a=1}^{N_a} q_{ia}^2
\end{aligned}
\tag{3.14}
$$

In our previous work on the Wolf summation with a shifted potential[38] [Chapter 2] it was shown, that the summation over the long-ranged bonded parts, counting over all interactions including the self interaction, is oscillating around zero. A more robust behaviour of the summation is obtained by neglecting this summation, leading to results in better agreement to results from simulations with the Ewald method. Here we also neglect this summation (line 3 of eq. 3.14) and get

$$
\begin{aligned}
E^{\mathrm{mDSF}} =& \frac{1}{2}\sum_{\substack{i=1\\(r_{iajb}<R_c)\\\text{inter}}}^{N}\sum_{a=1}^{N_a}\sum_{j\neq i}^{N}\sum_{b=1}^{N_b} q_{ia}q_{jb}\left[\frac{\operatorname{erfc}(\alpha r_{iajb})}{r_{iajb}} - \frac{\operatorname{erfc}(\alpha R_c)}{R_c} - \left(\frac{\partial\phi^{\mathrm{short}}(r)}{\partial r}\right)_{r=R_c}\cdot\frac{\exp(\beta(r_{iajb}-R_c))-1}{\beta}\right] \\
&+ \frac{1}{2}\sum_{\substack{i=1\\\text{intra}}}^{N}\sum_{a=1}^{N_a}\sum_{b\neq a}^{N_b} q_{ia}q_{ib}\left[-\frac{\operatorname{erfc}(\alpha R_c)}{R_c} + \left(\frac{\partial\phi^{\mathrm{short}}(r)}{\partial r}\right)_{r=R_c}\cdot\frac{1}{\beta}\right] \\
&+ \frac{1}{2}\sum_{\substack{i=1\\\text{intra}}}^{N}\sum_{a=1}^{N_a}\sum_{b\neq a}^{N_b} q_{ia}q_{ib}\left[\frac{\operatorname{erfc}(\alpha r_{iaib})}{r_{iaib}} - \left(\frac{\partial\phi^{\mathrm{short}}(r)}{\partial r}\right)_{r=R_c}\cdot\frac{\exp(\beta(r_{iaib}-R_c))}{\beta}\right]\cdot(1-\psi_{i,ab}) \\
&- \frac{1}{2}\left[\frac{\operatorname{erfc}(\alpha R_c)}{R_c} - \frac{1}{\beta}\left(\frac{\partial\phi^{\mathrm{short}}(r)}{\partial r}\right)_{r=R_c}\right]\sum_{\substack{i=1\\\text{self}}}^{N}\sum_{a=1}^{N_a} q_{ia}^2
\end{aligned}
\tag{3.15}
$$

The model parameters of the Wolf summation (R_c and α) as well as parameter β need to be carefully defined in order to obtain good results. We use a cutoff radius of at least 14 Å, because for lower values we have not found satisfying results for the Wolf method (evaluated in comparison to results from the Ewald summation). The optimal damping factor α varies with the density of the system. We use an iterative scheme proposed in our

previous work[38] [Chapter 2] to estimate the optimal damping factor α for each simulation. At the beginning of the simulation a low number of MC trial moves are carried out with an initial α-value, whereby we also calculate the energy for other α-values (i.e. for a predefined grid of values) and the energy for the Ewald summation. In the next iteration step the α-value with the lowest energy deviation from the Ewald summation is chosen and the iteration is continued until two successive steps achieve the same value for α. Based on our previous work[38] [Chapter 2] we expect that a constant value of the damping factor α for the entire range of densities also gives reasonable results, provided the parameter identification is done for liquid phase densities. The results in this case are rather sensitive to the value of α.

We have seen that parameter β of the switching function can be set constant. We recommend a value of $\beta = 0.3\,\text{Å}^{-1}$ for a cutoff radius of $R_c = 14\,\text{Å}$ or a value of $\beta = 0.25\,\text{Å}^{-1}$ for $R_c = 16\,\text{Å}$. As a side remark we mention that for small systems Ewald methods using fast Fourier transform could be more efficient than cutoff based methods, due to their use of smaller cutoffs (e.g. $8\,\text{Å}$ vs. $14\,\text{Å}$). But for larger systems the cutoff based methods are more efficient and can also be parallelized well.

3.2 Molecular Simulation Technique

3.2.1 Molecular Model

We assess the proposed method for electrostatic interactions through molecular simulations for several molecular substances described with classical force fields as well as with a polarizable force field. The transferable anisotropic Mie (TAMie) force field[42–45] [Chapter 4] is applied to describe ethers, ketones, alkanes and nitrogen with a classical non-polarizable force field. For methanol we use the force field proposed by Schnabel et al.[46] and for water we apply the SPC/E water model[47].

In all these force fields the intermolecular potential is described with a united-atom Mie potential, i.e. a generalized Lennard-Jones potential, and partial point charges to threat the effective electrostatic interactions

$$u(r_{ab}) = c_{ab}\epsilon_{ab}\left[\left(\frac{\sigma_{ab}}{r_{ab}}\right)^{n_{ab}} - \left(\frac{\sigma_{ab}}{r_{ab}}\right)^{6}\right] + \frac{q_a q_b}{r_{ab}} \tag{3.16}$$

In this pair potential r_{ab} denotes the distance between two interaction sites a and b, ϵ_{ab} and σ_{ab} are the well depth and diameter parameter, respectively, q_a is the partial charge, ϵ_0 denotes the vacuum permittivity and n_{ab} is the repulsive exponent. A fixed attractive exponent of $m = 6$ is used for all substances. In the previous section we used a notation to indicate site a is located on molecule i. Here, we use index a instead of ia, because

all force field parameters are specific to an interaction site (or a site-pair ab) and do not require mentioning on what molecule each interaction site is located. The prefactor c_{ab} is defined as

$$c_{ab} = \left(\frac{n_{ab}}{n_{ab}-6}\right)\left(\frac{n_{ab}}{6}\right)^{6/(n_{ab}-6)} \tag{3.17}$$

The force fields applied in this work tabulate parameters ϵ_{aa} and σ_{aa} defined between two interaction sites of same type α. Parameters ϵ_{ab} and σ_{ab} between two different interactions sites are determined using Lorentz-Berthelot combining rules[48,49] and the repulsive exponents of the Mie potentials n_{ab} are combined as an arithmetic average[50]. For mixtures a correction for the ϵ-parameter located on two different types of molecules, can be introduced

$$\epsilon_{ab} = \left(\epsilon_{aa}\epsilon_{bb}\right)^{1/2}\left(1-\kappa_{ab}\right) \tag{3.18}$$

For the interaction between alkyl- and nitrogen groups for the mixture of n-pentane with nitrogen we use the mixture parameters $\kappa_{\mathrm{CH_3,N}} = 0.0087$ and $\kappa_{\mathrm{CH_2,N}} = 0.0509$ from previous work[45] [Chapter 4].

In polarizable force fields one or more inducible dipole moments can be added to the molecular model, accounting for the redistribution of the electron density due to a surrounding electric field (as induced by surrounding molecules). One way to model this induced dipole moment is the charge-on-spring model, which is also referred to as Drude oscillator model or shell model. In this model the polarizable dipole moment is described through a pair of partial charges with opposite sign connected with a harmonic spring. The positive core charge q_D is located on the polarizable site, whereas the shell charge $-q_D$, which is connected with the core charge through the harmonic spring, is freely moveable. The harmonic spring with the spring constant k_D for a (small) molecule in vacuum has a length of zero. If there is an electric field from the surrounding of the molecule acting on the polarizable site, the position of the shell charge will be displaced because the electrostatic force balances the spring force and an energy minimum is reached. According to the Born-Oppenheimer approximation, the dynamics of electron structure reconfiguration is fast and effectively decoupled from the comparably slow movement of atomic nuclei, which means that the electron structure and thus the polarizability are effectively in an energetic minimum, for the time scale of classical force field simulations. That necessitates an energy minimization of all polarizable dipole sites in the system after every MC trial move or after every MD time step.

A defined scalar-valued polarizability α_D can be realized through a small spring constant and a small charge (and countercharge) or a larger spring constant and a larger charge.

The charges are defined as

$$q_D = \sqrt{\alpha_D k_D} \tag{3.19}$$

where α_D is the atomic polarizability (that has no relation to the damping parameter α discussed in the previous section). The charge-on-spring model is simple because the polarizability tensor of a molecule is represented as a collection of charge-on-spring sites, each representing scalar valued polarizabilities. This model is no longer pairwise additive because the position of the shell charges have to be determined self-consistently at every Monte Carlo step, corresponding to an energy minimization regarding the position of all the charges on spring.

In our simulations we use a polarizable Stockmayer fluid[51] with a reduced permanent dipole moment of $|\boldsymbol{\mu^*}| = {}^{|\boldsymbol{\mu}|}/\sqrt{\epsilon\sigma^3} = 1.0$ and a reduced polarizability of $\alpha_D^* = {}^{\alpha}/\sigma^3 = 0.03$. For molecular simulations of real fluids we suggest a cutoff radius of at least $R_c = 14$Å. For the Stockmayer fluid, if for a moment we consider the Lennard-Jones as a model for argon, this requirement corresponds to a dimensionless cutoff radius of about $R_c^* = R_c/\sigma \geq 4$. In our simulations we use $R_c^* = 4$ with $\beta^* = \beta \cdot \sigma = 1.05$. For the charge-on-spring site a spring constant of $k_D = 4184\,{}^{\mathrm{kJ}}/_{\mathrm{mol\AA}^2}$ is chosen, which in dimensionless units corresponds to $k_D^* = {}^{k_D \cdot \sigma^2}/_{\epsilon} = 38528$. This value leads to results which are equivalent to a point-dipole and was seen to be numerically stable[52]. The permanent dipole is modeled with a pair of two point charges with opposite sign, separated by a fixed distance of $d = 0.1 \cdot \sigma$. That separation distance is also sufficiently small to resemble the properties of a point dipolar fluid[53].

3.2.2 Monte Carlo Simulations

Vapor-liquid phase coexistence properties can be efficiently determined using Monte Carlo simulations in the grand canonical ensemble $\{\mu, V, T\}$ and a post-processing step using the histogram reweighting technique. A detailed overview of the simulation technique is given by Hemmen et al[42] and we only briefly review the main aspects of this method.

In the grand canonical ensemble the excess chemical potential μ, volume V and temperature T are defined variables, whereas the molecule number N and the energy E are fluctuating quantities. To sample the probability distribution $P(N)$ a transition matrix scheme[54,55] is applied. On the fly a bias potential is determined from the transition matrix to sample the N-space evenly. A parallelized simulation approach is obtained by splitting the N-space in windows of defined width ΔN, where each window can be calculated in an individual simulation in parallel. For pure components we use a width of $\Delta N = 10$ for moderate densities and $\Delta N = 5$ for high densities. In binary mixtures at given Temperature T the $\boldsymbol{N} = (N_1, N_2)$-space is divided into windows of $\Delta N_1 \times \Delta N_2 = 10 \times 10$. Suitable

conditions of the chemical potential μ and the temperature T for each N-window are estimated with the PC-SAFT[56] equation of state prior the simulation. The phase equilibrium properties are determined as a post processing step by iterating the chemical potential μ using the histogram reweighting technique to obtain the probability distribution $P(N)$ at other conditions.[57–60]

For substances described with a classical force field we use simulation boxes with a volume of $V = 33000\,\text{Å}^3$ for pure components and $V = 44000\,\text{Å}^3$ or $V = 30000\,\text{Å}^3$ for mixtures. Simulations for mixtures and pure components with a window of $\Delta N = 10$ are carried out with an equilibration period of 10 million steps and a production period of 50 million steps. In windows with $\Delta N = 5$ we use 15 million equilibration steps and 25 million production steps. The MC moves used in the simulations are molecule insertion 15%, molecule deletion 15%, partial molecule reconfiguration (regrow) 10%, translational displacement 30% and rotation 30% for a single molecule, respectively.

The interactions of polarizable force fields are not pairwise additive. Therefore the multiparticle move method[61] is used to sample the phase space efficiently. In this method all molecules in the systems were either displaced or rotated simultaneously. Because of the efficient sampling, the probabilities of different MC moves were set to 15% for multiparticle translation, 15% for multiparticle rotation, 35% for insertion, and 35% for deletion. Simulations with polarizable force fields used 1 million steps for equilibration and 5 million steps for production in a simulation box volume of $V^* = {}^{V}/_{\sigma^3} = 512$.

Analytical tail-corrections[40,62] are used for the Mie potential beyond a spherical cutoff radius of $R_c = 14\,\text{Å}$, except for the polarizable Stockmayer fluid where a cutoff radius of $R_c^* = 4$ is used. A configurational bias (CBMC) scheme is applied[63,64] to ensure sufficient statistic for insertion, deletion and reconfiguration. The number of CBMC-trial steps for insertions or deletions of an interaction site are increased (up to 8) for higher densities (see Supporting Information [Appendix B]). If the Ewald summation is employed to calculate the electrostatic potential, a maximum index of $k_{max} = 9$ in the Fourier space expansion and a damping factor of $\kappa = 7,59/L$ for a cubic box length of L is used[40]. For our simulations this Ewald-parametrization was found to be reliable, so that more conservative parameter sets gave non-distinguishable results within our statistical uncertainties.

The position of the shell charges of the polarizable sites were calculated self consistently at every MC step using the following iteration scheme[65]

$$\boldsymbol{r}_{D,i}(n) = \frac{\boldsymbol{F}_{D,i}(n-1)}{k_D} \tag{3.20}$$

where $\boldsymbol{r}_{D,i}(n)$ is the position of the shell charge i in the n'th step of the iteration and $\boldsymbol{F}_{D,i}(n-1)$ is the force acting on the shell charge. As convergence criterion

$$\max_{i=1\ldots N} |\boldsymbol{r}^*_{D,i}(n) - \boldsymbol{r}^*_{D,i}(n-1)| < 2.86 \cdot 10^{-4} \tag{3.21}$$

is used. (The odd value of the convergence criterion of $2.86 \cdot 10^{-4}$ enters because our calculations for other fluids are performed in Angstrom-units, rather than in dimensionless units).

The relative dielectric constant ϵ_r is calculated in NVT ensemble simulations from fluctuations in the net dipole moment $\boldsymbol{M} = \sum_i \boldsymbol{\mu}_i$ according to[66,67]

$$\epsilon_r = 1 + \frac{\langle \boldsymbol{M}^2 \rangle - \langle \boldsymbol{M} \rangle^2}{3\epsilon_0 V k_B T} \tag{3.22}$$

where k_B is the Boltzmann constant. Using the Ewald summation for calculating the electrostatic interactions usually requires a correction to the relative dielectric constant. In our test case conditions this factor vanishes. For shifted force methods Izvekov et al.[68] showed, that no correction is necessary. The dielectric constant is a very slowly decaying property, therefore, 50 million steps are used for equilibration and 200 million steps for production.

3.2.3 Molecular Dynamics Simulations

Dynamic properties were obtained by a combination of Monte Carlo and molecular dynamics simulations. In order to calculate the self diffusion coefficient and the shear viscosity at given temperature T and density $\rho = N/V$ the simulations are carried out in an NVT ensemble (i.e. constant number of particles N ,volume V and temperature T) with 500 molecules in the cubic simulation box. As an initial phase for calculating transport properties, we conduct a MC run, where the configurational space of the system is equilibrated in 5 million steps. The MC moves are divided in 40% translational displacement, 40% rotation and 20% partial molecule reconfiguration (regrow). After reaching the assigned number of MC-equilibration steps, an average energy $\langle E \rangle$ is calculated during $5 \cdot 10^5$ MC steps. Then the MC simulation proceeds until an instantaneous energy of the system is almost equal to the average energy, with $\left(E(r^N) - \langle E \rangle\right) / E(r^N) < 10^{-3}$. This approach has the advantage, that a representative configuration is swiftly achieved and a subsequent MD run can be conducted with a short MD-equilibration phase and a very weak thermostat coupling. For the MD run, each molecule is assigned with an initial velocity according to a Maxwell velocity distribution at the temperature T of the system. A Berendsen thermostat[69] is used to control the constant temperature T. Dynamic properties are calculated in a production period of 2 ns using a velocity Verlet algorithm with a time step of 1.5 fs.

The self diffusion coefficient D is calculated using the Green-Kubo relation[70]

$$D = \frac{1}{3}\int_0^\infty \langle v(\tau_0+\tau)v(\tau_0)\rangle \mathrm{d}\tau \tag{3.23}$$

with the auto correlation function of the velocities $\langle v(\tau_0+\tau)v(\tau)\rangle$ which is sampled every time step τ. For the shear viscosity η the Green Kubo relation considers the auto-correlation of elements of the pressure tensor P_{xy}, as

$$\eta = \frac{V}{k_B T}\int_0^\infty \langle P_{xy}(\tau)P_{xy}(0)\rangle \mathrm{d}\tau \tag{3.24}$$

To achieve a higher efficiency and accuracy a time decomposition method[71] is used. Analytical tail corrections and the parameters of the Ewald summation within the MD simulations are the same as summarized in the preceding section on Monte Carlo sampling.

3.3 Results and Discussion

In order to assess the modified Wolf summation, we compare results of this method to results from the Ewald summation. The Ewald approach serves as a reference because it is exact in the limit of a large cutoff radius and large numbers of Fourier series index-vectors. As a consequence, error formulae exist for cutoff errors in the Ewald approach, which makes the Ewald summation unambiguous as a reference method.
We first consider deviations of the modified Wolf summation for calculated electrostatic energies and forces. Subsequently we investigate vapor-liquid equilibria, because equilibrium properties are particularly sensitive towards (systematic) errors of the computational methods and lastly we analyse how well transport properties are calculated with the proposed modified Wolf summation method. An assessment of energy conservation is given in the Supporting Information [Appendix B].

3.3.1 Correlation coefficients

In order to assess the modified Wolf summation we regard electrostatic energies and forces. A sensitive and relevant measure for the energy as determined from the modified shifted force Wolf summation are energy differences ΔE between two Monte Carlo steps calculated with the Wolf summation and the Ewald summation as 'reference'. With these energy differences the correlation coefficient

$$CORR(\Delta E) = \frac{\sum_{i=1}^{S}\left(\Delta E_i^{\mathrm{Wolf}} - \langle \Delta E^{\mathrm{Wolf}}\rangle\right)\left(\Delta E_i^{\mathrm{Ewald}} - \langle \Delta E^{\mathrm{Ewald}}\rangle\right)}{\sqrt{\sum_{i=1}^{S}\left(\Delta E_i^{\mathrm{Wolf}} - \langle \Delta E^{\mathrm{Wolf}}\rangle\right)^2 \sum_{i=1}^{S}\left(\Delta E_i^{\mathrm{Ewald}} - \langle \Delta E^{\mathrm{Ewald}}\rangle\right)^2}} \tag{3.25}$$

is estimated over S samples. If the correlation coefficient is equal to 1 the energy differences of the Wolf summation are captured indistinguishable from the Ewald summation. To assess the accuracy of the forces, the magnitude and the direction of the electrostatic force vector on each site in the system is analysed. The magnitude of the force vector is also evaluated with a correlation coefficient $CORR(F)$. We define correlation coefficient $CORR(F)$ analogous to eq. 3.25, but with the magnitude of the force vectors $|\boldsymbol{F}_j|$ of each site j, instead of energy differences ΔE. The direction of the force vectors is measured by calculating the angle Φ between the vectors from the Wolf and Ewald summation

$$\cos(\Phi) = \frac{\boldsymbol{F}_j^{\text{Wolf}} \cdot \boldsymbol{F}_j^{\text{Ewald}}}{|\boldsymbol{F}_j^{\text{Wolf}}| \cdot |\boldsymbol{F}_j^{\text{Ewald}}|} \tag{3.26}$$

and evaluating the distribution. Prior to sampling the quantities $CORR(\Delta E)$, $CORR(F)$, and $\cos(\Phi)$ for a number of 10^4 samples, the optimal damping parameter α was determined (for a certain window of molecule numbers).

The correlation coefficients $CORR(\Delta E)$ of the energy differences and $CORR(F)$ of the magnitude of the force vectors are shown in Fig. 3.2 and 3.3 for varying molecule numbers N. Two substances, namely dimethyl ether and acetone, are thereby considered. In all cases the modified shifted force method gives correlation coefficients closer to unity, which means closer to the behaviour of the Ewald summation and thus provides considerably improved results compared to the original method[17]. Figures 3.2 and 3.3 also show that the observables (ΔE and $|\boldsymbol{F}_j|$) have lower fluctuations for the modified shifted force Wolf method compared with the original method, as indicated by the standard deviations given to a few values of N.

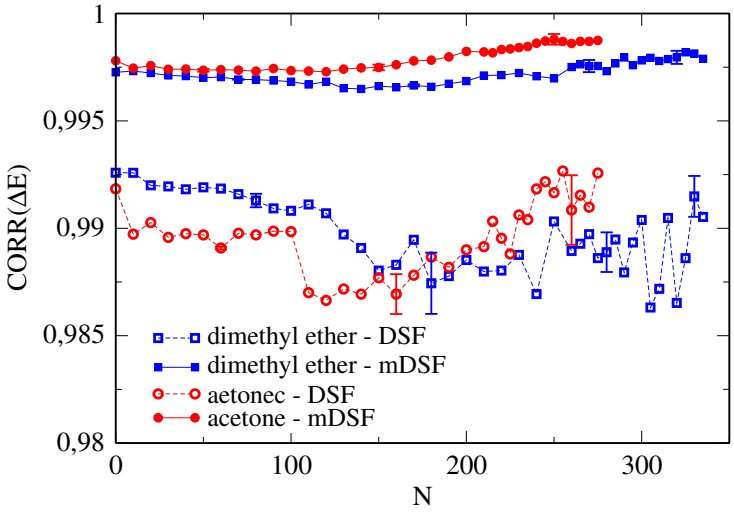

Figure 3.2: Correlations coefficients of energy differences between two Monte Carlo steps ΔE for damped shifted force method (DSF) and the modified damped shifted force method (mDSF) in a dimethyl ether and acetone system ($V = 33000\,\text{Å}^3$, $R_c = 16\,\text{Å}$, $\beta = 0.25\,\text{Å}^{-1}$).

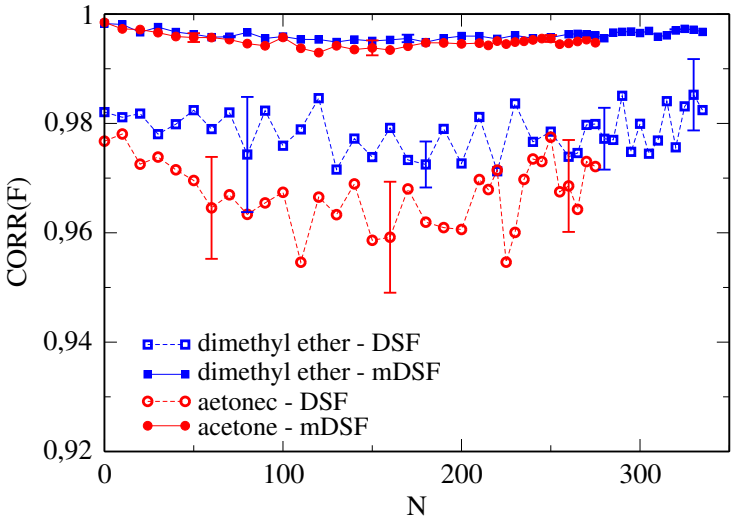

Figure 3.3: Correlations coefficients of the magnitude of the force vectors $|\boldsymbol{F}_j|$ for damped shifted force method (DSF) and the modified damped shifted force method (mDSF) in a dimethyl ether and acetone system ($V = 33000\,\text{Å}^3$, $R_c = 16\,\text{Å}$, $\beta = 0.25\,\text{Å}^{-1}$).

The normalized distribution $P(\Phi)$ of angles Φ between force vectors of the modified and the original shifted force methods and the Ewald summation are shown in Fig. 3.4. For low as well as for high densities the width of the distribution is more narrow around zero for the modified shifted force Wolf method compared to the original shifted force method. The proposed modification of the shifted force approach thus improves the direction of the force vectors. Generally, the direction of the force vectors as calculated from both Wolf summation methods has lower deviations from the reference Ewald values for high densities, than for low densities, which is in accordance with intuition because of the low number of molecules within the cutoff sphere for low densities.

3.3.2 VLE calculations

Vapor-liquid phase equilibrium properties of pure components are calculated for dimethyl ether, methanol, acetone and SPC/E water using a classical non-polarizable force field. Furthermore, we investigate a polarizable Stockmayer fluid. Simulations were performed applying the Ewald summation, the modified shifted force Wolf approach, as well as the original shifted force Wolf method. As observables of the vapor-liquid equilibrium properties we consider coexistence densities, ρ^{L} and ρ^{V}, and vapor pressures, p^{sat}, and for these observables $P \in \left\{p^{\mathrm{sat}},\ \rho^{\mathrm{L}},\ \rho^{\mathrm{V}}\right\}$ we discuss relative deviations of results of both Wolf methods from the Ewald summation (seen as reference), defined as

$$ERR = \frac{P^{\mathrm{Wolf}} - P^{\mathrm{Ewald}}}{P^{\mathrm{Ewald}}} \tag{3.27}$$

We determine properties P as the mean average of results from three separate simula-

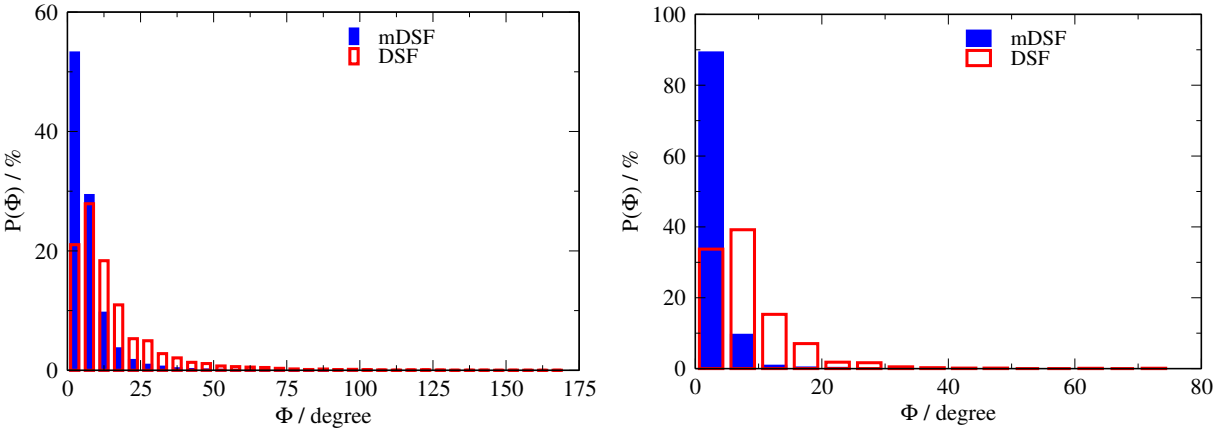

Figure 3.4: Probability distribution for errors in the direction of molecular force vectors: Normalized distribution $P(\Phi)$ of angles Φ between force vectors from the modified damped shifted force method (mDSF) and the damped shifted force method (DSF) towards force vectors from the Ewald summation. A perfect result would lead to a single bar (100%) for the angle bin at $\Phi = 0$. Diagram (a): dimethyl ether at rather low density, with $\Delta N = 50 - 60$. Diagram (b) acetone at liquid-like density, with $\Delta N = 250 - 255$ molecules. Both systems with $V = 33000\,\text{Å}^3$, $R_c = 16\,\text{Å}$, $\beta = 0.25\,\text{Å}^{-1}$.

tions. The calculation of the standard deviations for the relative deviations is explained elsewhere[38] [Chapter 2].

Fig. 3.5 displays the relative deviations of the equilibrium properties for all four substances. The proposed modified shifted force Wolf method, in all cases, leads to markedly lower deviations in vapor pressure and in coexisting densities than the original shifted force method. All deviations of the modified method are, for the majority of all considered temperatures, well below 1%. The mean absolute average deviation for the entire range of considered temperatures and averaged over all 4 substances is 0.15% for vapor pressure and 0.17% and 0.30% for liquid and vapor densities, respectively. The original shifted force approach, in contrast gives values of 8.05%, 0.32% and 8.70% for p^{sat}, ρ^{L}, and ρ^{V}, respectively. The range of deviations observed for the original shifted force Wolf method are in agreement to results of Kolafa et al.[37], who studied water with the TIP4P/2005 model[72]. We further note, that, unexpectedly, the modified shifted force approach described in this work leads to better results than the modified Wolf summation without a force-shifting scheme presented in our earlier work[38] [Chapter 2].

Determining phase equilibria of polarizable force fields from Monte Carlo techniques is computationally rather demanding. The Wolf method is in these cases particularly beneficial. Fig. 3.6 presents deviations of a polarizable Stockmayer fluid. All deviations of the modified shifted force method are lower than 1% and thus significant lower than the deviations of the original shifted force method.

Furthermore, two non-polarizable mixtures are investigated. The vapor-liquid phase equilibrium of a acetone/nitrogen mixture at a temperature of 480 K and a n-pentane/nitrogen

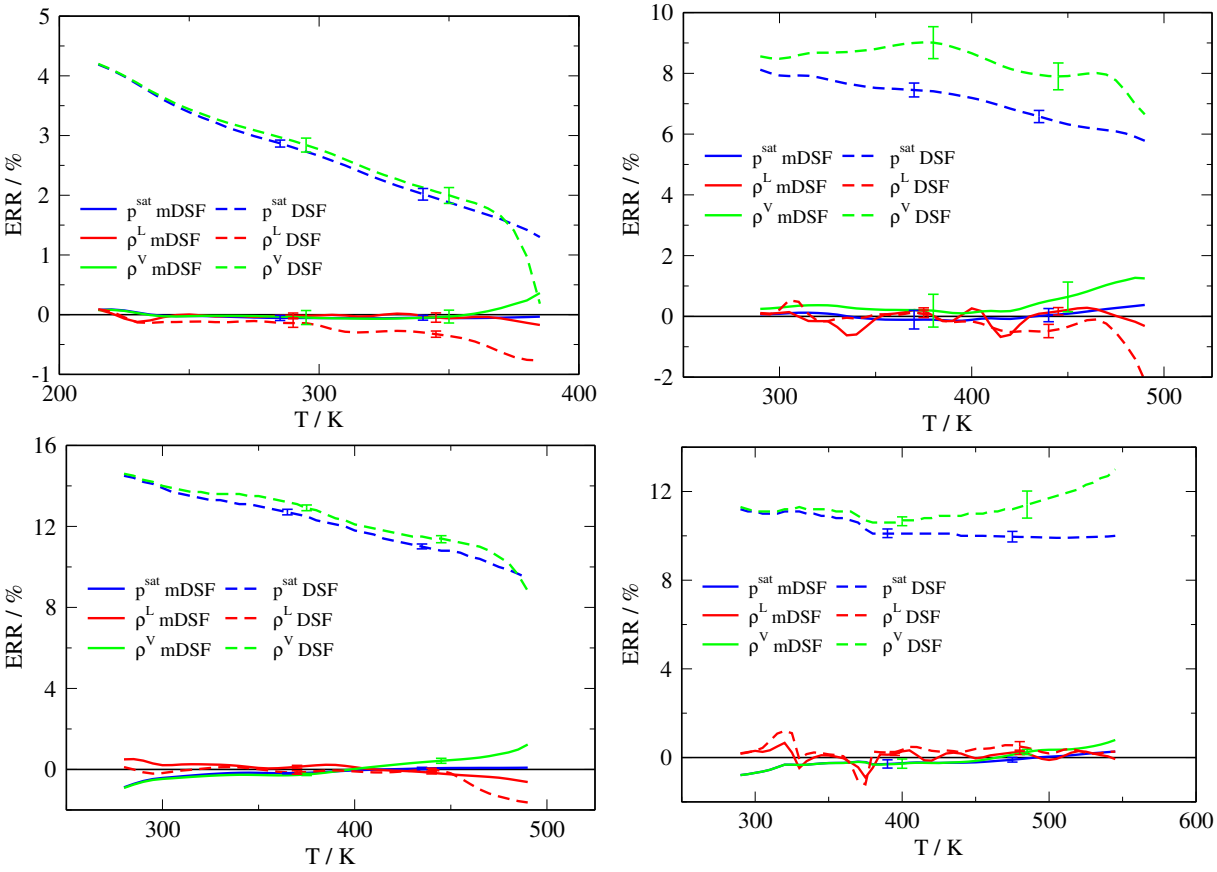

Figure 3.5: Relative deviation of vapor liquid equilibrium properties (vapor pressure p^{sat}, coexisting liquid and vapor density ρ^{L}, ρ^{V}) over temperature T for a dimethyl ether system (top left), methanol system (top right), acetone system (bottom left) and SPC/E water system (bottom right) (non-polarizable force fields) with $V = 33000\,\text{Å}^3$ and $R_c = 14\,\text{Å}$. The continuous lines represent the modified damped shifted force method (mDSF) with $\beta = 0.3\,\text{Å}^{-1}$ and the dashed lines represent the damped shifted force method (DSF).

mixture at 422.7 K are shown on the left of Fig. 3.7. On the right the relative deviations of the phase coexistence densities are shown. The agreement of the phase equilibrium of the modified shifted force method and the Ewald summation is good and the relative deviations of the densities is always lower than 1%.

3.3.3 Dynamic Properties

Dynamic properties, like the self diffusion coefficient and the shear viscosity, are meaningful for assessing the description of forces within molecular dynamic simulations. Fig. 3.8 shows the viscosity of acetone at one state point, as obtained from three methods for the electrostatic energies. Both, the modified shifted force method and the original shifted force Wolf summation are in good agreement with the result obtained using the Ewald summation. All differences are well within the statistical error of the simulation results. Further results for another state point of acetone and results for dimethyl ether at two

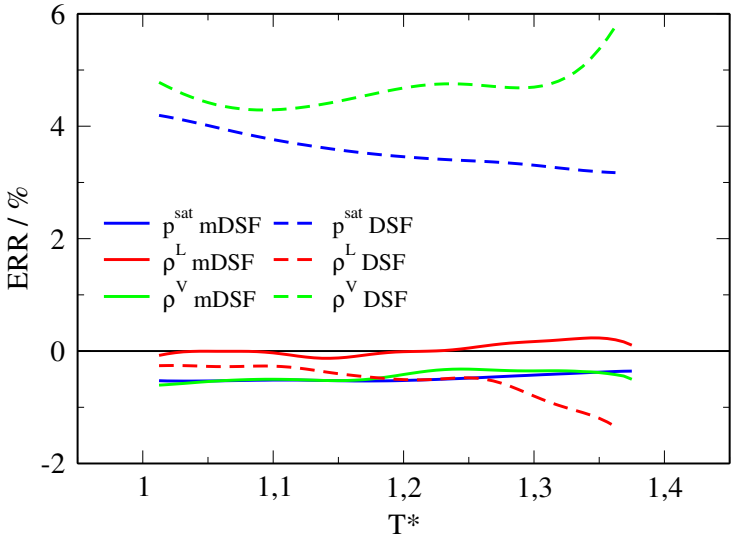

Figure 3.6: Polarizable Stockmayer fluid: Relative deviation of vapor liquid equilibrium properties (vapor pressure $p^{*,\mathrm{sat}}$, coexisting liquid and vapor density $\rho^{*,\mathrm{L}}$, $\rho^{*,\mathrm{V}}$) for varying reduced temperature $T^* = {}^{T\cdot k_B}/_{\epsilon}$ for a fluid with permanent dipole moment $|\boldsymbol{\mu}^*| = 1.0$ and polarizability $\alpha_D^* = 0.03$. Results for $V^* = 512$ and $R_c^* = 4$. The continuous lines represent the modified damped shifted force method (mDSF) with $\beta^* = 1.05$ and the dashed lines represent the damped shifted force method (DSF).

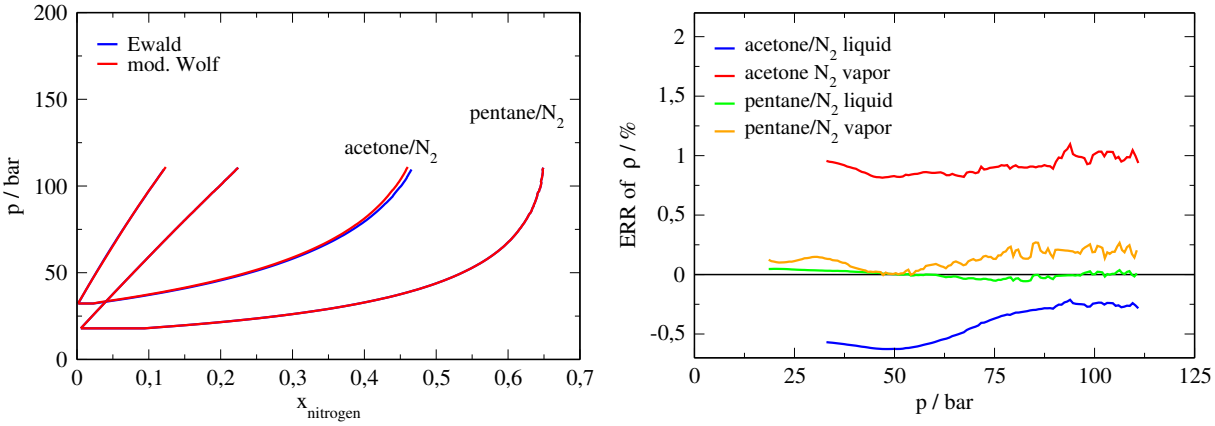

Figure 3.7: Vapor-liquid equlibrium (left) and relative deviations of coexisting densities (right) of a acetone/nitrogen mixture at $T = 480\,\mathrm{K}$ ($V = 44000\,\mathrm{Å}^3$, $R_c = 14\,\mathrm{Å}$, $\beta = 0.3\,\mathrm{Å}^{-1}$) and a n-pentane/nitrogen mixture at $T = 422.7\,\mathrm{K}$ ($V = 30000\,\mathrm{Å}^3$, $R_c = 14\,\mathrm{Å}$, $\beta = 0.3\,\mathrm{Å}^{-1}$).

states are summarized in Table 3.1. Self diffusion coefficients at the same state points are compared in Table 3.2. For all examples we find both shifted force Wolf methods in good agreement to results obtained with the Ewald summation. The good agreement of the original shifted force method with the Ewald summation for dynamic properties (in contrast to phase equilibrium properties) might be due to the fact that we determined dynamic properties in a closed ensemble, i.e. without fluctuating molecule numbers.

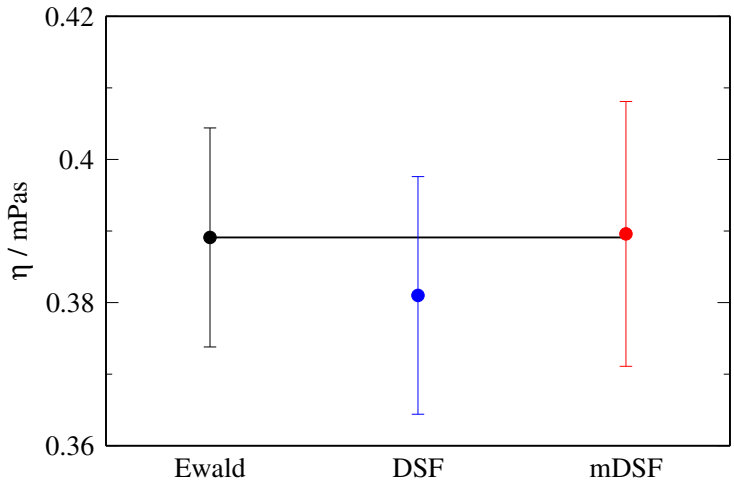

Figure 3.8: Shear viscosity η for acetone at $\rho = 784.66\,\mathrm{kg/m^3}$ and $T = 298.14\,\mathrm{K}$ calculated with the Ewald, damped shifted force (DSF) and modified damped shifted force (mDSF) method ($N = 500$, $R_c = 14\,\text{Å}$, $\beta = 0.3\,\text{Å}^{-1}$).

Table 3.1: Shear viscosities η calculated with the Ewald, damped shifted force (DSF) and modified damped shifted force (mDSF) method for a dimethyl ether and acetone system ($N = 500$, $R_c = 14\,\text{Å}$, $\beta = 0.3\,\text{Å}^{-1}$).

			η / mPas		
	ρ / kg/m³	T / K	Ewald	SF	mSF
dimethyl ether	590.80	353.12	0.0986 ± 0.0016	0.0964 ± 0.0017	0.0997 ± 0.0022
dimethyl ether	685.98	293.14	0.1702 ± 0.0057	0.1685 ± 0.0047	0.1685 ± 0.0049
acetone	755.68	323.14	0.2987 ± 0.0090	0.3013 ± 0.0148	0.3050 ± 0.0105
acetone	784.66	298.14	0.3891 ± 0.0153	0.3810 ± 0.0166	0.3896 ± 0.0185

Table 3.2: Self diffusion coefficients D calculated with the Ewald, damped shifted force (DSF) and modified damped shifted force (mDSF) method for a dimethyl ether and acetone system ($N = 500$, $R_c = 14\,\text{Å}$, $\beta = 0.3\,\text{Å}^{-1}$).

			D / cm²/s · 10^{-5}		
	ρ / kg/m³	T / K	Ewald	DSF	mDSF
dimethyl ether	590.80	353.12	13.7469 ± 0.1162	13.7197 ± 0.1318	13.7318 ± 0.1236
dimethyl ether	685.98	293.14	6.6818 ± 0.0866	6.7264 ± 0.1210	6.6666 ± 0.0817
acetone	755.68	323.14	3.5065 ± 0.0695	3.5548 ± 0.0729	3.5176 ± 0.0737
acetone	784.66	298.14	2.3738 ± 0.0537	2.3874 ± 0.0565	2.3574 ± 0.0630

3.3.4 Dielectric Constant

A good measure for the accuracy of an electrostatic method is the calculation of the relative dielectric constant ϵ_r. This property shows the orientational contribution to the screening behavior, which is strongly influenced by molecular forces and torques. The

relative dielectric constant is calculated for a Stockmayer fluid with a reduced permanent dipole moment of $|\boldsymbol{\mu}^*| = 1.0$. The dielectric constant for varying reduced cutoff radii R_c^* and reduced damping parameters $\alpha^* = \alpha \cdot \sigma$ are shown in Fig. 3.9. All results of the modified damped shifted force method reproduce, within the statistical errors, the values obtained from Ewald summation and from literature[73] ($\epsilon_r = 8.6 \pm 0.1$). The effect of slightly varying mDSF parameters on the dielectric constant seems to be small.

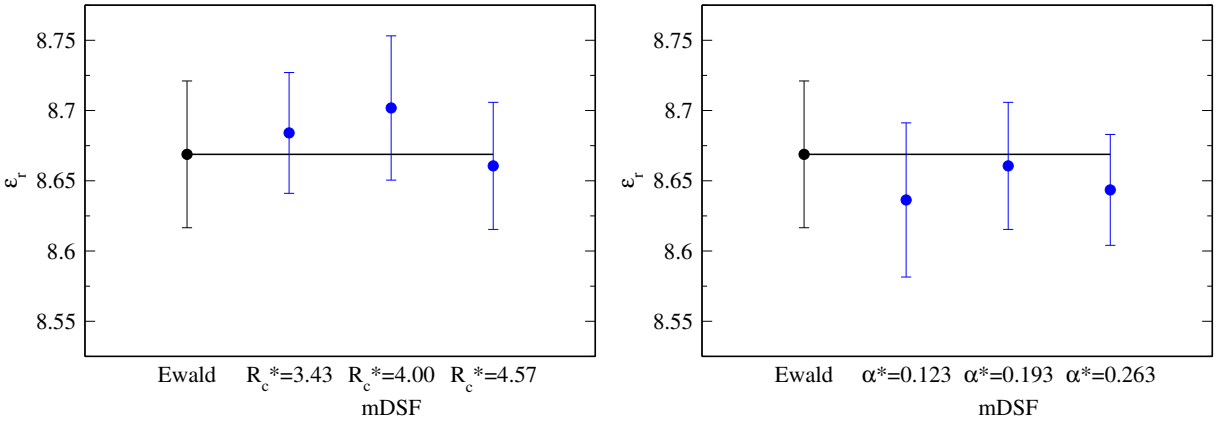

Figure 3.9: Relative dielectric constant ϵ_r for a Stockmayer fluid with permanent dipole moment $|\boldsymbol{\mu}^*| = 1$ at $T^* = 1$ and $\rho^* = 0.8$ calculated with Ewald summation and modified damped shifted force (mDSF) method. In the left figure the reduced cutoff radius R_c^* is varied and the dielectric constant is calculated using an optimal damping parameter α^* form the iterative scheme, respectively ($N = 616$, $\beta^*_{R_c^*=3.43} = 1.4$, $\beta^*_{R_c^*=4.00} = 1.05$, $\beta^*_{R_c^*=4.57} = 0.88$). In the right figure the damping parameter α^* is varied for a cutoff radius of $R_c^* = 4.57$, which has an assigned optimal damping parameter of $\alpha^{*,\mathrm{opt}}_{R_c^*=4.57} = 0.193$.

3.4 Conclusion

In this work we propose a modified shifted force approach of the Wolf summation. The modification improves both, the electrostatic energy and the forces of molecular fluids. We applied the modified method within Monte Carlo simulations in a grand canonical ensemble to calculate phase equilibrium properties for molecules described by force fields with static partial point charges and their mixtures and we considered the phase equilibrium of polarizable Stockmayer fluid. The modified shifted force method in all cases gave results in close agreement to results from the Ewald summation. For simulations with polarizable force fields an accurate description of the energy as well as the force is needed to obtain reliable results. To assess dynamic properties, we analysed self diffusion coefficient and the shear viscosity in molecular dynamics simulations. Results of the modified shifted force approach of the Wolf summation were thereby found in good agreement to results form the Ewald summation.

Bibliography

[1] Ewald, P. P. (1921) Die Berechnung optischer und elektrostatischer Gitterpotentiale. *Ann. Phys. 369*, 253–287.

[2] Hockney, R. W., and Eastwood, J. W. *Computer simulation using particles*; Taylor & Francis Group: New York, 1988.

[3] Darden, T., York, D., and Pedersen, L. (1993) Particle mesh Ewald: An N log(N) method for Ewald sums in large systems. *J. Chem. Phys. 98*, 10089–10092.

[4] Essmann, U., Perera, L., Berkowitz, M. L., Darden, T., Lee, H., and Pedersen, L. G. (1995) A smooth particle mesh Ewald method. *J. Chem. Phys. 103*, 8577–8593.

[5] Onsager, L. (1936) Electric moments of molecules in liquids. *J. Am. Chem. Soc. 58*, 1486–1493.

[6] Greengard, L., and Rokhlin, V. (1987) A fast algorithm for particle simulations. *J. Comput. Phys. 73*, 325–348.

[7] Brooks III, C. L. (1987) The influence of long-range force truncation on the thermodynamics of aqueous ionic solutions. *J. Chem. Phys. 86*, 5156–5162.

[8] Schreiber, H., and Steinhauser, O. (1992) Cutoff size does strongly influence molecular dynamics results on solvated polypeptides. *Biochemistry 31*, 5856–5860.

[9] Feller, S. E., Pastor, R. W., Rojnuckarin, A., Bogusz, S., and Brooks, B. R. (1996) Effect of electrostatic force truncation on interfacial and transport properties of water. *J. Phys. Chem. 100*, 17011–17020.

[10] Spohr, E. (1997) Effect of electrostatic boundary conditions and system size on the interfacial properties of water and aqueous solutions. *J. Chem. Phys. 107*, 6342–6348.

[11] Cisneros, G. A., Karttunen, M., Ren, P., and Sagui, C. (2014) Classical electrostatics for biomolecular simulations. *Chem. Rev. 114*, 779–814.

[12] Wolf, D., Keblinski, P., Phillpot, S., and Eggebrecht, J. (1999) Exact method for the simulation of Coulombic systems by spherically truncated, pairwise r^{-1} summation. *J. Chem. Phys. 110*, 8254–8282.

[13] Toxvaerd, S., and Dyre, J. C. (2011) Communication: Shifted forces in molecular dynamics. *J. Chem. Phys. 134*, 081102.

[14] Zahn, D., Schilling, B., and Kast, S. M. (2002) Enhancement of the Wolf damped Coulomb potential: Static, dynamic, and dielectric properties of liquid water from molecular simulation. *J. Phys. Chem. B 106*, 10725–10732.

[15] Kast, S. M., Schmidt, K. F., and Schilling, B. (2003) Integral equation theory for correcting truncation errors in molecular simulations. *Chem. Phys. Lett. 367*, 398–404.

[16] Fukuda, I., Yonezawa, Y., and Nakamura, H. (2008) Consistent molecular dynamics scheme applying the Wolf summation for calculating electrostatic interaction of particles. *J. Phys. Soc. Jpn. 77*, 114301.

[17] Fennell, C. J., and Gezelter, J. D. (2006) Is the Ewald summation still necessary? Pairwise alternatives to the accepted standard for long-range electrostatics. *J. Chem. Phys. 124*, 234104.

[18] Fukuda, I., Yonezawa, Y., and Nakamura, H. (2011) Molecular dynamics scheme for precise estimation of electrostatic interaction via zero-dipole summation principle. *J. Chem. Phys. 134*, 164107.

[19] Yonezawa, Y. (2012) A long-range electrostatic potential based on the Wolf method charge-neutral condition. *J. Chem. Phys. 136*, 244103.

[20] Fukuda, I. (2013) Zero-multipole summation method for efficiently estimating electrostatic interactions in molecular system. *J. Chem. Phys. 139*, 174107.

[21] Kale, S., and Herzfeld, J. (2011) Pairwise long-range compensation for strongly ionic systems. *J. Chem. Theory Comput. 7*, 3620–3624.

[22] McCann, B. W., and Acevedo, O. (2013) Pairwise alternatives to Ewald summation for calculating long-range electrostatics in ionic liquids. *J. Chem. Theory Comput. 9*, 944–950.

[23] Fanourgakis, G. S. (2015) An extension of Wolf's method for the treatment of electrostatic interactions: application to liquid water and aqueous solutions. *J. Phys. Chem. B 119*, 1974–1985.

[24] Brommer, P., Beck, P., Chatzopoulos, A., Gähler, F., Roth, J., and Trebin, H.-R. (2010) Direct Wolf summation of a polarizable force field for silica. *J. Chem. Phys. 132*, 194109.

[25] Lamichhane, M., Gezelter, J. D., and Newman, K. E. (2014) Real space electrostatics for multipoles. I. Development of methods. *J. Chem. Phys. 141*, 134109.

[26] Stenqvist, B., Trulsson, M., Abrikosov, A. I., and Lund, M. (2015) Direct summation of dipole-dipole interactions using the Wolf formalism. *J. Chem. Phys. 143*, 014109.

[27] Demontis, P., Spanu, S., and Suffritti, G. B. (2001) Application of the Wolf method for the evaluation of Coulombic interactions to complex condensed matter systems: aluminosilicates and water. *J. Chem. Phys. 114*, 7980–7988.

[28] Mahadevan, T., and Garofalini, S. (2007) Dissociative water potential for molecular dynamics simulations. *J. Phys. Chem. B 111*, 8919–8927.

[29] Mendoza, F. N., López-Lemus, J., Chapela, G. A., and Alejandre, J. (2008) The wolf method applied to the liquid-vapor interface of water. *J. Chem. Phys. 129*, 024706.

[30] Avendaño, C., Gil-Villegas, A., and González-Tovar, E. (2008) Computer simulation of charged hard spherocylinders. *J. Chem. Phys. 128*, 044506.

[31] Kikugawa, G., Apostolov, R., Kamiya, N., Taiji, M., Himeno, R., Nakamura, H., and Yonezawa, Y. (2009) Application of MDGRAPE-3, a special purpose board for molecular dynamics simulations, to periodic biomolecular systems. *J. Comput. Chem. 30*, 110–118.

[32] Muscatello, J., and Bresme, F. (2011) A comparison of Coulombic interaction methods in non-equilibrium studies of heat transfer in water. *J. Chem. Phys. 135*, 234111.

[33] Jiménez-Serratos, G., Avendano, C., Gil-Villegas, A., and González-Tovar, E. (2011) Computer simulation of charged hard spherocylinders at low temperatures. *Mol. Phys. 109*, 27–36.

[34] Yonezawa, Y., Fukuda, I., Kamiya, N., Shimoyama, H., and Nakamura, H. (2011) Free energy landscapes of alanine dipeptide in explicit water reproduced by the force-switching Wolf method. *J. Chem. Theory Comput. 7*, 1484–1493.

[35] Hansen, J. S., Schrøder, T. B., and Dyre, J. C. (2012) Simplistic Coulomb forces in molecular dynamics: Comparing the Wolf and shifted-force approximations. *J. Phys. Chem. B 116*, 5738–5743.

[36] Vlugt, T., Garcia-Perez, E., Dubbeldam, D., Ban, S., and Calero, S. (2008) Computing the heat of adsorption using molecular simulations: the effect of strong Coulombic interactions. *J. Chem. Theory Comput. 4*, 1107–1118.

[37] Kolafa, J., Moučka, F., and Nezbeda, I. (2008) Handling electrostatic interactions in molecular simulations: A systematic study. *Collect. Czech. Chem. Commun. 73*, 481–506.

[38] Waibel, C., and Gross, J. (2018) Modification of the Wolf Method and Evaluation for Molecular Simulation of Vapor–Liquid Equilibria. *J. Chem. Theory Comput. 14*, 2198–2206.

[39] Hens, R., and Vlugt, T. J. (2018) Molecular Simulation of Vapor–Liquid Equilibria Using the Wolf Method for Electrostatic Interactions. *J. Chem. Eng. Data 63*, 1096–1102.

[40] Allen, M. P., and Tildesley, D. J. *Computer simulation of liquids*; Oxford University Press: New York, 1987.

[41] Shah, J. K., Marin-Rimoldi, E., Mullen, R. G., Keene, B. P., Khan, S., Paluch, A. S., Rai, N., Romanielo, L. L., Rosch, T. W., Yoo, B., and Maginn, E. J. (2017) Cassandra: An open source Monte Carlo package for molecular simulation. *J. Comput. Chem. 38*, 1727–1739.

[42] Hemmen, A., Panagiotopoulos, A. Z., and Gross, J. (2015) Grand Canonical Monte Carlo Simulations Guided by an Analytic Equation of State - Transferable Anisotropic Mie Potentials for Ethers. *J. Phys. Chem. B 119*, 7087–7099.

[43] Hemmen, A., and Gross, J. (2015) Transferable Anisotropic United-Atom Force Field Based on the Mie Potential for Phase Equilibrium Calculations: n-Alkanes and n-Olefins. *J. Phys. Chem. B 119*, 11695–11707.

[44] Weidler, D., and Gross, J. (2016) Transferable Anisotropic United-Atom Force Field Based on the Mie Potential for Phase Equilibria: Aldehydes, Ketones, and Small Cyclic Alkanes. *Ind. Eng. Chem. Res. 55*, 12123–12132.

[45] Waibel, C., Stierle, R., and Gross, J. (2018) Transferability of cross-interaction pair potentials: Vapor-liquid phase equilibria of n-alkane/nitrogen mixtures using the TAMie force field. *Fluid Phase Equilib. 456*, 124–130.

[46] Schnabel, T., Srivastava, A., Vrabec, J., and Hasse, H. (2007) Hydrogen bonding of methanol in supercritical CO2: comparison between 1H NMR spectroscopic data and molecular simulation results. *J. Phys. Chem. B 111*, 9871–9878.

[47] Berendsen, H. J. C., Grigera, J. R., and Straatsma, T. P. (1987) The missing term in effective pair potentials. *J. Phys. Chem. 91*, 6269–6271.

[48] Lorentz, H. (1881) Ueber die Anwendung des Satzes vom Virial in der kinetischen Theorie der Gase. *Ann. Phys. 248*, 127–136.

[49] Berthelot, D. (1898) Sur le mélange des gaz. *Compt. Rendus 126*, 1703–1706.

[50] Potoff, J. J., and Bernard-Brunel, D. A. (2009) Mie potentials for phase equilibria calculations: Application to alkanes and perfluoroalkanes. *J. Phys. Chem. B 113*, 14725–14731.

[51] Kiyohara, K., Gubbins, K. E., and Panagiotopoulos, A. Z. (1997) Phase coexistence properties of polarizable Stockmayer fluids. *J. Chem. Phys. 106*, 3338–3347.

[52] Lamoureux, G., and Roux, B. (2003) Modeling induced polarization with classical Drude oscillators: Theory and molecular dynamics simulation algorithm. *J. Chem. Phys. 119*, 3025–3039.

[53] Drunsel, F., Zmpitas, W., and Gross, J. (2014) A new perturbation theory for electrolyte solutions. *J. Chem. Phys. 141*, 054103.

[54] Errington, J. R. (2003) Direct calculation of liquid–vapor phase equilibria from transition matrix Monte Carlo simulation. *J. Chem. Phys. 118*, 9915–9925.

[55] Paluch, A. S., Shen, V. K., and Errington, J. R. (2008) Comparing the use of Gibbs ensemble and grand-canonical transition-matrix Monte Carlo methods to determine phase equilibria. *Ind. Eng. Chem. Res. 47*, 4533–4541.

[56] Gross, J., and Sadowski, G. (2001) Perturbed-chain SAFT: An equation of state based on a perturbation theory for chain molecules. *Ind. Eng. Chem. Res. 40*, 1244–1260.

[57] Ferrenberg, A. M., and Swendsen, R. H. (1989) Optimized monte carlo data analysis. *Phys. Rev. Lett. 63*, 1195.

[58] Wilding, N. B. (1995) Critical-point and coexistence-curve properties of the Lennard-Jones fluid: a finite-size scaling study. *Phys. Rev. E 52*, 602.

[59] Panagiotopoulos, A. Z., Wong, V., and Floriano, M. A. (1998) Phase equilibria of lattice polymers from histogram reweighting Monte Carlo simulations. *Macromolecules 31*, 912–918.

[60] Potoff, J. J., and Panagiotopoulos, A. Z. (1998) Critical point and phase behavior of the pure fluid and a Lennard-Jones mixture. *J. Chem. Phys. 109*, 10914–10920.

[61] Moučka, F., Nezbeda, I., and Smith, W. R. (2013) Computationally efficient Monte Carlo simulations for polarisable models: multi-particle move method for water and aqueous electrolytes. *Mol. Simulat. 39*, 1125–1134.

[62] Smit, B. (1992) Phase diagrams of Lennard-Jones fluids. *J. Chem. Phys. 96*, 8639–8640.

[63] Siepmann, J. I., and Frenkel, D. (1992) Configurational bias Monte Carlo: a new sampling scheme for flexible chains. *Mol. Phys. 75*, 59–70.

[64] Frenkel, D., Mooij, G., and Smit, B. (1992) Novel scheme to study structural and thermal properties of continuously deformable molecules. *J. Phys. Condens. Matter 4*, 3053.

[65] Jiang, H., Moultos, O. A., Economou, I. G., and Panagiotopoulos, A. Z. (2016) Gaussian-charge polarizable and nonpolarizable models for CO2. *J. Phys. Chem. B 120*, 984–994.

[66] Neumann, M. (1983) Dipole moment fluctuation formulas in computer simulations of polar systems. *Mol. Phys. 50*, 841–858.

[67] Neumann, M., and Steinhauser, O. (1983) On the calculation of the dielectric constant using the Ewald-Kornfeld tensor. *Chem. Phys. Lett. 95*, 417–422.

[68] Izvekov, S., Swanson, J. M., and Voth, G. A. (2008) Coarse-graining in interaction space: A systematic approach for replacing long-range electrostatics with short-range potentials. *J. Phys. Chem. B 112*, 4711–4724.

[69] Berendsen, H. J., Postma, J. v., van Gunsteren, W. F., DiNola, A., and Haak, J. (1984) Molecular dynamics with coupling to an external bath. *J. Chem. Phys. 81*, 3684–3690.

[70] McQuarrie, D. A. *Statistical Mechanics*; Univ. Science Books: Sausalito, Calif., 2000.

[71] Zhang, Y., Otani, A., and Maginn, E. J. (2015) Reliable viscosity calculation from equilibrium molecular dynamics simulations: a time decomposition method. *J. Chem. Theory Comput. 11*, 3537–3546.

[72] Abascal, J. L., and Vega, C. (2005) A general purpose model for the condensed phases of water: TIP4P/2005. *J. Chem. Phys. 123*, 234505.

[73] Gray, C., Sainger, Y., Joslin, C., Cummings, P., and Goldman, S. (1986) Computer simulation of dipolar fluids. Dependence of the dielectric constant on system size: A comparative study of Ewald sum and reaction field approaches. *J. Chem. Phys. 85*, 1502–1504.

Chapter 4

Transferability of Cross-Interaction Pair Potentials: Vapor-Liquid Phase Equilibria of n-Alkane/Nitrogen Mixtures Using the TAMie Force Field

The content of this chapter is a literal quote of the publication

Waibel, Stierle, Gross, Fluid Phase Equilibria, 456, 2018, 124-130.

In comparison to the published work, the abstract is here omitted. Additions or deletions compared to the published work are marked with angular brackets.

Transferable force fields used in molecular simulations are appealing for engineering applications because they allow predicting physical properties in the absence of experimental data. Transferable force fields decompose the total interaction of molecules into van der Waals contributions, usually described as pair-wise interactions only, and static electrostatic interactions, commonly characterized by fixed (non-polarizable) partial point charges. One speaks of a united-atom model, when the van der Waals contribution of hydrogen atoms are considered together with larger neighboring atoms. The van der Waals interaction of a methyl-group (-CH_3) for example, is then lumped into one effective van der Waals interaction site.
What is needed for predicting physical properties of mixtures with transferable force fields are cross-wise van der Waals potentials. These cross-wise potentials should be determined by quantum mechanical calculations. When a unique functional form of potential is assumed for the van der Waals interactions, the cross-wise potential is deter-

mined by scalar-valued cross-coefficients (say $\epsilon_{\alpha\beta}$ and $\sigma_{\alpha\beta}$). Simple combining rules, like the Berthelot-Lorentz combining rules[1,2], can be assumed for these coefficients. In fact, transferable force fields of united-atom groups are adjusted to pure components assuming the Berthelot-Lorentz rules or other combining rules to hold.

In simulations of mixtures it is then apparent to also assume combing rules for defining the cross-interactions between unlike van der Waals interaction sites of different molecules. The Berthelot-Lorentz combining rules for the interactions of unlike molecules lead to good predictions for some[3–7], but not generally for all mixtures, as several studies show[8–11]. In fact, considering the severe assumptions one has to make to derive combining rules, such as the Berthelot-Lorentz rules, it is somewhat surprising that they are at all valuable for practical applications.

Several studies analyze combining rules for the van der Waals cross-coefficients ($\epsilon_{\alpha\beta}$ and $\sigma_{\alpha\beta}$) with focus on phase equilibrium properties and these studies arrive at different conclusions[3,8,10,12,13]. Potoff et al. study various mixtures and find the Kong combing rule[14] to yield better predictions for some mixtures compared with the Berthelot-Lorentz combining rules, whereas the Berthelot-Lorentz rule is to be preferred for other mixtures. Delhommelle and Millié[8] clearly articulate a recommendation for the Kong combining rule and point out deficiencies in the description of experimental mixture data for the Berthelot-Lorentz rule. These authors considered simple binary mixtures for more unambiguity. The finding is reemphasized in a subsequent study of Desgranges and Delhommelle[15]. A study of Schnabel et al.[10] compares eleven combining rule considering 44 binary mixtures. The authors show that no combing rule outperforms the Berthelot-Lorentz rule significantly. The study shows that the Lorentz rule (arithmetic combining rule for the van der Waals size parameter $\sigma_{\alpha\beta}$) gives results in good agreement to experimental mixture densities. That is a convincing and conclusive finding, because Rouha and Nezbeda[12] as well as Boda and Henderson[13] point out that mixture density data are very sensitive towards the cross-size parameter $\sigma_{\alpha\beta}$ (as compared to $\epsilon_{\alpha\beta}$). Schnabel et al. further show that good results for phase equilibria of mixture require pairwise adjusted cross-energy parameters $\epsilon_{\alpha\beta}$[10].

When phase equilibria are targeted, it is intuitive to use binary phase equilibrium data for determining the cross-energy parameter[5,16–25]. Other choices, such as excess quantities (e.g. excess Gibbs energies), however, have also been proposed as suitable observables for adjusting cross-energy parameters[26–28]. Furthermore, second virial coefficients are regarded suitable for identifying cross-wise parameters[29,30]. The path is appealing, because second virial coefficients are well measurable or alternatively, it is often possible to use high-level quantum mechanical calculations for only single pairs of molecules. As a disadvantage, however, most force fields are not able to reproduce pure component virial coefficients, because emphasis is laid on liquid states in parameterizing effective

(non-polarizable) charges and effective pair-wise van der Waals potentials.

Usually the cross-energy parameter is written as a re-scaled Berthelot rule, $\epsilon_{\alpha\beta} = \sqrt{\epsilon_{\alpha\alpha}\epsilon_{\beta\beta}} \cdot \xi_{ij}$, where i and j indicate species and α and β are for (united-)atom groups of these species, respectively. This form of writing the cross-energy on the one hand shows that the geometric Berthelot rule is already a good estimate that is modified with an adjustable parameter ξ_{ij}. On the other hand, this form clarifies, that the correction parameter ξ_{ij} is defined for species i and j, i.e. the same correction parameter is used for all (united-)atom groups α of the molecules i and atom groups β on species j, with $i \neq j$.

The scheme of adjusting a cross-energy parameter was used to describe the vapor-liquid equilibria of different binary systems with good results[5,11,19,31,32]. Applying the so-obtained binary parameters to ternary systems with no further adjustment to ternary mixtures leads to reliable results[33,34]. Applications range from molecular simulations of humid air[34] to aqueous solutions[35], electrolytes[36], pressure effects on homogeneous nucleation[37], gas storage in geological structures[25], carbon dioxide solubility[23], to composite analysis of Saturn's moon Titan[38].

As suggested by Schnabel et al.[10], in this work we use the standard Lorentz combining rule for the size parameter and an adjustable cross-energy parameter. However, we define transferable cross-energy parameters for each (united-)atom group individually: $\epsilon_{\alpha\beta} = \sqrt{\epsilon_{\alpha\alpha}\epsilon_{\beta\beta}} \cdot (1 - \kappa_{\alpha\beta})$, with $\kappa_{\alpha\beta}$ as an adjustable parameter. This approach defines adjustable cross-energy parameters for united-atom groups of different species, as corrections to the Berthelot combining rule. We show that this approach is transferable among alkane-nitrogen mixtures and how to adjust parameters $\kappa_{\alpha\beta}$ efficiently using the Perturbed-Chain Polar Statistical Associating Fluid Theory (PCP-SAFT) equation of state[39–41].

The PCP-SAFT model is an analytical equation of state that is suitable to accelerate convergence when adjusting force field parameters to experimental data. In previous work, we used PCP-SAFT for locally approximating the actual objective function and for minimizing the objective function in the parameter-space of the force field. The objective function from the PCP-SAFT equation of state is only approximate, which is why the procedure is iterative. Once convergence is achieved, however, the analytical model does not affect the final result anymore and the problem thus converges to the true minimum. The convergence is very swift, requiring only a few molecular simulation runs for evaluating the objective function, even for multidimensional optimization problems. The method has been applied to obtaining force field parameters of pure components[7,11,42,43] and of cross-interaction parameters of mixtures[23]. The approach has not been applied to individual pairs of atoms or united-atom groups.

A different approach that is also using an analytical equation of state was proposed by Müller and Jackson together with coworkers[44,45]. Their method relies on the SAFT-γ equation of state[46] and uses parameters of the analytic model directly as force field

parameters. The procedure is therefore not iterative, but limits the force fields to coarse-grained models, where molecules are represented as tangentially bonded spherical interaction sites without electrostatic contributions. Their force-field enables fast calculations on large systems and, in case of molecular dynamics simulations, long calculation times[45]. In this study we define cross-energy parameters $\epsilon_{\alpha\beta}$ for individual (united-)atom groups, which are adjusted to experimental phase equilibrium data and investigate the transferability of these parameters. Phase equilibria of n-alkane/nitrogen mixtures are regarded as an example, whereby the cross-energy parameters $\epsilon_{\mathrm{CH_3,N}}$ and $\epsilon_{\mathrm{CH_2,N}}$ are adjusted to three mixtures (the training set) using Monte Carlo simulations in the grand canonical ensemble. The transferability of the force field is then confirmed for several n-alkane/nitrogen mixtures that were not member of the training set. The PCP-SAFT equation of state is used to make the parameter regression efficient.

4.1 Molecular Model

This work extends work on the TAMie force field[7,11,43], wherein the van der Waals energy contribution is limited to pair-wise potentials and where fixed (partial) point-charges are regarded, omitting static polarizability. According to the TAMie model, molecules are decomposed into united-atom groups, such as a methyl-group -CH_3. We thus consider a molecule i to be composed of interaction sites α that interact to the interaction sites β of molecule j, according to

$$\phi_{\alpha\beta}(r_{\alpha\beta}) = c_{\alpha\beta}\ \epsilon_{\alpha\beta}\left[\left(\frac{\sigma_{\alpha\beta}}{r_{\alpha\beta}}\right)^{n_{\alpha\beta}} - \left(\frac{\sigma_{\alpha\beta}}{r_{\alpha\beta}}\right)^{6}\right] + \frac{q_\alpha q_\beta}{4\pi\varepsilon_0\ r_{\alpha\beta}} \tag{4.1}$$

with $r_{\alpha\beta}$ as the distance between interaction site α and site β. The first term is a Mie potential, where we fixed the attractive exponent to the value 6, because this represents the leading term in the expansion of attractive (dispersive) interactions. The repulsive exponent $n_{\alpha\beta}$ is treated as an adjustable parameter, just like the energy parameter $\epsilon_{\alpha\beta}$ and the size parameter $\sigma_{\alpha\beta}$. The coefficient $c_{\alpha\beta}$ is defined to enforce a minimum value of the potential $\phi_{\alpha\beta}(r_{\min}) = -\epsilon_{\alpha\beta}$, as

$$c_{\alpha\beta} = \frac{n_{\alpha\beta}}{n_{\alpha\beta} - 6}\left(\frac{n_{\alpha\beta}}{6}\right)^{6/(n_{\alpha\beta}-6)} \tag{4.2}$$

The second term of eq. 4.1 represents the electrostatic potential between the (partial) charges q_α and q_β separated by distance $r_{\alpha\beta}$ and ε_0 denotes the dielectric constant.
Pure component parameters for charges q_α are unambiguous (as indicated by the single index for interaction site α). Pure component parameters of the van der Waals contribution are usually tabulated as values of like-like interactions, i.e. as $\epsilon_{\alpha\alpha}$ and $\sigma_{\alpha\alpha}$. To

clarify our nomenclature, we note that an interaction site α may thus either represent a united-atom group (when $\epsilon_{\alpha\alpha}$ and $\sigma_{\alpha\alpha}$ are non-zero) or a partial charge (with q_α non-zero) or both at the same time. Because a conformal approach is taken, where only one mathematical type of pair potential is considered, the task of defining a cross-potential reduces to defining cross-coefficients $\epsilon_{\alpha\beta}$ and $\sigma_{\alpha\beta}$. Formally of course, the cross-potential should be determined by quantum mechanical calculations. In practice, however, one can get a first estimate of the cross-potential by assuming combining rules, such as the Berthelot-Lorentz[1,2] rules

$$\epsilon_{\alpha\beta} = \sqrt{\epsilon_{\alpha\alpha}\,\epsilon_{\beta\beta}} \tag{4.3}$$

$$\sigma_{\alpha\beta} = \left(\sigma_{\alpha\alpha} + \sigma_{\beta\beta}\right)/2 \tag{4.4}$$

and an arithmetic combining rule[47] for the repulsive exponent

$$n_{\alpha\beta} = \left(n_{\alpha\alpha} + n_{\beta\beta}\right)/2 \tag{4.5}$$

The Berthelot-Lorentz rules can according to London's theory be derived when the same dimensionless frequency dependence of the dynamic polarizability is assumed for both interaction sites. In this work, we improve the agreement of molecular simulations to experimental data by treating the cross-energy parameter $\epsilon_{\alpha\beta}$ as adjustable. It is convenient to determine $\epsilon_{\alpha\beta}$ by introducing a correction to the Berthelot combining rule, according to

$$\epsilon_{\alpha\beta} = \sqrt{\epsilon_{\alpha\alpha}\,\epsilon_{\beta\beta}}(1 - \kappa_{\alpha\beta}) \tag{4.6}$$

with $\kappa_{\alpha\beta}$ as an adjustable parameter. This parameter defines the cross-wise pair potential between two united-atom groups, i.e. sites α and β. We have $\kappa_{\alpha\alpha} = 0$ and we further define $\kappa_{\alpha\beta} = 0$ for any pair of sites located on the same molecule i. We thus limit $\kappa_{\alpha\beta} \neq 0$ to pairs of site α of molecule i and β of molecule j with $i \neq j$. Further, $\kappa_{\alpha\beta}$ is symmetric. We then have the task of identifying the non-diagonal elements of the symmetric matrix of $\kappa_{\alpha\beta}$ elements, by simultaneously optimizing agreement of molecular simulation data to a large set of experimental data for many mixtures. In order to facilitate the cumbersome iterative adjustment of the $\kappa_{\alpha\beta}$ matrix, we make use of an analytic equation of state.

4.2 Cross-Interaction Energy Parameters estimated from PCP-SAFT Equation of State

In this section, we derive a relation between the binary correction parameter $\kappa_{\alpha\beta}$ of the TAMie force field to the binary interaction parameter k_{ij} of the PCP-SAFT equation of state. This relation will be helpful because the analytic PCP-SAFT equation of state

allows us to estimate optimal $\kappa_{\alpha\beta}$ to a large set of experimental data simultaneously for many mixtures. The procedure is iterative because the PCP-SAFT model is not perfect in predicting the outcome of molecular simulation results. The final result of the iteration, however, is not altered by the quality of the PCP-SAFT model.

Here, we re-derive a relation, that was published earlier by Schacht et al.[23]. According to the PCP-SAFT equation of state molecules are assumed as chains of spherical segments. The pure component parameters are the number $\hat{m}_i$ of spherical segments. Parameter $\hat{m}_i$ is a real number (i.e. not limited to integer values). Similar to the parameters in eq. 4.1, each segment-segment interaction is characterized by an energy parameter $\hat{\epsilon}_{ii}$ and a size parameter $\hat{\sigma}_{ii}$. As opposed to the TAMie force field, where all electrostatic interactions are captured by partial charges, in PCP-SAFT these interactions are described as associating interactions reflecting the effectively short-ranged (hydrogen bonding) interactions and as dipole-dipole or other multipolar interactions.

If the electrostatic part in PCP-SAFT and in the TAMie force field is assumed equivalent, one can for the van der Waals attraction of PCP-SAFT and of the TAMie force field write a first-order perturbation expansion of the Helmholtz energy. Setting these terms approximately equal, we get

$$\sum_i \sum_j x_i x_j \hat{m}_i \hat{m}_j \hat{\sigma}_{ij}^3 \hat{\epsilon}_{ij} \hat{I}_{ij} \approx \sum_i \sum_j x_i x_j \sum_\alpha^{K_i} \sum_\beta^{K_j} N_\alpha N_\beta \sigma_{\alpha\beta}^3 \epsilon_{\alpha\beta} I_{\alpha\beta} \tag{4.7}$$

where we formalized that index α runs over all K_i types of united-atom groups that molecule type i comprises. Further, N_α denotes the number of united-atom groups of a particular type α. For n-hexane, for example, $K_i \in \{\mathrm{CH_3}, \mathrm{CH_2}\}$ and further $N_{\mathrm{CH_3}} = 2$ and $N_{\mathrm{CH_2}} = 4$. The abbreviations $\hat{I}_{ij}$ and $I_{\alpha\beta}$ denote correlation integrals, i.e. integrals over distance vector with the dimensionless van der Waals potential multiplied by the radial distribution function as the integrand. According to the one-fluid approach, the dimensionless correlation integrals are approximately equal for a given density and temperature. This approximation is certainly more coarse for non-spherical, multi-segmented molecules as compared to mixtures of spherical fluids (of similar size parameters).

We are not interested in estimating the pure component properties, i.e. we ignore terms with $i = j$ in Eq. 4.7. Focusing instead on the cross-energy contribution we demand

$$\hat{m}_i \hat{m}_j \hat{\sigma}_{ij}^3 \hat{\epsilon}_{ij} \frac{1}{\varphi_{ij}} = \sum_\alpha^{K_i} \sum_\beta^{K_j} N_\alpha N_\beta \sigma_{\alpha\beta}^3 \epsilon_{\alpha\beta} \tag{4.8}$$

where φ_{ij} is a parameter defined to enforce equality of left and right hand expression. We use eq. 4.6 and analogously for the PCP-SAFT equation of state $\hat{\epsilon}_{ij} = \sqrt{\hat{\epsilon}_{ii}\, \hat{\epsilon}_{jj}}(1 - k_{ij})$ to

obtain

$$k_{ij} = 1 - \frac{\sum_{\alpha}^{K_i} \sum_{\beta}^{K_j} N_\alpha N_\beta \sigma_{\alpha\beta}^3 \sqrt{\epsilon_{\alpha\alpha}\, \epsilon_{\beta\beta}}(1-\kappa_{\alpha\beta})}{\hat{m}_i \hat{m}_j \hat{\sigma}_{ij}^3 \sqrt{\hat{\epsilon}_{ii}\, \hat{\epsilon}_{jj}}} \varphi_{ij} \tag{4.9}$$

This equation is the desired relation between a binary correction parameter of the PCP-SAFT model (k_{ij}) and the appropriate binary correction parameters of the TAMie force field ($\kappa_{\alpha\beta}$).

4.3 Procedure for iterating cross-energy parameters in force fields

We proceed to describe the procedure for iterating cross-energy parameters of the TAMie force field using an analytic equation of state through eq. 4.9. The procedure requires a defined training set of mixture properties, like vapor-liquid equilibria data $\{x^{\mathrm{v/l}}, p, T\}$ and a defined objective function

$$f_{\mathrm{obj}}\left(\boldsymbol{\kappa}_{\alpha\beta}\right) = \frac{1}{\sum_{k=1}^{N^{\mathrm{set}}} N_k^{\mathrm{exp}}} \sum_{k=1}^{N^{\mathrm{set}}} \sum_{n=1}^{N_k^{\mathrm{exp}}} \left[\left(x_{k,n}^{\mathrm{sim,l}}\left(\boldsymbol{\kappa}_{\alpha\beta}\right) - x_{k,n}^{\mathrm{exp,l}} \right)^2 + \left(x_{k,n}^{\mathrm{sim,v}}\left(\boldsymbol{\kappa}_{\alpha\beta}\right) - x_{k,n}^{\mathrm{exp,v}} \right)^2 \right] \tag{4.10}$$

where index k runs over all mixtures of the training set and n over all experimental data points. Superscripts l and v are for the liquid and vapor phase, respectively. The general procedure is

1. Conduct molecular simulations with an estimate for the cross-energy parameter. Usually one will initially use $\kappa_{\alpha\beta} = 0$.

2. For every mixture of the training set: adjust φ_{ij} by minimizing the deviation of the PCP-SAFT model to the results of the molecular simulation data. Note, that all quantities other than φ_{ij} are fully determined in eq. 4.9.

3. Now treat the appropriate elements of the $\kappa_{\alpha\beta}$-matrix as degrees of freedom in eq. 4.9. Determine $\kappa_{\alpha\beta}$-elements by simultaneously minimizing the deviations of PCP-SAFT to experimental data.

4. Conduct molecular simulations with the new estimates of $\kappa_{\alpha\beta}$ values.

5. If convergence criterion is not met, return to point 2, above.

For every iteration using molecular simulations, we thus conduct two optimizations with the PCP-SAFT equation of state. First we determine φ_{ij}-values by minimizing the deviations of PCP-SAFT to simulated data (step 2), then we determine $\kappa_{\alpha\beta}$ values by

minimizing deviations of PCP-SAFT to experimental data (step 3). The dimensionality of both optimizations, however, is different. Parameter φ_{ij} is in step 2 adjusted for every mixture of the training set. In this work we test the procedure with a relatively low dimensionality. We will only consider n-alkane/nitrogen mixtures, and we use training data for 3 mixtures. Three φ_{ij} parameters are regressed in step 2. The dimensionality of the $\kappa_{\alpha\beta}$-matrix is two in our case, i.e. $\kappa_{\mathrm{CH_3,N}}$ and $\kappa_{\mathrm{CH_2,N}}$, because we identified $\kappa_{\mathrm{CH_3,CH_2}} \approx 0$ in our earlier work[7]. Therefore, the dimensionality of the optimization in step 3, in our application, is two.

We note that the procedure can be defined such that the quality of the PCP-SAFT model does not alter the final result. If the procedure converges, the final result is unaffected by the analytic equation of state, as shown in the appendix of Hemmen and Gross[7]. It is thereby only necessary to bias the optimization in step 3 using the residuals of step 2. For details in the implementation we refer to Hemmen et al.[7].

That is important, because all approximations in eq. 4.7 and in assuming $\hat{I}_{ij} \approx I_{\alpha\beta}$ are best defendable for Lennard-Jones fluids, i.e. for Mie potentials with all $n_{\alpha\alpha} = 12$. In the development of PCP-SAFT, a Lennard-Jones fluid was assumed as a preliminary step (before model constants were refined by regressing real fluid properties). The PCP-SAFT model insofar approximately reproduces the properties of Lennard-Jones fluids. In the TAMie force field, however, the repulsive exponent is treated as an adjustable parameter. For linear alkanes, for example, all repulsive exponents are $n_{\alpha\beta} = 14$. The adjustable parameter φ_{ij} then deviates considerably from unity. The iteration, nonetheless converges rapidly, as practical applications show.

4.4 Molecular Simulation Method

We conduct grand canonical ensemble $\{\mu, V, T\}$ Monte Carlo simulations to determine vapor-liquid phase equilibria properties for binary mixtures. In the grand canonical ensemble the number of molecules N and the energy E are fluctuating quantities, whereas the excess chemical potential μ, volume V and temperature T are specified.

To simplify the sampling of ensemble averages for binary mixtures we divide the $\boldsymbol{N} = (N_1, N_2)$-space for given temperature T into windows of $\Delta N_1 \times \Delta N_2 = 10 \times 10$ molecules. This makes separate simulations for each $\boldsymbol{N}$-window possible, in which trial moves inserting or deleting molecules outside the defined windows are trivially rejected.

The probability distribution $P(\boldsymbol{N}; \boldsymbol{\mu}, V, T)$ is sampled using a Transition Matrix scheme[48,49]. By applying a bias function the $\boldsymbol{N}$-space is sampled evenly. The bias function is determined on the fly from the Transition Matrix method. Utilizing the PCP-SAFT equation of state[39] enables us to estimate suitable $\{\boldsymbol{\mu} = (\mu_1, \mu_2),\ \boldsymbol{N} = (N_1, N_2)\}$ conditions for a representative equilibrium point. Moreover, the entire relevant $\boldsymbol{N}$-range is defined with

help of the analytic equation of state.
The vapor-liquid equilibrium is determined as a post processing step using the histogram reweighting method[50–53]. For a more detailed description of the simulation technique, we refer to Hemmen et al.[11]. Vapor-liquid equilibria (VLE) are determined for increasing pressure using the histogram reweighting technique. It is not possible to calculate phase equilibria all the way to the critical point. We terminate the VLE calculation when the two peaks in the probability distribution $P(\boldsymbol{N};\boldsymbol{\mu},V,T)$ for the vapor and for the liquid phase, respectively, overlap considerably. As termination criterion we use the ratio of the local minimum between the two peaks in the probability distribution to the maximum of the smaller of the two peaks. We require that calculations in the direction of increasing pressures only proceeds if this ratio is smaller than 0.05.
Critical points of mixtures can be determined using the Binder parameter[54]. We determine the condition, when the Binder-parameter equals the Ising-value. Extrapolating these conditions for different simulation volumes to infinite volume, using finite size scaling rules, yields the critical point[55].

4.5 Simulation Details

We used five different Monte Carlo moves in our simulation: particle insertion 15%, particle deletion 15%, translational displacement 30%, rotation 30% and particle regrowth 10%. The statistics of insertion, deletion and reconfiguration is improved by applying a configurational bias scheme with increasing step numbers for windows at higher densities. For a detailed description of the used configurational bias scheme we refer to the literature[56,57]. Every van der Waals interaction site is inserted and deleted with N_{CBMC} trial positions. We use $N_{\mathrm{CBMC}} = 1$ for low densities and up to $N_{\mathrm{CBMC}} = 12$ for windows with highest molecule numbers. For mixtures of two species we use a simple arithmetic average $c = N_1/N_1^{\max} + N_2/N_2^{\max}$ as criterion for increasing the number of CBMC-trial steps as $N_{\mathrm{CBMC}} = \mathrm{INT}(\exp(2.5 \cdot c))$. The maximum relevant molecule numbers $N_i^{\max}$ for a binary isothermal vapor-liquid equilibrium are calculated *a priori* using the PCP-SAFT equation of state. We found low sensitivity to the detailed choice in increasing N_{CBMC}, as long as the highest densities are calculated with $N_{\mathrm{CBMC}} = 12$, approximately.
The cut-off radius for calculation of the Mie potential for all interactions is set to $R_c = 14\,\text{Å}$. Analytical tail corrections[58,59] are used beyond the cut-off radius R_c (see supplementary material [Appendix C]). The electrostatic potential is calculated using Ewald summation with a maximum index of $k_{\max} = 9$ in the Fourier series expansion and a damping factor of $\kappa = 7,59L$ for a cubic box of length L[58].
Volumes of the simulation boxes are by default $V = 30\,000\,\text{Å}^3$, $V = 60\,000\,\text{Å}^3$ for high temperatures and additionally $V = 21\,952\,\text{Å}^3$ and $V = 40\,000\,\text{Å}^3$ for the determination

of the critical point. For each $\boldsymbol{N}$-window we used 10 million Monte Carlo trial moves for equilibration and 50 million for production.

The molecular model for the n-alkanes is taken from the TAMie force field[7]. For nitrogen we use the TraPPE force field[4]. The two nitrogen Lennard-Jones atoms are a fixed bond distance of 1.098 Å apart and both carry a negative point charge. A compensating positive point charge is placed at the center of mass of the two nitrogen atoms. We marginally modify the Lennard-Jones parameters ($\epsilon_{\alpha\alpha}$ and $\sigma_{\alpha\alpha}$) of the nitrogen atoms, $\alpha = \mathrm{N}$, with the optimization scheme described in ref.[7]. Doing so slightly improved agreement to experimental phase equilibrium data, as shown in the supplementary material [Appendix C]. The parameters for nitrogen are listed in Table 4.1.

Table 4.1: Parameters of the proposed TAMie force field for n-alkanes: energy parameter ϵ, size parameter σ, repulsive exponent n, and point charge q in units of electron charge. (COM: center of mass). The nitrogen force field is a marginal reparameterization (in Lennard-Jones parameters) of the TraPPE model[4].

site α	$\epsilon_{\alpha\alpha}/k_B$/K	$\sigma_{\alpha\alpha}$/Å	$n_{\alpha\alpha}$	q_α/e	
N≡ (nitrogen)	35.913	3.3136	12	−0.482	[4]
COM (nitrogen)	-	-	-	+0.964	
$CH_3(sp^3)$	136.318	3.6034	14	-	[7]
$CH_2(sp^3)$	52.9133	4.0400	14	-	[7]

4.6 Results and Discussion

We consider phase equilibrium data of three binary mixtures {n-propane/nitrogen (T = 230 K), n-pentane/nitrogen (T = 344 K), n-hexane/nitrogen (T = 344 K)} as a training set for adjusting two cross-group parameters, $\kappa_{\mathrm{CH_3,N}}$ and $\kappa_{\mathrm{CH_2,N}}$. The transferability of the cross-group parameters is subsequently assessed, both for varying temperatures in the same mixtures and for different mixtures, namely nitrogen in binary mixture with n-butane to n-dodecane.

The convergence behavior of the two-dimensional iterative optimization of the cross-interaction parameters ($\kappa_{\mathrm{CH_3,N}}$ and $\kappa_{\mathrm{CH_2,N}}$) is illustrated in Table. 4.2. The table shows the total sum of squared deviations between the simulated and experimental vapor-liquid equilibrium data, f_{obj}, as calculated according to eq. 4.10. The objective function is reduced to a minimum value with overlying statistical uncertainties. Statistical uncertainty is calculated from three simulations using the t-distribution and a 95% confidence interval. The statistical error of the second and third iterations are of the same order of magnitude as the mean value of iteration 1-3 (see Table. 4.2) we expect convergence. For all results presented below we used the binary interaction parameters $\kappa_{\alpha\beta}$ from the second iteration

of the optimization problem presented in Table 4.3.

Table 4.2: Value of the objective function $f_{\text{obj}}(\kappa_{\alpha\beta})$ and 95% confidence intervall $C_{95\%}$ of the training set, eq. (4.10) for proceeding iterations. The zeroth iteration shows the objective function for the starting values of the parameters (i.e. $\kappa_{\text{CH}_3,\text{N}} = 0$ and $\kappa_{\text{CH}_2,\text{N}} = 0$).

iteration	$f_{\text{obj}}(\kappa_{\alpha\beta})$	$C_{95\%}$
0	0.00704	
1	0.00213	$\pm$0.00013
2	0.00185	$\pm$0.00016
3	0.00218	

Table 4.3: Binary cross-interaction parameter for united-atom groups, with $\alpha \neq \beta$ for groups α and β belonging to two different molecule types $i \neq j$. Otherwise $\kappa_{\alpha\beta} = 0$.

group α	group β	$\kappa_{\alpha\beta}$	ref.
-CH_3	N$\equiv$ (nitrogen)	0.0087	
-CH_2-	N$\equiv$ (nitrogen)	0.0509	
-CH_3	-CH_2-	0	[7]

Fig. 4.1 compares results of molecular simulations applying the TAMie force field to experimental data of the training set. The figure gives calculation results obtained using the adjusted cross-energy parameters, $\kappa_{\text{CH}_3,\text{N}}$ and $\kappa_{\text{CH}_2,\text{N}}$. The calculated phase equilibrium line is in very good agreement with experimental data. The phase equilibrium calculation is only conducted up to a pressure of approximately 80% of the critical pressure. At higher pressures, the two peaks in the probability distribution $P(N_1, N_2)$, representing the vapor phase and the liquid phase of the grand canonical ensemble simulation, significantly overlap. The two cross-energy parameters $\kappa_{\text{CH}_3,\text{N}}$ and $\kappa_{\text{CH}_2,\text{N}}$ were adjusted using the PCP-SAFT equation of state. Values for the two cross-energy parameters are given in Table 4.3. The binary correction parameters k_{ij} used in the PCP-SAFT equation of state are listed in the supplementary material [Appendix C], together with the literature references for experimental data.

In Fig. 4.1 we also include calculation results obtained with all $\kappa_{\alpha\beta}$ parameters set to zero. The bubble point pressure is underestimated for that case, confirming the need to adjust cross-energy van der Waals parameters for a near-quantitative description of mixture phase equilibria.

It is interesting to compare the results obtained from the TAMie force field with other models. Fig. 4.2 compares the TAMie model to results from the TraPPE-UA (united atom) force field. The vapor pressure of alkanes is known to be overestimated by the TraPPE-UA model, which leads to overestimated mole fractions of alkane in the vapor

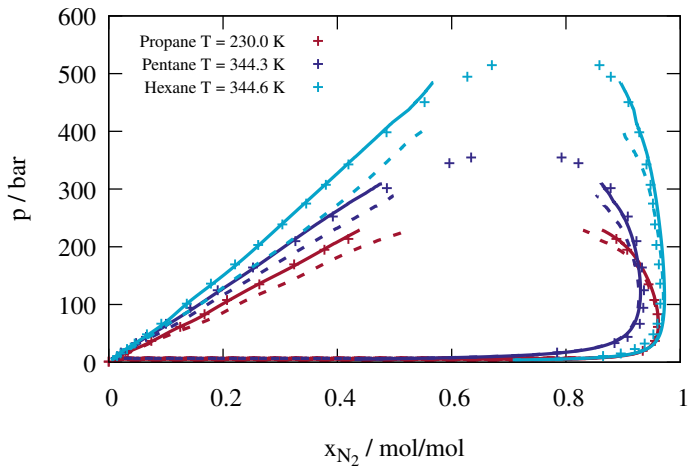

Figure 4.1: Vapor-liquid equilibria of n-propane/nitrogen, n-pentane/nitrogen and n-hexane/nitrogen mixtures: Experimental data[60–62] (symbols) and results from molecular simulations, without (dashed line) and with (solid line) adjusted $\kappa_{\alpha\beta}$ parameters.

phase. The bubble point pressures are at the same time predicted at too low values. The all-atom force field TraPPE-EH (explicit hydrogen) developed by Chen and Siepmann[63] is known to be a very accurate model for alkanes and has been applied to a mixture of propane with nitrogen[4]. Fig. 4.2 shows that results of TraPPE-EH are very similar to results of the TAMie model prior to adjusting cross-energy parameters. The bubble point is underestimated by more than 10%. This comparison clarifies, the need for determining cross-energy parameters for obtaining close agreement to experimental data is not a consequence of coarse-graining the -CH_2- group and the -CH_3 group as single interaction sites. As a side remark we mention that the TraPPE-EH force field is in much better agreement to pure component experimental data, in particular vapor pressure, of alkanes than reported in the original publication[63], as shown in the supplementary material [Appendix C].

We now proceed to investigate the robustness to extrapolations in temperature. Fig. 4.3 compares results of the TAMie model to experimental phase equilibrium data of n-propane/nitrogen mixtures at four temperatures. The agreement to experimental data is very good. The results can in particular be appreciated when compared to results of the PCP-SAFT equation of state, which describes the phase behavior well at low and moderate pressures but overpredicts the critical pressure considerably. In order to be more conclusive about the performance of the TAMie force field, we include a calculation of the critical point (determined using the Binder parameter[54]) at $T = 330\,\mathrm{K}$. The critical temperature is in very good agreement to the location where the experimental data suggests the critical point.

Defining binary cross-energy parameters to pairs of groups beyond the Berthelot com-

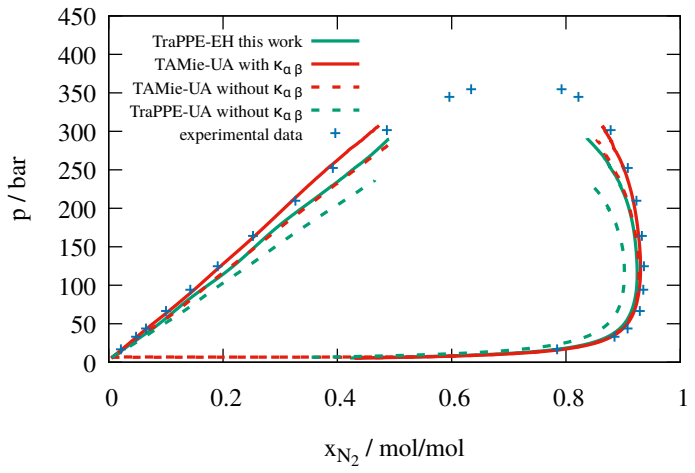

Figure 4.2: Vapor-liquid equilibria for n-pentane at $T = 344.3\,\mathrm{K}$. Comparison of results from molecular simulations using different force fields with experimental data[61]: TAMie with adjusted $\kappa_{\alpha\beta}$ (solid red line), TAMie without adjusted $\kappa_{\alpha\beta}$ (dashed red line), experimental data (blue triangles), TraPPE-EH (solid green line) and TraPPE-UA[64] (dashed green line).

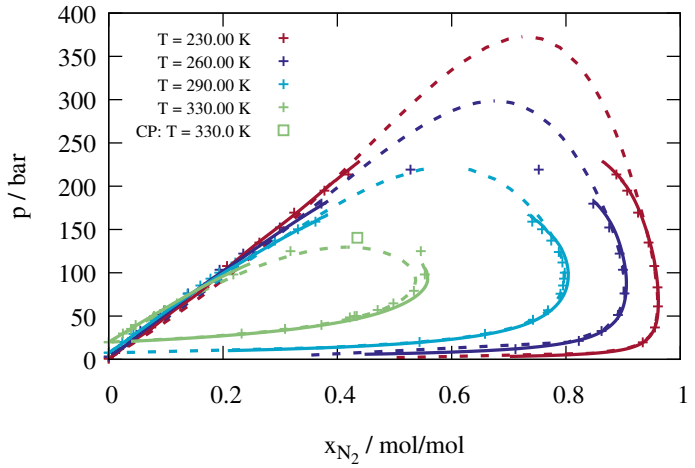

Figure 4.3: Vapor-liquid equilibria of n-propane/nitrogen mixtures at different temperatures: Experimental data[60,65] (symbols), results from PCP-SAFT model (dashed line) and from molecular simulation (solid line). Critical point for $T = 330.0\,\mathrm{K}$ was determined with the Binder-method.

bining rule is useful, if the so-obtained parameters are transferable to various mixtures including mixtures, where little or no experimental data is available. We test the transferability of the parameters by applying them to a number of binary n-alkane/nitrogen mixtures at various temperatures. Fig. 4.4 and Fig. 4.5 consider phase equilibria of mixtures of n-heptane/nitrogen and of n-decane/nitrogen, respectively, at various temperatures, comparing TAMie predictions with experimental data. Both mixtures were not part of

the training set. The good agreement of the TAMie model to the experimental data suggests reliable transferability of the binary cross-energy parameters. Results for the remaining binary mixtures (nitrogen in mixture with n-butane to n-dodecane) as well as tabulated numerical simulation data are given as supplementary material [Appendix C]. In the supplementary material we furthermore show that cross-energy parameters based on pairs of groups $\kappa_{\alpha\beta}$ lead to better results than adjusting a parameter κ_{ij} for a pair of species (i and j) that is subsequently treated as transferable among other species-pairs of the same homologous series.

For one temperature, we also determined the critical point of the n-heptane/nitrogen mixture. The critical pressure of $p_c = 282.31\,\text{bar}$ for $T = 452.9\,\text{K}$ as predicted from the TAMie model is in good agreement to the experimental value of $p_c = 288.60\,\text{bar}$.

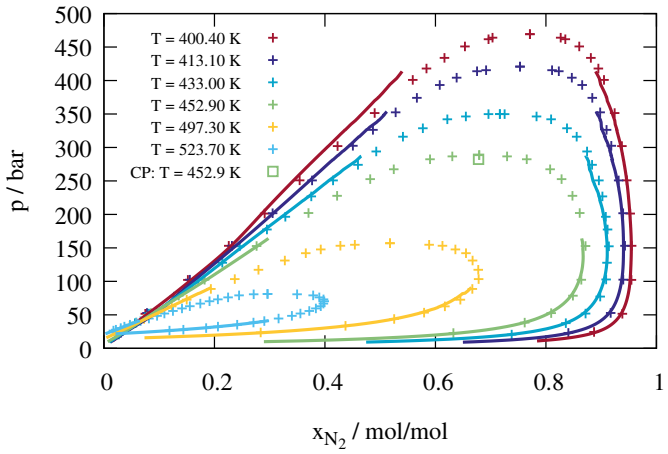

Figure 4.4: Vapor-liquid equilibria of n-heptane/nitrogen mixtures at different temperatures: Experimental data[66] (symbols) and predictions from molecular simulation (lines). Critical point for $T = 452.9\,\text{K}$ determined with the Binder-method.

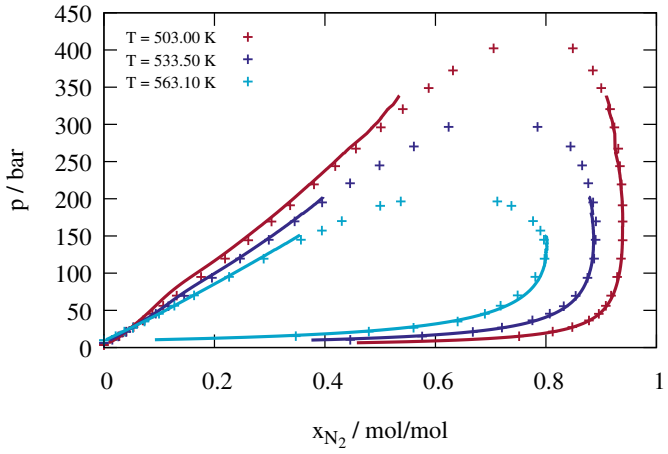

Figure 4.5: Vapor-liquid equilibria of n-decane/nitrogen mixtures at different temperatures: Experimental data[67] (symbols) and predictions from molecular simulation (lines).

4.7 Conclusion

This study investigates the transferability of cross-wise van der Waals energy parameters $\epsilon_{\alpha\beta}$ for individual pairs of (united-)atom groups. Phase equilibria of n-alkane/nitrogen mixtures are determined from Monte Carlo simulations and the cross-energy parameters (-CH_3 to N and -CH_2- to N) were simultaneously adjusted to experimental data of a training set consisting of three mixtures. The iteration of the cross-energy parameters is supported by an analytic equation of state (PCP-SAFT model), whereby convergence was already reached after the first iteration. The obtained cross-energy parameters were found to be transferable for temperatures not covered by the training set and they were seen to be transferable to mixtures not included in the training set. The agreement to experimental data is very good in all cases.

Bibliography

[1] Lorentz, H. (1881) Ueber die Anwendung des Satzes vom Virial in der kinetischen Theorie der Gase. *Ann. Phys. 248*, 127–136.

[2] Berthelot, D. (1898) Sur le mélange des gaz. *Compt. Rendus 126*, 1703–1706.

[3] Potoff, J., Errington, J., and Panagiotopoulos, A. (1999) Molecular simulation of phase equilibria for mixtures of polar and non-polar components. *Mol. Phys. 97*, 1073–1083.

[4] Potoff, J. J., and Siepmann, J. I. (2001) Vapor-liquid equilibria of mixtures containing alkanes, carbon dioxide, and nitrogen. *AIChE J. 47*, 1676–1682.

[5] Stoll, J., Vrabec, J., and Hasse, H. (2003) Vapor-liquid equilibria of mixtures containing nitrogen, oxygen, carbon dioxide, and ethane. *AIChE J. 49*, 2187–2198.

[6] Carrero-Mantilla, J., and Llano-Restrepo, M. (2003) Further Validation of a Set of Quadrupolar Potential Models for Ethylene and Propylene from the Prediction of some Binary Mixture Vapor-Liquid Equilibria by Gibbs-ensemble Molecular Simulation. *Mol. Simulat. 29*, 549–554.

[7] Hemmen, A., and Gross, J. (2015) Transferable Anisotropic United-Atom Force Field Based on the Mie Potential for Phase Equilibrium Calculations: n-Alkanes and n-Olefins. *J. Phys. Chem. B 119*, 11695–11707.

[8] Delhommelle, J., and Millie, P. (2001) Inadequacy of the Lorentz-Berthelot combining rules for accurate predictions of equilibrium properties by molecular simulation. *Mol. Phys. 99*, 619–625.

[9] Ungerer, P., Wender, A., Demoulin, G., Émeric Bourasseau,, and Mougin, P. (2004) Application of Gibbs Ensemble and NPT Monte Carlo Simulation to the Development of Improved Processes for H2S-rich Gases. *Mol. Simulat. 30*, 631–648.

[10] Schnabel, T., Vrabec, J., and Hasse, H. (2007) Unlike Lennard-Jones parameters for vapor-liquid equilibria. *J. Mol. Liq. 135*, 170 – 178.

[11] Hemmen, A., Panagiotopoulos, A. Z., and Gross, J. (2015) Grand Canonical Monte Carlo Simulations Guided by an Analytic Equation of State—Transferable Anisotropic Mie Potentials for Ethers. *J. Phys. Chem. B 119*, 7087–7099.

[12] Rouha, M., and Nezbeda, I. (2009) Non-Lorentz?Berthelot Lennard-Jones mixtures: A systematic study. *Fluid Phase Equilibr. 277*, 42 – 48.

[13] Boda, D., and Henderson, D. (2008) The effects of deviations from Lorentz?Berthelot rules on the properties of a simple mixture. *Mol. Phys. 106*, 2367–2370.

[14] Kong, C. L. (1973) Combining rules for intermolecular potential parameters. II. Rules for the Lennard-Jones (12–6) potential and the Morse potential. *J. Chem. Phys. 59*, 2464–2467.

[15] Desgranges, C., and Delhommelle, J. (2014) Evaluation of the grand-canonical partition function using expanded Wang-Landau simulations. III. Impact of combining rules on mixtures properties. *J. Chem. Phys. 140*, 104109.

[16] Vrabec, J., and Fischer, J. (1995) Vapour liquid equilibria of mixtures from the NpT plus test particle method. *Mol. Phys. 85*, 781–792.

[17] Vrabec, J., and Fischer, J. (1997) Vapor-liquid equilibria of the ternary mixture CH4 + C2H6 + CO2 from molecular simulation. *AIChE J. 43*, 212–217.

[18] Kronome, G., Szalai, I., Wendland, M., and Fischer, J. (2000) Extension of the NpT + test particle method for the calculation of phase equilibria of nitrogen + ethane. *J. Mol. Liq. 85*, 237 – 247.

[19] Vrabec, J., Stoll, J., and Hasse, H. (2005) Molecular models of unlike interactions in fluid mixtures. *Mol. Simulat. 31*, 215–221.

[20] Huang, Y.-l., Vrabec, J., and Hasse, H. (2009) Prediction of ternary vapor-liquid equilibria for 33 systems by molecular simulation. *Fluid Phase Equilibr. 287*, 62 – 69.

[21] Moučka, F., and Nezbeda, I. (2011) Water–methanol mixtures with non-Lorentz–Berthelot combining rules: A feasibility study. *J. Mol. Liq. 159*, 47–51.

[22] Liu, Y., Panagiotopoulos, A. Z., and Debenedetti, P. G. (2011) Monte Carlo Simulations of High-Pressure Phase Equilibria of CO2–H2O Mixtures. *J. Phys. Chem. B 115*, 6629–6635.

[23] Schacht, C. S., Vlugt, T. J. H., and Gross, J. (2011) Using an Analytic Equation of State to Obtain Quantitative Solubilities of CO2 by Molecular Simulation. *J. Phys. Chem. Lett. 2*, 393–396.

[24] Docherty, H., Galindo, A., Vega, C., and Sanz, E. (2006) A potential model for methane in water describing correctly the solubility of the gas and the properties of the methane hydrate. *J. Chem. Phys. 125*, 074510.

[25] Papadimitriou, N. I., Tsimpanogiannis, I. N., Economou, I. G., and Stubos, A. K. (2014) Influence of combining rules on the cavity occupancy of clathrate hydrates by Monte Carlo simulations. *Mol. Phys. 112*, 2258–2274.

[26] Meira Soares, V., Nieto de Castro, C., and Calado, J. Combining rules in molecular theories of solutions. 1972.

[27] Fischer, J., Müller, D., Chialvo, A., and Haile, J. M. (1989) The influence of unlike molecule interaction parameters on liquid mixture excess properties. *Fluid Phase Equilibr. 48*, 161 – 176.

[28] Möller, D., Óprzynski, J., Müller, A., and Fischer, J. (1992) Prediction of thermodynamic properties of fluid mixtures by molecular dynamics simulations: methane-ethane. *Mol. Phys. 75*, 363–378.

[29] Kohler, F., Fischer, J., and Wilhelm, E. (1982) Intermolecular force parameters for unlike pairs. *J. Mol. Struct. 84*, 245–250.

[30] Rouha, M., and Nezbeda, I. (2017) Second virial coefficients: a route to combining rules? *Mol. Phys. 115*, 1191–1199.

[31] Vrabec, J., lin Huang, Y., and Hasse, H. (2009) Molecular models for 267 binary mixtures validated by vapor-liquid equilibria: A systematic approach. *Fluid Phase Equilibr. 279*, 120 – 135.

[32] Elts, E., Windmann, T., Staak, D., and Vrabec, J. (2012) Fluid phase behavior from molecular simulation: Hydrazine, Monomethylhydrazine, Dimethylhydrazine and binary mixtures containing these compounds. *Fluid Phase Equilibr. 322-323*, 79 – 91.

[33] Huang, Y.-L., Miroshnichenko, S., Hasse, H., and Vrabec, J. (2009) Henry's Law Constant from Molecular Simulation: A Systematic Study of 95 Systems. *Int. J. Thermophys. 30*, 1791.

[34] Eckl, B., Schnabel, T., Vrabec, J., Wendland, M., and Hasse, H. (2009) Thermophysical Properties of Dry and Humid Air by Molecular Simulation Including Dew Point Calculations with the Mollier Ensemble. *Ind. Eng. Chem. Res. 48*, 10110–10119.

[35] Vlcek, L., Chialvo, A. A., and Cole, D. R. (2011) Optimized Unlike-Pair Interactions for Water-Carbon Dioxide Mixtures Described by the SPC/E and EPM2 Models. *J. Phys. Chem. B 115*, 8775–8784.

[36] Nezbeda, I., Moučka, F., and Smith, W. R. (2016) Recent progress in molecular simulation of aqueous electrolytes: force fields, chemical potentials and solubility. *Mol. Phys. 114*, 1665–1690.

[37] Horsch, M., Lin, Z., Windmann, T., Hasse, H., and Vrabec, J. (2011) The air pressure effect on the homogeneous nucleation of carbon dioxide by molecular simulation. *Atmos. Res. 101*, 519 – 526.

[38] Firanescu, G., Luckhaus, D., Patey, G. N., Atreya, S. K., and Signorell, R. (2011) The composition of liquid methane-nitrogen aerosols in Titan's lower atmosphere from Monte Carlo simulations. *Icarus 212*, 779 – 789.

[39] Gross, J., and Sadowski, G. (2001) Perturbed-Chain SAFT: An Equation of State Based on a Perturbation Theory for Chain Molecules. *Ind. Eng. Chem. Res. 40*, 1244–1260.

[40] Gross, J. (2005) An equation-of-state contribution for polar components: Quadrupolar molecules. *AIChE J. 51*, 2556–2568.

[41] Gross, J., and Vrabec, J. (2006) An equation-of-state contribution for polar components: Dipolar molecules. *AIChE J. 52*, 1194–1204.

[42] van Westen, T., Vlugt, T. J. H., and Gross, J. (2011) Determining Force Field Parameters Using a Physically Based Equation of State. *J. Phys. Chem. B 115*, 7872–7880, PMID: 21568280.

[43] Weidler, D., and Gross, J. (2016) Transferable Anisotropic United-Atom Force Field Based on the Mie Potential for Phase Equilibria: Aldehydes, Ketones, and Small Cyclic Alkanes. *Ind. Eng. Chem. Res. 55*, 12123–12132.

[44] Avendano, C., Lafitte, T., Galindo, A., Adjiman, C. S., Jackson, G., and Müller, E. A. (2011) SAFT-γ force field for the simulation of molecular fluids. 1. A single-site coarse grained model of carbon dioxide. *J. Phys. Chem. B 115*, 11154–11169.

[45] Müller, E. A., and Jackson, G. (2014) Force-Field Parameters from the SAFT-γ Equation of State for Use in Coarse-Grained Molecular Simulations. *Annu. Rev. Chem. Biomol. 5*, 405–427.

[46] Lymperiadis, A., Adjiman, C. S., Galindo, A., and Jackson, G. (2007) A group contribution method for associating chain molecules based on the statistical associating fluid theory (SAFT-γ). *J. Chem. Phys. 127*, 234903.

[47] Potoff, J. J., and Bernard-Brunel, D. A. (2009) Mie potentials for phase equilibria calculations: Application to alkanes and perfluoroalkanes. *J. Phys. Chem. B 113*, 14725–14731.

[48] Errington, J. R. (2003) Direct calculation of liquid–vapor phase equilibria from transition matrix Monte Carlo simulation. *J. Chem. Phys. 118*, 9915–9925.

[49] Paluch, A. S., Shen, V. K., and Errington, J. R. (2008) Comparing the use of Gibbs ensemble and grand-canonical transition-matrix Monte Carlo methods to determine phase equilibria. *Ind. Eng. Chem. Res. 47*, 4533–4541.

[50] Ferrenberg, A. M., and Swendsen, R. H. (1989) Optimized monte carlo data analysis. *Phys. Rev. Lett. 63*, 1195.

[51] Wilding, N. B. (1995) Critical-point and coexistence-curve properties of the Lennard-Jones fluid: a finite-size scaling study. *Phys. Rev. E 52*, 602.

[52] Panagiotopoulos, A. Z., Wong, V., and Floriano, M. A. (1998) Phase equilibria of lattice polymers from histogram reweighting Monte Carlo simulations. *Macromolecules 31*, 912–918.

[53] Potoff, J. J., and Panagiotopoulos, A. Z. (1998) Critical point and phase behavior of the pure fluid and a Lennard-Jones mixture. *J. Chem. Phys. 109*, 10914–10920.

[54] Binder, K. (1981) Finite size scaling analysis of ising model block distribution functions. *Z. Phys. B 43*, 119–140.

[55] Pérez-Pellitero, J., Ungerer, P., Orkoulas, G., and Mackie, A. D. (2006) Critical point estimation of the Lennard-Jones pure fluid and binary mixtures. *J. Chem. Phys. 125*, 054515.

[56] Siepmann, J. I., and Frenkel, D. (1992) Configurational bias Monte Carlo: a new sampling scheme for flexible chains. *Mol. Phys. 75*, 59–70.

[57] Frenkel, D., Mooij, G., and Smit, B. (1992) Novel scheme to study structural and thermal properties of continuously deformable molecules. *J. Phys. Condens. Matter 4*, 3053.

[58] Allen, M. P., and Tildesley, D. J. *Computer simulation of liquids*; Oxford University Press: New York, 1987.

[59] Smit, B. (1992) Phase diagrams of Lennard-Jones fluids. *J. Chem. Phys. 96*, 8639–8640.

[60] Grausø, L., Fredenslund, A., and Mollerup, J. (1977) Vapour-liquid equilibrium data for the systems C2H6 + N2, C2H4 + N2, C3H8 + N2, and C3H6 + N2. *Fluid Phase Equilibr. 1*, 13 – 26.

[61] Silva-Oliver, G., Eliosa-Jimenez, G., Garcia-Sanchez, F., and Avendano-Gomez, J. R. (2006) High-pressure vapor–liquid equilibria in the nitrogen–n-pentane system. *Fluid Phase Equilibr. 250*, 37 – 48.

[62] Eliosa-Jimenez, G., Silva-Oliver, G., Garcia-Sanchez, F., and de Ita de la Torre, A. (2007) High-Pressure Vapor-Liquid Equilibria in the Nitrogen + n-Hexane System. *J. Chem. Eng. Data 52*, 395–404.

[63] Chen, B., and Siepmann, J. I. (1999) Transferable Potentials for Phase Equilibria. 3. Explicit-Hydrogen Description of Normal Alkanes. *J. Phys. Chem. B 103*, 5370–5379.

[64] Martin, M. G., and Siepmann, J. I. (1998) Transferable Potentials for Phase Equilibria. 1. United-Atom Description of n-Alkanes. *J. Phys. Chem. B 102*, 2569–2577.

[65] Yucelen, B., and Kidnay, A. J. (1999) Vapor-Liquid Equilibria in the Nitrogen + Carbon Dioxide + Propane System from 240 to 330 K at Pressures to 15 MPa. *J. Chem. Eng. Data 44*, 926–931.

[66] Garcia-Sanchez, F., Eliosa-Jimenez, G., Silva-Oliver, G., and Godinez-Silva, A. (2007) High-pressure (vapor + liquid) equilibria in the (nitrogen + n-heptane) system. *J. Chem. Thermodyn. 39*, 893 – 905.

[67] Garcia-Sanchez, F., Eliosa-Jimenez, G., Silva-Oliver, G., and Garcia-Flores, B. E. (2009) Vapor-Liquid Equilibrium Data for the Nitrogen + n-Decane System from (344 to 563) K and at Pressures up to 50 MPa. *J. Chem. Eng. Data 54*, 1560–1568.

Chapter 5

Polarizable Transferable Anisotropic United-Atom Force Field Based on the Mie Potential for Phase Equilibria: n-Alkanes, Ethers, and Nitrogen

The content of this chapter is a literal quote of the publication

> *Waibel, Gross, Journal of Chemical Theory and Computation, 2018, submitted (reproduced with permission from ACS, unpublished work copyright 2018) [in the meantime it was published with minor modifications in Journal of Chemical Theory and Computation, 15 (4), 2019, 2561-2573].*

In comparison to the published work, the abstract is here omitted. Additions or deletions compared to the published work are marked with angular brackets.

Molecular simulations with transferable force fields allow the prediction of physical properties and phase equilibria of substances with scarce or absent experimental data. The most popular classical non-polarizable force fields with transferable parameters to calculate vapor-liquid equilibria are the Transferable Potentials for Phase Equilibria force field (TraPPE-UA)[1–7], the Optimized Potential for Liquid Simulations force field (OPLS-UA)[8–13], and the anisotropic united-atom model force field (AUA4)[14–18]. In recent years, an effort has been made within our group to develop a transferable classical force field for phase equilibria and thermodynamic properties, referred to as the Transferable Anisotropic Mie force field (TAMie)[19–23]. All of these force fields contain only pair-additive van der Waals and electrostatic interactions. However, the electron density of a molecule changes

depending on the electric field (exerted by surrounding molecules). The polarizability of molecules leads to induced dipole moments (or induced higher order multipoles captured by a polarizability tensor) when the considered molecule is immersed in a dense polar solution. In vapor phases, or in dense non-polar solvents, these induced dipole moments vanish. In classical force fields the (static) electronic polarization is partially accounted for by using effective static partial charges, where usually no attempt is made to resemble the electrostatic state of a molecule in vacuum. Effective constant partial charges, however, can not capture the density, temperature and composition-dependent effect of polarizability. It is therefore also questionable, whether interaction sites of a transferable force fields can indeed be expected to be transferable from one molecule to another molecule.

In this work, we briefly speak of polarizability when referring to the static electronic polarizability of molecules. Polarization effects can be included explicitly, by introducing a more detailed molecular model, leading to a many-body potential. In polarizable force fields for molecular simulation the treatment is usually conducted on the level of induced dipoles. There are three important approaches to include polarization into force fields: The fluctuating charge model[24,25], the inducible point dipole model[26], and the charge-on-spring model (named also Drude oscillator model or shell model)[27–29]. In the fluctuating charge model, the partial charges are redistributed within a molecule according to the electronegativity of each atom in response to the local electric field. Hence, the charges are treated dynamically and their values have to be adjusted in each simulation step. In this model, higher order multipoles are included, but the polarizability is restricted to the axis of two charges or to the plane of (say) three partial charges. In the inducible point dipole method, pre-defined interaction sites are assigned with inducible point dipoles, in addition to fixed point charges of a site, if applicable. This point dipole $\boldsymbol{\mu}_i$ on a site i is assumed linearly proportional as a response to the local electric field $\boldsymbol{E}_i$

$$\boldsymbol{\mu}_i = \boldsymbol{\alpha}_i \boldsymbol{E}_i \tag{5.1}$$

The polarizability tensor $\boldsymbol{\alpha}_i$ is thereby often assumed isotropic, so that $\boldsymbol{\alpha}_i$ can be replaced by a scalar-valued polarizability. The orientation and strength of the induced point dipoles have to be determined self-consistently in each simulation step. The charge-on-spring (COS) model replaces the inducible point dipole by a finite one, represented by two charges of opposite sign connected with a harmonic spring. The electronic polarization is simulated by an adjustment of the displacement of the charges in response to the local electric field, whereby the spring constant is connected to the polarizability $\boldsymbol{\alpha}_i$. Unlike the inducible point dipole model, the COS model avoids the complex calculation of dipole-dipole and charge-dipole interactions and is thus a direct extension of the additive non-polarizable models using only pairwise Colombic interactions. In force fields based

on the COS model, the total coulombic interaction usually has a contribution from static partial charges and a contribution from the charges on springs, with a separation and direction between these charges changes with molecular configurations. In all models, the induced polarization has to be solved self-consistently in each simulation step, because the polarizability state of a molecule acts back on surrounding molecules, and thus acts back on the local electric field $\boldsymbol{E}_i$ of the considered molecule. This many-body character increases the computational effort significantly, especially in Monte Carlo simulation schemes. For a more detailed review on these models, we refer to the literature[30–32]. In this work, we use the COS model to incorporate and analyse electronic polarization effects.

The attachment of inducible dipoles to certain interaction sites and determining appropriate values for the associated site polarizabilities is important in developing a force field that represents experimental data well. The inducible dipole sites are mostly distributed over the heavy atoms of a molecule. The (scalar-valued) polarizabilities, defining each inducible dipole site, can be adjusted to the molecular polarizability of the considered molecule[33–37]. The molecular polarizability can thereby be determined experimentally, or by ab initio calculations, or by a simple splitting of the molecular polarizability proportional to the molecular volume of each site[38]. In other approaches the polarizabilities assigned to individual sites are determined in combined quantum mechanical and molecular simulations[39,40] or by fitting to several ab initio electrostatic potential (ESP) maps of the molecule, which are perturbed with point charges[41–44].

For alkanes, ethers, and nitrogen there are transferable polarizable force fields available in literature. For linear alkanes in the liquid phase, Patel et al.[45] developed a force field based on the fluctuating charge model, which was later re-parametrized by Davis et al.[46,47]. Xie et al.[48] incorporated polarization into the CHARMM22[49] force field of alkanes with induced point dipoles, whereas Vorobyov et al.[50] parametrized a charge-on-spring model as part of the CHARMM Drude polarizable force field[51]. Furthermore, Szklarczyk et al.[52] extended the GROMOS non-polarizable force field[53] with a charge-on-spring model. The CHARMM Drude polarizable model is the only polarizable force field that includes ethers. Baker et al.[54] proposed this ether force field, which was re-parametrized by Vorobyov et al.[55]. For nitrogen, two polarizable force fields have been developed using a charge-on-spring model: Jordan et al.[56] proposed a phase transferable potential and Yu et al.[57] developed a physically motivated, ab initio force field.

In this study, we parameterize a polarizable force field (PTAMie) for n-alkanes, ethers, and nitrogen. The developed force field is parameterized using the same objective function with the same experimental data that led to a non-polarizable force field proposed in earlier work of our group (TAMie). The comparison between both force fields leads to a meaningful analysis, that shows whether polarizability improves predictions of phase

equilibria.

5.1 Force Field Development

The force field developed in this study is based on the Transferable Anisotropic Mie (TAMie) force field proposed from our group over the last years[19–23]. This force field uses a united-atom (UA) model, in which the molecule is coarse-grained by combining carbon and hydrogen atoms of aliphatic CH_x groups to one single interaction site. For the polarizable force field, we assume the same division of the molecule in interaction sites as in the classical TAMie force field. We thus have a predefined structure for the van der Waals interaction sites and the placement of the static partial charges. The parameters defining the intramolecular bonded interactions (bond lengths, angle bending and torsional potentials) used in the TAMie force field are adopted also to the polarizable force field. In the following section, we discuss the force field in detail, with a special focus on adding the effect of static polarizability.

5.1.1 Intermolecular Energy

Static electronic polarization is described by a charge-on-spring (COS) model with isotropic (i.e. scalar-valued) site polarizabilities α_i. In this model a finite inducible dipole $\boldsymbol{\mu}_i = \alpha_i \boldsymbol{E}_i$ is created through a pair of charges with opposite sign, connected by a harmonic spring. The positive core charge q_D is located on the polarizable site and is connected to the freely moveable shell charge $-q_D$ with the harmonic potential

$$u(r_{D,i}) = \frac{1}{2} k_D |\boldsymbol{r}_{D,i}|^2 \tag{5.2}$$

where $\boldsymbol{r}_D$ is the position of the shell charge relative to the core charge and k_D is the spring constant. The electric field caused by surrounding molecules causes the position of the shell to be shifted by $\boldsymbol{r}_D$ from the core against the harmonic spring. In the COS model the shifted position of the shell is the position where the electrostatic force $\boldsymbol{F}_{E,i} = q_{D,i}\boldsymbol{E}_i$ on COS site i cancels the spring force $\boldsymbol{F}_{k_D,i} = -k_D \boldsymbol{r}_{D,i}$, with

$$\boldsymbol{F}_{E,i} + \boldsymbol{F}_{k_D,i} = 0 \tag{5.3}$$

This condition corresponds to a minimum in energy with respect to shift position $\boldsymbol{r}_D$, which determines the shift position $\boldsymbol{r}_D$ as

$$\boldsymbol{r}_{D,i} = \frac{q_{D,i}}{k_D} \boldsymbol{E}_i \tag{5.4}$$

As a result, the finite inducible dipole $\boldsymbol{\mu}_i = q_{D,i}\boldsymbol{r}_{D,i}$ and eq. 5.1 determine the isotropic site polarizability to

$$\alpha_i = \frac{q_{D,i}^2}{k_D} \tag{5.5}$$

This equation shows that for a given value of the site-polarizability α_i, one can make a choice for the harmonic spring constant k_D, which then defines the charge $|q_{D,i}|$. We would like the induced dipole, represented by two separated charges, to resemble a point-dipole and we thus ensure that the distance $|\boldsymbol{r}_{D,i}|$ between the two charges of a COS site remain sufficiently small with respect to interatomic distances. A rather high spring constant k_D is chosen while maintaining numerical stability. We follow earlier work[51,58] and choose a value of $k_D = 4184\,{}^{\mathrm{kJ}}/_{\mathrm{mol\AA}^2}$ for all COS sites.

The polarizability tensor of the molecule is approximately reproduced by distribution of the isotropic COS sites over all interaction sites of the united-atom model. Several methods are available to define appropriate values of these site polarizabilities, as shown in the introduction. We obtain the polarizabilities from existing polarizable COS force fields and assume them as constant. For the CH_x sites of n-alkanes we take the polarizabilities from the polarizable all-atom CHARMM force field for alkanes[50]. In that force field the polarizable sites are located only at the heavy carbon atoms, which is compatible with our appoach. The values of the polarizabilities were determined by fitting to various ab initio ESP maps of the molecules[44], perturbed by partial charges. For ethers the polarizabilities of the CH_x groups are adopted from alkanes to get a transferable force field, like it was done for the van der Waals interaction parameters of the CH_x sites in the non-polarizable TAMie force field. The polarizability of the ether oxygen are taken from the polarizable all-atom CHARMM force field for ethers[54]. In the polarizable CHARMM force field, the site polarizabilities are scaled down for specific substance groups, whereas the scaling factor is substance specific and treated as an adjustable parameter. For our force field we use the unscaled polarizability of the ether oxygen. The unscaled values of the CH_x groups of the CHARMM ether force field are about the same size as the alkane values, so that compatibility can be assumed. For nitrogen we take the polarizabilities of the atoms from an ab initio force field for nitrogen proposed by Yu et al.[57]. The polarizabilities of different interaction sites are summarized in Table 5.1. We note that the COS charges q_D are defined through eq. 5.5, because the spring constant k_D and the polarizabilities α_i are given.

In addition to polarizable sites, molecules have static partial point-charges. For alkanes the partial charges of the united atom CH_x groups are set to zero, because these groups have no significant static polar contributions. For the other investigated substances the positions of the partial charges are taken from the non-polarizable TAMie force field.

Table 5.1: Polarizabilities of charge-on-spring sites used in the proposed PTAMie force field taken from literature.

pseudoatom i	$\alpha_i/(4\pi\epsilon_0 \text{Å}^3)$	ref
$CH_3(sp^3)$	2.051	[50]
$CH_2(sp^3)$	1.660	[50]
O_{ether}	0.828	[54]
N≡	1.141	[57]

Furthermore, the ratios between the charges of one functional group are adopted. For ethers a negative point charge is placed on the oxygen atom and two equal-valued counter charges are placed on the neighboring alkyl sites of the ether group. For nitrogen negative point charges are placed on the nitrogen atoms and a compensating positive point charge is placed on the center of mass of the two rigid connected nitrogen atoms. In a Monte Carlo simulation schemes it is possible that a molecule is considered at a position with large overlap to another molecule (with prohibitively large Lennard-Jones repulsion), where however a positive charge (say) placed in very close vicinity to a negative charge that is located off-center to a Lennard-Jones site. Such a configuration could, as an artifact, be acceptable, whereas in a molecular dynamics simulation would not visit such a configuration, because of a sufficiently large repulsive barrier. It is therefore required to protect partial charges located off-center from Lennard-Jones sites, from near distance configurations. We introduce a hard-sphere repulsive contour, by immediately rejecting any trial-configuration with Lennard-Jones repulsive pair energies of $\phi^{LJ}/(k_B T) > 450$.

If a static partial charge q and a COS inducible dipole with charges q_D are at the same interaction site, the charges can be combined. A modified COS site is formed with a core charge $q_c = q + q_D$ and moveable counter-charge attached to the spring $-q_D$. The potential energy of the COS inducible dipoles and static partial charges has two contributions: first, an electrostatic part between all charges of different interaction sites and, second, a polarization term, giving the energy needed to polarize[31]. The electrostatic energy contribution can be expressed as

$$U^{ele} = \frac{1}{4\pi\epsilon_0} \sum_i \sum_{j>i} \left[\frac{q_{c,i} q_{c,j}}{|\boldsymbol{r}_{c,i} - \boldsymbol{r}_{c,j}|} - \frac{q_{c,i} q_{D,j}}{|\boldsymbol{r}_{c,i} - \boldsymbol{r}_{s,j}|} - \frac{q_{D,i} q_{c,j}}{|\boldsymbol{r}_{s,i} - \boldsymbol{r}_{c,j}|} + \frac{q_{D,i} q_{D,j}}{|\boldsymbol{r}_{s,i} - \boldsymbol{r}_{s,j}|} \right] \tag{5.6}$$

accounting for core-core, core-shell, and shell-shell interactions of different interaction sites i and j. Here $\boldsymbol{r}$ are the positions of the core sites c (including static charge and core charge of the COS site) and charges attached to springs (shell sites) s ($\boldsymbol{r}_s = \boldsymbol{r}_c + \boldsymbol{r}_D$). The polarization energy is the energy stored in all harmonic springs, according to

$$U^{pol} = \sum_i \frac{1}{2} k_D |\boldsymbol{r}_{D,i}|^2 \tag{5.7}$$

Of course, the Coulombic interaction between the two charges of a COS-site are ignored. In classical force fields, like the TAMie force field, Coulombic (and van der Waals) interactions between the interaction sites separated by more than three bonds within a molecule are usually excluded. These interactions are included via bond-stretching, angle-bending, and torsion potentials. In some polarizable force fields, the dipole-dipole interactions between sites less than three bonds apart are explicitly included, whereas the charge-charge or charge-dipole interactions are further on excluded[51]. In our approach, these dipole-dipole interactions are omitted. We take the bonded potentials from the non-polarizable force field, where the interactions up to three bonds apart are already implicitly included. The same scheme was used for introducing polarizability into the GROMOS force field[52,59]. The short-ranged van der Waals interactions are described using a Mie potential, i.e. a generalized (n-m)-Lennard-Jones potential

$$u_{\mathrm{vdW}} = c_{ij}\epsilon_{ij}\left[\left(\frac{\sigma_{ij}}{r_{ij}}\right)^{n_{ij}} - \left(\frac{\sigma_{ij}}{r_{ij}}\right)^{6}\right] \tag{5.8}$$

where r_{ij} denotes the distance between two interaction sites i and j, The Mie potential is characterized through the energy parameter ϵ_{ij}, the size parameter σ_{ij} and the repulsive exponent n_{ij}. The attractive exponent is fixed to $m = 6$, whereas the repulsive exponent is used as degree of freedom in the TAMie force field and varies with the type of interaction site. For the polarizable force field we take the repulsive exponents of the van der Waals sites from the classical TAMie force field. The prefactor c_{ij} ensures the minimum of the potential to $-\epsilon_{ij}$ and is defined as

$$c_{ij} = \left(\frac{n_{ij}}{n_{ij}-6}\right)\left(\frac{n_{ij}}{6}\right)^{6/(n_{ij}-6)} \tag{5.9}$$

For unlike interaction sites Lorentz-Berthelot combining rules[60,61] are used

$$\sigma_{ij} = (\sigma_{ii} + \sigma_{jj})/2 \tag{5.10}$$

$$\epsilon_{ij} = \sqrt{\epsilon_{ii}\epsilon_{jj}} \tag{5.11}$$

and an arithmetic combining rule[62] for the repulsive exponents n_{ij}

$$n_{ij} = (n_{ii} + n_{jj})/2 \tag{5.12}$$

The Mie potential is applied to intermolecular interactions between two different molecules and intramolecular interactions within a molecule, if the interaction sites are separated

by more than three bonds.

5.1.2 Intramolecular Energy

The bonded interactions within a molecule are adopted from the classical TAMie force field, which uses the bonded interactions of several other force fields. Fixed bond lengths are used, and the center of the united atom interaction site of the methyl (CH_3) group is moved outward to better account for the effect of the bonded hydrogen atoms[63]. The bond length of a CH_3 group bonded to a CH_x group is extended by 0.2 Å. The intramolecular potential consists of angle bending and torsion. Furthermore, site-site interactions within a molecule, where the sites are separated more than three bonds, are taken into account. A harmonic potential is used for the angle-bending potential

$$u_{\text{bend}} = \frac{k_0}{2} (\theta - \theta_{\text{eq}})^2 \tag{5.13}$$

with bending angle θ, force constant k_0 and temperature-independent equilibrium angle θ_{eq}. The torsional potential between four neighbouring sites is (for the molecules considered here) represented by the OPLS-UA model[8], defined as

$$u_{\text{torsion}} = c_0 + c_1 [1 + \cos(\phi)] + c_2 [1 - \cos(2\phi)] + c_3 [1 + \cos(3\phi)] \tag{5.14}$$

where ϕ is the torsion angle. Parameters of the angle bending and torsional potentials as well as bond lengths are summarized in Tables 5.2-5.4, respectively.

Table 5.2: Bond lengths used in the proposed PTAMie force field taken from literature.

type		r_0/Å	ref
CH_3−CH_x	x ∈ {1, 2}	1.54 + 0.2	[19,20]
CH_x−CH_y	x,y ∈ {1, 2}	1.54	[1]
CH_3−CH_3 ethane	x ∈ {1, 2}	1.54 + 2 · 0.2	[19]
CH_3−O_{ether}		1.41 + 0.2	[20]
CH_2−O_{ether}		1.41	[6]
N≡N		1.098	[5]
N−COM_{nitrogen}		0.549	[5]

5.1.3 Optimization of Force Field Parameters

Similar to the development of the TAMie force field, we adjust the van der Waals parameters and static point charges of transferable groups to experimental data of several substances. The adjustable force field parameters $\mathbf{p} = (\epsilon_{ii}, \sigma_{ii}, q_i)$ are optimized by minimizing the objective function

Table 5.3: Bending angles and constants for the proposed PTAMie force field taken from literature.

bending site	$\theta/^\circ$	$k_0/k_B/K/rad^2$	ref
$CH_x{-}CH_2{-}CH_y$	114.0	62 500	[1,64]
$CH_x{-}O_{ether}{-}CH_y$	112.0	60 400	[6]
$C_{ether}{-}CH_2{-}CH_x$	112.0	50 300	[6]

Table 5.4: Torsional potential constants for the proposed PTAMie force field taken from literature.

torsion sites	c_0/k_B/K	c_1/k_B/K	c_2/k_B/K	c_3/k_B/K	ref
$CH_x{-}CH_2{-}CH_2{-}CH_y$	0.0	355.03	-68.19	791.32	[1,8]
$CH_x{-}CH_2{-}O_{ether}{-}CH_y$	0.0	725.35	-163.75	558.2	[6]
$CH_x{-}CH_2{-}CH_2{-}O_{ether}$	0.0	176.62	-53.34	769.93	[6]

$$f(\mathbf{p}) = \frac{1}{N^{\text{exp}}} \sum_{n=1}^{N^{\text{exp}}} \left(\frac{\Omega_n^{\text{sim}}(\mathbf{p}) - \Omega_n^{\text{exp}}}{\Omega_n^{\text{exp}}} \right)^2 \tag{5.15}$$

defined as the relative squared deviation between the simulated observables $\Omega_n^{\text{sim}}(\mathbf{p})$ and corresponding quasi-experimental observables Ω_n^{exp}, summed over all N^{exp} data points. The observables Ω in our optimization include vapor pressure p^{sat} and coexisting liquid density ρ^{L}.

The partial charges are varied along a predefined grid and, at each grid point, the Mie parameters (σ_{ii} and ϵ_{ii}) are simultaneously optimized for the set of partial charges using an optimization method proposed by van Westen et al.[65] and modified by Hemmen and Gross[19].

In the iterative optimization procedure for the Mie parameters, an analytical equation of state, the Perturbed-Chain Statistical Associating Fluid Theory (PC-SAFT) equation of state[66], is used to approximate the objective function. An iterative scheme is necessary because the molecular model of the PC-SAFT equation of state is more coarse-grained compared to our force field and it gives only approximate results. We stress, however, that the optimum of the optimization problem is not influenced by the approximations of the equation of state and does not alter the converged results (in the true minimum)[19]. This procedure ensures swift convergence: usually only three to five iterations are needed. The optimal static charge, with associated Mie parameters, is selected a posteriori. As initial guess for force field parametrization we use the values for the Mie parameters and partial charges of the non-polarizable TAMie force field. For quasi-experimental data, accurate multiparameter correlations provided by the NIST Chemistry webbook[67] are used for n-alkanes and from the DIPPR database[68] for ethers. For nitrogen, the highly

accurate equation of state of Span et al.[69] is used.

5.2 Molecular Simulation Technique

5.2.1 Monte Carlo Simulations

Vapor-liquid phase coexistence properties are obtained from Monte Carlo simulations in the grand canonical ensemble $\{\mu, V, T\}$ with transition matrix sampling where thermodynamic properties and phase equilibrium properties are determined in a post-processing step using the histogram reweighting technique. The transition matrix scheme[70,71] is applied to calculate the probability distribution $P(N)$. It is further used to determine a bias function on the fly, to sample the N-space evenly. For time-efficient sampling, the N-space is divided into windows, which can be run in parallel. A width of $\Delta N = 5$ or $\Delta N = 10$ molecules is used for pure components and a window of $\Delta N_1 \times \Delta N_2 = 10 \times 10$ or $\Delta N_1 \times \Delta N_2 = 5 \times 5$ is used for binary mixtures at a given temperature, whereby the statistical uncertainties[72] are not affected by the window size for a given number of applied sample steps. The PC-SAFT[66] equation of state is used to estimate suitable conditions of the chemical potential μ and the temperature T for each N-window. To obtain the vapor-liquid equilibrium the chemical potential μ is iterated in a post processing step, where the histogram reweighting technique is used to obtain the probability distribution $P(N)$ at other conditions[73–76]. A detailed overview of the simulation technique is given by Hemmen et al[20].

To sample the phase space for polarizable force fields efficiently, the multiparticle move method as proposed by Moučka et al.[77] is employed. In one Monte Carlo step, all molecules in the simulation box are either displaced or rotated simultaneously. This improves the computational efficiency for systems with many-body force fields, in contrast to classical pairwise additive force fields, where no computational efficiency is gained, because for multiparticle moves, the force on each molecule has to be calculated. The probabilities of different Monte Carlo moves are set to 15% for multiparticle translation, 15% for multiparticle rotation, 27.5% for insertion, 27.5% for deletion, and 15% for molecular reconfiguration (also referred to as regrow). In simulations with classical force fields we do not apply the multiparticle move method. The probabilities are then set to 30% for translation, 30% for rotation, 15% for insertion, 15% for deletion, and 10% for molecular reconfiguration. The average acceptance ratio of translation and rotation moves are adjusted to 30% in the equilibration period. For nitrogen no molecular reconfiguration is necessary, therefore the probability associated to this MC trial-step is added equally to the insertion and deletion trial steps. Simulations with the multiparticle move were carried out with at least 1 million steps for equilibration and 5 million steps for produc-

tion, whereas simulations without the multiparticle move were carried out with at least 10 million steps for equilibration and 50 million steps for production. A cubic simulation box of volume $V = 21952\,\text{Å}^3$ is used for all simulations. Although that is a rather small simulation volume, we have confirmed for non-polarizable force fields that the errors due to systems' finite size of most phase equilibrium properties are rather small. Exceptions are critical point properties, surface tensions (that are not investigated here), and energies or enthalpies of the vapor phase. We note, however, that values of the enthalpy of vaporization with weak errors due to systems' finite size can be obtained from the Clausius-Clapeyron relation.

Analytic tail-corrections[78,79] are applied for the Mie potential beyond a spherical cut-off radius of $R_c = 14\,\text{Å}$. To improve the statistics for insertion, deletion and reconfiguration a configurational bias scheme for each interaction site is applied[80,81]. We increase the number of configurational-bias trial steps from low densities (1 step) to high densities (8 steps). Critical points are determined using mixed-field finite-size scaling techniques[74,75]. In this study critical points are not determined by extrapoling to infinite system sizes, rather we report system size-dependent values. The enthalpy of vaporization is calculated using the Clausius-Clapeyron equation, because the so-determined values are significantly less system-size dependent for GCMC simulations, than starting from the average energies of the coexisting phases[23]. Further simulation details are summarized in the Supporting Information [Appendix D].

5.2.2 Energy Minimization

Following the Born-Oppenheimer approximation, electronic degrees of freedom are assumed to relax instantaneously to their ground state. Accordingly, for every MC-trial step the energy of the system needs to be minimal, with respect to the position of charges on springs (shells) relative to their countercharges (cores), as defined by eq. 5.4. The positions are not known *a priori*, but need to be calculated iteratively based on the force $\boldsymbol{F}_{D,i}$ acting on the shell charges, as

$$\boldsymbol{r}_{D,i}(n) = \frac{\boldsymbol{F}_{D,i}(n-1)}{k_D} \tag{5.16}$$

with the convergence criterion

$$\max_{i=1\ldots N} |\boldsymbol{r}_{D,i}(n) - \boldsymbol{r}_{D,i}(n-1)| < 10^{-3}\,\text{Å} \tag{5.17}$$

and n as the iteration number. This iterative scheme yielded good results for several tested systems[82,83].

5.2.3 Electrostatics

Compared to classical force fields, polarizable force fields require more extensive evaluations of electrostatic interactions, because, first, there are a higher number of charges in the system (2 for each polarizable dipole), and second, the iterative routine for calculating the positions of the shell charges requires repeated evaluation of acting forces. To calculate the electrostatic interactions efficiently, a Wolf summation with a shifted force approach[84] [Chapter 3] is used. The Wolf summation[85] is a spherical truncation method, which uses a charge-neutralization scheme within the cut-off sphere to describe the energy accurately. In previous studies it was shown that vapor-liquid equilibria can be calculated reliable using the Wolf summation[86,87] [Chapter 2]. To overcome the problem of force-discontinuities at the cut-off radius, a modified shifted force approach was applied to the Wolf summation, which describes the energy as well as the forces accurately[84] [Chapter 3]. The reliability of this method was investigated for vapor-liquid equilibria calculations in an ensemble with fluctuating particle number. The modified shifted force approach of the Wolf method is defined as

$$
\begin{aligned}
E^{\mathrm{mDSF}} =& \frac{1}{2}\sum_{i=1}^{N}\sum_{a=1}^{N_i^c}\sum_{\substack{j\neq i}}^{N}\sum_{b=1}^{N_j^c} q_{ia}q_{jb}\left[\frac{\mathrm{erfc}(\alpha r_{iajb})}{r_{iajb}} - \frac{\mathrm{erfc}(\alpha R_c)}{R_c} - \left(\frac{\partial\phi^{short}(r)}{\partial r}\right)_{r=R_c}\cdot\frac{\exp(\beta(r_{iajb}-R_c))-1}{\beta}\right] \\
&\quad \underset{\substack{(r_{iajb}<R_c)\\ \text{non bonded}}}{} \\
&+ \frac{1}{2}\sum_{i=1}^{N}\sum_{a=1}^{N_i^c}\sum_{b\neq a}^{N_i^c} q_{ia}q_{ib}\left[-\frac{\mathrm{erfc}(\alpha R_c)}{R_c} + \left(\frac{\partial\phi^{short}(r)}{\partial r}\right)_{r=R_c}\cdot\frac{1}{\beta}\right] \\
&\quad \underset{\text{bonded}}{} \\
&+ \frac{1}{2}\sum_{i=1}^{N}\sum_{a=1}^{N_i^c}\sum_{b\neq a}^{N_i^c} q_{ia}q_{ib}\left[\frac{\mathrm{erfc}(\alpha r_{iaib})}{r_{iaib}} - \left(\frac{\partial\phi^{short}(r)}{\partial r}\right)_{r=R_c}\cdot\frac{\exp(\beta(r_{iaib}-R_c))}{\beta}\right]\cdot(1-\psi_{i,ab}) \\
&\quad \underset{\text{bonded}}{} \\
&- \frac{1}{2}\left[\frac{\mathrm{erfc}(\alpha R_c)}{R_c} - \frac{1}{\beta}\left(\frac{\partial\phi^{short}(r)}{\partial r}\right)_{r=R_c}\right]\sum_{i=1}^{N}\sum_{a=1}^{N_i^c} q_{ia}^2
\end{aligned}
\tag{5.18}
$$

with index i and j counting molecules and a and b counting the partial charges in these molecules, respectively, N as the number of molecules, N_i^{c} as the number of partial charges of a particular molecule, q_{ia} as the partial charge, r_{iajb} as the distance between partial charge ia and jb, and R_c as the cut-off radius. The summation includes a damping parameter α and a parameter β which is associated with the cut-off radius. The electrostatic interactions of coulombic sites within a molecule, separated by up to three bonds apart are excluded. The operator $\psi_{i,ab}$ is introduced to exclude of intramolecular electrostatic interactions between sites less than three bonds apart: this operator is 1 for excluded electrostatic interactions and 0 for all other interactions. The derivative in above equation can be expressed as

$$\left(\frac{\partial \phi^{short}(r)}{\partial r}\right)_{r=R_c} = -\frac{2\alpha}{\sqrt{\pi}}\frac{\exp(-\alpha^2 R_c^2)}{R_c} - \frac{\mathrm{erfc}(\alpha R_c)}{R_c^2} \tag{5.19}$$

Despite the lengthy appearance of eq. 5.18 it is an expression of the interactions of electrostatics that is simple and effective in practical application. In our simulations we use a cut-off radius of 14 Å, with associated parameter $\beta = 0.3\,\text{Å}^{-1}$. To determine the best suited damping parameter α, which varies with density, we use an iterative scheme from our previous work[86] [Chapter 2].

If the Ewald summation[88] is employed to calculate the electrostatic potential, a maximum index of $k_{max} = 9$ in the Fourier space expansion and a damping factor of $\kappa = 7,59/L$ for a cubic box length of L is used[78] .

5.3 Results and Discussion

5.3.1 Alkanes

The Mie parameters determining the dispersion interactions between n-alkanes are obtained from the TAMie force-field (see Table 5.5). Adding polarazibility will not change the results for pure alkanes, but will modify predictions of mixture properties if any specie in the mixture is polar. To verify our MC implementation obeys this requirement, we determined the vapor-liquid properties of five n-alkanes (ethane, propane, n-butane, n-hexane, n-octane). We remark that in the non-polarizable TAMie force field ethane has a different Mie parameter set compared to the longer alkanes. The phase equilibrium properties are in excellent agreement with the results of the original TAMie force field. The absolute average deviation (AAD) of the simulated vapor pressure and the liquid density (observables of our objective function) compared to experimental data in the considered temperature range is 0.61% for ethane and 1.29% for all other investigated n-alkanes. For each component AADs of vapor pressure and liquid density, as well as enthalpy of vaporization and system-size dependent critical temperature (that is not part of the objective function) are shown in Table 5.6. All quantities are in excellent agreement with experimental data, which is also shown graphically in Fig. 5.1 – 5.3. For comparison, results of the non-polarizable TAMie force field and tabulated values with uncertainties are provided in the Supporting Information [Appendix D].

Table 5.5: Pair potential parameters of UA-groups: energy parameter ε, size parameter σ, repulsive exponent n, and point charge q for the PTAMie force field. The repulsive exponents n for all groups are taken from the classical TAMie force field[19,20,22] [Chapter 4].

	PTAMie					
pseudoatom i	$M_i/(\mathrm{g/mol})$	$\varepsilon_{ii}/k_B/\mathrm{K}$	$\sigma_{ii}/\mathrm{Å}$	n_{ii}	charge q_i/e	ref
CH_3 (sp^3)	15.035	136.318	3.6034	14	-	[19]
CH_2 (sp^3)	14.027	52.9133	4.04	14	-	[19]
CH_3 (sp^3) ethane	15.035	130.780	3.6463	14	-	[19]
O_{ether}	15.999	55.338	3.098	12	–0.3	this work
CH_x neighbor ether O					+0.15	this work
N≡	14.007	35.537	3.309	12	–0.482	this work
COM_{N_2}	-	-	-	-	+0.964	this work

Table 5.6: Absolute average deviations (saturation pressure p^{sat}, liquid density ρ^{L}, enthalpy of vaporization $\Delta^{\mathrm{LV}}h$, critical temperature T_c) of the PTAMie force field from quasi-experimental data[67–69].

substance	AAD $p^{\mathrm{sat}}/\%$	AAD $\rho^{\mathrm{L}}/\%$	AAD $\Delta^{\mathrm{LV}}h/\%$	AD $T_c/\%$
ethane	0.60	0.62	1.96	0.28
propane	0.84	0.48	1.73	0.47
n-butane	2.12	1.11	0.81	0.27
n-hexane	2.13	0.62	2.49	0.81
n-octane	2.54	0.46	1.71	1.00
dimethyl ether	2.21	1.18	0.66	0.75
diethyl ether	3.74	1.88	0.97	1.13
di-n-propyl ether	3.15	2.73	0.48	0.69
di-n-butyl ether	2.87	1.15	2.63	1.28
methyl ethyl ether	4.78	2.48	0.72	0.35
methyl n-propyl ether	2.35	1.42	–[a]	0.88
nitrogen	0.62	0.32	0.68	0.21

[a] no reasonable quasi-experimental data available

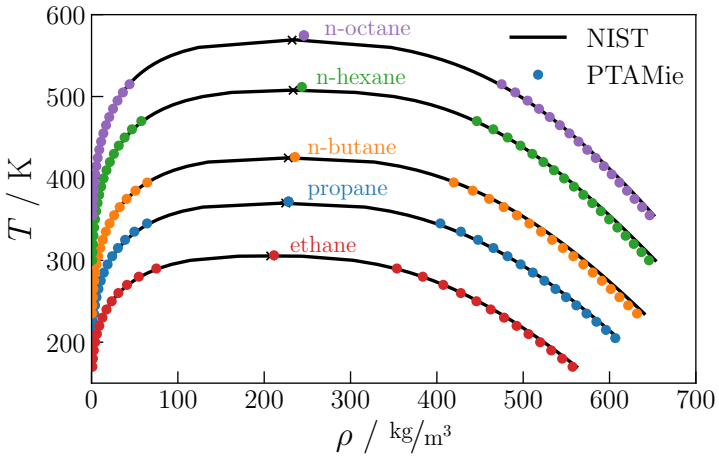

Figure 5.1: Vapor-liquid coexistence curve of simulated n-alkanes. Symbols represent simulation results for the PTAMie force field and black solid lines and crosses are quasi-experimental data[67]. Results coincide, within statistical uncertainty, to results from the TAMie force field.

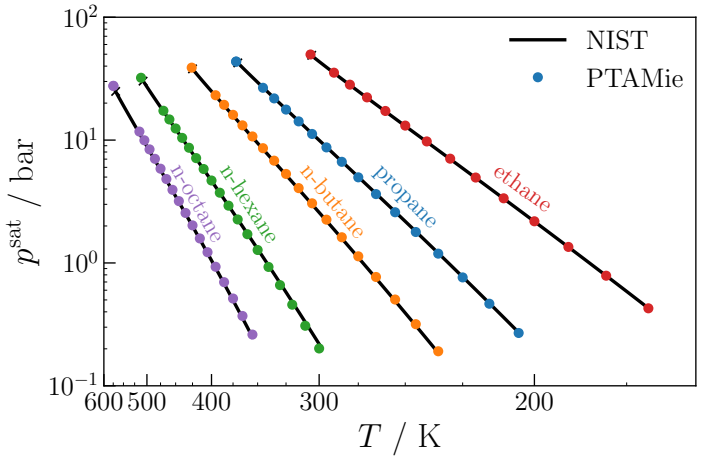

Figure 5.2: Vapor pressures of n-alkanes. Symbols represent simulation results for the PTAMie force field and solid lines are quasi-experimental data[67]. Results coincide, within statistical uncertainty, to results from the TAMie force field.

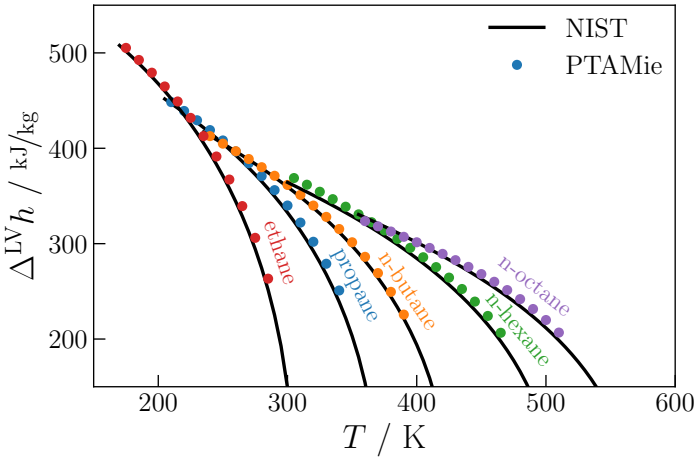

Figure 5.3: Enthalpy of vaporization of n-alkanes. Symbols represent simulation results for the PTAMie force field and solid lines are quasi-experimental data[67]. Results coincide, within statistical uncertainty, to results from the TAMie force field.

5.3.2 Ethers

In the non-polarizable TAMie force field, dimethyl-ether, as the smallest member of the homologous series of ethers was individually parameterized, whereas transferability of parameters was assumed for the remaining ethers[20,21]. For the polarizable force field we wish to include dimethyl ether together will all other ethers as part of a transferable ether-parameterization. The result is only one transferable set of parameters for the homologous series of ethers.

For the optimization of the force field parameters dimethyl ether, diethyl ether, and di-n-propyl ether are considered. The Mie potential parameters of the CH_3 and CH_2 groups are taken from the alkanes, whereas for the ether oxygen the Mie parameters ($\epsilon_{O(ether)}$, $\sigma_{O(ether)}$) are simultaneously adjusted for fixed static charges. The fixed charges are located at the position of ether oxygen (negative partial charge $q_{O(ether)}$) and the neighboring alkyl sites (positive counter charge with $q_{CH_x(ether)} = -0.5 \cdot q_{O(ether)}$). The static partial charge $q_{O(ether)}$ is a further degree of freedom, which is varied along a predefined grid. For each grid point the Mie potential parameters $\epsilon_{O(ether)}$, $\sigma_{O(ether)}$ are optimized.

Fig. 5.4 shows the results of the parameter optimization for varying static partial charges $q_{O(ether)}$. An optimum for our objective function (including p^{sat} and ρ^{L}) is found for a point charge of $q_{O(ether)} = -0.35\,e$, whereas for $q_{O(ether)} = -0.3\,e$ the deviation is only slightly larger. The optimum is found for a different value of the fixed partial charge as compared to our previous work for the non-polarizable ether force field[20]. For the non-polarizable force field, the optimal value of the partial charge for a simultaneous optimization of several ethers approached zero. A non-zero value was for the non-polarizable force field

enforced based on the observation that each ether optimized individually has, as expected, a non-zero partial charge.
For the polarizable force field, we decide to use a partial charge of $q_{\mathrm{O(ether)}} = -0.3\,\mathrm{e}$. For this value, the deviations for all three considered substances are approximately in the same range, as Fig. 5.4 shows. The optimized force field parameters are listed in Table 5.5.

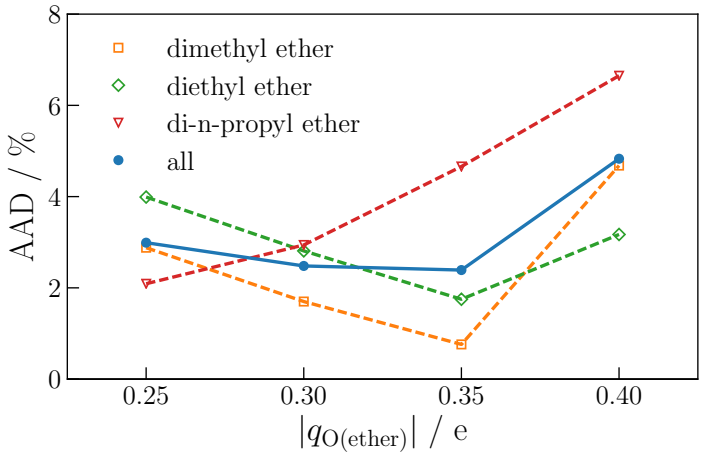

Figure 5.4: Simultaneous force field optimization for dimethyl ether, diethyl ether and di-n-propyl ether: Absolute average deviations of simulated vapor pressure and liquid density data to experimental data[68] for varying static partial charge $q_{\mathrm{O(ether)}}$ of the ether oxygen. The temperature range correspondents to $0.56 \leq T/T_c^{exp} \leq 0.96$. For each solid symbol the two parameters $\epsilon_{\mathrm{O(ether)}}$ and $\sigma_{\mathrm{O(ether)}}$ were optimized.

Simulation results for dimethyl ether, diethyl ether, and dipropyl ether, as members of the objective function, are in good agreement with experimental data (Table 5.6 and Fig. 5.4 – 5.7). The liquid density shows a higher deviation to experimental data than other typical force field parameterization. The liquid density is a quantity that is usually easy to reproduce accurately, when enforced in the parameter estimation procedure of a force field. In our approach, we use squared relative deviations to experimental liquid densities over large ranges of temperature with equal weight to squared relative deviations in vapor pressures. The resulting force field parameters are the optimal compromise for the chosen objective function and for the chosen molecular model (i.e. the functional form of the intermolecular interaction and the specifics of the intramolecular interactions), when applied to a collection of 3 ether substances. In comparison to the non-polarizable force field (see Supporting Information [Appendix D]) the AADs for diethyl ether and dipropyl ether are improved, whereas for dimethyl ether they deteriorated slightly.

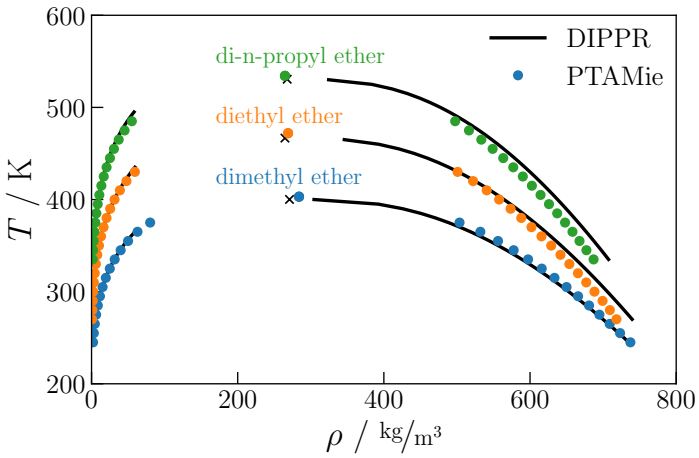

Figure 5.5: Vapor-liquid coexistence curve of simulated ethers. Symbols represent simulation results for the PTAMie force field and black solid lines and crosses are quasi-experimental data[68]. Quasi-Experimental vapor density is approximated up to $0.25 \cdot \rho_c$ using the second virial coefficient.

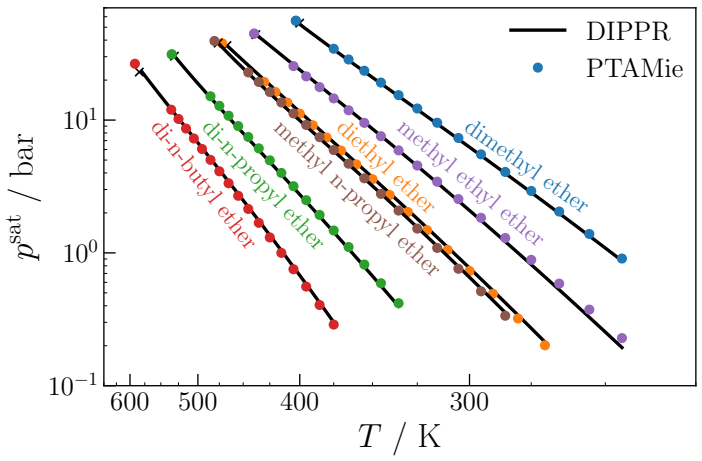

Figure 5.6: Vapor pressures of ethers. Symbols represent simulation results for the PTAMie force field and solid lines are quasi-experimental data[68].

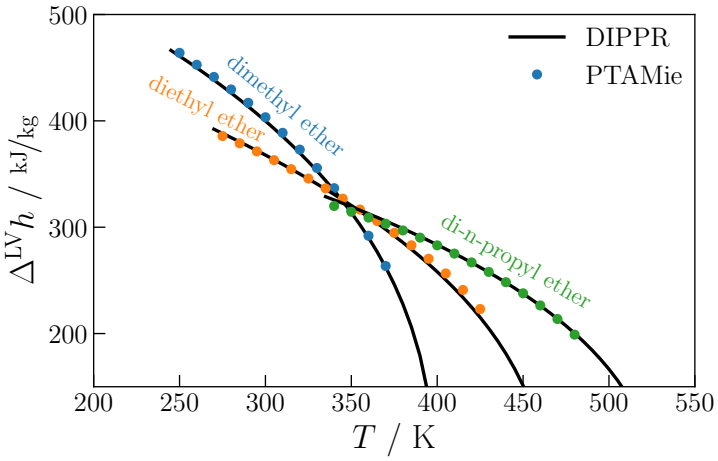

Figure 5.7: Enthalpy of vaporization of ethers. Symbols represent simulation results for the PTAMie force field and solid lines are quasi-experimental data[68].

Transferability of Parameters

The transferability of the force field parameters to ethers which are not part of the objective function is assessed considering di-n-butyl ether, methyl ethyl ether and methyl n-propyl ether. As shown in Fig. 5.6 and Fig. 5.8 – 5.9, the predictions are in good agreement with experimental data. Only for methyl ethyl ether the errors of vapor pressure and liquid density are slightly higher than for the two other substances. No experimental data for the enthalpy of vaporization of methyl n-propyl is reported in literature.

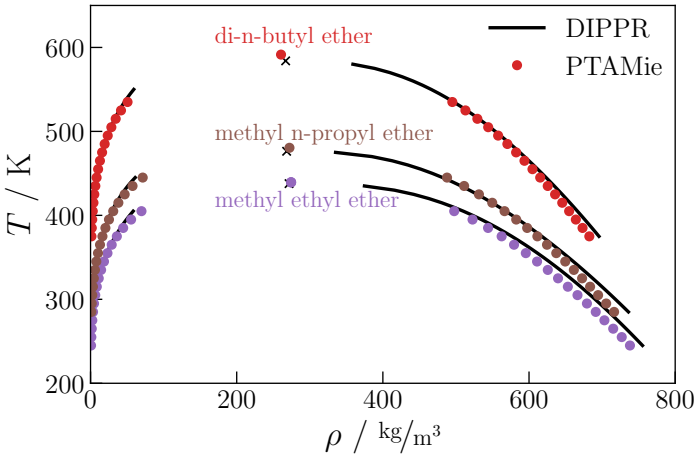

Figure 5.8: Vapor-liquid coexistence curve of simulated ethers. Symbols represent simulation results for the PTAMie force field and black solid lines and crosses are quasi-experimental data[68]. Quasi-Experimental vapor density is approximated up to $0.25 \cdot \rho_c$ using the second virial coefficient.

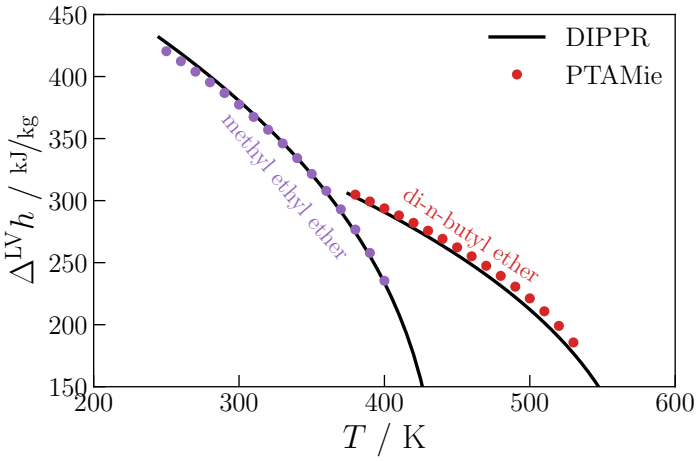

Figure 5.9: Enthalpy of vaporization of ethers. Symbols represent simulation results for the PTAMie force field and solid lines are quasi-experimental data[68].

5.3.3 Nitrogen

Nitrogen is rather polarizable but has a zero vacuum dipole moment, because it is a symmetric and linear molecule. It is modeled with three fixed static point charges, two negative charges on the nitrogen atom positions and a positive countercharge with twice the absolute value in the center, between the atoms. Introducing two polarizable dipole sites to the location of the nitrogen atoms has a rather small impact on thermodynamic properties of the pure substance. Nevertheless, including explicit polarizability could improve the prediction of mixture properties with polar substances.

The parameter optimization is done similarly as in the previous sections. As shown in Fig. 5.10, the deviations between results from molecular simulations and experimental data become smaller with decreasing charge. For charges lower than 1.01 e the AAD's decrease very slowly and the magnitude is within the statistical uncertainty. We choose a charge of $q_{\mathrm{COM(N_2)}} = +0.964\,\mathrm{e}$, because the charge distribution with this charge matches the experimental gas-phase quadrupol moment of nitrogen. The optimized parameters are summarized in Table 5.5.

For all calculated properties the AAD is lower than 0.7% (see Table 5.6) which is comparable to the non-polarizable TAMie force field. Overall, the simulation results are in excellent agreement to experimental data, as shown graphically in Figs. 5.11 - 5.13.

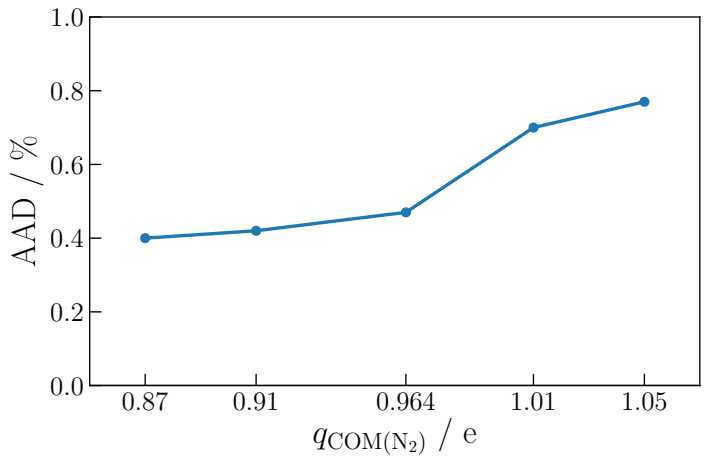

Figure 5.10: Force field optimization for nitrogen: Absolute average deviations of simulated vapor pressure and liquid density data to experimental data[69] for varying static partial charge $q_{\mathrm{COM(N_2)}}$ at the center of mass of the nitrogen molecule. The temperature range correspondents to $0.56 \leq T/T_c^{exp} \leq 0.96$. For each solid symbol the two parameters ϵ_{N} and σ_{N} were optimized.

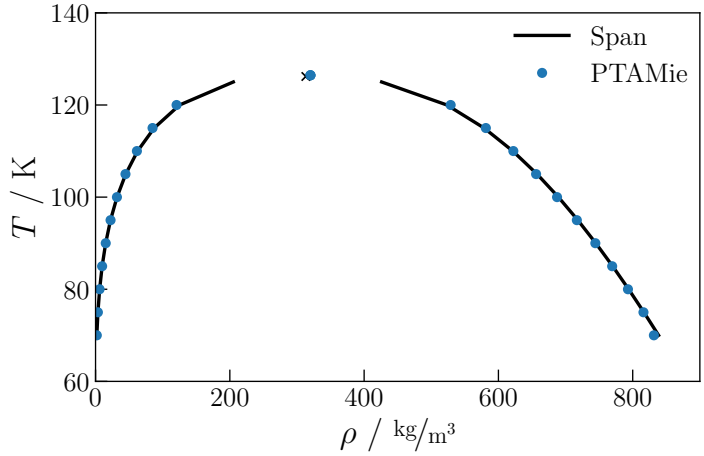

Figure 5.11: Vapor-liquid coexistence curve of nitrogen. Symbols represent simulation results for the PTAMie force field and black solid lines and crosses are quasi-experimental data[69].

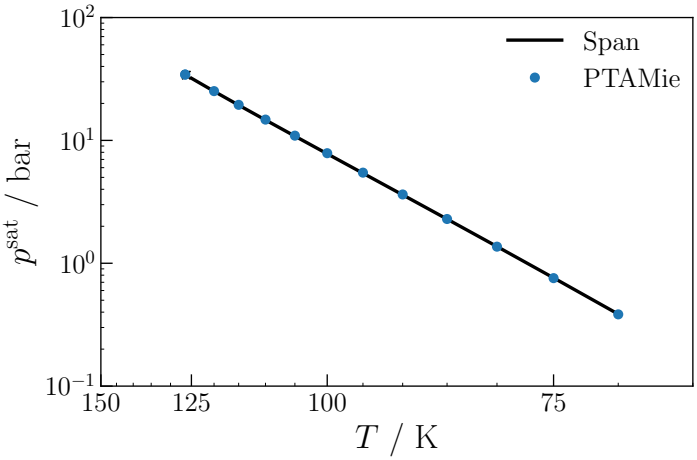

Figure 5.12: Vapor pressures of nitrogen. Symbols represent simulation results for the PTAMie force field and solid lines are quasi-experimental data[69].

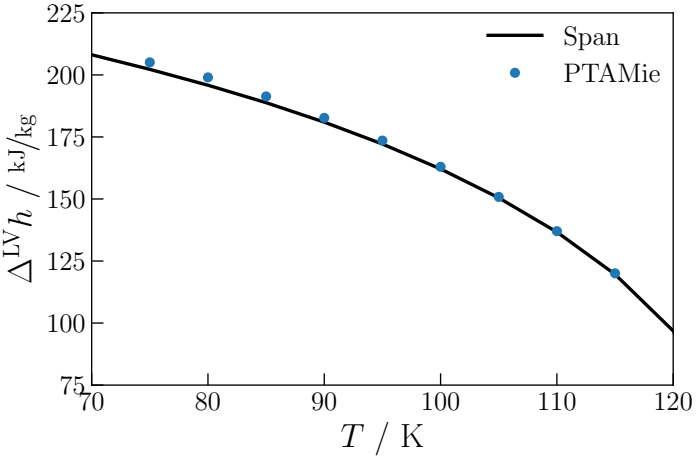

Figure 5.13: Enthalpy of vaporization of nitrogen. Symbols represent simulation results for the PTAMie force field and solid lines are quasi-experimental data[69].

5.3.4 Mixtures

Transferable force fields are particularly valuable for predicting the properties and phase equilibria of mixtures. In this study we compare predictions from a non-polarizable transferable force field (TAMie) to predictions from a polarizable transferable force field (PTAMie). The comparison is meaningful, because both force fields use the same intramolecular force field, and were parameterized using the same objective function with the same experimental data. The comparison thus singles out the role of polarizability in predicting phase equilibria.

Three binary mixtures, of non-polar species with weakly polar substances are here regarded. The vapor-liquid phase equilibria of n-hexane and nitrogen at 411 K, n-pentane and nitrogen at 398.3 K, and dimethyl ether and nitrogen at 318.15 K are shown in Fig. 5.14 - Fig. 5.16, respectively. Results from molecular simulation are found in good overall agreement with experimental data. For the n-alkane/nitrogen mixtures the bubble point pressure is slightly underestimated, whereas for the dimethyl ether/nitrogen mixture excellent agreement is obtained. It is important to observe that results obtained from the polarizable PTAMie force field almost coincide with results from the non-polarizable TAMie force field. Only for the mixture dimethyl ether/nitrogen we find slightly different results. The fact that no improvement from the polarizable force field can be observed compared to the non-polarizable case is somewhat expected for the rather weakly polar substances considered thusfar. The study of more polar mixtures requires a further extension of the force field. Results of the n-alkane/nitrogen mixtures can be further improved by using binary cross interaction parameters, as we showed in our previous work[22] [Chapter 4] for the non-polarizable TAMie force field.

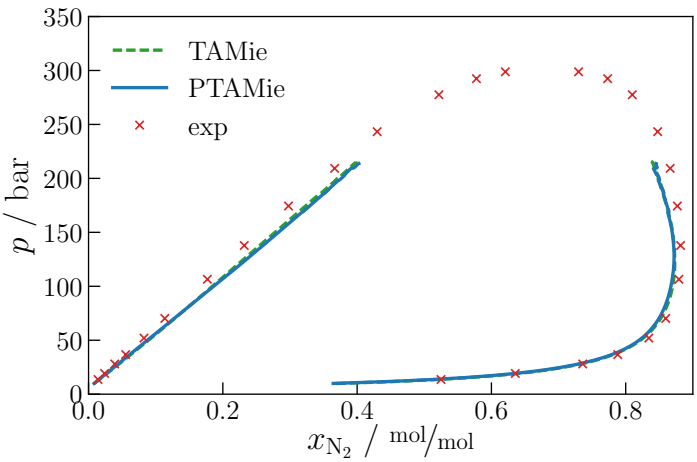

Figure 5.14: Vapor-liquid equilibria for a mixture of n-hexane and nitrogen at 411 K. Predictive simulation results using the non-polarizable TAMie (dashed green line) and polarizable PTAMie (solid blue line) force field are compared to experimental data[89] (red crosses).

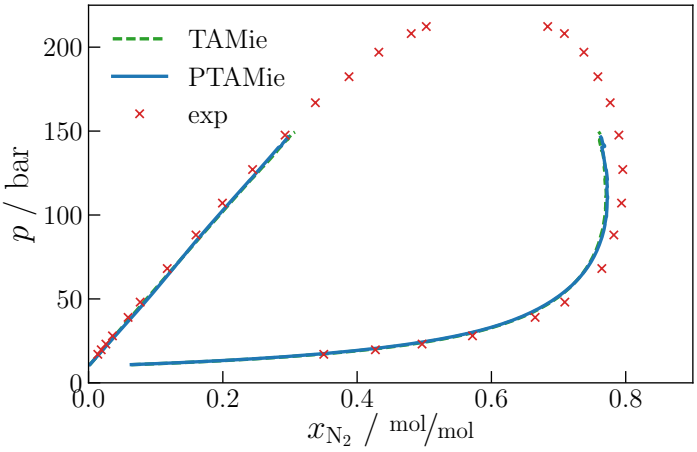

Figure 5.15: Vapor-liquid equilibria for a mixture of n-pentane and nitrogen at 398.3 K. Predictive simulation results using the non-polarizable TAMie (dashed green line) and polarizable PTAMie (solid blue line) force field are compared to experimental data[90] (red crosses).

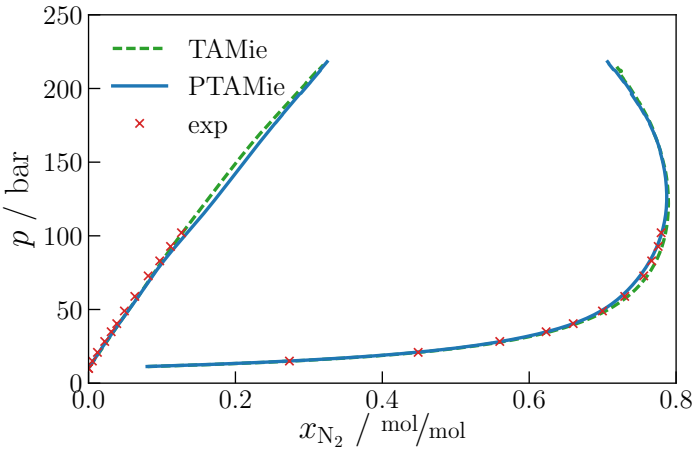

Figure 5.16: Vapor-liquid equilibria for a mixture of dimethyl ether and nitrogen at 318.15 K. Predictive simulation results using the non-polarizable TAMie (dashed green line) and polarizable PTAMie (solid blue line) force field are compared to experimental data[91] (red crosses).

5.4 Conclusion

A polarizable force field for n-alkanes, ethers and nitrogen based on the classical TAMie force field is proposed. Explicit electronic polarization is included using a charge-on-spring model located on all united-atom groups. The force field accurately predicts vapor pressures, enthalpies of vaporization, and to (a lesser extent) liquid densities over a wide range of conditions. Furthermore, the transferability of the parameters was assessed based

on the predictions of pure-component VLE of molecules within the homologous series and the predictions of the VLE of several binary mixtures. The results justify the use of non-polarizable TAMie force fields for mildly polar substances. We expect significant improvements for mixtures including strong polar components. The extension of the force field to such strongly polar components is considered in future work.

Bibliography

[1] Martin, M. G., and Siepmann, J. I. (1998) Transferable Potentials for Phase Equilibria. 1. United-Atom Description of n-Alkanes. *J. Phys. Chem. B 102*, 2569–2577.

[2] Martin, M. G., and Siepmann, J. I. (1999) Novel Configurational-Bias Monte Carlo Method for Branched Molecules. Transferable Potentials for Phase Equilibria. 2. United-Atom Description of Branched Alkanes. *J. Phys. Chem. B 103*, 4508–4517.

[3] Wick, C. D., Martin, M. G., and Siepmann, J. I. (2000) Transferable Potentials for Phase Equilibria. 4. United-Atom Description of Linear and Branched Alkenes and Alkylbenzenes. *J. Phys. Chem. B 104*, 8008–8016.

[4] Chen, B., Potoff, J. J., and Siepmann, J. I. (2001) Monte Carlo Calculations for Alcohols and Their Mixtures with Alkanes. Transferable Potentials for Phase Equilibria. 5. United-Atom Description of Primary, Secondary, and Tertiary Alcohols. *J. Phys. Chem. B 105*, 3093–3104.

[5] Potoff, J. J., and Siepmann, J. I. (2001) Vapor–liquid equilibria of mixtures containing alkanes, carbon dioxide, and nitrogen. *AIChE J. 47*, 1676–1682.

[6] Stubbs, J. M., Potoff, J. J., and Siepmann, J. I. (2004) Transferable Potentials for Phase Equilibria. 6. United-Atom Description for Ethers, Glycols, Ketones, and Aldehydes. *J. Phys. Chem. B 108*, 17596–17605.

[7] Wick, C. D., Stubbs, J. M., Rai, N., and J. Ilja Siepmann, W. (2005) Transferable Potentials for Phase Equilibria. 7. Primary, Secondary, and Tertiary Amines, Nitroalkanes and Nitrobenzene, Nitriles, Amides, Pyridine, and Pyrimidine. *J. Phys. Chem. B 109*, 18974–18982.

[8] Jorgensen, W. L., Madura, J. D., and Swenson, C. J. (1984) Optimized Intermolelcular Potential Functions for Liquid Hydrocarbons. *J. Am. Soc. 106*, 6638–6646.

[9] Jorgensen, W. L., and Swenson, C. J. (1985) Optimized Intermolelcular Potential Functions for Amides and Peptides. Structure and Properties of Liquid Amides. *J. Am. Soc. 107*, 569–578.

[10] Jorgensen, W. L., and Swenson, C. J. (1985) Optimized Intermolelcular Potential Functions for Amides and Peptides. Hydration of Amides. *J. Am. Soc. 107*, 1489–1496.

[11] Jorgensen, W. L. (1986) Optimized Intermolecular Potential Functions for Liquid Alcohols. *J. Phys. Chem. 90*, 1276–1284.

[12] Jorgensen, W. L., and Tirado-Rives, J. (1988) The OPLS Force Field for Proteins. Energy Minimization for Crystals of Cyclic Peptides and Crambin. *J. Am. Chem. Soc. 110(8)*, 1657–1666.

[13] Briggs, J. M., Matsui, T., and Jorgensen, W. L. (1990) Monte Carlo Simulations of Liquid Alkyl Ethers with the OPLS Potential Functions. *J. Comp. Chem. 11(8)*, 958–971.

[14] Ungerer, P., Beauvais, C., Delhommelle, J., Boutin, A., Rousseau, B., and Fuchs, A. H. (2000) Optimization of the anisotropic united atoms intermolecular potential for n-alkanes. *J. Chem. Phys. 112*, 5499–5510.

[15] Bourasseau, E., Haboudou, M., Boutin, A., Fuchs, A. H., and Ungerer, P. (2003) New optimization method for intermolecular potentials: Optimization of a new anisotropic united atoms potential for olefins: Prediction of equilibrium properties. *J. Chem. Phys. 118*, 3020–3034.

[16] Kranias, S., Pattou, D., Lévy, B., and Boutin, A. (2003) An optimized potential for phase equilibria calculation for ketone and aldehyde molecular fluids. *Phys. Chem. Chem. Phys. 5*, 4175–4179.

[17] Ferrando, N., Lachet, V., Teuler, J.-M., and Boutin, A. (2009) Transferable force field for alcohols and polyalcohols. *J. Phys. Chem. B 113*, 5985–5995.

[18] Ferrando, N., Lachet, V., Pérez-Pellitero, J., Mackie, A. D., Malfreyt, P., and Boutin, A. (2011) A transferable force field to predict phase equilibria and surface tension of ethers and glycol ethers. *J. Phys. Chem. B 115*, 10654–10664.

[19] Hemmen, A., and Gross, J. (2015) Transferable Anisotropic United-Atom Force Field Based on the Mie Potential for Phase Equilibrium Calculations: n-Alkanes and n-Olefins. *J. Phys. Chem. B 119*, 11695–11707.

[20] Hemmen, A., Panagiotopoulos, A. Z., and Gross, J. (2015) Grand Canonical Monte Carlo Simulations Guided by an Analytic Equation of State - Transferable Anisotropic Mie Potentials for Ethers. *J. Phys. Chem. B 119*, 7087–7099.

[21] Weidler, D., and Gross, J. (2016) Transferable Anisotropic United-Atom Force Field Based on the Mie Potential for Phase Equilibria: Aldehydes, Ketones, and Small Cyclic Alkanes. *Ind. Eng. Chem. Res. 55*, 12123–12132.

[22] Waibel, C., Stierle, R., and Gross, J. (2018) Transferability of cross-interaction pair potentials: Vapor-liquid phase equilibria of n-alkane/nitrogen mixtures using the TAMie force field. *Fluid Phase Equilibr. 456*, 124–130.

[23] Weidler, D., and Gross, J. (2018) Individualized force fields for alkanes, olefins, ethers and ketones based on the transferable anisotropic Mie potential. *Fluid Phase Equilibr.*

[24] Rappe, A. K., and Goddard III, W. A. (1991) Charge equilibration for molecular dynamics simulations. *The Journal of Physical Chemistry 95*, 3358–3363.

[25] Rick, S. W., Stuart, S. J., and Berne, B. J. (1994) Dynamical fluctuating charge force fields: Application to liquid water. *J. Chem. Phys. 101*, 6141–6156.

[26] Vesely, F. J. (1977) N-particle dynamics of polarizable Stockmayer-type molecules. *J. Comput. Phys. 24*, 361–371.

[27] Drude, P. *Lehrbuch der Optik*; S. Hirzel: Leipzig, 1900.

[28] Born, M., and Huang, K. *Dynamical theory of crystal lattices*; Clarendon press: London, 1954.

[29] Straatsma, T., and McCammon, J. (1990) Molecular dynamics simulations with interaction potentials including polarization development of a noniterative method and application to water. *Molecular Simulation 5*, 181–192.

[30] Yu, H., and Van Gunsteren, W. F. (2005) Accounting for polarization in molecular simulation. *Computer Physics Communications 172*, 69–85.

[31] Rick, S. W., and Stuart, S. J. (2002) Potentials and algorithms for incorporating polarizability in computer simulations. *Reviews in computational chemistry 18*, 89–146.

[32] Cieplak, P., Dupradeau, F.-Y., Duan, Y., and Wang, J. (2009) Polarization effects in molecular mechanical force fields. *Journal of Physics: Condensed Matter 21*, 333102.

[33] Applequist, J., Carl, J. R., and Fung, K.-K. (1972) Atom dipole interaction model for molecular polarizability. Application to polyatomic molecules and determination of atom polarizabilities. *Journal of the American Chemical Society 94*, 2952–2960.

[34] Thole, B. T. (1981) Molecular polarizabilities calculated with a modified dipole interaction. *Chem. Phys. 59*, 341–350.

[35] Miller, K. J. (1990) Calculation of the molecular polarizability tensor. *Journal of the American Chemical Society 112*, 8543–8551.

[36] Van Duijnen, P. T., and Swart, M. (1998) Molecular and atomic polarizabilities: Thole's model revisited. *The Journal of Physical Chemistry A 102*, 2399–2407.

[37] Wang, J., Cieplak, P., Li, J., Hou, T., Luo, R., and Duan, Y. (2011) Development of polarizable models for molecular mechanical calculations I: parameterization of atomic polarizability. *J. Phys. Chem. B 115*, 3091–3099.

[38] Blair, S. A., and Thakkar, A. J. (2014) Relating polarizability to volume, ionization energy, electronegativity, hardness, moments of momentum, and other molecular properties. *J. Chem. Phys. 141*, 074306.

[39] Vosmeer, C. R., Rustenburg, A. S., Rice, J. E., Horn, H. W., Swope, W. C., and Geerke, D. P. (2012) QM/MM-based fitting of atomic polarizabilities for use in condensed-phase biomolecular simulation. *Journal of chemical theory and computation 8*, 3839–3853.

[40] Vosmeer, C. R., Kiewisch, K., Keijzer, K., Visscher, L., and Geerke, D. P. (2014) A comparison between QM/MM and QM/QM based fitting of condensed-phase atomic polarizabilities. *Physical Chemistry Chemical Physics 16*, 17857–17862.

[41] Stern, H. A., Kaminski, G. A., Banks, J. L., Zhou, R., Berne, B., and Friesner, R. A. (1999) Fluctuating charge, polarizable dipole, and combined models: parameterization from ab initio quantum chemistry. *J. Phys. Chem. B 103*, 4730–4737.

[42] Banks, J. L., Kaminski, G. A., Zhou, R., Mainz, D. T., Berne, B. J., and Friesner, R. A. (1999) Parametrizing a polarizable force field from ab initio data. I. The fluctuating point charge model. *J. Chem. Phys. 110*, 741–754.

[43] Kaminski, G. A., Stern, H. A., Berne, B. J., and Friesner, R. A. (2004) Development of an accurate and robust polarizable molecular mechanics force field from ab initio quantum chemistry. *The Journal of Physical Chemistry A 108*, 621–627.

[44] Anisimov, V. M., Lamoureux, G., Vorobyov, I. V., Huang, N., Roux, B., and MacKerell, A. D. (2005) Determination of electrostatic parameters for a polarizable force field based on the classical Drude oscillator. *Journal of Chemical Theory and Computation 1*, 153–168.

[45] Patel, S., and Brooks, C. L. (2004) CHARMM fluctuating charge force field for proteins: I parameterization and application to bulk organic liquid simulations. *J. Comput. Chem. 25*, 1–16.

[46] Davis, J. E., Warren, G. L., and Patel, S. (2008) Revised charge equilibration potential for liquid alkanes. *J. Phys. Chem. B 112*, 8298–8310.

[47] Davis, J. E., and Patel, S. (2010) Revised charge equilibration parameters for more accurate hydration free energies of alkanes. *Chemical physics letters 484*, 173–176.

[48] Xie, W., Pu, J., MacKerell, A. D., and Gao, J. (2007) Development of a polarizable intermolecular potential function (PIPF) for liquid amides and alkanes. *Journal of chemical theory and computation 3*, 1878–1889.

[49] MacKerell, A. D. et al. (1998) All-Atom Empirical Potential for Molecular Modeling and Dynamics Studies of Proteins. *J. Phys. Chem. B 102*, 3586–3616.

[50] Vorobyov, I. V., Anisimov, V. M., and MacKerell, A. D. (2005) Polarizable empirical force field for alkanes based on the classical drude oscillator model. *J. Phys. Chem. B 109*, 18988–18999.

[51] Lemkul, J. A., Huang, J., Roux, B., and MacKerell Jr, A. D. (2016) An empirical polarizable force field based on the classical drude oscillator model: development history and recent applications. *Chemical reviews 116*, 4983–5013.

[52] Szklarczyk, O. M., Bachmann, S. J., and van Gunsteren, W. F. (2014) A polarizable empirical force field for molecular dynamics simulation of liquid hydrocarbons. *J. Comput. Chem. 35*, 789–801.

[53] Oostenbrink, C., Villa, A., Mark, A. E., and Van Gunsteren, W. F. (2004) A biomolecular force field based on the free enthalpy of hydration and solvation: the GROMOS force-field parameter sets 53A5 and 53A6. *J. Comput. Chem. 25*, 1656–1676.

[54] Baker, C. M., and MacKerell, A. D. (2010) Polarizability rescaling and atom-based Thole scaling in the CHARMM Drude polarizable force field for ethers. *Journal of molecular modeling 16*, 567–576.

[55] Vorobyov, I., Anisimov, V. M., Greene, S., Venable, R. M., Moser, A., Pastor, R. W., and MacKerell, A. D. (2007) Additive and classical drude polarizable force fields for linear and cyclic ethers. *Journal of chemical theory and computation 3*, 1120–1133.

[56] Jordan, P. C., van Maaren, P. J., Mavri, J., van der Spoel, D., and Berendsen, H. J. (1995) Towards phase transferable potential functions: Methodology and application to nitrogen. *J. Chem. Phys. 103*, 2272–2285.

[57] Yu, K., McDaniel, J. G., and Schmidt, J. (2011) Physically motivated, robust, ab initio force fields for CO2 and N2. *J. Phys. Chem. B 115*, 10054–10063.

[58] Lamoureux, G., and Roux, B. (2003) Modeling induced polarization with classical Drude oscillators: Theory and molecular dynamics simulation algorithm. *J. Chem. Phys. 119*, 3025–3039.

[59] Visscher, K. M., Vosmeer, C. R., Luirink, R. A., and Geerke, D. P. (2017) A systematic approach to calibrate a transferable polarizable force field parameter set for primary alcohols. *J. Comput. Chem. 38*, 508–517.

[60] Lorentz, H. (1881) Ueber die Anwendung des Satzes vom Virial in der kinetischen Theorie der Gase. *Ann. Phys. 248*, 127–136.

[61] Berthelot, D. (1898) Sur le mélange des gaz. *Compt. Rendus 126*, 1703–1706.

[62] Potoff, J. J., and Bernard-Brunel, D. A. (2009) Mie potentials for phase equilibria calculations: Application to alkanes and perfluoroalkanes. *J. Phys. Chem. B 113*, 14725–14731.

[63] Toxvaerd, S. (1990) Molecular dynamics calculation of the equation of state of alkanes. *J. Chem. Phys. 93*, 4290–4295.

[64] Van der Ploeg, P., and Berendsen, H. (1982) Molecular dynamics simulation of a bilayer membrane. *J. Chem. Phys. 76*, 3271–3276.

[65] van Westen, T., Vlugt, T. J., and Gross, J. (2011) Determining force field parameters using a physically based equation of state. *J. Phys. Chem. B 115*, 7872–7880.

[66] Gross, J., and Sadowski, G. (2001) Perturbed-chain SAFT: An equation of state based on a perturbation theory for chain molecules. *Ind. Eng. Chem. Res. 40*, 1244–1260.

[67] Linstrom, P., and Mallard, W., Eds. *NIST Chemistry WebBook, NIST Standard Reference Database Number 69*; National Institute of Standards and Technology: Gaithersburg MD, 20899; http://doi.org/10.18434/T4D303, (retrieved May 2013).

[68] Rowley, R. L., Wilding, W. V., Oscarson, J. L., Yang, Y., Zundel, N. A., Daubert, T. E., and Danner, R. P. *DIPPR Data Compilation of Pure Chemical Properties*; AIChE, New York, 2009.

[69] Span, R., Lemmon, E. W., Jacobsen, R. T., Wagner, W., and Yokozeki, A. (2000) A Reference Equation of State for the Thermodynamic Properties of Nitrogen for Temperatures from 63.151 to 1000 K and Pressures to 2200 MPa. *J. Phys. Chem. Ref. Data 29*, 1361–1433.

[70] Errington, J. R. (2003) Direct calculation of liquid–vapor phase equilibria from transition matrix Monte Carlo simulation. *J. Chem. Phys. 118*, 9915–9925.

[71] Paluch, A. S., Shen, V. K., and Errington, J. R. (2008) Comparing the use of Gibbs ensemble and grand-canonical transition-matrix Monte Carlo methods to determine phase equilibria. *Ind. Eng. Chem. Res. 47*, 4533–4541.

[72] Virnau, P., and Müller, M. (2004) Calculation of free energy through successive umbrella sampling. *J. Chem. Phys. 120*, 10925–10930.

[73] Ferrenberg, A. M., and Swendsen, R. H. (1989) Optimized monte carlo data analysis. *Phys. Rev. Lett. 63*, 1195.

[74] Wilding, N. B. (1995) Critical-point and coexistence-curve properties of the Lennard-Jones fluid: a finite-size scaling study. *Phys. Rev. E 52*, 602.

[75] Panagiotopoulos, A. Z., Wong, V., and Floriano, M. A. (1998) Phase equilibria of lattice polymers from histogram reweighting Monte Carlo simulations. *Macromolecules 31*, 912–918.

[76] Potoff, J. J., and Panagiotopoulos, A. Z. (1998) Critical point and phase behavior of the pure fluid and a Lennard-Jones mixture. *J. Chem. Phys. 109*, 10914–10920.

[77] Moučka, F., Nezbeda, I., and Smith, W. R. (2013) Computationally efficient Monte Carlo simulations for polarisable models: multi-particle move method for water and aqueous electrolytes. *Mol. Simulat. 39*, 1125–1134.

[78] Allen, M. P., and Tildesley, D. J. *Computer simulation of liquids*; Oxford University Press: New York, 1987.

[79] Smit, B. (1992) Phase diagrams of Lennard-Jones fluids. *J. Chem. Phys. 96*, 8639–8640.

[80] Siepmann, J. I., and Frenkel, D. (1992) Configurational bias Monte Carlo: a new sampling scheme for flexible chains. *Mol. Phys. 75*, 59–70.

[81] Frenkel, D., Mooij, G., and Smit, B. (1992) Novel scheme to study structural and thermal properties of continuously deformable molecules. *J. Phys. Condens. Matter 4*, 3053.

[82] Jiang, H., Moultos, O. A., Economou, I. G., and Panagiotopoulos, A. Z. (2016) Gaussian-charge polarizable and nonpolarizable models for CO2. *J. Phys. Chem. B 120*, 984–994.

[83] Jiang, H., Economou, I. G., and Panagiotopoulos, A. Z. (2017) Phase equilibria of water/CO2 and water/n-alkane mixtures from polarizable models. *J. Phys. Chem. B 121*, 1386–1395.

[84] Waibel, C., Simon, F. M., and Gross, J. A Modified Shifted Force Approach to the Wolf Summation. *Submitted to J. Chem. Theory Comput.*

[85] Wolf, D., Keblinski, P., Phillpot, S., and Eggebrecht, J. (1999) Exact method for the simulation of Coulombic systems by spherically truncated, pairwise r^{-1} summation. *J. Chem. Phys. 110*, 8254–8282.

[86] Waibel, C., and Gross, J. (2018) Modification of the Wolf Method and Evaluation for Molecular Simulation of Vapor–Liquid Equilibria. *J. Chem. Theory Comput. 14*, 2198–2206.

[87] Hens, R., and Vlugt, T. J. (2018) Molecular Simulation of Vapor–Liquid Equilibria Using the Wolf Method for Electrostatic Interactions. *J. Chem. Eng. Data 63*, 1096–1102.

[88] Ewald, P. P. (1921) Die Berechnung optischer und elektrostatischer Gitterpotentiale. *Ann. Phys. 369*, 253–287.

[89] Eliosa-Jiménez, G., Silva-Oliver, G., García-Sánchez, F., and de Ita de la Torre, A. (2007) High-Pressure Vapor- Liquid Equilibria in the Nitrogen+ n-Hexane System. *J. Chem. Eng. Data 52*, 395–404.

[90] Silva-Oliver, G., Eliosa-Jiménez, G., García-Sánchez, F., and Avendaño-Gómez, J. R. (2006) High-pressure vapor–liquid equilibria in the nitrogen–n-pentane system. *Fluid Phase Equilibr. 250*, 37–48.

[91] Laursen, T., Rasmussen, P., and Andersen, S. I. (2002) VLE and VLLE measurements of dimethyl ether containing systems. *J. Chem. Eng. Data 47*, 198–202.

Chapter 6

Conclusion

Monte Carlo simulations in the grand canonical ensemble are carried out to calculate vapor-liquid phase equilibria for multiple substances. The underlying behavior of the molecules is represented by force fields, which in most cases contain electrostatic interactions. Evaluation of these electrostatic interactions usually requires computational demanding algorithms. For more efficient calculations a new self-energy term for the Wolf summation, a damped and cutoff-neutralized spherically truncation method, is proposed, leading to an improved description of the energy, especially for open ensembles (i.e. for systems with fluctuating particle number). The original Wolf summation produces discontinuities in the resulting forces. Application of a naive shifted force approach reduces this shortcoming, but impairs the energy description. Therefore, in this thesis a modified shifted force extension is proposed, describing the energy as well as the forces accurately. Both methods are used to calculate vapor-liquid equilibria of dimethyl ether, methanol, acetone, and SPC/E water as well as binary mixtures using classical force fields, which only require calculation of energies in Monte Carlo simulations. All results are in good agreement with results of the Ewald summation, which is seen as the reference in this study. Self-diffusion coefficients and shear viscosities are calculated with molecular dynamics simulations to assess the accuracy of the forces of the modified shifted force approach. Furthermore, the vapor-liquid equilibria of a polarizable Stockmayer fluid is calculated with Monte Carlo simulations, requiring an accurate description of both, energy and forces. All modified shifted force results are in good agreement with the Ewald summation results. An advantage of the proposed pairwise cutoff methods is the approximately linear scaling with system size, while maintaining an accurate description of energy and forces. This allows computationally more efficient simulations, and provides an alternative to the Ewald summation.

The quality of molecular simulation results depends strongly on the used force fields. Mixture properties can be improved using cross-wise van der Waals energy parameters. In this thesis the cross energy parameters for individual pairs of (united-) atom groups in n-

alkane/nitrogen mixtures are adjusted to a training set of three mixtures using an analytic equation of state. Additionally, transferability to other temperatures and mixtures, which are not included in the training set, is investigated. Good agreement with experimental data is obtained for all mixtures, and, therefore, the cross-energy parameters can be assumed transferable.

Another possibility to improve simulation results is a more detailed description of the energy landscape of molecules. The electron distribution of a molecule, which depends on its environment, can be described more realistically by adding explicit electronic polarization to the force field. In this thesis a polarizable transferable force field for n-alkanes, ethers, and nitrogen based on the non-polarizable TAMie force field is developed using the charge-on-spring model to include polarization effects. Vapor-liquid equilibria properties predicted with this force field are in good agreement with experimental data, but only small improvements in contrast to the non-polarizable case are realized. Also, for mixtures, where the influence of the surrounding environment should have bigger effects, solely minor improvement can be achieved. This might be due to the fact, that only weakly polar substances are studied in this thesis. Whether improvements can be realized for mixtures with strong polar substances, justifying the significantly higher computational effort for polarizable force fields, should be studied in future work.

Appendices

Appendix A

Supporting Information to Chapter 2

A.1 Further Vapor-Liquid Equilibria Results

In this section relative deviations of vapor pressures and coexisting liquid and vapor densities for further volumes and cut off radii are presented.

$V = 33000\,\text{Å}^3$, $R_c = 16\,\text{Å}$

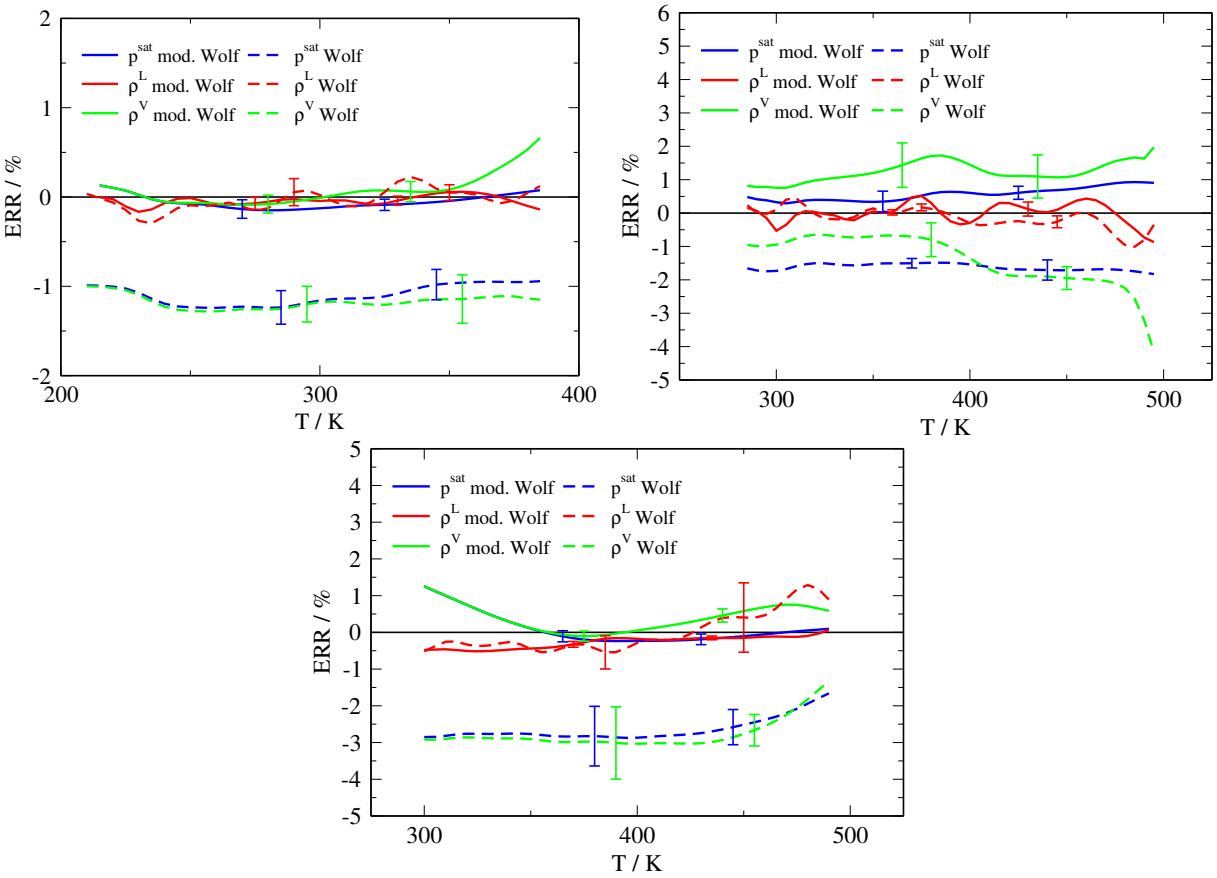

Figure A.1: Relative deviation of vapor liquid equilibrium properties (vapor pressure p^{sat}, coexisting liquid and vapor density ρ^L, ρ^V) over temperature T for a dimethyl ether system (top left) and methanol system (top right) and acetone system (bottom) with a volume of $33000\,\text{Å}^3$ and a cut-off radius of $R_c = 16\,\text{Å}$. The continuous lines represent the modified Wolf summation, and the dashed lines represent the original Wolf summation.

$V = 64000\,\text{Å}^3$, $R_c = 14\,\text{Å}$

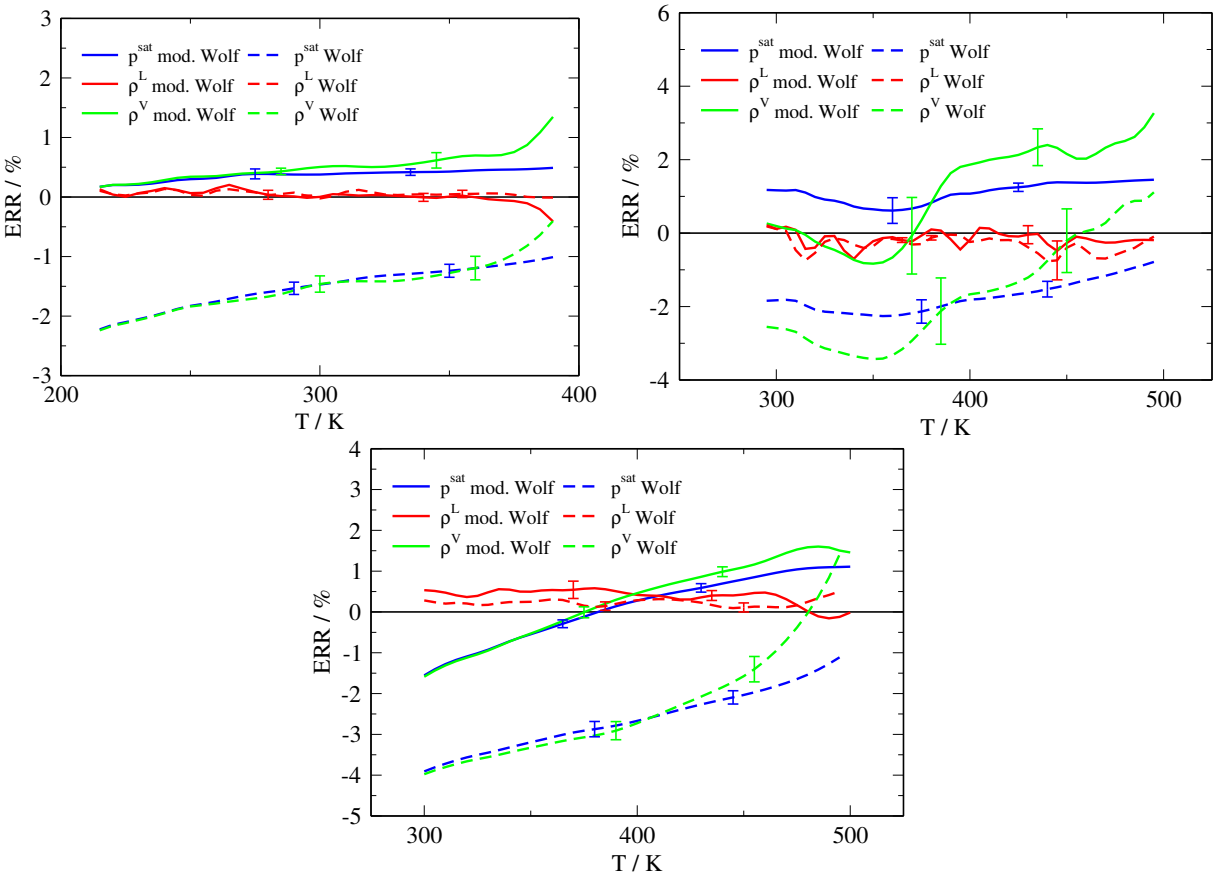

Figure A.2: Relative deviation of vapor liquid equilibrium properties (vapor pressure p^{sat}, coexisting liquid and vapor density ρ^L, ρ^V) over temperature T for a dimethyl ether system (top left), methanol system (top right) and acetone system (bottom) with a volume of $64000\,\text{Å}^3$ and a cut-off radius of $R_c = 14\,\text{Å}$. The continuous lines represent the modified Wolf summation, and the dashed lines represent the original Wolf summation.

$V = 64000\,\text{Å}^3$, $R_c = 16\,\text{Å}$

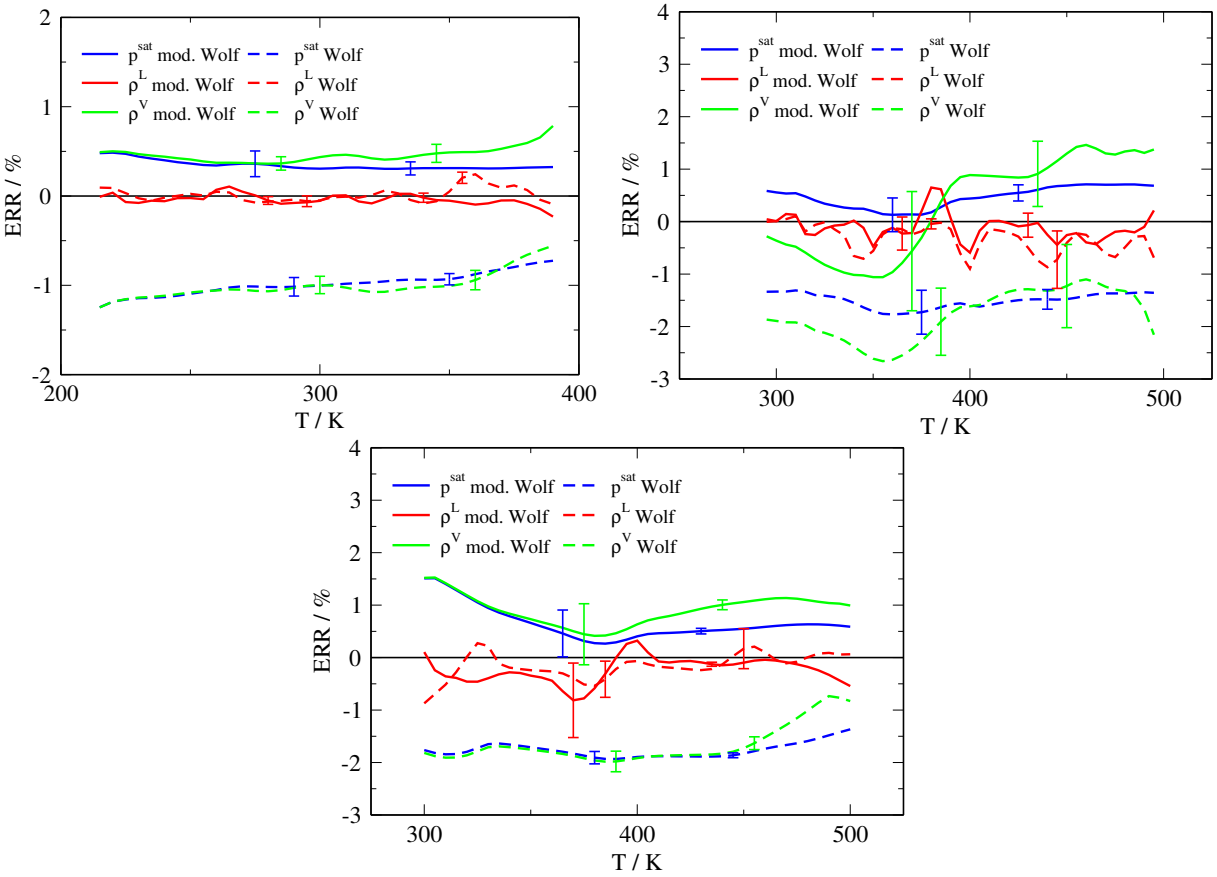

Figure A.3: Relative deviation of vapor liquid equilibrium properties (vapor pressure p^{sat}, coexisting liquid and vapor density ρ^L, ρ^V) over temperature T for a dimethyl ether system (top left), methanol system (top right) and acetone system (bottom) with a volume of $64000\,\text{Å}^3$ and a cut-off radius of $R_c = 16\,\text{Å}$. The continuous lines represent the modified Wolf summation, and the dashed lines represent the original Wolf summation.

Appendix B

Supporting Information to Chapter 3

B.1 Details of the Configurational Bias Scheme

The statistics of insertion, deletion and reconfiguration is improved using a configurational bias (CBMC) scheme with N_{CBMC} trial positions per CBMC-group of interaction sites. The number of trial steps is increased from $N_{\mathrm{CBMC}} = 1$ for low densities up to $N_{\mathrm{CBMC}} = 8$ for high densities. As a criterion for increasing the number of CBMC-steps the particle number N^* is used. For pure substances the dimensionless particle number is defined as $N^* = N/N^{\max}$, where $N^{\max}$ is the highest particle number for which simulations are performed. For mixtures a simple arithmetic average $N^* = N_1/N_1^{\max} + N_2/N_2^{\max}$ is applied. The number of CBMC-trial steps for a dimensionless particle number are shown in Table B.1.

Table B.1: Number of CBMC steps for different dimensionless particle numbers.

N^*	CBMC steps per site
$< 1/2.7$	1
$\geq 1/2.7 \wedge < 1/1.9$	2
$\geq 1/1.9 \wedge < 1/1.6$	3
$\geq 1/1.6 \wedge < 1/1.3$	4
$\geq 1/1.3 \wedge < 1/1.16$	6
$\geq 1/1.16$	8

B.2 Self Term of the Original Shifted Force Wolf Summation

In this section two assumptions about the self term of the original damped shifted force method are evaluated. The self term of the original Wolf summation

$$E^{\text{DSP, self}} = -\left[\frac{\operatorname{erfc}(\alpha R_c)}{2R_c} + \frac{\alpha}{\pi^{1/2}}\right] \sum_{i=1}^{N} q_i^2 \tag{B.1}$$

is compared to the self term resulting from the general form of the Wolf summation using a shifted force approach

$$E^{\text{DSF, self}} = -\left[\frac{\operatorname{erfc}(\alpha R_c)}{2R_c} - \left(\frac{\partial \phi^{\text{short}}(r)}{\partial r}\right)_{r=R_c} \cdot \frac{R_c}{2} + \frac{\alpha}{\pi^{1/2}}\right] \sum_{i=1}^{N} q_i^2 \tag{B.2}$$

by calculating phase equilibrium properties in the grand canonical ensemble. There are no appreciable differences between the two assumptions, as can be seen in Fig. B.1. But if the self term is neglected altogether, no sensible results can be obtained in the grand canonical ensemble.

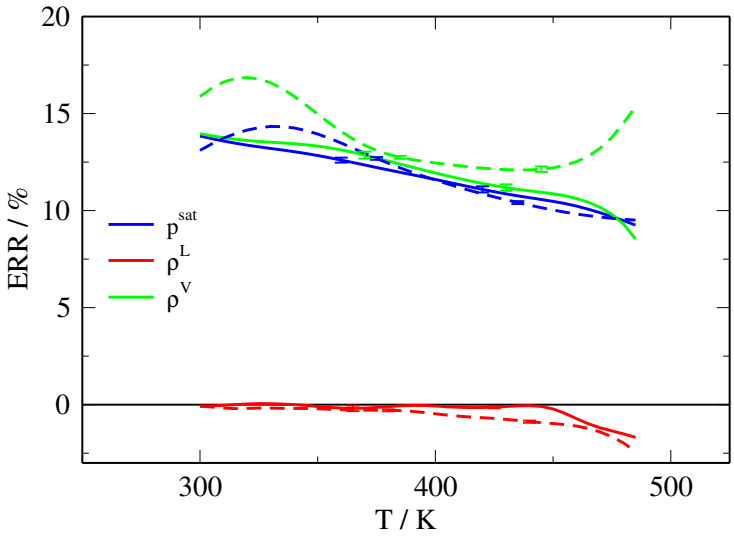

Figure B.1: Relative deviation of vapor liquid equilibrium properties (vapor pressure p^{sat}, coexisting liquid and vapor density ρ^{L}, ρ^{V}) over temperature T for acetone (TAMie force field[1], $V = 33000\,\text{Å}^3$, $R_c = 14\,\text{Å}$). The continuous lines represent the original Wolf shifted force summation with the self term of the original Wolf summation, and the dashed lines represent the original Wolf shifted force summation with a self term resulting from the general form of the Wolf summation.

B.3 Energy Conservation

The energy conservation of the modified damped shifted force method is assessed by calculating the energy with a molecular dynamics simulation in the microcanonical ensemble (NVE) and comparing the fluctuations of the energy with the mean energy. In Fig. B.2 the energy fluctuations over time are shown, also for the Ewald summation and the damped shifted force method. For all methods the energy has only small fluctuations around the mean energy. This implies an accurate energy conservation. The deviation between the Ewald summation and the mDSF method is slightly higher compared to the deviation between the Ewald summation and the DSF method. But a closer look at the single energy contributions and the temperature in Fig. B.3 shows that the mDSF method has lower deviations to the Ewald summation than the DSF method. The better behavior for the total energy results only from a cancellation of errors.

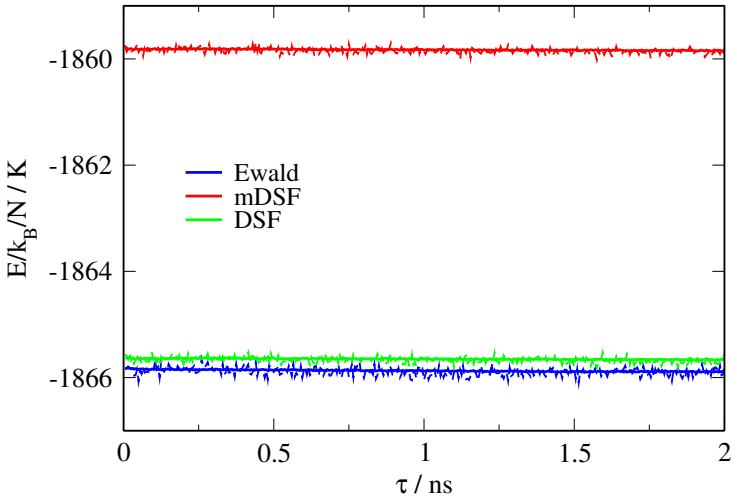

Figure B.2: Running average (solid line) and current value (dashed line) of the system energy over time for a acetone system in a NVE molecular dynamics simulation in the production period for Ewald summation, modified damped shifted force method (mDSF) and damped shifted force method (DSF). The starting energy of the molecular dynamics simulation after the previous Monte Carlo run is set to $^{E^{\mathrm{pot+kin}}}/_{k_B N} = -3203\,\mathrm{K}$ and the other simulation parameters are $N = 500$, $V = 61456\,\text{Å}^3$, $R_c = 14\,\text{Å}$, and $\beta = 0.3\,\text{Å}^{-1}$.

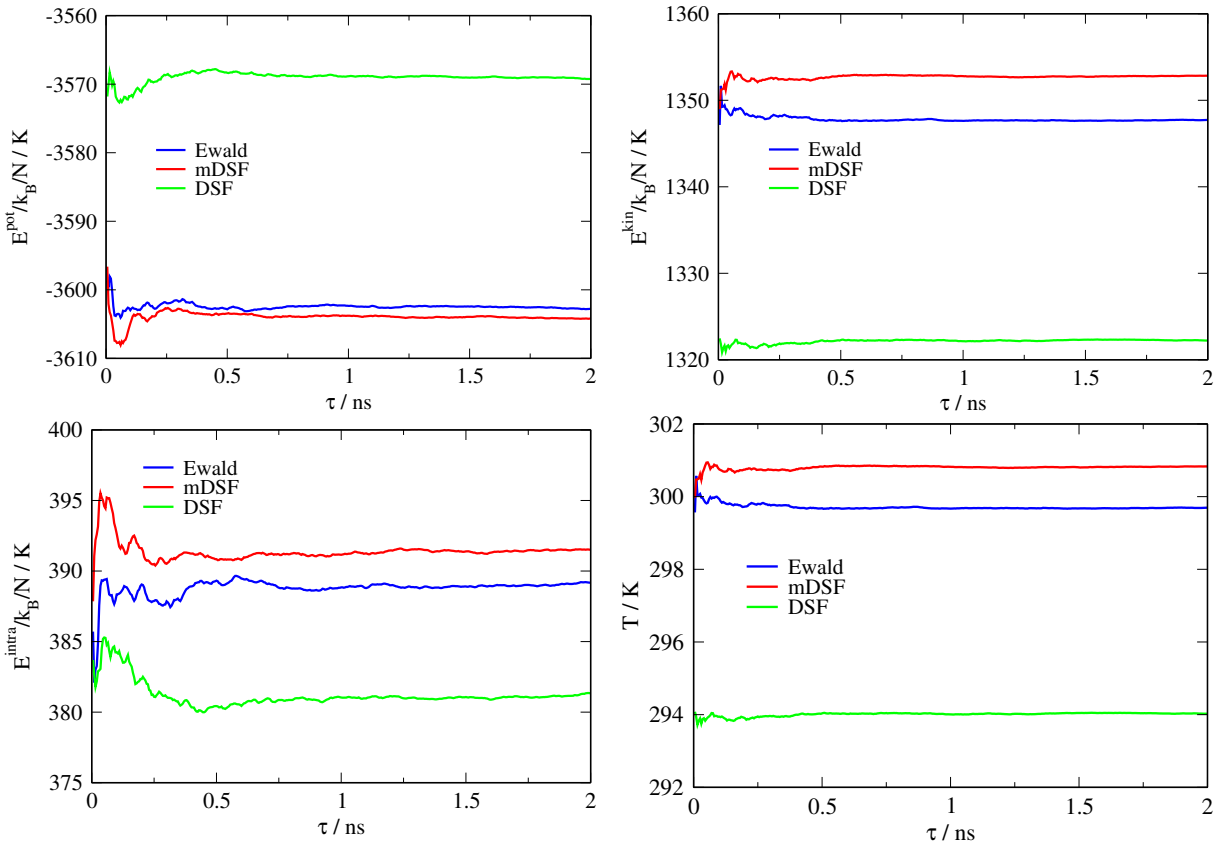

Figure B.3: Running average of the potential energy (top left), kinetic energy (top right), intramolecular energy (bottom left), and temperature (bottom right) over time for a acetone system in a NVE molecular dynamics simulation in the production period for Ewald summation, modified damped shifted force method (mDSF) and damped shifted force method (DSF). The starting energy of the molecular dynamics simulation after the previous Monte Carlo run is set to ${}^{E^{\mathrm{pot+kin}}}/_{k_B N} = -3203\,\mathrm{K}$ and the other simulation parameters are $N = 500$, $V = 61456\,\mathrm{Å}^3$, $R_c = 14\,\mathrm{Å}$, and $\beta = 0.3\,\mathrm{Å}^{-1}$.

B.4 Stockmayer Fluid

Vapor-liquid phase equilibrium (VLE) properties are reported for the non-polarizable and polarizable Stockmayer fluid with a permanent dipole of $|\boldsymbol{\mu}^*| = 1.0$ and with polarizability $\alpha_D^* = 0.03$ or $\alpha_D^* = 0.06$ for the polarizable case. Definitions of the dimensionless units are tabulated in Table B.2.

Kiyohara et al.[2] calculated VLE properties of non-polarizable and polarizable Stockmayer fluids in the grand canconical ensemble using the histogram reweighting method. Their results differ from results obtained in this work, both, for non-polarizable and polarizable Stockmayer fluids.

Table B.2: Dimensionless units.

dipole moment	$\boldsymbol{\mu}^* = \frac{\boldsymbol{\mu}}{\sqrt{4 \cdot \pi \cdot \epsilon_0 \cdot \epsilon \cdot \sigma^3}}$
polarizability	$\alpha_D^* = \frac{\alpha}{4 \cdot \pi \cdot \epsilon_0 \cdot \sigma^3}$
length	$r^* = \frac{r}{\sigma}$
temperature	$T^* = \frac{T \cdot k_B}{\epsilon}$
pressure	$p^* = \frac{p \cdot \sigma^3}{\epsilon}$
density	$\rho^* = \rho \cdot \sigma^3$
volume	$V^* = \frac{V}{\sigma^3}$
spring constant	$k_D^* = \frac{k_D \cdot \sigma^2}{\epsilon}$
excess chemical potential	$\frac{\mu}{k_B T} = \frac{\mu^{\mathrm{tot}}}{k_B T} - \ln\left(\frac{\Lambda^3}{\sigma^3}\right)$
damping parameter	$\alpha^* = \alpha \cdot \sigma$
β-parameter	$\beta^* = \beta \cdot \sigma$

Non-Polarizable Stockmayer fluid

Fig. B.4 shows VLE properties for a non-polarizable Stockmayer fluid with a permanent dipole of $|\boldsymbol{\mu}^*| = 1.0$. Simulation data from this work are in very good agreement to the benchmark results form Shen et al. as reported on the NIST Standard Reference Simulation Website[3], whereas the simulation data from Kiyohara et al. overestimate the vapor pressure and vapor density.

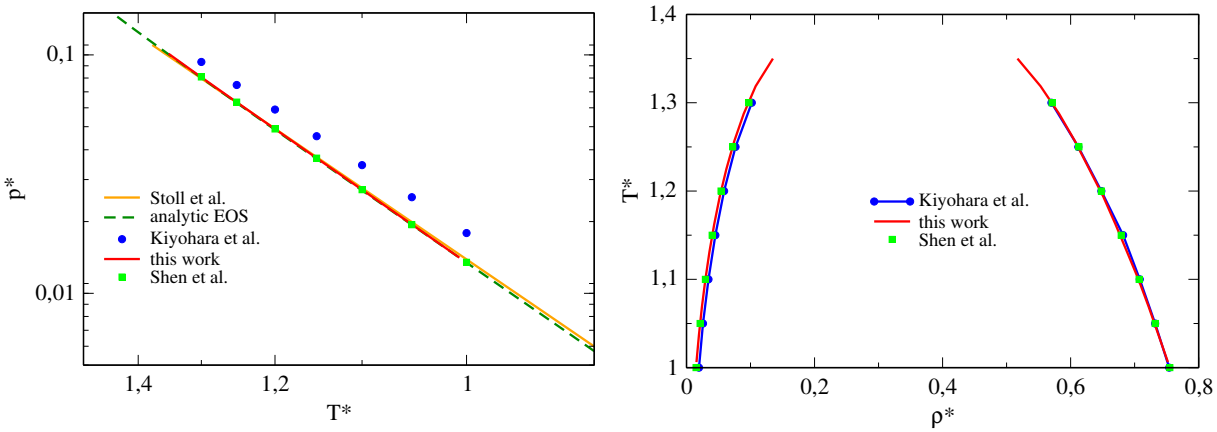

Figure B.4: Non-polarizable Stockmayer fluid with a permanent dipole of $|\boldsymbol{\mu}^*| = 1.0$: vapor pressure (left) and vapor-liquid coexistence curve (right). Simulation results from Kiyohara et al.[2] (blue circles), from Stoll et al.[4], from Shen et al.[3], and of this work (red line, $V^* = 512$, Ewald summation) are presented. Predictions of an analytic equation of state are also included[5].

Polarizable Stockmayer fluid

Fig. B.5 and B.6 show the phase equilibrium of polarizable Stockmayer fluids with a permanent dipole of $|\boldsymbol{\mu}^*| = 1.0$ and an additional polarizability of $\alpha_D^* = 0.03$ and $\alpha_D^* = 0.06$, respectively. With increasing polarizability the effective dipole moment increases and VLE shifts to lower pressures and higher temperatures. The vapor pressure and the vapor density of Kiyohara et al. are higher than the values found in our simulations. We don't consider these deviations as worrying, because a similar offset was seen for the non-polarizable case, where we found support for our results through the work of Stoll et al.[4] and Shen et al.[3] (as reported on the NIST Standard Reference Simulation Website). As a corollary of our study we find that an analytic equation of state developed by Kleiner and Gross[5] based on Wertheim's renormalized perturbation theory for polarizable fluids[6,7] is in excellent agreement with the data from molecular simulations. That is a fascinating observation, because in the year 2006, when the equation of state was proposed, the only vapor-liquid data for polarizable fluids were derived by Kiyohara et al. and it was thus unknown how accurate the equation of state represents vapor-liquid equilibria. Tabulated values for the VLE properties are given in Table B.3.

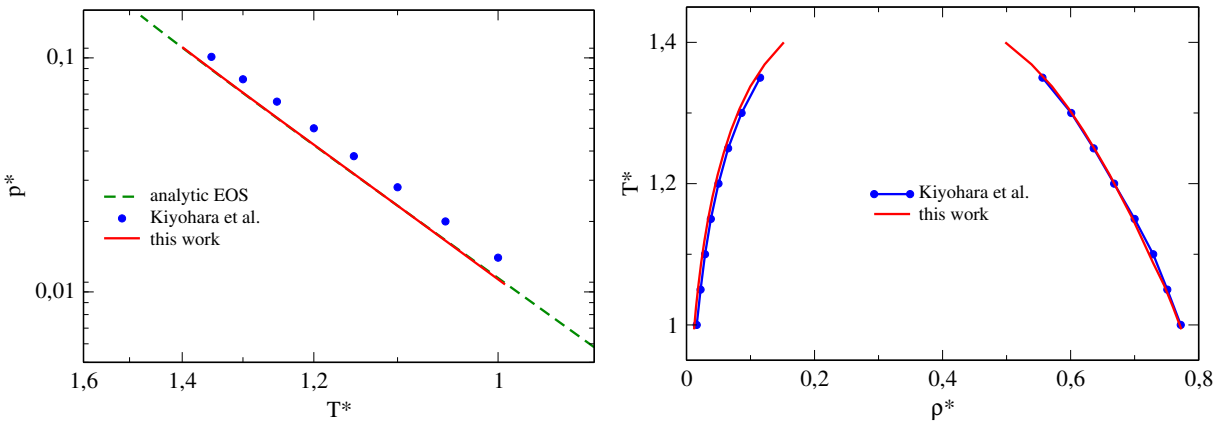

Figure B.5: Polarizable Stockmayer fluid with a permanent dipole of $|\boldsymbol{\mu}^*| = 1.0$ and a polarizability of $\alpha_D^* = 0.03$: vapor pressure (left) and vapor-liquid coexistence curve (right). Simulation results from Kiyohara et al.[2] and of this work (red line, $V^* = 512$, mDSF method with $R_c^* = 4$ and $\beta^* = 1.05$) are presented. Predictions from an analytic equation of state proposed by Kleiner and Gross[5] based on Werheim's renormalized perturbation theory for polarizable fluids[6,7] are also included.

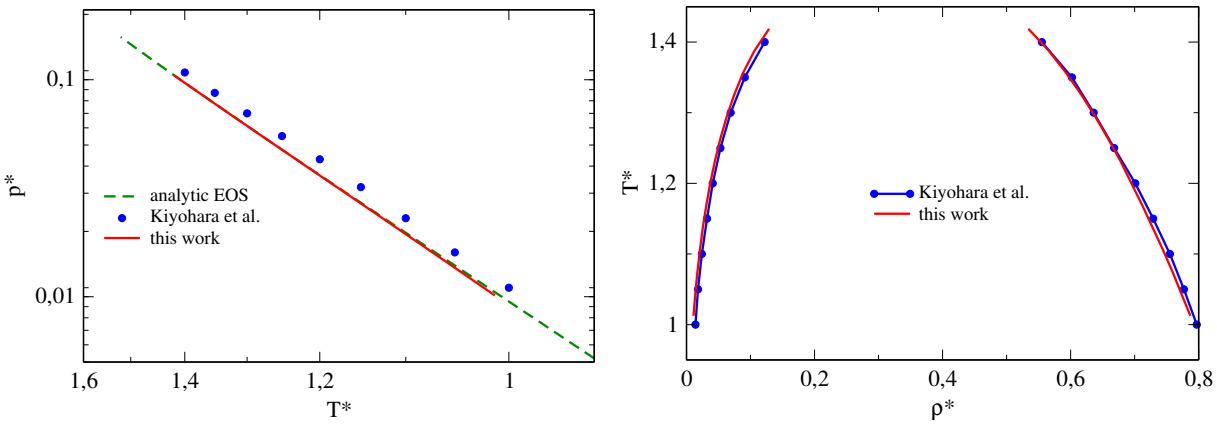

Figure B.6: Vapor pressure (left) and vapor-liquid coexistence curve (right) of polarizable Stockmayer fluid with a permanent dipole of $|\boldsymbol{\mu}^*| = 1.0$ and a polarizability of $\alpha_D^* = 0.06$. Simulation results from Kiyohara et al.[2] and of this work (red line, $V^* = 512$, mDSF method with $R_c^* = 4$ and $\beta^* = 1.05$) are presented. Predictions from an analytic equation of state proposed by Kleiner and Gross[5] based on Werheim's renormalized perturbation theory for polarizable fluids[6,7] are also included.

Table B.3: Tabulated values of reduced vapor pressures $p^{*,\mathrm{sat}}$, coexisting densities $\rho^{*,\mathrm{L}}$ and $\rho^{*,\mathrm{V}}$, and excess chemical potentials $\mu/k_BT = \mu^{\mathrm{tot}}/k_BT - \ln(\Lambda^3/\sigma^3)$ for polarizable Stockmayer fluids with a permanent dipole of $|\boldsymbol{\mu}^*| = 1.0$ and a polarizability of $\alpha_D^* = 0.03$ and $\alpha_D^* = 0.06$ ($V^* = 512$, mDSF method with $R_c^* = 4$ and $\beta^* = 1.05$).

$\alpha_D^* = 0.03$					$\alpha_D^* = 0.06$				
T^*	$p^{*,\mathrm{sat}}$	$\rho^{*,\mathrm{L}}$	$\rho^{*,\mathrm{V}}$	μ/k_BT	T^*	$p^{*,\mathrm{sat}}$	$\rho^{*,\mathrm{L}}$	$\rho^{*,\mathrm{V}}$	μ/k_BT
0.994	0.011	0.773	0.012	-4.604	1.013	0.010	0.787	0.011	-4.683
1.025	0.014	0.760	0.015	-4.405	1.044	0.013	0.773	0.014	-4.481
1.056	0.017	0.746	0.019	-4.220	1.075	0.016	0.759	0.017	-4.295
1.088	0.021	0.729	0.023	-4.049	1.106	0.020	0.744	0.021	-4.122
1.119	0.026	0.713	0.028	-3.891	1.138	0.025	0.728	0.026	-3.962
1.150	0.032	0.697	0.034	-3.745	1.169	0.030	0.712	0.031	-3.814
1.181	0.038	0.679	0.041	-3.609	1.200	0.036	0.695	0.037	-3.675
1.213	0.046	0.661	0.049	-3.482	1.231	0.043	0.678	0.044	-3.547
1.244	0.054	0.641	0.058	-3.363	1.263	0.051	0.659	0.053	-3.427
1.275	0.063	0.620	0.069	-3.253	1.294	0.059	0.639	0.063	-3.314
1.306	0.073	0.597	0.083	-3.150	1.325	0.069	0.617	0.074	-3.209
1.338	0.085	0.571	0.100	-3.053	1.356	0.080	0.593	0.088	-3.111
1.369	0.097	0.539	0.122	-2.962	1.388	0.092	0.566	0.106	-3.019
1.400	0.111	0.498	0.152	-2.877	1.419	0.105	0.534	0.129	-2.932

Bibliography

[1] Weidler, D., and Gross, J. (2016) Transferable Anisotropic United-Atom Force Field Based on the Mie Potential for Phase Equilibria: Aldehydes, Ketones, and Small Cyclic Alkanes. *Ind. Eng. Chem. Res. 55*, 12123–12132.

[2] Kiyohara, K., Gubbins, K. E., and Panagiotopoulos, A. Z. (1997) Phase coexistence properties of polarizable Stockmayer fluids. *J. Chem. Phys. 106*, 3338–3347.

[3] Shen, V. K., Siderius, D. W., Krekelberg, W. P., and Hatch, H. W., Eds. *NIST Standard Reference Simulation Website, NIST Standard Reference Database Number 173*; National Institute of Standards and Technology: Gaithersburg MD, 20899; http://doi.org/10.18434/T4M88Q, (retrieved March 16, 2018).

[4] Stoll, J., Vrabec, J., and Hasse, H. (2003) Comprehensive study of the vapour–liquid equilibria of the pure two-centre Lennard–Jones plus pointdipole fluid. *Fluid Phase Equilibria 209*, 29–53.

[5] Kleiner, M., and Gross, J. (2006) An equation of state contribution for polar components: Polarizable dipoles. *AIChE journal 52*, 1951–1961.

[6] Wertheim, M. (1977) Theory of polar fluids. III. *Molecular Physics 34*, 1109–1129.

[7] Wertheim, M. (1979) Theory of polar fluids: V. Thermodynamics and thermodynamic perturbation theory. *Molecular Physics 37*, 83–94.

Appendix C

Supporting Information to Chapter 4

The Supporting Information to Chapter 4 consists of two parts. The first part is presented in this Appendix. The second part contains tabulated simulation data and can be found at

https://doi.org/10.1016/j.fluid.2017.09.024

C.1 Tail Correction for the TAMie Force Field

The tail correction[1,2] of the energy for the Mie potential with fixed attractive exponent (see equation giving the Mie potential in paper) reads

$$U^{tail} = \frac{2\pi}{V} \sum_{\alpha=1}^{K} \sum_{\beta=1}^{K} N_\alpha N_\beta c_{\alpha\beta} \epsilon_{\alpha\beta} \sigma_{\alpha\beta}^3 \left(\frac{1}{n_{\alpha\beta} - 3} \left(\frac{\sigma_{\alpha\beta}}{r_c} \right)^{n_{\alpha\beta}-3} - \frac{1}{3} \left(\frac{\sigma_{\alpha\beta}}{r_c} \right)^3 \right) \tag{C.1}$$

where indices α and β run over all K different types of united-atom groups and $N_{\alpha/\beta}$ denotes the number of united-atom groups in the system. Further V is the volume of the simulation box and r_c is the cut-off radius. The coefficients $\epsilon_{\alpha\beta},\ \sigma_{\alpha\beta}, n_{\alpha\beta}$ and $c_{\alpha\beta}$ of the Mie potential are defined in the paper.

C.2 Pure Component Properties of Nitrogen from modified TraPPE Force Field

The force field for nitrogen used in this study is a slight reparameterization (Lennard-Jones parameters) of the TraPPE force field[3]. The vapor pressure, which in the original TraPPE model is systematically lower than experimental data, is thereby mildly improved. Deviations to quasi-experimental data are reported as absolute average deviations (AAD), as

$$\mathrm{AAD}\% = \frac{100}{N^{\mathrm{exp}}} \sum_{j=1}^{N^{\mathrm{exp}}} \left| \frac{\Omega_j^{\mathrm{sim}} - \Omega_j^{\mathrm{exp}}}{\Omega_j^{\mathrm{exp}}} \right| \tag{C.2}$$

with the number of experimental values N^{exp} and the experimental and simulation observables Ω_j^{exp} and Ω_j^{sim}, respectively. Vapor pressure and liquid densities were used as quantities for optimizing the Lennard-Jones parameters. Quasi-experimental data is generated from the highly accurate equation of state of Span et al.[4].
Deviations of some properties to to quasi-experimental data are given in Table C.1. The phase behavior is illustrated in Fig. C.1 and C.2.

Table C.1: Absolute average deviations (saturation pressure, liquid density, vapor density, critical pressure, critical temperature) of the TraPPE force field and the modified TraPPE model of nitrogen from quasi-experimental data[4].

force field	AAD p^{sat}/%	AAD ρ^{L}/%	AAD ρ^{V}/%	AAD p^{crit}/%	AAD T^{crit}/%
modif. TraPPE	0.50	1.17	2.21	1.63	0.42
TraPPE	0.71	1.05	3.35	2.44	0.65

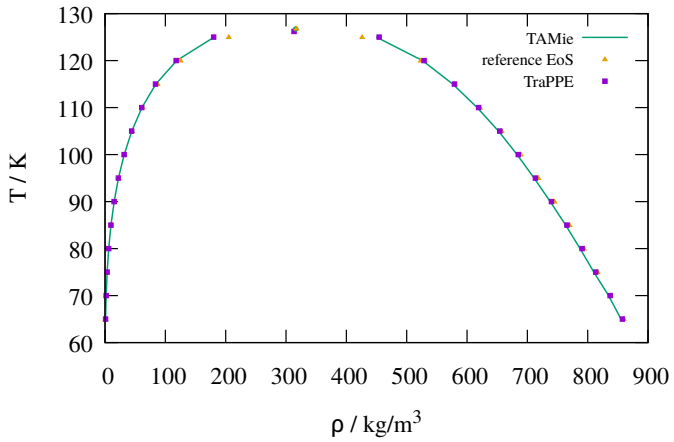

Figure C.1: Vapor-liquid equilibria of nitrogen: equation of state date[4] (orange triangles) and simulation data with the modified TraPPE model (green line) and the TraPPE force field (purple squares).

C.3 Pure Component Properties for Propane from TraPPE-EH Force Field

We report phase equilibrium properties for propane using the TraPPE-EH force field proposed by Chen and Siepmann[5]. Figure C.3 and C.4 show a comparison of the TraPPE-EH model to experimental data for propane.

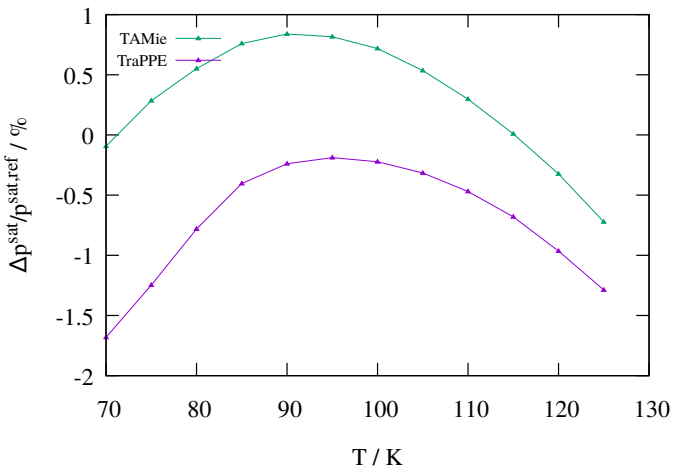

Figure C.2: Errors in vapor pressure of nitrogen in comparison to a highly accurate equation of state[4]: comparison of the modified TraPPE model (green line) and the TraPPE force field (purple squares).

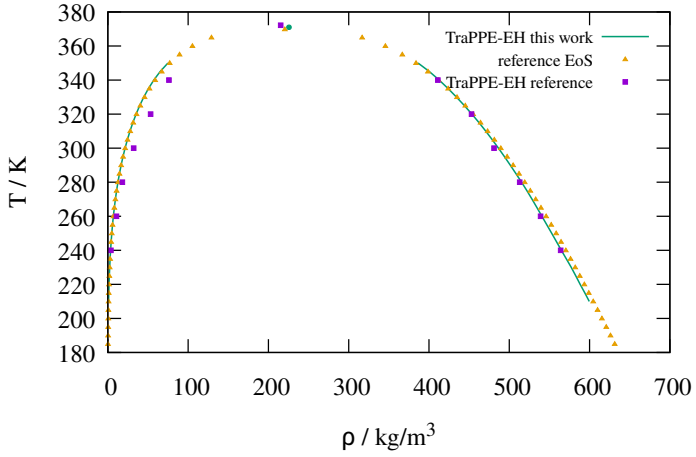

(a) Phase behavior.

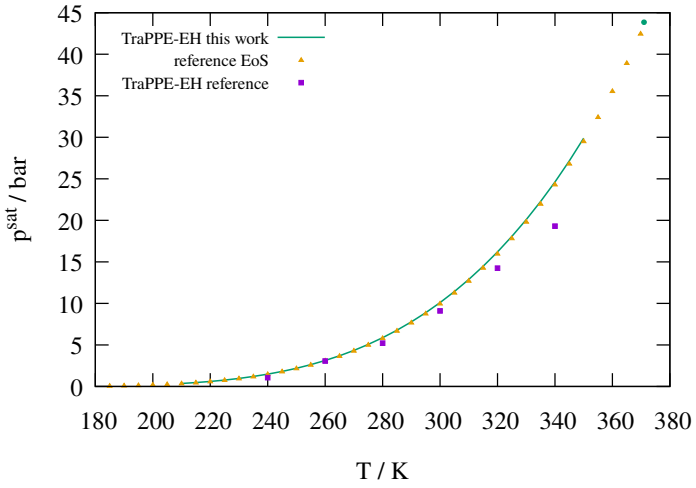

(b) Vapor-pressure.

Figure C.3: Vapor-liquid equilibria of TraPPE-EH propane: equation of state date[6] (orange triangles), this work (TraPPE-EH) (green line) and TraPPE-EH reference[5] (purple squares).

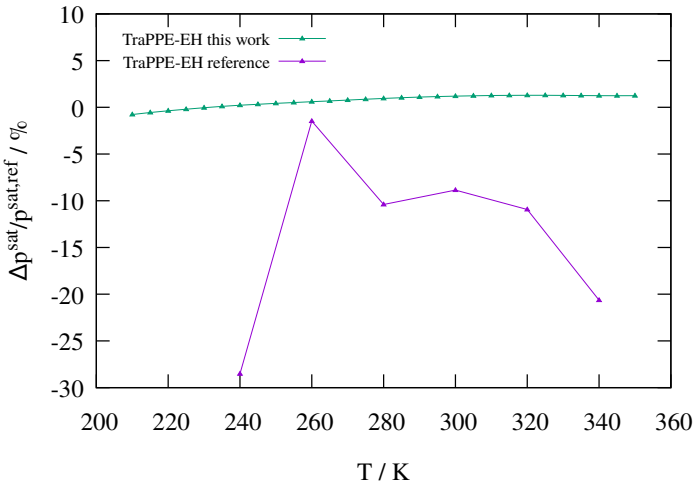

Figure C.4: Errors of vapor-liquid equilibria of TraPPE-EH propane in comparison to a highly accurate equation of state[6]: this work (TraPPE-EH) (green) and TraPPE-EH reference[5] (purple).

C.4 Pure Component Properties for n-Pentane from TraPPE-EH Force Field

We report phase equilibrium properties for n-pentane using the TraPPE-EH force field proposed by Chen and Siepmann[5]. Figure C.5 and C.6 show a comparison of the TraPPE-EH model to experimental data for n-pentane.

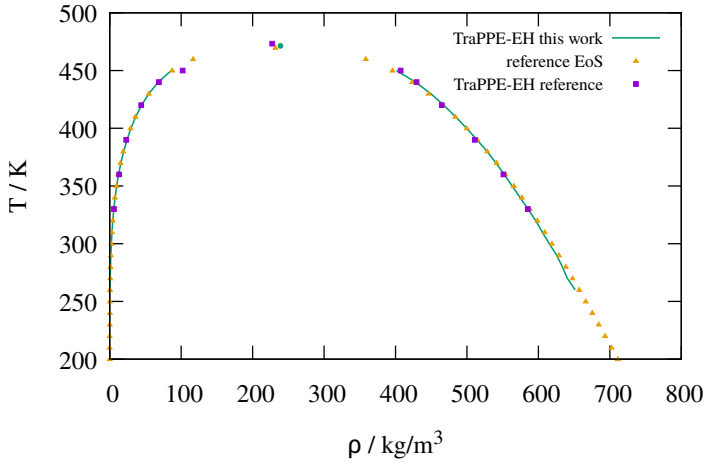

(a) Phase behavior.

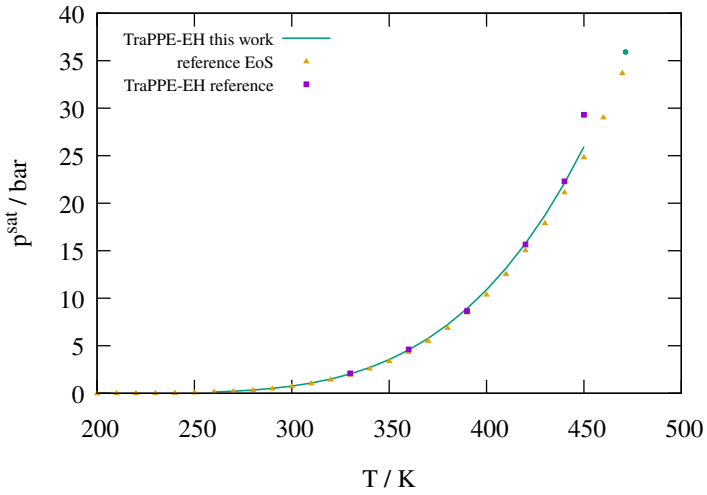

(b) Vapor-pressure.

Figure C.5: Vapor-liquid equilibria of TraPPE-EH n-pentane: equation of state date[7] (orange triangles), this work (TraPPE-EH) (green line) and TraPPE-EH reference[5] (purple squares).

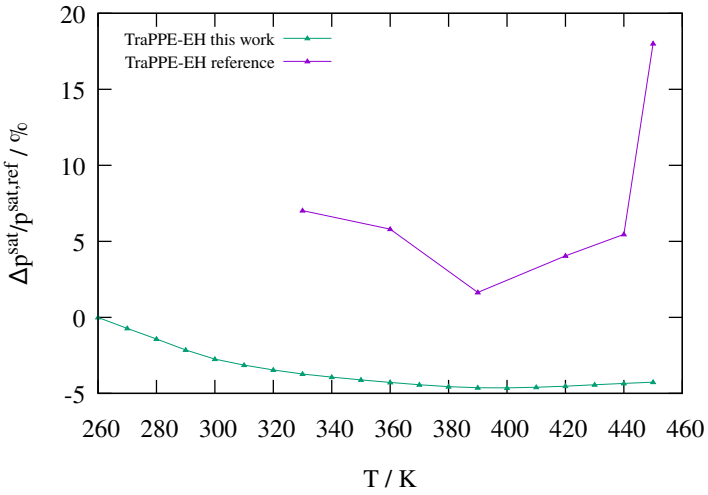

Figure C.6: Errors in vapor pressure of TraPPE-EH pentane in comparison to a highly accurate equation of state[7]: simulated data (green) and TraPPE-EH reference[5] (purple).

C.5 Binary interaction parameters k_{ij} for the PCP-SAFT equation of state

Table C.2: Binary interaction parameters k_{ij} for the PCP-SAFT equation of state, adjusted to experimental vapor-liquid equilibrium data.

n-alkane	k_{i,N_2}	ref. exp. data
propane	0.0327	[8,9]
butane	0.0806	[10–13]
pentane	0.0670	[14,15]
hexane	0.0765	[16]
heptane	0.1225	[17]
octane	0.1341	[18]
nonane	0.1521	[19]
decane	0.1505	[20]
dodecane	0.1661	[21]

C.6 Comparison of segment-wise $\kappa_{\alpha\beta}$ and molecule-wise κ_{ij} parameter

In this work we propose using binary van der Waals cross-energy parameters defined for each pair of interaction sites. In literature these cross-energy parameters are often defined as corrections to the Berthelot combining rule applied to a pair of species, which means that the same correction parameter κ_{ij} is used for all pairs of van der Waals sites of unlike species. To compare results for vapor-liquid equilibria obtained from segment-wise $\kappa_{\alpha\beta}$ parameters with an approach using a molecular κ_{ij} parameter, we used a similar optimization scheme for both parameter identifications. Once a molecular parameter κ_{ij} is defined, it is treated as transferable to other pairs of species within the same homologous series. That is more ambiguous (for example if multifunctional species were considered) compared to our approach, where the pair of interaction sites uniquely define the cross-energy parameter. The approach, however, is most comparable to our approach. The parameter, κ_{ij} was adjusted to the vapor-liquid phase equilibrium of n-pentane at $T = 344.3\,\mathrm{K}$. The resulting cross-energy parameter $\kappa_{ij} = 0.0307$ is then used for both cross interactions (-CH_3 to N and -CH_2- to N) between nitrogen an alkane sites.

Fig. C.7 compares the results for calculation with a molecular κ_{ij} parameter and calculations with segment-wise $\kappa_{\alpha\beta}$ parameters to experimental data for the training mixture of n-pentane. The simulation results are in good agreement with experimental data for both types of cross-energy parameters and there are only marginal differences between the results obtained by segment-wise and molecular cross parameters. Fig. C.8

and C.9 consider phase equilibria for other n-alkane/nitrogen mixtures (propane/nitrogen, n-hexane/nitrogen and n-decane/nitrogen) to test transferability of the κ_{ij} parameter. For the liquid phase the approach with a molecular cross-interaction parameter underestimates the mole fraction of nitrogen in the propane/nitrogen mixture and slightly overestimates the mole fraction x_{N2} for the n-hexane/nitrogen mixture, whereas the segment-wise parameter is in excellent agreement with experimental data for both systems.

Results for separate adjustments of κ_{ij} to each n-alkane/nitrogen mixture individually leads to the results in Table C.3. We observe a systematic increase in κ_{ij} with increasing n-alkane chain length. While each parameter yields the best result for each mixture individually, transferability is limited.

In this comparison of van der Waals cross-energy parameters based on segment-pairs and based on molecular pairs, we find that a segment-wise treatment delivers superior transferability. We expect similar results for other functional groups.

Table C.3: Binary molecular interaction parameters κ_{ij} for the TAMie force field adjusted separately and combined for three example n-alkanes.

n-alkane	κ_{i,N_2}
propane	0.0218
n-pentane	0.0307
n-hexane	0.0381
{propane, n-pentane, n-hexane}	0.0300

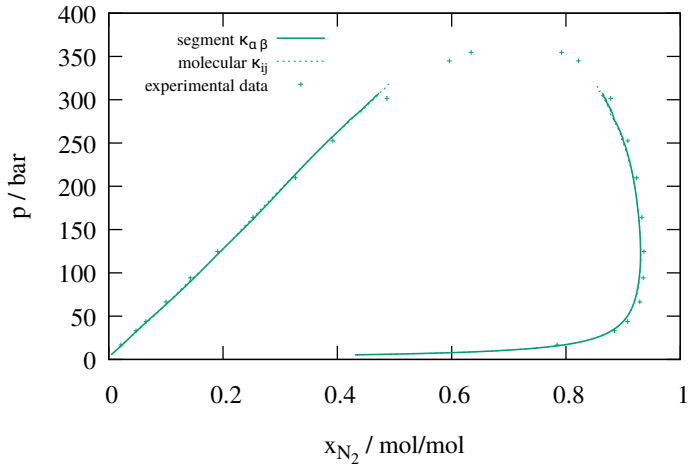

Figure C.7: Vapor-liquid equilibria of n-pentane/nitrogen mixtures at $T = 344.3\,\text{kelvin}$. Experimental data[14,15] (crosses), molecular simulation using the TAMie force field with molecular κ_{ij} adjusted to n-pentane (dashed) and molecular simulation using the TAMie force field with segment-wise $\kappa_{\alpha\beta}$ (solid).

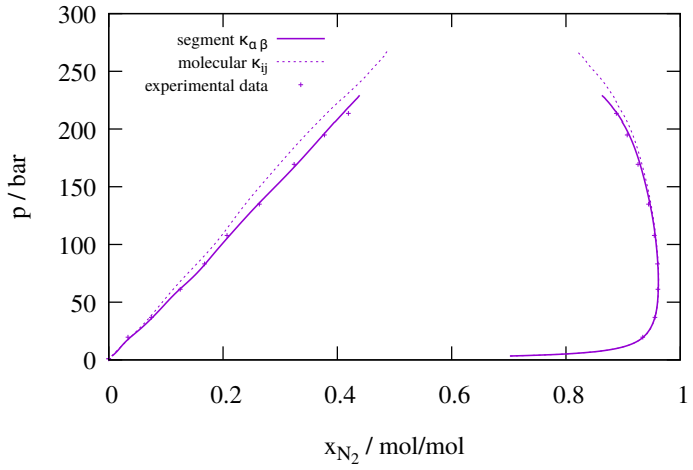

Figure C.8: Vapor-liquid equilibria of propane/nitrogen mixtures at $T = 230.0\,\mathrm{K}$. Experimental data[8,9] (crosses), molecular simulation using the TAMie force field with molecular κ_{ij} adjusted to n-pentane (dashed) and molecular simulation using the TAMie force field with segment-wise $\kappa_{\alpha\beta}$ (solid).

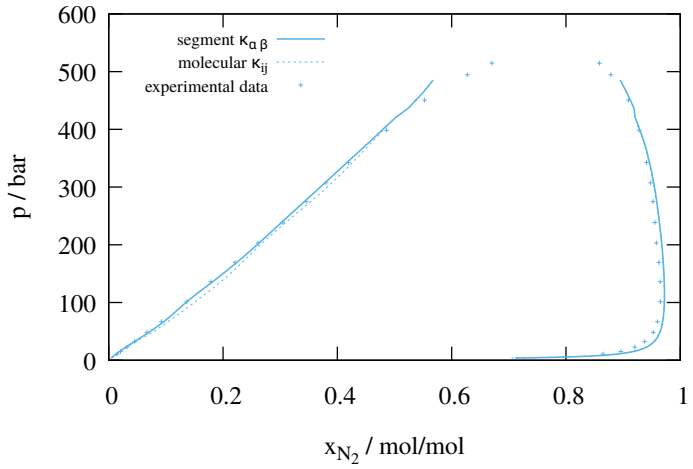

Figure C.9: Vapor-liquid equilibria of n-hexane/nitrogen mixtures at $T = 344.6\,\mathrm{K}$. Experimental data[16] (crosses), molecular simulation using the TAMie force field with molecular κ_{ij} adjusted to n-pentane (dashed) and molecular simulation using the TAMie force field with segment-wise $\kappa_{\alpha\beta}$ (solid).

C.7 Vapor-liquid equilibrium predictions for nitrogen/alkane mixtures

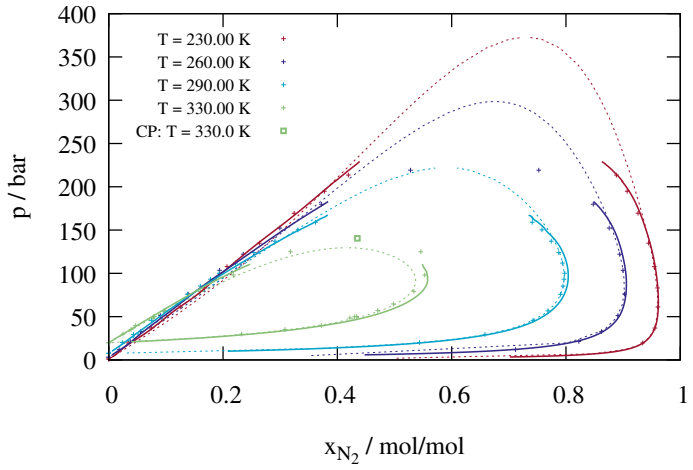

Figure C.10: Vapor-liquid equilibria of n-propane/nitrogen mixtures at different temperatures. Experimental data[8,9] (crosses), PCP-SAFT (dashed) and molecular simulation using the TAMie force field (solid). Critical point for $T = 330.0\,\mathrm{K}$ predicted from the TAMie force field with Binder method.

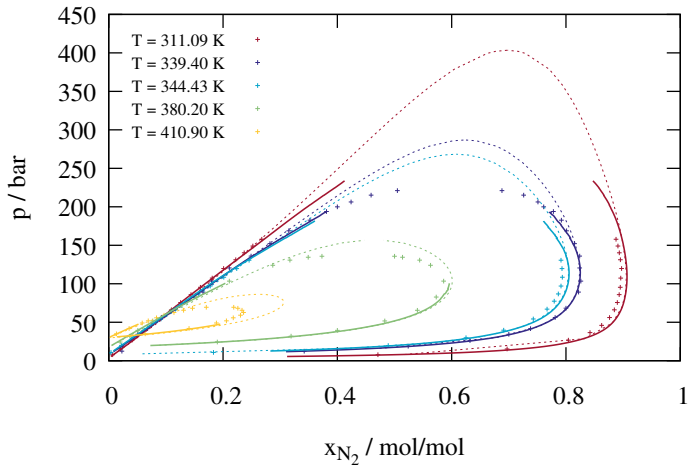

Figure C.11: Vapor-liquid equilibria of n-butane/nitrogen mixtures at different temperatures. Experimental data[10–13] (crosses), PCP-SAFT (dashed) and molecular simulation using the TAMie force field (solid).

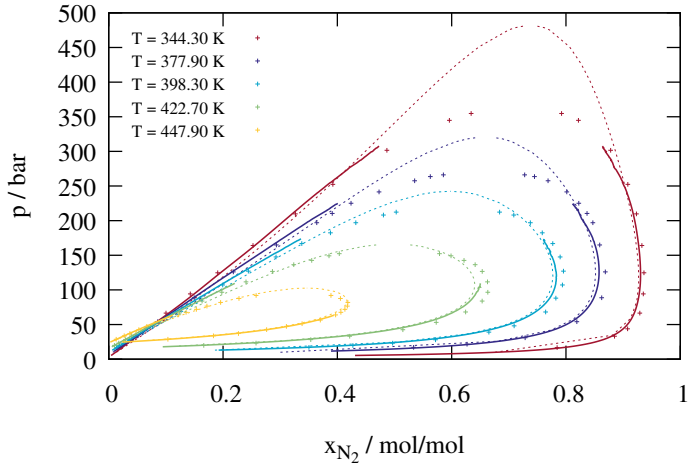

Figure C.12: Vapor-liquid equilibria of n-pentane/nitrogen mixtures at different temperatures. Experimental data[14,15] (crosses), PCP-SAFT (dashed) and molecular simulation using the TAMie force field (solid).

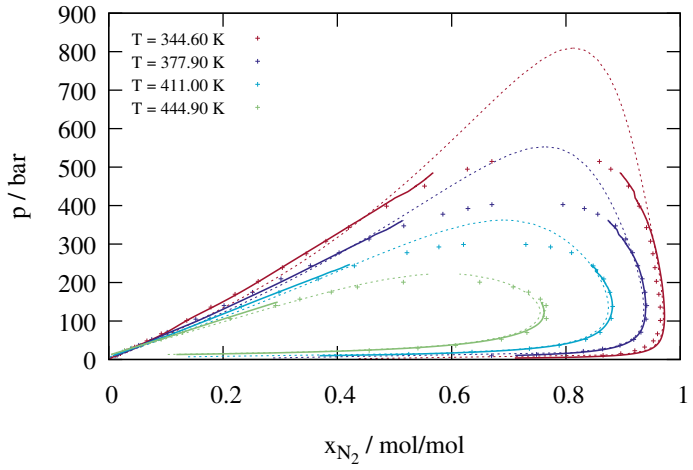

Figure C.13: Vapor-liquid equilibria of n-hexane/nitrogen mixtures at different temperatures. Experimental data[16] (crosses), PCP-SAFT (dashed) and molecular simulation using the TAMie force field (solid).

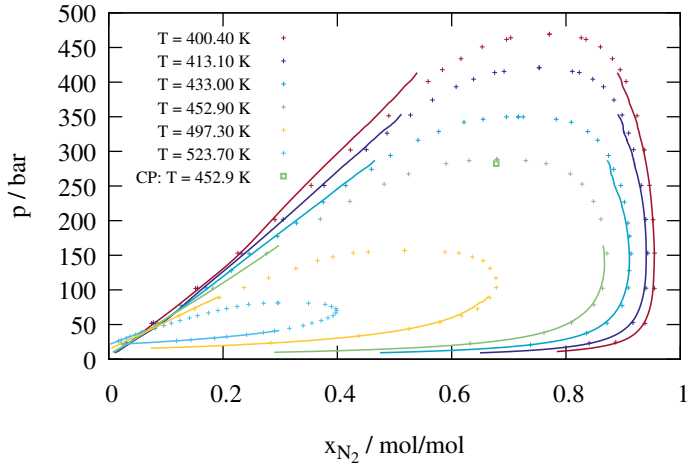

Figure C.14: Vapor-liquid equilibria of n-heptane/nitrogen mixtures at different temperatures. Experimental data[17] (crosses) and molecular simulation using the TAMie force field (solid). Critical point for $T = 452.9\,\mathrm{K}$ predicted with Binder method.

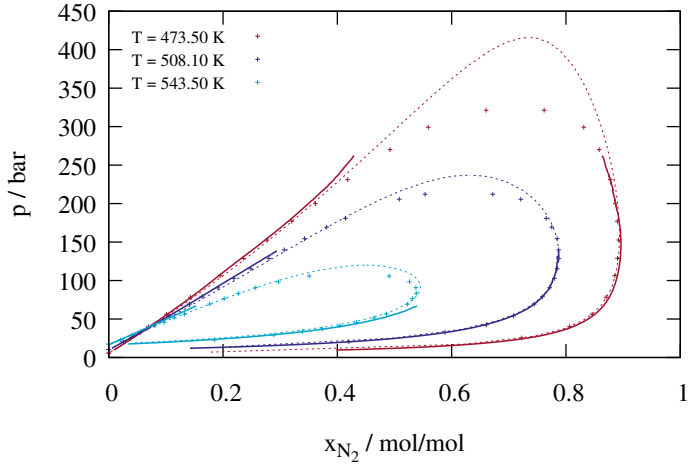

Figure C.15: Vapor-liquid equilibria of n-octane/nitrogen mixtures at different temperatures. Experimental data[18] (crosses), PCP-SAFT (dashed) and molecular simulation using the TAMie force field (solid).

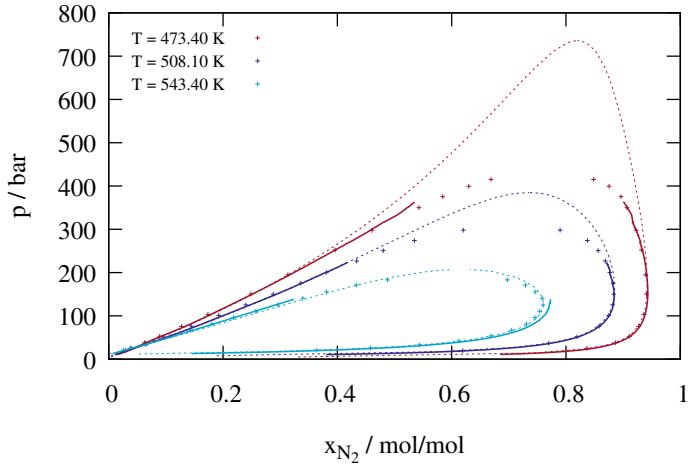

Figure C.16: Vapor-liquid equilibria of n-nonane/nitrogen mixtures at different temperatures. Experimental data[19] (crosses), PCP-SAFT (dashed) and molecular simulation using the TAMie force field (solid).

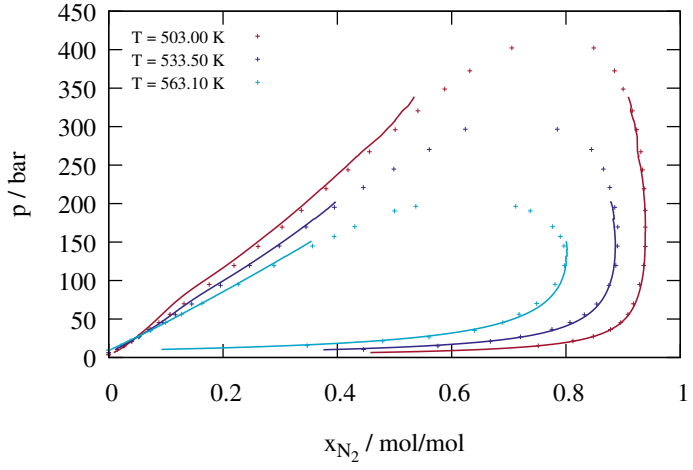

Figure C.17: Vapor-liquid equilibria of n-decane/nitrogen mixtures at different temperatures. Experimental data[20] (crosses) and molecular simulation using the TAMie force field (solid).

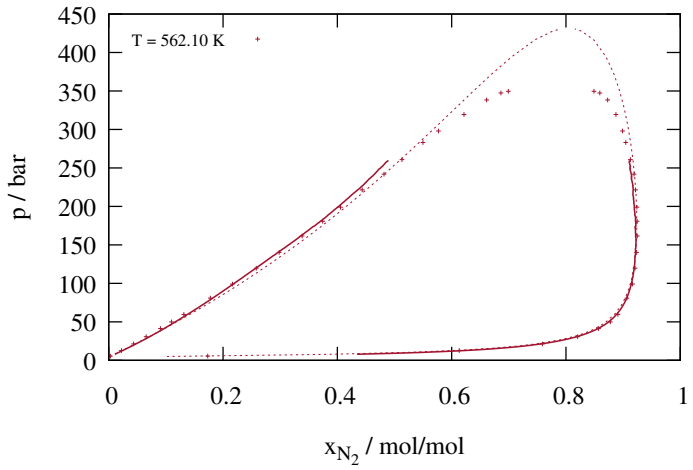

Figure C.18: Vapor-liquid equilibrium of n-dodecane/nitrogen mixtures at different temperatures. Experimental data[21] (crosses), PCP-SAFT (dashed) and molecular simulation using the TAMie force field (solid).

Bibliography

[1] Allen, M. P., and Tildesley, D. J. *Computer simulation of liquids*; Oxford University Press: New York, 1987.

[2] Smit, B. (1992) Phase diagrams of Lennard-Jones fluids. *J. Chem. Phys. 96*, 8639–8640.

[3] Potoff, J. J., and Siepmann, J. I. (2001) Vapor-liquid equilibria of mixtures containing alkanes, carbon dioxide, and nitrogen. *AIChE J. 47*, 1676–1682.

[4] Span, R., Lemmon, E. W., Jacobsen, R. T., Wagner, W., and Yokozeki, A. (2000) A Reference Equation of State for the Thermodynamic Properties of Nitrogen for Temperatures from 63.151 to 1000 K and Pressures to 2200 MPa. *J. Phys. Chem. Ref. Data 29*, 1361–1433.

[5] Chen, B., and Siepmann, J. I. (1999) Transferable Potentials for Phase Equilibria. 3. Explicit-Hydrogen Description of Normal Alkanes. *J. Phys. Chem. B 103*, 5370–5379.

[6] Miyamoto, H., and Watanabe, K. (2000) A Thermodynamic Property Model for Fluid-Phase Propane. *Int. J. of Thermophys. 21*, 1045–1072.

[7] Span, R. *Multiparameter equations of state: an accurate source of thermodynamic property data*; Springer: Berlin, 2013; p 367.

[8] Grausø, L., Fredenslund, A., and Mollerup, J. (1977) Vapour-liquid equilibrium data for the systems C2H6 + N2, C2H4 + N2, C3H8 + N2, and C3H6 + N2. *Fluid Phase Equilibr. 1*, 13 – 26.

[9] Yucelen, B., and Kidnay, A. J. (1999) Vapor-Liquid Equilibria in the Nitrogen + Carbon Dioxide + Propane System from 240 to 330 K at Pressures to 15 MPa. *J. Chem. Eng. Data 44*, 926–931.

[10] V.G., S., S.D., B., I.E., N., G.F., G., and O.A., B. (1969) *Gazovaya Promyshlennost' 14*, 41–45.

[11] Brown, T., Niesen, V., Sloan, E., and Kidnay, A. (1989) Vapor-liquid equilibria for the binary systems of nitrogen, carbon dioxide, and n-butane at temperatures from 220 to 344 K. *Fluid Phase Equilibr. 53*, 7 – 14.

[12] Shibata, S. K., and Sandler, S. I. (1989) High-pressure vapor-liquid equilibria involving mixtures of nitrogen, carbon dioxide, and n-butane. *J. Chem. Eng. Data 34*, 291–298.

[13] Malewski, M. K. F., and Sandler, S. I. (1989) High-pressure vapor-liquid equilibria of the binary mixtures nitrogen + n-butane and argon + n-butane. *J. Chem. Eng. Data 34*, 424–426.

[14] Kalra, H., Robinson, D. B., and Besserer, G. J. (1977) The equilibrium phase properties of the nitrogen-n-pentane system. *J. Chem. Eng. Data 22*, 215–218.

[15] Silva-Oliver, G., Eliosa-Jimenez, G., Garcia-Sanchez, F., and Avendano-Gomez, J. R. (2006) High-pressure vapor–liquid equilibria in the nitrogen–n-pentane system. *Fluid Phase Equilibr. 250*, 37 – 48.

[16] Eliosa-Jimenez, G., Silva-Oliver, G., Garcia-Sanchez, F., and de Ita de la Torre, A. (2007) High-Pressure Vapor-Liquid Equilibria in the Nitrogen + n-Hexane System. *J. Chem. Eng. Data 52*, 395–404.

[17] Garcia-Sanchez, F., Eliosa-Jimenez, G., Silva-Oliver, G., and Godinez-Silva, A. (2007) High-pressure (vapor + liquid) equilibria in the (nitrogen + n-heptane) system. *J. Chem. Thermodyn. 39*, 893 – 905.

[18] Eliosa-Jimenez, G., Garcia-Sanchez, F., Silva-Oliver, G., and Macias-Salinas, R. (2009) Vapor-liquid equilibrium data for the nitrogen + n-octane system from (344.5 to 543.5) K and at pressures up to 50 {MPa}. *Fluid Phase Equilibr. 282*, 3 – 10.

[19] Silva-Oliver, G., Eliosa-Jimenez, G., Garcia-Sanchez, F., and Avendano-Gomez, J. R. (2007) High-pressure vapor-liquid equilibria in the nitrogen-n-nonane system. *J. of Supercrit. Fluid. 42*, 36 – 47.

[20] Garcia-Sanchez, F., Eliosa-Jimenez, G., Silva-Oliver, G., and Garcia-Flores, B. E. (2009) Vapor-Liquid Equilibrium Data for the Nitrogen + n-Decane System from (344 to 563) K and at Pressures up to 50 MPa. *J. Chem. Eng. Data 54*, 1560–1568.

[21] Garcia-Cordova, T., Justo-Garcia, D. N., Garcia-Flores, B. E., and Garcia-Sanchez, F. (2011) Vapor-Liquid Equilibrium Data for the Nitrogen + Dodecane System at Temperatures from (344 to 593) K and at Pressures up to 60 MPa. *J. Chem. Eng. Data 56*, 1555–1564.

Appendix D

Supporting Information to Chapter 5

D.1 Simulation Details

Simulation details of each calculated system are given in Table D.1, containing used force field, number of equilibration and production moves (N^{equil}, N^{prod}), the width of a simulation window ΔN, and the maximum number of particles N^{max}. For all simulations a box volume of $V = 21952\,\text{Å}^3$ is used.

Table D.1: Simulation Details.

substance	force field	$N^{equil}/10^6$	$N^{prod}/10^6$	ΔN	N_1^{max}	N_2^{max}
ethane	PTAMie	1	5	5	260	-
propane	PTAMie	1	5	5	190	-
n-butane	PTAMie	1	5	5	150	-
n-hexane	PTAMie	1	5	5	110	-
n-octane	PTAMie	1	5	5	90	-
dimethyl ether	PTAMie	1	5	10	220	-
diethyl ether	PTAMie	1	5	5	135	-
di-n-propyl ether	PTAMie	1	5	5	95	-
di-n-butyl ether	PTAMie	1	5	5	85	-
methyl ethyl ether	PTAMie	1	5	10	180	-
methyl n-propyl ether	PTAMie	1	5	5	150	-
nitrogen	PTAMie	5	5	10	420	-
ethane	TAMie	10	50	10	260	-
propane	TAMie	10	50	10	190	-
n-butane	TAMie	10	50	10	150	-
n-hexane	TAMie	10	50	10	110	-
n-octane	TAMie	10	50	10	90	-
dimethyl ether	TAMie	10	50	10	220	-
diethyl ether	TAMie	10	50	10	135	-
di-n-propyl ether	TAMie	10	50	10	95	-
di-n-butyl ether	TAMie	10	50	10	85	-
methyl ethyl ether	TAMie	10	50	10	180	-
methyl n-propyl ether	TAMie	10	50	10	150	-
nitrogen	TAMie	10	50	10	420	-
n-hexane/nitrogen (411 K)	PTAMie	1	5	5	110	110
n-pentane/nitrogen (398.3 K)	PTAMie	1	5	5	110	170
dimethyl ether/nitrogen (318.15 K)	PTAMie	1	5	10	200	280
n-hexane/nitrogen (411 K)	TAMie	10	50	5	110	110
n-pentane/nitrogen (398.3 K)	TAMie	10	50	5	110	170
dimethyl ether/nitrogen (318.15 K)	TAMie	10	50	10	200	280

Enthalpy of Vaporization

The enthalpy of vaporization is calculated using the Clausius-Clapeyron equation, where the gradient $\mathrm{d}p/\mathrm{d}T$ is determined by the gradient $\mathrm{d}\ln(p)/\mathrm{d}(1/T)$

$$\Delta^{lv}h = -\frac{p}{T}\left(v^g - v^l\right)\frac{\mathrm{d}\ln(p)}{\mathrm{d}(1/T)}$$

Configurational Bias Scheme

The statistics of insertion, deletion, and reconfiguration is improved using a configurational bias (CBMC) scheme with N_{CBMC} trial positions per CBMC-group of interaction sites. The number of trial steps is increased from $N_{\mathrm{CBMC}} = 1$ for low densities up to $N_{\mathrm{CBMC}} = 8$ for high densities. As criterion for increasing the number of CBMC-steps the particle number N^* is used. For pure substances the dimensionless particle number is defined as $N^* = N/N^{\max}$, where $N^{\max}$ is the highest particle number for which simulations are performed (see Table D.1). For mixtures a simple arithmetic average $N^* = N_1/N_1^{\max} + N_2/N_2^{\max}$ is applied. The number of CBMC-trial steps for a dimensionless particle number are shown in Table D.2.

Table D.2: Number of CBMC steps for different dimensionless particle numbers.

N^*	CBMC steps per site
$< 1/2.7$	1
$\geq 1/2.7 \wedge < 1/1.9$	2
$\geq 1/1.9 \wedge < 1/1.6$	3
$\geq 1/1.6 \wedge < 1/1.3$	4
$\geq 1/1.3 \wedge < 1/1.16$	6
$\geq 1/1.16$	8

D.2 Uncertainty of Results

Our results are the sample mean of 3 independent samples. The numbers between brackets are the uncertainties in the last digit calculated using the 95% confidence interval with the student's t-distribution. The uncertainty is defined as

$$\mathrm{err} = t^* \frac{s}{\sqrt{n}}$$

where n is the number of independent samples (in our case $n = 3$), t^* the critical value from the student's t-distribution with $\nu = n - 1$ degrees of freedom, and s the corrected sample standard deviation

$$s = \sqrt{\frac{1}{n-1}\sum_{i=1}^{n}(x_i - \bar{x})^2}$$

If the results are from a single simulation, there are no brackets.

D.3 Results - Polarizable PTAMie Force Field

N-Alkanes (PTAMie)

Table D.3: Critical properties of n-alkanes calculated with the polarizable PTAMie force field.

substance	simulation results			experimental data[1]		
	T_c/K	p_c/bar	ρ_c/$^{\mathrm{kg}}/_{\mathrm{m}^3}$	T_c/K	p_c/bar	ρ_c/$^{\mathrm{kg}}/_{\mathrm{m}^3}$
ethane	306.1(4)	49.8(3)	211(1)	305.3	49.0	207.5
propane	371.6(3)	43.5(2)	228(2)	369.9	42.5	224.9
n-butane	426.1(9)	38.9(5)	235.6(7)	425.0	38.0	227.8
n-hexane	512(2)	32.2(3)	244(1)	507.6	30.2	233.5
n-octane	575(2)	27.6(7)	246(2)	568.9	24.9	232.3

Table D.4: Tabulated values of vapor pressures, coexisting densities and enthalpies of vaporization for n-alkanes calculated with the polarizable PTAMie force field.

ethane				
T/K	p^{sat}/bar	ρ^{L}/$^{\mathrm{kg}}/_{\mathrm{m}^3}$	ρ^{V}/$^{\mathrm{kg}}/_{\mathrm{m}^3}$	$\Delta^{\mathrm{LV}}h$/$^{\mathrm{kJ}}/_{\mathrm{kg}}$
175	0.5857(8)	551.3(8)	1.236(2)	505.2(5)
195	1.729(5)	526(1)	3.36(2)	479.3(9)
215	4.10(2)	499.3(6)	7.52(4)	449.1(5)
235	8.33(3)	470.2(3)	14.83(5)	412.8(3)
255	15.09(6)	437(1)	26.95(9)	367(1)
275	25.1(1)	396.07(8)	47.3(2)	306.1(2)

propane				
T/K	p^{sat}/bar	$\rho^{L}/{}^{\mathrm{kg}}/_{\mathrm{m}^3}$	$\rho^{\mathrm{V}}/{}^{\mathrm{kg}}/_{\mathrm{m}^3}$	$\Delta^{\mathrm{LV}}h/{}^{\mathrm{kJ}}/_{\mathrm{kg}}$
210	0.357(4)	601(2)	0.914(9)	448(1)
230	0.958(9)	579.1(8)	2.28(2)	429.4(5)
250	2.16(2)	556(1)	4.85(3)	408.2(8)
270	4.27(3)	531.0(8)	9.24(3)	384.3(6)
290	7.64(3)	504.2(5)	16.26(5)	356.1(2)
310	12.65(2)	474(2)	27.0(2)	322(1)
330	19.70(3)	438.1(7)	43.8(3)	279(1)
n-butane				
T/K	p^{sat}/bar	$\rho^{\mathrm{L}}/{}^{\mathrm{kg}}/_{\mathrm{m}^3}$	$\rho^{\mathrm{V}}/{}^{\mathrm{kg}}/_{\mathrm{m}^3}$	$\Delta^{\mathrm{LV}}h/{}^{\mathrm{kJ}}/_{\mathrm{kg}}$
240	0.248(2)	627(2)	0.731(7)	413(1)
260	0.625(5)	606(1)	1.72(1)	396.9(6)
280	1.359(8)	585.8(5)	3.55(1)	380.2(3)
300	2.63(1)	564(1)	6.60(2)	361.6(9)
320	4.65(2)	540(1)	11.40(2)	339.9(8)
340	7.66(2)	513.96(6)	18.59(8)	315.3(3)
360	11.896(4)	485.2(6)	29.2(2)	286.2(5)
380	17.65(3)	451(2)	45.39(9)	249(1)
n-hexane				
T/K	p^{sat}/bar	$\rho^{\mathrm{L}}/{}^{\mathrm{kg}}/_{\mathrm{m}^3}$	$\rho^{\mathrm{V}}/{}^{\mathrm{kg}}/_{\mathrm{m}^3}$	$\Delta^{\mathrm{LV}}h/{}^{\mathrm{kJ}}/_{\mathrm{kg}}$
305	0.250(1)	641(3)	0.879(5)	369(2)
325	0.551(2)	623(1)	1.848(6)	354.4(8)
345	1.091(2)	604(1)	3.504(7)	338.7(8)
365	1.972(2)	585.0(8)	6.103(8)	322.5(5)
385	3.310(2)	564(1)	9.96(1)	305.0(7)
405	5.230(3)	542(1)	15.53(4)	285.8(7)
425	7.87(1)	517(1)	23.4(1)	264.4(6)
445	11.39(5)	490(2)	34.8(3)	239(1)
465	16.0(1)	456(1)	51.9(8)	207(1)

n-octane				
T/K	p^{sat}/bar	$\rho^{\mathrm{L}}/{}^{\mathrm{kg}}/_{\mathrm{m}^3}$	$\rho^{\mathrm{V}}/{}^{\mathrm{kg}}/_{\mathrm{m}^3}$	$\Delta^{\mathrm{LV}}h/{}^{\mathrm{kJ}}/_{\mathrm{kg}}$
360	0.312(3)	642(1)	1.21(1)	323.6(8)
380	0.600(5)	625(2)	2.23(2)	313(1)
400	1.069(6)	607(3)	3.84(2)	301(2)
420	1.792(7)	589(3)	6.30(3)	289(2)
440	2.86(1)	569.2(6)	9.94(6)	275.7(3)
460	4.36(2)	548.0(5)	15.18(9)	260.0(4)
480	6.42(3)	525(1)	22.6(1)	241.9(7)
500	9.16(5)	498(2)	33.0(1)	220(1)

Ethers (PTAMie)

Table D.5: Critical properties of ethers calculated with the polarizable PTAMie force field.

substance	simulation results			experimental data[2]		
	T_c/K	p_c/bar	$\rho_c/{}^{\mathrm{kg}}/_{\mathrm{m}^3}$	T_c/K	p_c/bar	$\rho_c/{}^{\mathrm{kg}}/_{\mathrm{m}^3}$
dimethyl ether	403.1(7)	55.9(8)	284(2)	400.1	53.7	270.9
diethyl ether	472.0(6)	37.8(3)	268.9(4)	466.7	36.4	264.6
di-n-propyl ether	534.25(9)	31.2(2)	265(1)	530.6	30.3	267.7
di-n-butyl ether	591(3)	26.5(6)	261(2)	584.0	23.0	267.0
methyl ethyl ether	439.4(7)	44.8(7)	274(2)	437.8	44.0	271.6
methyl n-propyl ether	480(1)	39.4(3)	272(2)	476.3	38.0	268.3

Table D.6: Tabulated values of vapor pressures, coexisting densities and enthalpies of vaporization for ethers calculated with the polarizable PTAMie force field.

dimethyl ether				
T/K	p^{sat}/bar	$\rho^{\mathrm{L}}/{}^{\mathrm{kg}}/_{\mathrm{m}^3}$	$\rho^{\mathrm{V}}/{}^{\mathrm{kg}}/_{\mathrm{m}^3}$	$\Delta^{\mathrm{LV}}h/{}^{\mathrm{kJ}}/_{\mathrm{kg}}$
250	1.13(1)	730(2)	2.58(2)	463.9(9)
270	2.46(1)	702(1)	5.33(1)	441.3(5)
290	4.75(2)	673(2)	9.95(1)	417(1)
310	8.39(1)	642(2)	17.20(6)	388.7(8)
330	13.75(2)	606.8(9)	28.1(2)	355.7(7)
350	21.26(9)	567.2(5)	44.6(6)	316(1)
370	31.4(2)	518(3)	70(1)	264(2)

diethyl ether				
T/K	p^{sat}/bar	$\rho^{\mathrm{L}}/{}^{\mathrm{kg}}/_{\mathrm{m}^3}$	$\rho^{\mathrm{V}}/{}^{\mathrm{kg}}/_{\mathrm{m}^3}$	$\Delta^{\mathrm{LV}}h/{}^{\mathrm{kJ}}/_{\mathrm{kg}}$
275	0.255(3)	714(2)	0.845(9)	386(1)
295	0.602(7)	693.8(9)	1.89(2)	371.3(5)
315	1.25(1)	671(3)	3.77(3)	355(1)
335	2.36(2)	647.8(4)	6.84(4)	336.5(2)
355	4.09(2)	622(2)	11.53(3)	317(1)
375	6.61(2)	595(1)	18.38(3)	294.7(5)
395	10.12(2)	566(1)	28.3(1)	270(1)
415	14.86(4)	532(2)	43.0(3)	241(1)
di-n-propyl ether				
T/K	p^{sat}/bar	$\rho^{\mathrm{L}}/{}^{\mathrm{kg}}/_{\mathrm{m}^3}$	$\rho^{\mathrm{V}}/{}^{\mathrm{kg}}/_{\mathrm{m}^3}$	$\Delta^{\mathrm{LV}}h/{}^{\mathrm{kJ}}/_{\mathrm{kg}}$
340	0.498(6)	682(4)	1.83(2)	320(2)
360	0.95(1)	663(4)	3.36(3)	309(2)
380	1.69(2)	643(2)	5.79(6)	297(1)
400	2.82(3)	620(2)	9.5(1)	283(1)
420	4.47(4)	596(2)	15.0(1)	267(1)
440	6.77(5)	570(1)	22.8(2)	248.3(9)
460	9.87(7)	541.2(6)	33.8(3)	226.4(5)
480	13.9(1)	507(1)	49.9(3)	199.0(4)
di-n-butyl ether				
T/K	p^{sat}/bar	$\rho^{\mathrm{L}}/{}^{\mathrm{kg}}/_{\mathrm{m}^3}$	$\rho^{\mathrm{V}}/{}^{\mathrm{kg}}/_{\mathrm{m}^3}$	$\Delta^{\mathrm{LV}}h/{}^{\mathrm{kJ}}/_{\mathrm{kg}}$
380	0.343(1)	677.9(3)	1.450(7)	304.8(6)
400	0.650(3)	659(4)	2.65(1)	294(2)
420	1.146(6)	641(3)	4.54(2)	282(2)
440	1.90(1)	620(1)	7.39(2)	269.2(3)
460	3.00(1)	599(2)	11.55(1)	255(1)
480	4.549(5)	576(1)	17.49(9)	239.4(5)
500	6.64(2)	551.1(7)	25.9(3)	221.2(5)
520	9.39(4)	521(3)	37.9(6)	199(2)

methyl ethyl ether				
T/K	p^{sat}/bar	$\rho^{\mathrm{L}}/{}^{\mathrm{kg}}/_{\mathrm{m}^3}$	$\rho^{\mathrm{V}}/{}^{\mathrm{kg}}/_{\mathrm{m}^3}$	$\Delta^{\mathrm{LV}}h/{}^{\mathrm{kJ}}/_{\mathrm{kg}}$
250	0.294(2)	733(5)	0.861(6)	420(3)
270	0.724(4)	709(2)	1.99(1)	403.9(9)
290	1.548(8)	685(2)	4.04(2)	387(1)
310	2.96(1)	660(2)	7.44(4)	367(1)
330	5.20(2)	632.8(8)	12.74(7)	346.1(6)
350	8.50(4)	603.4(6)	20.7(2)	321.5(7)
370	13.15(6)	571(2)	32.3(3)	293(2)
390	19.4(1)	534(2)	49.7(5)	258(2)
methyl n-propyl ether				
T/K	p^{sat}/bar	$\rho^{\mathrm{L}}/{}^{\mathrm{kg}}/_{\mathrm{m}^3}$	$\rho^{\mathrm{V}}/{}^{\mathrm{kg}}/_{\mathrm{m}^3}$	$\Delta^{\mathrm{LV}}h/{}^{\mathrm{kJ}}/_{\mathrm{kg}}$
290	0.417(5)	711(3)	1.33(1)	385(1)
310	0.913(8)	689(1)	2.77(2)	368.0(7)
330	1.79(1)	667(1)	5.20(2)	351(1)
350	3.19(2)	643(2)	8.96(1)	332.1(6)
370	5.29(1)	618(2)	14.54(3)	311.9(7)
390	8.280(8)	590.1(8)	22.66(5)	289.4(5)
410	12.359(5)	558(1)	34.3(1)	262.9(5)
430	17.76(5)	522(3)	51.7(4)	230.6(9)

Nitrogen (PTAMie)

Table D.7: Critical properties of nitrogen calculated with the polarizable PTAMie force field.

substance	simulation results			experimental data[1]		
	T_c/K	p_c/bar	$\rho_c/{}^{\mathrm{kg}}/_{\mathrm{m}^3}$	T_c/K	p_c/bar	$\rho_c/{}^{\mathrm{kg}}/_{\mathrm{m}^3}$
nitrogen	126.5(3)	34.4(3)	320(1)	126.2	34.0	313.2

Table D.8: Tabulated values of vapor pressures, coexisting densities and enthalpies of vaporization for nitrogen calculated with the polarizable PTAMie force field.

nitrogen				
T/K	p^{sat}/bar	$\rho^{\mathrm{L}}/{}^{\mathrm{kg}}/_{\mathrm{m}^3}$	$\rho^{\mathrm{V}}/{}^{\mathrm{kg}}/_{\mathrm{m}^3}$	$\Delta^{\mathrm{LV}}h/{}^{\mathrm{kJ}}/_{\mathrm{kg}}$
75	0.757(5)	816(11)	3.48(3)	205(1)
85	2.29(2)	769(5)	9.80(8)	191.3(7)
95	5.46(2)	717(2)	22.4(1)	173.5(5)
105	10.93(3)	656(4)	44.6(4)	150.9(9)
115	19.48(8)	581.3(4)	85(1)	120.1(7)

Mixtures (PTAMie)

Table D.9: Tabulated values of binary mixture properties calculated with the polarizable PTAMie force field.

n-hexane/nitrogen $T = 411\,\mathrm{K}$				
p^{sat}/bar	$x_{\mathrm{N_2}}/{}^{\mathrm{mol}}/_{\mathrm{mol}}$	$y_{\mathrm{N_2}}/{}^{\mathrm{mol}}/_{\mathrm{mol}}$	$\rho^{\mathrm{L}}/{}^{1}/_{\mathrm{Å}^3}$	$\rho^{\mathrm{V}}/{}^{1}/_{\mathrm{Å}^3}$
9.951	0.00829	0.36436	0.00375	0.00019
21.769	0.03156	0.67055	0.00380	0.00041
33.543	0.05480	0.76442	0.00385	0.00062
45.282	0.07816	0.80856	0.00390	0.00083
56.954	0.10140	0.83292	0.00395	0.00104
68.529	0.12427	0.84784	0.00400	0.00124
80.013	0.14685	0.85748	0.00405	0.00145
91.419	0.16937	0.86392	0.00411	0.00165
102.754	0.19183	0.86820	0.00416	0.00184
114.012	0.21403	0.87095	0.00421	0.00204
125.188	0.23574	0.87213	0.00427	0.00223
136.283	0.25692	0.87158	0.00432	0.00241
147.298	0.27788	0.86992	0.00437	0.00260
158.233	0.29854	0.86693	0.00443	0.00279
169.075	0.31964	0.86445	0.00448	0.00296
179.845	0.33953	0.85934	0.00453	0.00314
190.538	0.35864	0.85311	0.00459	0.00332
201.129	0.37851	0.84900	0.00464	0.00349
211.626	0.39855	0.84579	0.00469	0.00366

n-pentane/nitrogen $T = 398.3\,\mathrm{K}$				
$p^{\mathrm{sat}}/\mathrm{bar}$	$x_{\mathrm{N_2}}/\mathrm{mol}/\mathrm{mol}$	$y_{\mathrm{N_2}}/\mathrm{mol}/\mathrm{mol}$	$\rho^{\mathrm{L}}/1/\mathrm{Å}^3$	$\rho^{\mathrm{V}}/1/\mathrm{Å}^3$
10.861	0.00193	0.06371	0.00416	0.00024
22.609	0.02770	0.46864	0.00421	0.00047
34.288	0.05389	0.60968	0.00426	0.00070
45.948	0.07957	0.67803	0.00431	0.00092
57.545	0.10429	0.71845	0.00436	0.00115
69.103	0.12809	0.74364	0.00441	0.00137
80.628	0.15192	0.75905	0.00446	0.00160
92.115	0.17653	0.76810	0.00450	0.00182
103.552	0.20168	0.77200	0.00455	0.00204
114.929	0.22688	0.77205	0.00459	0.00227
126.233	0.25254	0.77130	0.00463	0.00249
137.498	0.27696	0.76605	0.00468	0.00272
dimethyl ether/nitrogen $T = 318.15\,\mathrm{K}$				
$p^{\mathrm{sat}}/\mathrm{bar}$	$x_{\mathrm{N_2}}/\mathrm{mol}/\mathrm{mol}$	$y_{\mathrm{N_2}}/\mathrm{mol}/\mathrm{mol}$	$\rho^{\mathrm{L}}/1/\mathrm{Å}^3$	$\rho^{\mathrm{V}}/1/\mathrm{Å}^3$
11.298	0.00164	0.07981	0.00818	0.00030
20.874	0.01404	0.44508	0.00823	0.00054
30.459	0.02731	0.58489	0.00826	0.00077
40.107	0.04131	0.65844	0.00828	0.00102
49.835	0.05531	0.70056	0.00830	0.00127
59.548	0.06885	0.72665	0.00831	0.00151
69.255	0.08218	0.74520	0.00833	0.00176
78.990	0.09622	0.75945	0.00834	0.00201
88.766	0.11168	0.77040	0.00835	0.00227
98.570	0.12839	0.77836	0.00836	0.00252
108.367	0.14536	0.78368	0.00837	0.00276
118.136	0.16176	0.78659	0.00837	0.00301
127.876	0.17743	0.78726	0.00838	0.00326
137.603	0.19262	0.78605	0.00839	0.00351
147.321	0.20762	0.78307	0.00840	0.00377
157.020	0.22286	0.77892	0.00840	0.00402
166.707	0.23822	0.77233	0.00840	0.00429
176.387	0.25423	0.76421	0.00840	0.00457
186.085	0.27020	0.75267	0.00841	0.00486
195.794	0.28668	0.73968	0.00841	0.00516
205.497	0.30406	0.72710	0.00841	0.00546
215.222	0.31985	0.71090	0.00843	0.00576

D.4 Results - Non-Polarizable TAMie Force Field

All pure substance results for the non-polarizable TAMie force field are calculated with the Ewald summation.

Table D.10: Absolute average deviations (saturation pressure p^{sat}, liquid density ρ^{L}, enthalpy of vaporization $\Delta^{\mathrm{LV}}h$, critical temperature T_c) of the non-polarizable TAMie force field from quasi-experimental data[1–3].

substance	AAD p^{sat}/%	AAD ρ^{L}/%	AAD $\Delta^{\mathrm{LV}}h$/%	AD T_c/%
ethane	0.67	0.66	1.88	0.27
propane	0.58	0.47	1.74	0.53
n-butane	1.98	1.09	0.79	0.24
n-hexane	2.93	0.67	2.45	0.84
n-octane	2.46	0.51	1.70	1.02
dimethyl ether	0.33	0.79	1.51	0.6
diethyl ether	7.1	1.26	2.10	1.47
di-n-propyl ether	3.92	2.42	0.74	0.57
di-n-butyl ether	3.34	0.84	2.65	1.39
methyl ethyl ether	4.56	0.84	1.82	1.06
methyl n-propyl ether	4.73	1.31	–[a]	1.35
nitrogen	0.59	0.85	0.61	0.15

[a] no reasonable quasi-experimental data available

N-Alkanes (TAMie)

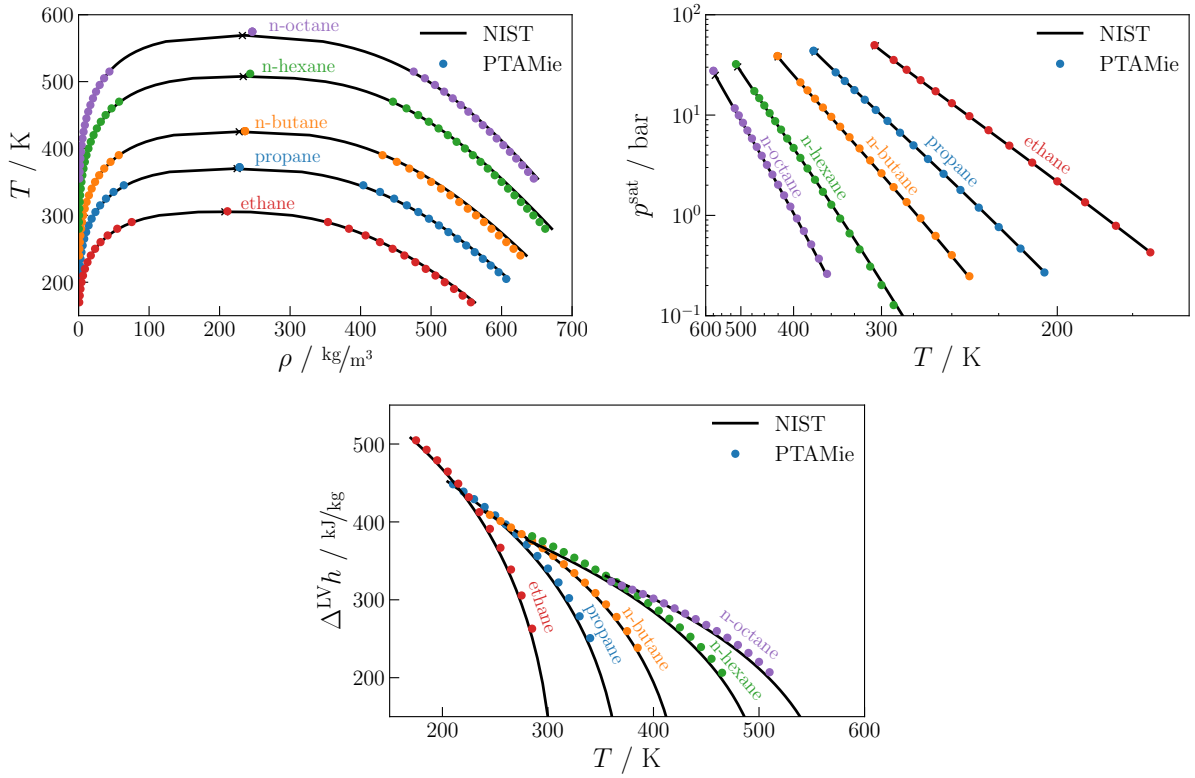

Figure D.1: Vapor-liquid coexistence curve, vapor pressures, and enthalpy of vaporization of simulated n-alkanes. Symbols represent simulation results for the TAMie force field and black solid lines and crosses are quasi-experimental data[1].

Table D.11: Critical properties of n-alkanes calculated with the non-polarizable TAMie force field.

substance	simulation results			experimental data[1]		
	T_c/K	p_c/bar	ρ_c/kg/m³	T_c/K	p_c/bar	ρ_c/kg/m³
ethane	306.1	49.8	211.1	305.3	49.0	207.5
propane	371.9	43.7	228.3	369.9	42.5	224.9
n-butane	426.0	38.8	236.1	425.0	38.0	227.8
n-hexane	511.9	32.2	243.4	507.6	30.2	233.5
n-octane	574.7	27.6	246.4	568.9	24.9	232.3

Table D.12: Tabulated values of vapor pressures, coexisting densities and enthalpies of vaporization for n-alkanes calculated with the non-polarizable TAMie force field.

ethane				
T/K	p^{sat}/bar	$\rho^{\mathrm{L}}/\mathrm{kg/m^3}$	$\rho^{\mathrm{V}}/\mathrm{kg/m^3}$	$\Delta^{\mathrm{LV}}h/\mathrm{kJ/kg}$
175	0.59	550.50	1.24	504.72
195	1.73	525.92	3.36	479.07
215	4.10	499.44	7.53	449.09
235	8.34	470.08	14.85	412.56
255	15.10	436.60	26.99	366.79
275	25.15	395.77	47.46	305.55
propane				
T/K	p^{sat}/bar	$\rho^{\mathrm{L}}/\mathrm{kg/m^3}$	$\rho^{\mathrm{V}}/\mathrm{kg/m^3}$	$\Delta^{\mathrm{LV}}h/\mathrm{kJ/kg}$
210	0.36	601.29	0.92	448.32
230	0.96	579.02	2.29	429.25
250	2.17	555.88	4.87	408.38
270	4.28	530.96	9.27	384.29
290	7.66	504.15	16.27	356.25
310	12.67	473.86	27.03	322.26
330	19.72	437.88	43.85	278.85
n-butane				
T/K	p^{sat}/bar	$\rho^{\mathrm{L}}/\mathrm{kg/m^3}$	$\rho^{\mathrm{V}}/\mathrm{kg/m^3}$	$\Delta^{\mathrm{LV}}h/\mathrm{kJ/kg}$
245	0.32	621.84	0.92	408.98
265	0.77	601.36	2.09	392.82
285	1.62	580.39	4.18	375.65
305	3.06	557.87	7.61	356.30
325	5.30	533.66	12.93	334.29
345	8.59	507.14	20.86	308.67
365	13.17	477.31	32.59	277.97
385	19.35	441.61	50.75	238.38

n-hexane				
T/K	$p^{\mathrm{sat}}/\mathrm{bar}$	$\rho^{\mathrm{L}}/\mathrm{kg/m^3}$	$\rho^{\mathrm{V}}/\mathrm{kg/m^3}$	$\Delta^{\mathrm{LV}}h/\mathrm{kJ/kg}$
285	0.10	658.01	0.37	381.64
305	0.25	640.63	0.88	368.31
325	0.55	622.87	1.85	354.05
345	1.09	604.51	3.51	338.80
365	1.98	585.37	6.12	322.66
385	3.32	564.71	9.99	305.23
405	5.25	542.14	15.57	286.09
425	7.90	517.23	23.47	264.53
445	11.42	489.39	34.74	239.32
465	16.01	455.89	51.85	206.32
n-octane				
T/K	$p^{\mathrm{sat}}/\mathrm{bar}$	$\rho^{\mathrm{L}}/\mathrm{kg/m^3}$	$\rho^{\mathrm{V}}/\mathrm{kg/m^3}$	$\Delta^{\mathrm{LV}}h/\mathrm{kJ/kg}$
360	0.31	641.61	1.21	323.30
380	0.60	625.03	2.23	312.95
400	1.07	607.14	3.84	301.58
420	1.79	588.13	6.30	289.03
440	2.85	568.27	9.92	275.22
460	4.36	547.52	15.13	259.86
480	6.41	524.71	22.49	242.03
500	9.13	498.47	32.89	220.30

Ethers (TAMie)

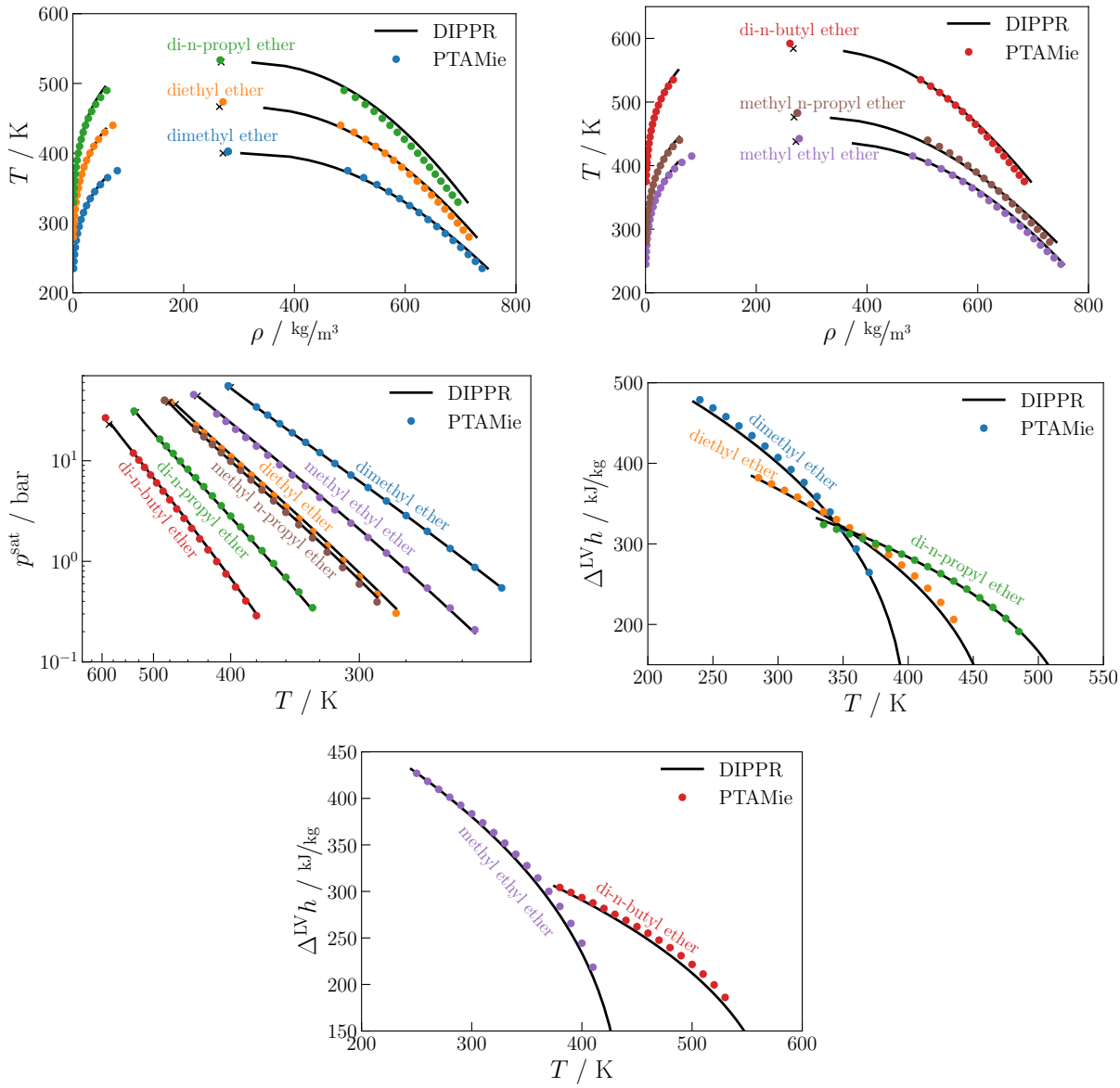

Figure D.2: Vapor-liquid coexistence curve, vapor pressures, and enthalpy of vaporization of simulated ethers. Symbols represent simulation results for the TAMie force field and black solid lines and crosses are quasi-experimental data[2]. Quasi-Experimental vapor density is approximated up to $0.25 \cdot \rho_c$ using the second virial coefficient.

Table D.13: Critical properties of ethers calculated with the non-polarizable TAMie force field.

substance	simulation results			experimental data[2]		
	T_c/K	p_c/bar	ρ_c/kg/m³	T_c/K	p_c/bar	ρ_c/kg/m³
dimethyl ether	402.5	55.4	280.2	400.1	53.7	270.9
diethyl ether	473.6	38.1	270.9	466.7	36.4	264.6
di-n-propyl ether	533.6	31.1	266.1	530.6	30.3	267.7
di-n-butyl ether	592.1	26.7	261.0	584.0	23.0	267.0
methyl ethyl ether	442.4	45.4	277.7	437.8	44.0	271.6
methyl n-propyl ether	482.7	39.9	274.1	476.3	38.0	268.3

Table D.14: Tabulated values of vapor pressures, coexisting densities and enthalpies of vaporization for ethers calculated with the non-polarizable TAMie force field.

dimethyl ether				
T/K	p^{sat}/bar	ρ^{L}/kg/m³	ρ^{V}/kg/m³	$\Delta^{\mathrm{LV}}h$/kJ/kg
240	0.69	732.92	1.63	478.87
260	1.64	707.05	3.64	457.88
280	3.38	679.57	7.17	434.38
300	6.26	649.20	12.93	407.20
320	10.67	616.64	21.78	376.25
340	17.02	580.22	35.14	339.55
360	25.78	537.39	55.71	293.73
diethyl ether				
T/K	p^{sat}/bar	ρ^{L}/kg/m³	ρ^{V}/kg/m³	$\Delta^{\mathrm{LV}}h$/kJ/kg
265	0.15	730.53	0.51	396.37
285	0.38	710.02	1.22	382.04
305	0.85	688.91	2.59	366.57
325	1.68	665.55	4.94	349.00
345	3.04	641.39	8.66	330.18
365	5.10	615.03	14.19	309.36
385	8.03	586.59	22.23	286.34
405	12.05	555.32	33.94	260.11
425	17.41	518.32	51.59	227.31

di-n-propyl ether				
T/K	p^{sat}/bar	$\rho^{\mathrm{L}}/\mathrm{kg}/\mathrm{m}^3$	$\rho^{\mathrm{V}}/\mathrm{kg}/\mathrm{m}^3$	$\Delta^{\mathrm{LV}}h/\mathrm{kJ}/\mathrm{kg}$
305	0.12	718.63	0.50	340.01
325	0.29	700.05	1.09	329.48
345	0.59	680.00	2.14	318.18
365	1.10	659.45	3.86	306.44
385	1.93	638.93	6.58	294.10
405	3.18	616.79	10.69	279.86
425	4.98	592.23	16.70	263.09
445	7.48	565.71	25.20	243.91
465	10.81	536.04	37.24	221.16
485	15.15	500.28	55.33	191.25
di-n-butyl ether				
T/K	p^{sat}/bar	$\rho^{\mathrm{L}}/\mathrm{kg}/\mathrm{m}^3$	$\rho^{\mathrm{V}}/\mathrm{kg}/\mathrm{m}^3$	$\Delta^{\mathrm{LV}}h/\mathrm{kJ}/\mathrm{kg}$
380	0.34	679.58	1.45	304.27
400	0.65	661.39	2.63	293.40
420	1.14	642.27	4.51	281.71
440	1.89	622.12	7.34	268.93
460	2.99	601.21	11.48	255.14
480	4.52	578.45	17.40	239.61
500	6.61	552.88	25.77	221.56
520	9.35	523.23	37.71	199.63
methyl ethyl ether				
T/K	p^{sat}/bar	$\rho^{\mathrm{L}}/\mathrm{kg}/\mathrm{m}^3$	$\rho^{\mathrm{V}}/\mathrm{kg}/\mathrm{m}^3$	$\Delta^{\mathrm{LV}}h/\mathrm{kJ}/\mathrm{kg}$
250	0.27	744.17	0.79	426.99
270	0.67	719.32	1.84	409.71
290	1.45	695.62	3.77	392.65
310	2.80	670.36	7.00	373.77
330	4.94	642.07	12.05	351.91
350	8.12	612.85	19.58	327.67
370	12.61	581.75	30.65	300.04
390	18.72	544.51	47.14	265.61
410	26.81	497.10	73.82	218.55

methyl n-propyl ether				
T/K	p^{sat}/bar	ρ^{L}/kg/m³	ρ^{V}/kg/m³	$\Delta^{\mathrm{LV}}h$/kJ/kg
270	0.16	739.96	0.53	403.99
290	0.40	718.89	1.25	388.85
310	0.87	696.81	2.62	372.54
330	1.71	674.23	4.95	355.14
350	3.07	650.39	8.59	336.42
370	5.11	624.82	14.00	316.11
390	8.03	597.03	21.85	293.63
410	12.02	566.28	33.18	267.90
430	17.32	530.59	49.81	236.53

Nitrogen (TAMie)

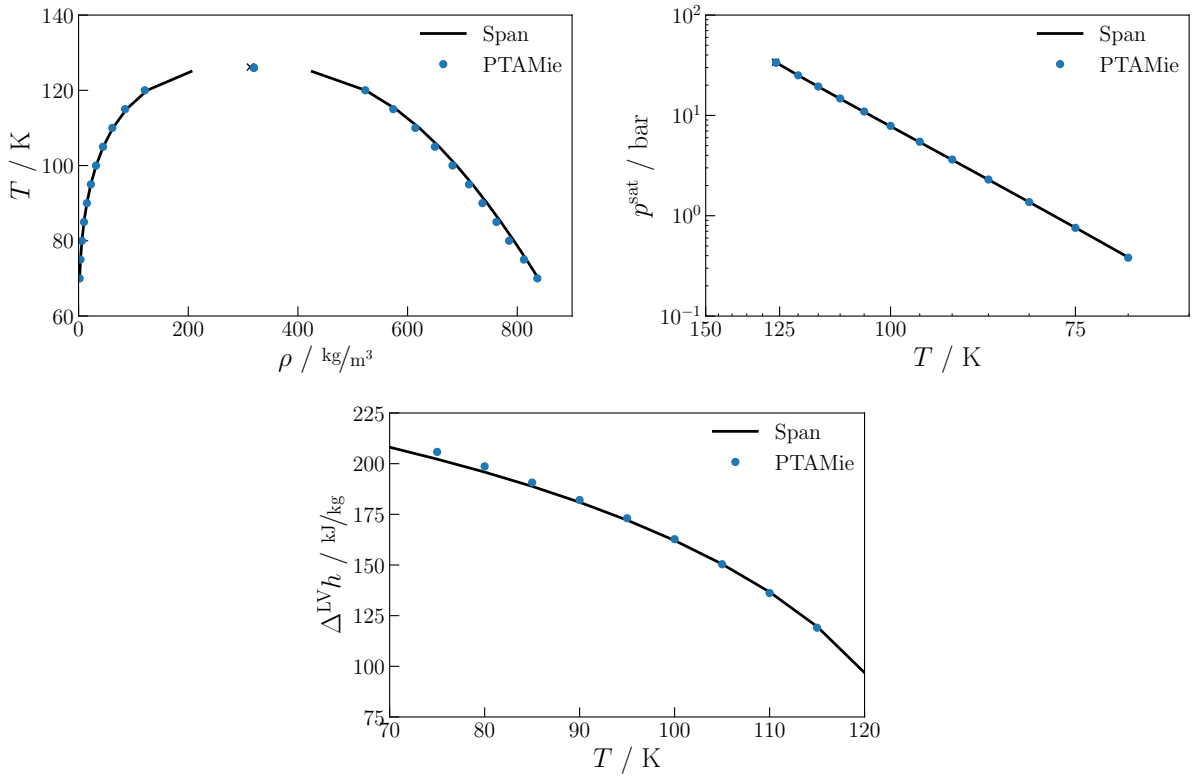

Figure D.3: Vapor-liquid coexistence curve, vapor pressures, and enthalpy of vaporization of simulated nitrogen. Symbols represent simulation results for the TAMie force field and black solid lines and crosses are quasi-experimental data[3].

Table D.15: Critical properties of nitrogen calculated with the non-polarizable TAMie force field.

substance	simulation results			experimental data[1]		
	T_c/K	p_c/bar	ρ_c/kg/m³	T_c/K	p_c/bar	ρ_c/kg/m³
nitrogen	126.0	33.6	319.6	126.2	34.0	313.2

Table D.16: Tabulated values of vapor pressures, coexisting densities and enthalpies of vaporization for nitrogen calculated with the non-polarizable TAMie force field.

nitrogen				
T/K	p^{sat}/bar	ρ^{L}/kg/m³	ρ^{V}/kg/m³	$\Delta^{\mathrm{LV}}h$/kJ/kg
75	0.76	812.25	3.49	205.80
85	2.30	761.96	9.83	190.67
95	5.47	711.93	22.39	173.09
105	10.93	649.74	44.54	150.37
115	19.42	573.86	84.84	119.05

Mixtures (TAMie)

Table D.17: Tabulated values of binary mixture properties calculated with the non-polarizable TAMie force field.

n-hexane/nitrogen $T = 411\,\mathrm{K}$				
p^{sat}/bar	$x_{\mathrm{N_2}}$/mol/mol	$y_{\mathrm{N_2}}$/mol/mol	ρ^{L}/1/Å³	ρ^{V}/1/Å³
9.862	0.00845	0.36922	0.00374	0.00019
21.722	0.03268	0.67398	0.00379	0.00041
33.503	0.05642	0.76656	0.00385	0.00062
45.216	0.07969	0.81022	0.00390	0.00083
56.859	0.10256	0.83494	0.00395	0.00104
68.427	0.12498	0.85027	0.00400	0.00124
79.917	0.14689	0.86017	0.00406	0.00144
91.326	0.16834	0.86661	0.00411	0.00164
102.655	0.18945	0.87051	0.00416	0.00184
113.901	0.21038	0.87262	0.00421	0.00203
125.065	0.23116	0.87310	0.00426	0.00222
136.145	0.25184	0.87230	0.00432	0.00241
147.141	0.27251	0.87057	0.00437	0.00259
158.056	0.29296	0.86752	0.00442	0.00278
168.892	0.31327	0.86357	0.00447	0.00296
179.652	0.33322	0.85851	0.00453	0.00314
190.320	0.35379	0.85451	0.00458	0.00332
200.913	0.37357	0.84928	0.00463	0.00349
211.442	0.39177	0.84203	0.00469	0.00366

n-pentane/nitrogen $T = 398.3\,\mathrm{K}$				
$p^{\mathrm{sat}}/\mathrm{bar}$	$x_{\mathrm{N_2}}/{}^{\mathrm{mol}}/_{\mathrm{mol}}$	$y_{\mathrm{N_2}}/{}^{\mathrm{mol}}/_{\mathrm{mol}}$	$\rho^{\mathrm{L}}/{}^{1}/_{\mathrm{Å}^3}$	$\rho^{\mathrm{V}}/{}^{1}/_{\mathrm{Å}^3}$
10.806	0.00191	0.06363	0.00417	0.00024
22.590	0.02737	0.47312	0.00422	0.00047
34.333	0.05255	0.61212	0.00427	0.00070
46.022	0.07791	0.68010	0.00432	0.00092
57.662	0.10314	0.71919	0.00436	0.00115
69.258	0.12813	0.74297	0.00441	0.00137
80.799	0.15306	0.75764	0.00446	0.00160
92.284	0.17807	0.76605	0.00450	0.00182
103.716	0.20327	0.76989	0.00455	0.00205
115.093	0.22881	0.77079	0.00459	0.00227
126.413	0.25432	0.76880	0.00463	0.00250
137.668	0.27995	0.76560	0.00467	0.00272
148.862	0.30508	0.76091	0.00472	0.00294
dimethyl ether/nitrogen $T = 318.15\,\mathrm{K}$				
$p^{\mathrm{sat}}/\mathrm{bar}$	$x_{\mathrm{N_2}}/{}^{\mathrm{mol}}/_{\mathrm{mol}}$	$y_{\mathrm{N_2}}/{}^{\mathrm{mol}}/_{\mathrm{mol}}$	$\rho^{\mathrm{L}}/{}^{1}/_{\mathrm{Å}^3}$	$\rho^{\mathrm{V}}/{}^{1}/_{\mathrm{Å}^3}$
11.256	0.00146	0.08047	0.00811	0.00030
20.788	0.01431	0.44707	0.00813	0.00053
30.373	0.02732	0.58844	0.00815	0.00077
39.991	0.04085	0.66237	0.00816	0.00101
49.637	0.05469	0.70649	0.00818	0.00125
59.300	0.06826	0.73514	0.00819	0.00149
68.979	0.08137	0.75466	0.00821	0.00174
78.676	0.09434	0.76821	0.00823	0.00198
88.386	0.10771	0.77760	0.00824	0.00223
98.108	0.12183	0.78386	0.00826	0.00248
107.835	0.13654	0.78761	0.00827	0.00273
117.563	0.15145	0.78932	0.00829	0.00298
127.288	0.16634	0.78928	0.00830	0.00323
137.006	0.18124	0.78767	0.00831	0.00349
146.711	0.19634	0.78438	0.00832	0.00374
156.398	0.21186	0.77943	0.00832	0.00400
166.066	0.22805	0.77304	0.00833	0.00426
175.712	0.24520	0.76565	0.00833	0.00453
185.346	0.26260	0.75573	0.00832	0.00480
194.967	0.28029	0.74418	0.00832	0.00508
204.577	0.29760	0.73077	0.00833	0.00537
214.134	0.31616	0.72019	0.00832	0.00563

Bibliography

[1] Linstrom, P., and Mallard, W., Eds. *NIST Chemistry WebBook, NIST Standard Reference Database Number 69*; National Institute of Standards and Technology: Gaithersburg MD, 20899; http://doi.org/10.18434/T4D303, (retrieved May 2013).

[2] Rowley, R. L., Wilding, W. V., Oscarson, J. L., Yang, Y., Zundel, N. A., Daubert, T. E., and Danner, R. P. *DIPPR Data Compilation of Pure Chemical Properties*; AIChE, New York, 2009.

[3] Span, R., Lemmon, E. W., Jacobsen, R. T., Wagner, W., and Yokozeki, A. (2000) A Reference Equation of State for the Thermodynamic Properties of Nitrogen for Temperatures from 63.151 to 1000 K and Pressures to 2200 MPa. *Journal of Physical and Chemical Reference Data 29*, 1361–1433.

Statement on authorship

This thesis led to publications that have been published or submitted previously. In the following, these publications are listed together with a statement on the contributions of the author of the present thesis.

- Chapter 2: C. Waibel and J. Gross: Modification of the Wolf Method and Evaluation for Molecular Simulation of Vapor–Liquid Equilibria, Journal of Chemical Theory and Computation, 14 (4), 2018, 2198-2206.
  The author planned and carried out the study and wrote the manuscript.

- Chapter 3: C. Waibel, F. M. Feinler and J. Gross: A Modified Shifted Force Approach to the Wolf Summation, Journal of Chemical Theory and Computation, 2018, submitted [in the meantime it was published with minor modifications in Journal of Chemical Theory and Computation, 15 (1), 2019, 572-583].
  The author planned and carried out the study and wrote the manuscript. In the development of the modified shifted force method the author was supported by Mathias Feinler during his bachelor thesis. The supervision of the bachelor thesis was provided by J. Gross and, whereby the daily supervision and a significant part of the scientific exchange was given with the author.

- Chapter 4: C. Waibel, R. Stierle, and J. Gross: Transferability of cross-interaction pair potentials: Vapor-liquid phase equilibria of n-alkane/nitrogen mixtures using the TAMie force field, Fluid Phase Equilibria, 456, 2018, 124-130.
  The author estimated the binary interaction parameters of the PCP-SAFT equation of state in cooperation with Rolf Stierle. Together they wrote the introduction and the corresponding part of the manuscript. All remaining parts of the study were carried out and written by the author.

- Chapter 5: C. Waibel and J. Gross: Polarizable Transferable Anisotropic United-Atom Force Field Based on the Mie Potential for Phase Equilibria: n-Alkanes, Ethers, and Nitrogen, Journal of Chemical Theory and Computation, 2018, submitted [in the meantime it was published with minor modifications in Journal of

Chemical Theory and Computation, 15 (4), 2019, 2561-2573].
The author planned and carried out the study and wrote the manuscript.